ACS Partner Journal
CHEM & BIO ENGINEERING

pubs.acs.org/ChemBioEng Article

Fundamental Insights into Intracrystalline Diffusional Influences on Mixture Separations in Fixed Bed Adsorbers

Published as part of Chem & Bio Engineering virtual special issue "Advanced Separation Materials and Processes".

Rajamani Krishna*

Cite This: *Chem Bio Eng.* 2024, 1, 53−66 Read Online

ACCESS | Metrics & More | Article Recommendations | Supporting Information

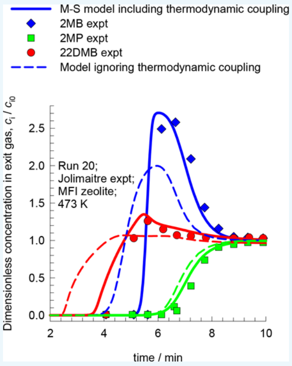

ABSTRACT: This article has the objective of elucidating the variety of factors that quantify influences of intracrystalline diffusion on mixture separations in fixed bed devices packed with microporous crystalline adsorbents such as metal-organic frameworks (MOFs) and zeolites. Such diffusional influences may act either synergistically or anti-synergistically to the mixture adsorption equilibrium, providing the ratio of the diffusivities $Đ_1/Đ_2 \gg 1$. Experimental data on transient mixture uptake inside single crystals display overshoots in the loadings of the more mobile guest species; this overshoot can be quantitatively captured by use of the Maxwell−Stefan (M-S) diffusion formulation that takes proper account of thermodynamic coupling influences; if such thermodynamic influences are ignored, as is done in the Linear Driving Force (LDF) model, overshoots are not realizable. The use of the M-S formulation to simulate transient breakthroughs in fixed bed adsorbers provides a quantitative match with experiments; the match is significantly poorer if thermodynamic coupling effects are ignored. For a fixed bed of length L, packed with adsorbent particles of radius r_c and operating with an interstitial gas velocity, v, the diffusional influences are quantified by two separate parameters: (a) diffusional time constant, $Đ_1/r_c^2$, and gas−particle contact time L/v. The transient breakthroughs are uniquely dependent on the product $(Đ_1/r_c^2)(L/v)$; this result is of practical importance for scaling up from small scale laboratory units to large scale industrial units that use different particle sizes, bed dimensions, and gas velocities.

KEYWORDS: *fixed bed adsorber, kinetic separations transient uptake, Maxwell−Stefan equations, microporous crystalline adsorbents, thermodynamic coupling, transient breakthrough, uphill diffusion*

1. INTRODUCTION

Though the initial research activities in the development of metal-organic frameworks (MOFs) were largely triggered by applications to CO_2 capture, more recent developments have expanded the scope and breadth of the targeted mixtures to include C_2H_2/CO_2, SF_6/N_2, C_2H_4/C_2H_6, C_3H_6/C_3H_8, C_3H_4(propyne)/C_3H_6, propyne/propadiene, alkane isomers, and C4 hydrocarbon separations. The primary aim in all such MOF developments is to supplant currently used separation technologies such as distillation, absorption, and extraction by pressure swing adsorption (PSA) technologies utilizing MOFs as adsorbents. While technologies such as distillation operate under *steady-state* conditions, PSA technologies involve *transient* operations, consisting of adsorption−desorption cycles carried out in multiple beds. The sequence of component breakthroughs and the product purities that are realizable in adsorption/desorption cycles are often governed by a combination of mixture adsorption equilibrium and intracrystalline diffusion of guest molecules inside the pores of the host materials.

The focus of this article is on two different scenarios in which intradiffusional influences act (a) synergistically or (b) anti-synergistically to the mixture adsorption equilibrium. The latter scenario is exploited to reverse the hierarchy of the component breakthroughs. In the published literature, the term "kinetic separations" is often used to imply anti-synergistic diffusional influences and selectivity reversals.[1−4] Here, we analyze both categories of diffusional influences under the common moniker of kinetic separations.

To elucidate the rationale for harnessing diffusional influences, let us consider separation of 50/50 C_3H_6/C_3H_8 mixtures in a fixed bed adsorber packed with Fe_2(dobdc). Bloch et al.[5] have established that each alkene molecule attaches *side-on* to an Fe(II) atom in the framework; the alkene/alkane selectivities are about 15. Fe_2(dobdc) has one-dimensional hexagonal channels of 11 Å, and intracrystalline diffusional influences are not of significant importance.[6,7] Figure 1 shows

Received: October 6, 2023
Revised: November 5, 2023
Accepted: November 19, 2023
Published: January 4, 2024

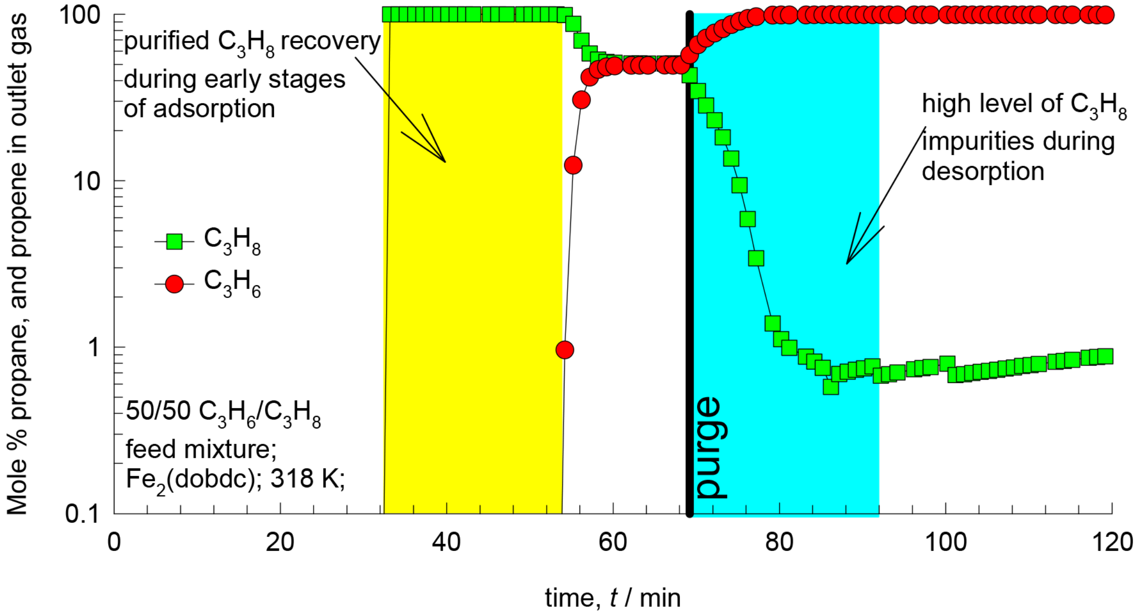

Figure 1. Adsorption/desorption cycles for separation of 50/50 C_3H_6/C_3H_8 mixtures in a fixed bed adsorber packed with Fe_2(dobdc)[5] and operating at 318 K. The desorption cycle is initiated by nitrogen purge.

the experimental data of Bloch et al.[5] on the adsorption/desorption cycles. For a certain interval of time during the adsorption cycle (indicated by a yellow bar), the saturated alkane of high purity can be recovered.

The desorption cycle is initiated by a nitrogen purge. During the early stages of desorption (indicated by a cyan colored bar), it is evident that the product gas mixture contains significantly more than about 0.5% C_3H_8. Polymer grade alkenes, with purities >99.95%, cannot be recovered from the cumulative desorbed gas mixture. This is due to the presence of finite amounts of saturated alkane at the termination of the adsorption cycle. Broadly speaking, the attainment of high alkene purities in the desorption cycle is only possible if the saturated alkanes are virtually excluded from the pores. This objective is met with NbOFFIVE-1-Ni (=KAUST-7),[8] UTSA-280,[9] ZIF-8,[10,11] Chabazite (CHA) zeolite,[3,12] or Co-gallate,[13−15] that almost completely exclude the saturated alkane from the pores due to strong diffusional limitations.

Diffusional influences can also be harnessed to act synergistically with the mixture adsorption equilibrium in order to enhance the efficacy of separations. As illustration of such synergy, we consider the experimental data of Jolimaître et al.[16] for separations of mixtures of 2-methylbutane (2MB), 2-methylpentane (2MP), and 2,2-dimethylbutane (22DMB) mixtures at 473 K in a fixed bed packed with extrudates of Mobil Five (MFI) zeolite. The Research Octane Numbers (RONs) of these alkanes are 93.5, 74.5, and 94. The objective of this mixture separation is to produce a high-RON product for incorporation into the gasoline pool. Figure 2 panels a and b present the transient breakthrough experimental data (indicated by colored symbols) of Jolimaître et al.[16] for (a) 2MP/22DMB binary mixtures and (b) 2MB/2MP/22DMB ternary mixtures at 473 K. The experimental data on unary isotherms can be fitted with the 1-site Langmuir isotherm model $q = q_{sat}bp/(1 + bp)$; the ratios of Langmuir constants are $b_{2MP}/b_{2MB} = 3.08$, $b_{2MP}/b_{22DMB} = 1.78$, and $b_{22DMB}/b_{2MB} = 1.73$. The experimental data on the unary intracrystalline Maxwell−Stefan (M-S) diffusivities, determined from unary breakthrough experiments,[16] for each of the three guest alkanes show $Đ_{2MB}/Đ_{2MP} = 1.5$. $Đ_{2MB}/Đ_{22DMB} = 80$, and $Đ_{2MB}/Đ_{22DMB} = 120$; see Figure S13 and published works.[17−22] For 2MP/22DMB mixtures, both adsorption and diffusion favor 2MP; consequently, 22DMB with the higher RON is rejected into the gas phase, as is desirable. The continuous solid lines in Figure 2a are simulations of the breakthrough ignoring diffusional influences. It is noteworthy that the difference in the breakthrough times of 22DMB and 2MP is larger in the experiments than in the simulations due to adsorption/diffusion synergy. The net result of this synergy is that the productivity of 22DMB, with higher RON, is enhanced.

For separation of 2MB/2MP/22DMB ternary mixtures, the experiments show that the component to break through the earliest is 22DMB, the component that has the intermediate adsorption strength. Indeed, the breakthrough simulation ignoring diffusional influences (indicated by the continuous solid lines) anticipates that 2MB should break through first. For the 2MB/22DMB pair, there is anti-synergy between adsorption and diffusion. The reversal in the hierarchy of breakthroughs must be ascribed to diffusional influences that strongly hinders the uptake of the bulky 22DMB. Earlier breakthrough of 22DMB is desirable because the di-branched isomer 22DMB has the higher value of RON, than the mono-branched 2MB, and 2MP. The data in Figure 2a,b highlight both synergistic and anti-synergistic influences, for the respective 2MP/22DMB and 2MB/22DMB binary pairs. Both of these influences are beneficial for high-RON product recovery in the 2MB/2MP/22DMB ternary mixture.

The experimental data presented in Figure 2 were conducted in a laboratory scale fixed bed with a length of 0.798 m with an internal diameter of 0.016 m. The interstitial gas velocity, v, used in the experiments is 0.02 m s^{-1} and the average contact time between the feed gas mixture and the MFI extrudates (of 1 mm × 4 mm size) ≈ 40 s. The scaleup of data for kinetically driven separations from laboratory to commercial scale units is not straightforward. Commercial scale fixed bed adsorbers usually operate at significantly higher values of the interstitial gas velocity v than in laboratory units, by a factor of about 10−100;

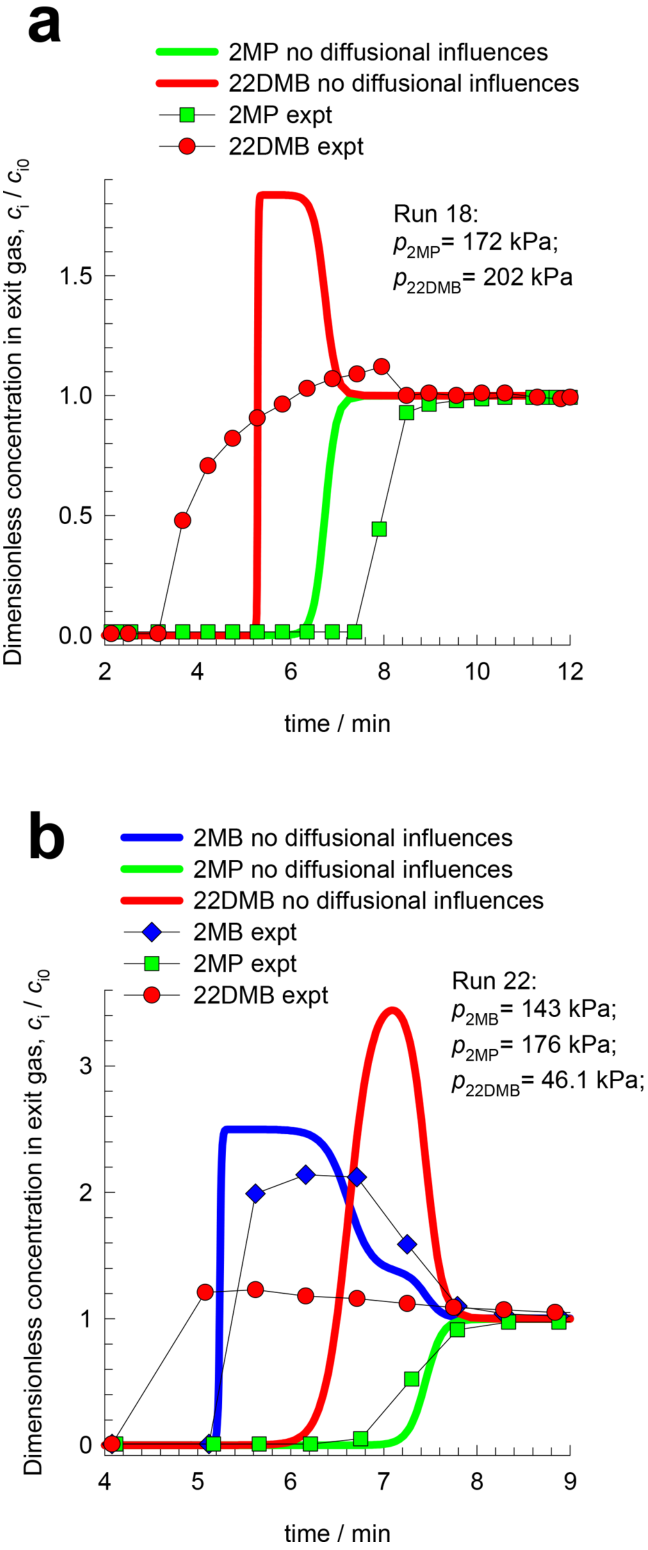

Figure 2. Transient breakthrough experiments of Jolimaître et al.[16] for (a) 2MP/22DMB binary mixtures and (b) 2MB/2MP/22DMB ternary mixtures at 473 K. The experimental data correspond to Runs 18 and 22. The continuous colored lines are the simulations in which diffusional influences are ignored. The input data on unary isotherms and simulation details are provided in the Supporting Information.

see Figure S60. From pressure drop considerations, the particle sizes used in commercial units are often larger than those in laboratory scale equipment. The important question that arises is the following: How do we ensure that the beneficial synergistic and anti-synergistic influences witnessed in the laboratory experiments also manifest when scaling up to industrial scale units? To answer this question, we need a fundamental understanding of the variety of factors that quantify intracrystalline diffusion influences in fixed bed mixture separations using microporous crystalline adsorbents; the development of such insights is the primary objective of this article. The secondary objective of this article is to specify the minimum level of complexity that is essential in the modeling of transient breakthroughs for mixture separations. Such breakthrough simulation models are essential in the development of PSA technologies, which serve as natural end goals of MOF developments.

The Supporting Information provides (a) derivation of the Maxwell−Stefan diffusion formulation, (b) computational modeling details of transient mixture uptakes within crystals and adsorber breakthroughs, (c) structural details of host materials discussed in this article, (d) data on unary isotherm data fits used for Ideal Adsorbed Solution Theory (IAST) calculations for all guest/host combinations, (e) guest diffusivities, and (f) detailed simulation results for transient breakthroughs for several different mixtures.

2. TRANSIENT MIXTURE UPTAKE

We begin our discussions with the modeling of transient mixture uptake within single microporous crystals. The set of partial differential equations describing the time derivative of the component molar loadings in a spherical crystallite of radius r_c is[23,24]

$$\rho \frac{\partial q_i(r, t)}{\partial t} = -\frac{1}{r^2}\frac{\partial}{\partial r}(r^2 N_i) \tag{1}$$

The Maxwell−Stefan equation describing the dependence of the intracrystalline fluxes N_i on the gradients of component chemical potentials is[23−26]

$$N_i = -\rho Đ_i \frac{q_i}{RT}\frac{\partial \mu_i}{\partial r} \tag{2}$$

The M-S diffusivity $Đ_i$ equals the corresponding diffusivity for a unary system, determined at the same pore occupancy; the diffusivity for any species i in a mixture remains invariant to the choice of the partner species.[6,25−29] Other variables in eqs 1 and 2, are described in the Nomenclature section.

We relate the $\partial \mu_i / \partial r$ to the gradients in the molar loadings $\partial q_i / \partial r$ by defining thermodynamic correction factors Γ_{ij}

$$\frac{q_i}{RT}\frac{\partial \mu_i}{\partial r} = \sum_{j=1}^{n} \Gamma_{ij} \frac{\partial q_j}{\partial r} \qquad \Gamma_{ij} = \frac{q_i}{p_i}\frac{\partial p_i}{\partial q_j};\ i, j = 1, 2, ..\ n \tag{3}$$

The thermodynamic correction factors Γ_{ij} can be calculated by differentiation of the IAST model describing the mixture adsorption equilibrium. Finite values of the off-diagonal elements Γ_{ij} $(i \neq j)$ contribute to "thermodynamic coupling influences".[23]

The spatial-averaged component loadings are defined by

$$\bar{q}_i(t) = \frac{3}{r_c^3}\int_0^{r_c} q_i(r, t) r^2\, dr \tag{4}$$

The diffusional time constant, $Đ_i / r_c^2$, can be determined by fitting to match the experimental uptake data.

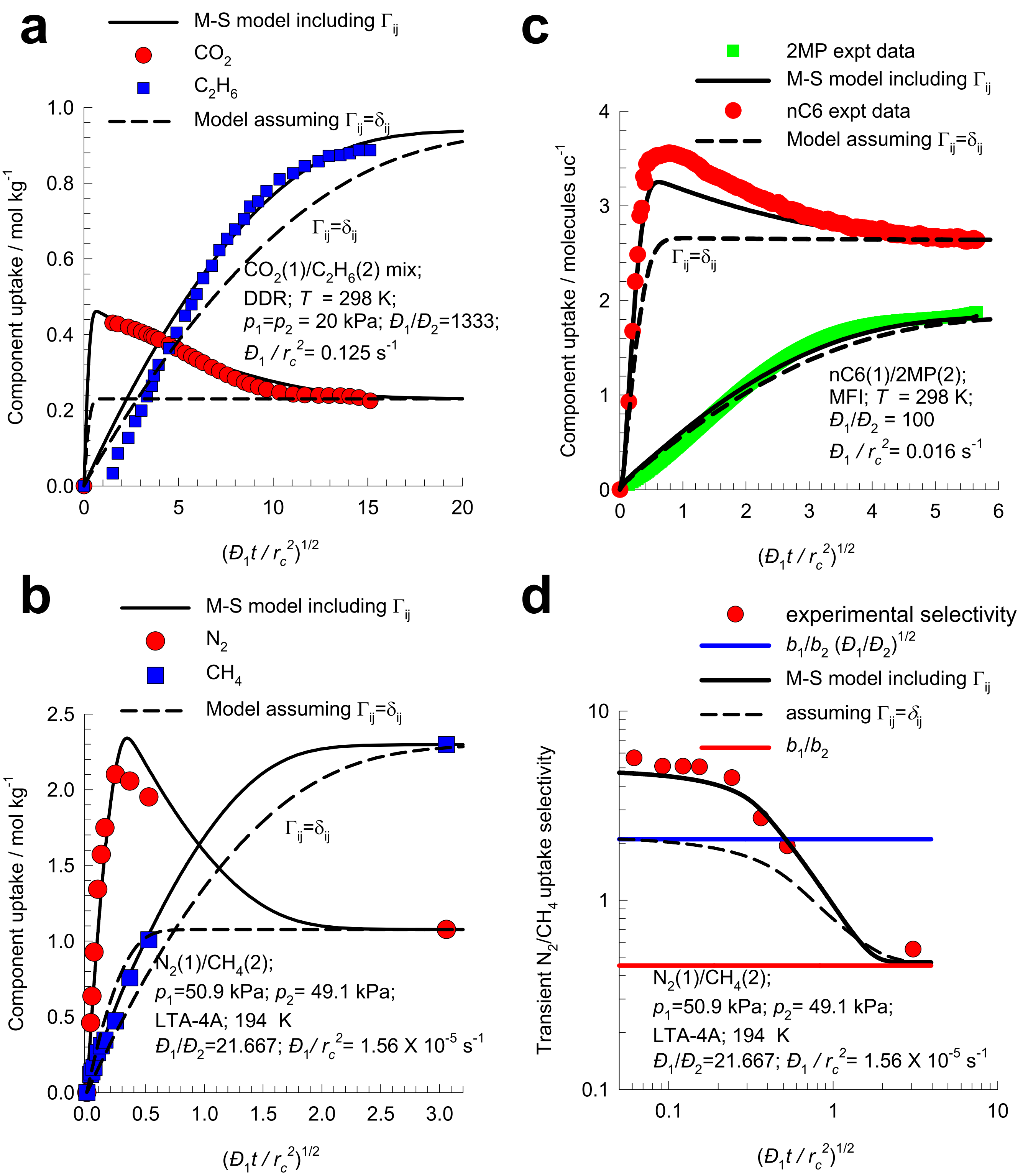

Figure 3. (a) Transient uptake of $CO_2(1)/C_2H_6(2)$ gas mixtures within crystals of DDR zeolite.[30,31,38,45] (b) Transient uptake of $N_2(1)/CH_4(2)$ mixture within LTA-4A crystals.[6,32] (c) Transient uptake of nC6(1)/2MP(2) mixtures in MFI zeolite crystals.[33,38] The continuous solid lines are simulations based on eqs 2 and 3. The dashed lines are the simulations based on eq 5. (d) Transient uptake selectivity of $N_2(1)/CH_4(2)$ mixture within LTA-4A. The input data and computational details are provided in the Supporting Information.

As an illustration, Figure 3a panels a−c present experimental data for transient uptake of (a) 20/20 CO_2/C_2H_6 gas mixtures in Deca-Dodecasil 3 Rhombohedral (DDR) zeolite,[30,31] (b) N_2/CH_4 mixtures in LTA-4A zeolite,[32] and (c) *n*-hexane (nC6)/2-methylpentane (2MP) mixtures in MFI crystals.[33] The anti-synergistic diffusion scenario holds for (a, b) whereas in (c) there is synergy between adsorption and diffusion. The *x*-axes are modified time parameters $\sqrt{Đ_i t/r_c^2}$. In all three experiments, there is a pronounced overshoot in the loading of the more mobile guest component, whereas the tardier partner approaches equilibrium in a monotonous manner. The continuous solid lines are the calculations of $\bar{q}_i(t)$ from numerical solution of eqs 1−4; the computational details are provided in the Supporting Information. The experimentally observed overshoots are quantitatively captured by the simulations in which thermodynamic coupling effects are duly accounted for by eq 3. The overshoots in the loading of the more mobile guest represent signatures of the occurrence of uphill diffusion.[34,35] Additional evidence of uphill diffusion of more mobile partners (component 1) are available for $N_2(1)/CH_4(2)$ uptake in Ba-ETS-4[36] (see Figures S53 and S54), $O_2(1)/N_2(2)$ uptake in Carbon Molecular Sieve (CMS),[37,38] C_3H_6/C_3H_8 uptake in CHA zeolite, and ZIF-8 (see Figures S71 and S82).[3,6,11,23]

If thermodynamic coupling effects are ignored and we assert $\Gamma_{ij} \to \delta_{ij}$, the Kronecker delta, $\delta_{ij}(i = j) = 1; \delta_{ij}(i \neq j) = 0$, eqs 2 and 3 degenerate to yield a set of uncoupled flux expressions[39]

$$N_i = -\rho Đ_i \frac{\partial q_i}{\partial r} \qquad i = 1, 2 \tag{5}$$

Even though eq 5 is strictly valid at low pore occupancies. A large number of implementations of intracrystalline diffusion in models for fixed-bed adsorbers ignore the contribution of the off-diagonal elements Γ_{ij} $(i \neq j)$; see the reviews of Shafeeyan,[40] Ben-Masour,[41] Li,[42] and Zhang.[43] The influence of thermodynamic coupling is underscored in this article by a comparison of simulations taking due account of Γ_{ij} $(i \neq j)$ with simulations in which the assumption $\Gamma_{ij} \to \delta_{ij}$ is invoked, as is commonly done in Linear Driving Force (LDF) implementations.

The dashed black lines in Figure 3 are simulations based on the simplified eq 5; we note that this simplification is unable to anticipate the overshoots in the component loadings of the more mobile partners in all three data sets.

For $N_2(1)/CH_4(2)$ mixtures in LTA-4A, Figure 3d is a plot of the transient uptake selectivity, defined by $\frac{\bar{q}_1(t)/\bar{q}_2(t)}{p_{10}/p_{20}}$ as a function of $\sqrt{Đ_i t / r_c^2}$. As $t \to \infty$, the uptake selectivity will approach the value of the adsorption selectivity, which equals the ratio of the Langmuir constants $\frac{b_1}{b_2} = 0.451$. At short contact times, $\sqrt{Đ_i t / r_c^2} < 1$, the transient uptake selectivity is strongly in favor of the more mobile nitrogen. If thermodynamic coupling effects are ignored, and we assert $\Gamma_{ij} \to \delta_{ij}$, the following simplified expression can be derived for the transient uptake selectivity as the product of the adsorption equilibrium selectivity and the diffusion selectivity[3,36]

$$\frac{\bar{q}_1(t)/\bar{q}_2(t)}{p_{10}/p_{20}} = \frac{b_1}{b_2}\sqrt{\frac{Đ_1}{Đ_2}} \tag{6}$$

The right member of eq 6 is commonly used to define the kinetic selectivity. We note that the experimental uptake selectivity in favor of nitrogen is significantly enhanced above the value determined from the simplified eq 6 due to the influence of thermodynamic coupling, embodied in the factors Γ_{ij}.

From the data in Figure 3 we may conclude that, for manifestation of synergistic, or anti-synergistic, influences, the product of the diffusional time constant and gas−crystal contact time should be sufficient small, e.g., $(Đ_i t/r_c^2) \ll 1$, along with the requirement $Đ_1/Đ_2 \gg 1$.

In the LDF model of Glueckauf,[44] the simplified eq 5 is invoked and, furthermore, the solution to the set of partial differential eq 1 is obviated by writing the time derivative of the spatially averaged component loadings as follows

$$\rho \frac{\partial \bar{q}_i(t)}{\partial t} = -\frac{15 Đ_i}{r_c^2}(q_i^* - \bar{q}_i(t)) \qquad i = 1, 2, ..., n \tag{7}$$

where q_i^* is the molar loading that is in equilibrium with the bulk fluid mixture surrounding the crystal. Equation 7 is valid for the condition $\frac{Đ_i t}{r_c^2} > 0.1$, along with the assumption $\frac{\partial \bar{q}_i(t)}{\partial t} \approx \frac{\partial q_i^*}{\partial t}$.[44] The LDF model predicts that each component will approach equilibrium following

$$\frac{(q_i^* - \bar{q}_i(t))}{(q_i^* - q_i(r_c, 0))} = \exp\left(-\frac{15 Đ_i}{r_c^2} t\right) \qquad i = 1, 2 ... n \tag{8}$$

Equation 8 implies that the approach to equilibrium for each species will be monotonous, i.e., without overshoots. The calculations of the Glueckauf LDF model are remarkably close to the values indicated by the dashed lines in Figure 3a−c;[45] see the comparisons presented in Figures S11, S27, and S44. The inability of the LDF model to anticipate overshoots is entirely ascribable to the neglect of the thermodynamic coupling effects. Put another way, the LDF model is of inadequate accuracy for modelling of kinetic separations; this has also been established in published works.[23,45,46]

3. DIFFUSIONAL INFLUENCES IN FIXED BED ADSORBERS

For an *n*-component gas mixture flowing through a fixed bed maintained under isothermal and isobaric conditions, the molar concentrations in the gas phase at any position and instant of time are obtained by solving the following set of partial differential equations for each of the species *i* in the gas mixture[1,4,6]

$$-D_{ax}\frac{\partial^2 c_i(t, z)}{\partial z^2} + \frac{\partial c_i(t, z)}{\partial t} + \frac{\partial (v(t, z)\, c_i(t, z))}{\partial z} + \frac{(1 - \varepsilon)}{\varepsilon}\rho \frac{\partial \bar{q}_i(t, z)}{\partial t} = 0 \qquad i = 1, 2, ..., n \tag{9}$$

In eq 9, t is the time, z is the distance along the adsorber, ε is the bed voidage, D_{ax} is the axial dispersion coefficient, v is the interstitial gas velocity, and $\bar{q}_i(t,z)$, calculated using eq 4, is the *spatially averaged* molar loading within the crystallites of radius r_c, monitored at position z, and at time t. The interstitial gas velocity is related to the *superficial* gas velocity by

$$v = \frac{u}{\varepsilon} \tag{10}$$

Ruthven et al.[1] state that more detailed models that include radial dispersion are generally not necessary. They also make the following remark: "when mass transfer resistance is significantly greater than axial dispersion, one may neglect the axial dispersion term and assume plug flow". This is the situation that manifests for kinetically controlled separations, the focus of the present article. Consequently, all of the analysis and breakthrough simulations presented in this paper were carried out using the plug flow assumption.

Combination of the discretized partial differential equations (PDEs) along with the algebraic equations describing mixture adsorption equilibrium (IAST or mixed-gas Langmuir model) results in a set of differential-algebraic equations (DAEs), which are solved using a sparse matrix solver based on the semi-implicit Runge−Kutta method; further numerical details are provided in the Supporting Information.

If the value of $Đ_i/r_c^2$ of each guest component is large enough to ensure that intracrystalline gradients are absent and the entire crystallite particle can be considered to be in thermodynamic equilibrium with the surrounding bulk gas phase at time t and position z of the adsorber,

$$\overline{q}_i(t, z) = q_i(t, z) \tag{11}$$

Indeed, the invocation of eq 11 results in the breakthrough simulation curves presented as continuous solid lines in Figure 2a,b.

As validation of the breakthrough simulation methodology using the Maxwell−Stefan equations, eqs 2 and 3, we simulate the experiments of Jolimaître et al.[16] for (a) 2MP/22DMB binary mixtures and (b) 2MB/2MP/22DMB ternary mixtures at 473 K. In Figure 4a,b, the Maxwell−Stefan diffusivities are taken to be those determined from unary breakthrough experiments of Jolimaître et al.[16] The M-S model implementation provides a quantitative match with the experimental breakthroughs. The same set of input parameters for M-S diffusivities is also able to match experimental breakthroughs for six different experimental data sets with good accuracy; see Figure S16. In all six cases, ignoring thermodynamic coupling effects and using the simplified eq 5 result in significantly poorer agreement with experiments; see Figure S16.

Additional evidence stressing the need for using the Maxwell−Stefan formulation, including thermodynamic coupling, for modeling breakthroughs in fixed bed adsorbers is provided in the Supporting Information for CO_2/C_2H_6 mixtures with DDR (Figures S28 and S29), N_2/CH_4 mixtures with LTA-4A, Ba-RPZ, and Ba-ETS-4 (Figures S47, S54, and S55), C_2H_4/C_2H_6 mixtures with Co-gallate (Figure S62), C_3H_6/C_3H_8 mixtures with CHA zeolite, and ZIF-8 (Figures S78, S79, S82, and S83).

4. INFLUENCE OF PARTICLE SIZE AND CONTACT TIMES IN FIXED BED ADSORBERS

Having validated the breakthrough model incorporating the M-S diffusion formulation, we proceed to examine the influence of particle size and contact times for kinetic separations, either synergistic or anti-synergistic.

We first consider the synergistic separation of 2MP/22DMB binary mixtures at 473 K in beds packed with MFI extrudates operating at conditions corresponding to Run 18 of Jolimaître et al.[16] For the four sets of simulations presented in Figure 5a, the diffusional time constant is varied, $Đ_1/r_c^2$ =1.25 × 10^{-3}, 5.0 × 10^{-3}, 1.0 × 10^{-2}, and 0.1 s^{-1}, and the ratio $Đ_1/Đ_2$ = 80 and contact time L/v = 42.3 s are maintained. The dimensionless concentrations at the exit of the adsorber, c_i/c_{i0}, are plotted as a function of the modified time parameter $\frac{Q_0 t}{m_{\text{ads}}} = \frac{t}{L/v}\frac{\varepsilon}{(1-\varepsilon)\rho}$, where Q_0 is the volumetric flow rate of the feed mixture, L is the length of the packed bed, and m_{ads} is the mass of adsorbent. With increasing diffusional influences, i.e., decreasing values of $Đ_1/r_c^2$, the time interval between the breakthroughs of 22DMB and 2MP increases; this increase is desirable because it implies that a larger amount of the higher RON product, 22DMB, can be recovered. To emphasize this point, Figure 5b plots the productivity of the 92+ RON product as a function of the diffusional time constant $Đ_1/r_c^2$. Larger particle sizes and stronger diffusional influences result in improved values of 92+ RON productivity.

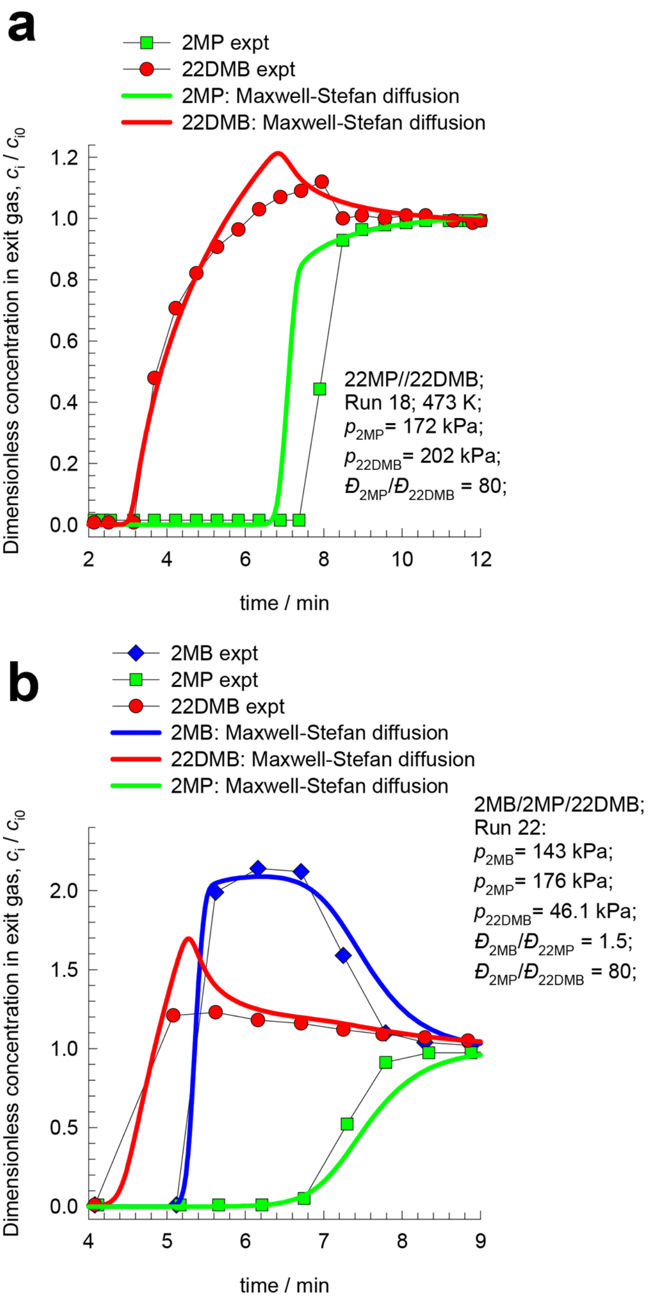

Figure 4. Transient breakthrough experiments of Jolimaître et al.[16] for (a) 2MP/22DMB binary mixtures and (b) 2MB/2MP/22DMB ternary mixtures at 473 K. The experimental data correspond to Runs 18 and 22. The continuous solid lines are simulations based on of eqs 1−4 and 9. The input data and computational details are provided in the Supporting Information.

For any chosen value of the particle size, i.e., chosen value of $Đ_1/r_c^2$, the severity of diffusional influences are also dependent on the contact time between the gas mixture and the adsorbent, L/v; long contact times allow the adsorbent particles to equilibrate, a scenario that is undesirable for synergistic separations.

To highlight the influence of L/v, Figure 5c presents four sets of simulations in which the contact time between the gas mixture and extrudates is varied, L/v = 42.3, 79.5, 159, and 795 s, and the ratio $Đ_1/Đ_2$ = 80 and $Đ_1/r_c^2$ =1.25 × 10^{-3} s^{-1} are maintained. It

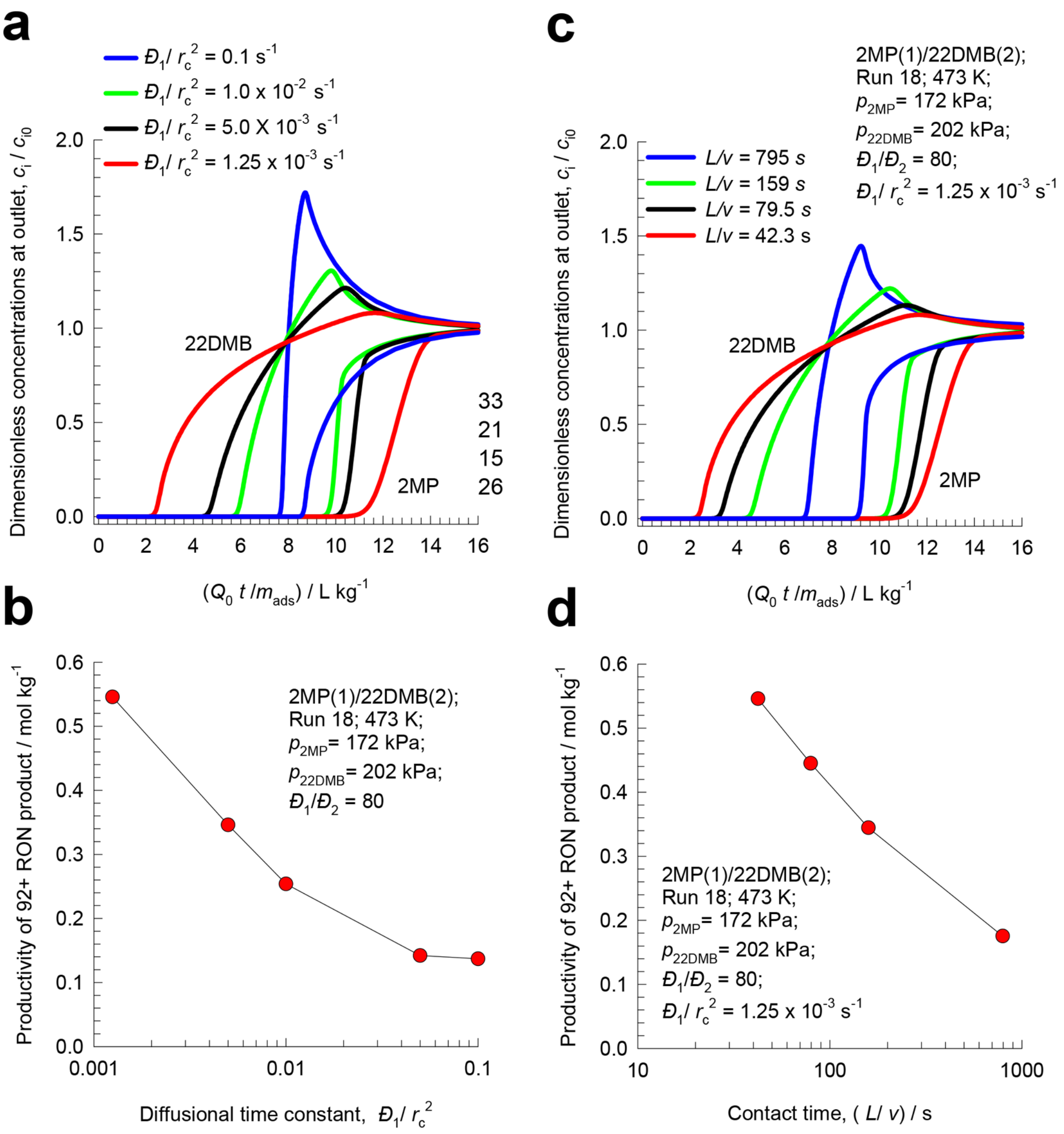

Figure 5. (a) Transient breakthrough for 2MP/22DMB binary mixtures at 473 K in beds packed with MFI extrudates operating at conditions corresponding to Run 18 of Jolimaître et al.[16] For the four sets of simulations, the diffusional time constant is varied, $Đ_1/r_c^2 = 1.25 \times 10^{-3}$, 5.0×10^{-3}, 1.0×10^{-2}, and 0.1 s^{-1}, and the ratio $Đ_1/Đ_2 = 80$ and contact time $L/v = 42.3$ s are maintained. The dimensionless concentrations at the exit of the adsorber, c_i/c_{i0}, are plotted as a function of the modified time parameter $\frac{Q_0 t}{m_{\mathrm{ads}}} = \frac{t}{L/v}\frac{\varepsilon}{(1-\varepsilon)\rho}$, where Q_0 is the volumetric flow rate of feed mixture and m_{ads} is the mass of adsorbent. (b) Productivity of 92+ RON, plotted as a function of $Đ_1/r_c^2$. (c) For the four sets of simulations, the contact time between the gas mixture and extrudates is varied, L/v = 42.3, 79.5, 159, and 795 s, and $Đ_1/r_c^2 = 1.25 \times 10^{-3}$ s^{-1} and $Đ_1/Đ_2 = 80$ are maintained. (d) Productivity of 92+ RON, plotted as a function of the contact time, L/v. The input data and computational details are provided in the Supporting Information.

is to be noted that, since the interstitial gas velocities are varied, the sets of simulations automatically take account of any changes in bed voidage, ε. With decreasing L/v, there is a larger time interval during which a high-RON product can be recovered. Figure 5d plots the productivity of the 92+ RON product as a function of the contact time; the results underscore the benefits of shorter contact times, i.e., stronger diffusional limitations, to achieve the desired high RON product.

Combining the results of Figure 5a,b, we conclude that the best combination is $Đ_1/r_c^2 = 1.25 \times 10^{-3}$ s^{-1}, along with L/v = 42.3 s, yielding the product $(Đ_1/r_c^2)(L/v) = 0.052$. This value conforms with the thumb rule $(Đ_1/r_c^2)(L/v) \ll 1$ reached on the basis of the transient mixture uptake data in Figure 3.

Wang et al.[47] demonstrate the importance of pore size adjustment in improving separations of C_2H_2/CO_2 mixtures. The work of He et al.[48] demonstrates that use of Y-bptc allows both diffusion and adsorption to act synergistically in favor of C_2H_2. Both crystal size and ratio of diffusivities, $Đ_1/Đ_2$, have a strong influence on the productivities of purified C_2H_2;[24] see calculations in Figure S40. The intracrystalline diffusivity of a guest molecule is dependent not only on the pore size and structure[49] but also on the adsorption strength.[50]

We now turn our attention to anti-synergistic separations. The separation of CO_2/C_2H_6 mixtures to produce purified C_2H_6, while capturing the CO_2 is relevant in the context of natural gas processing. Due to azeotrope formation, current technologies for CO_2/C_2H_6 separations require use of extractive distillation, which is energy demanding. An energy-efficient alternative to extractive distillation is to use PSA technology,

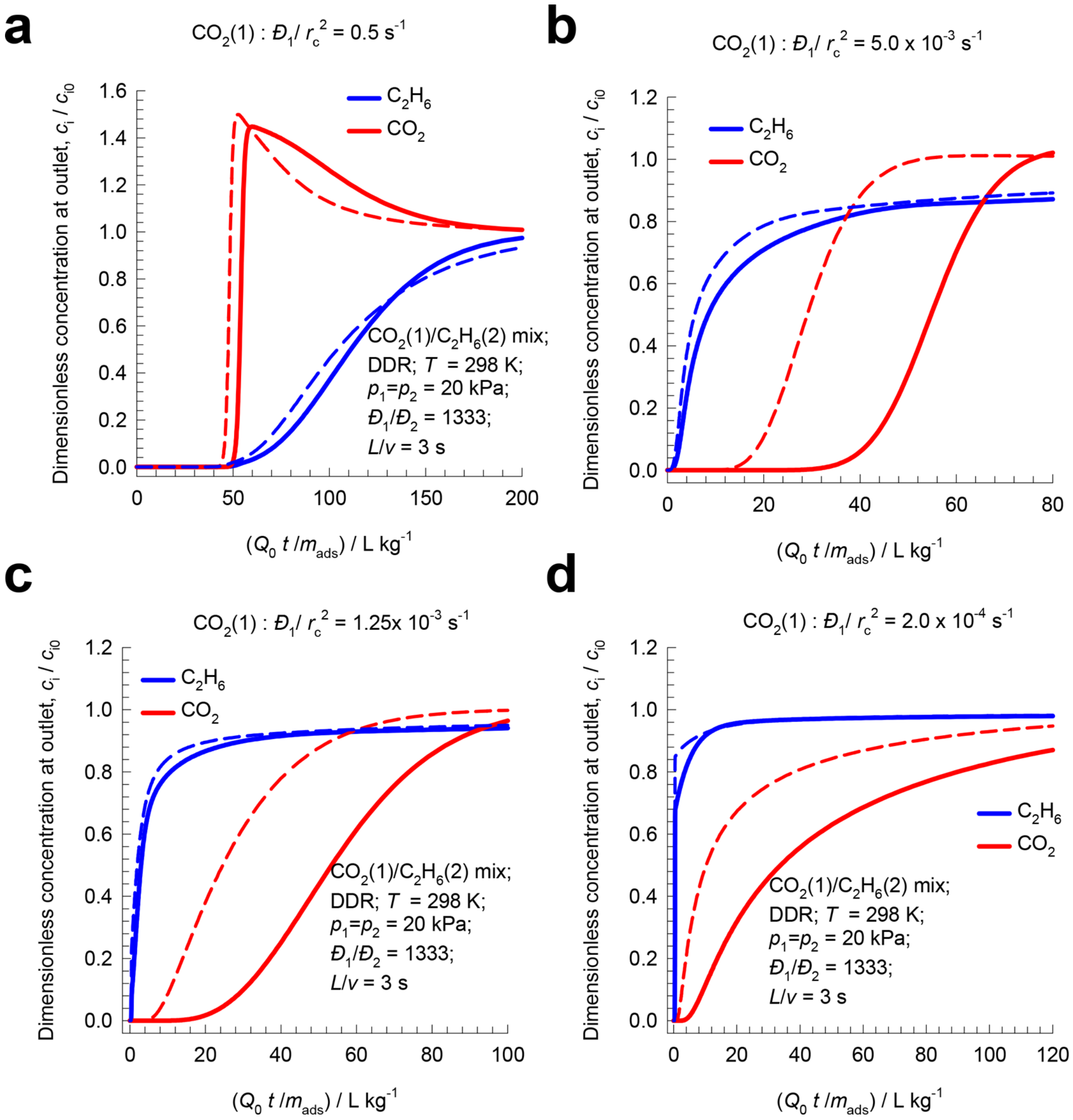

Figure 6. Influence of diffusional time constant ($Đ_1/r_c^2$) on transient breakthrough simulations for the adsorption cycle for 50/50 $CO_2(1)/C_2H_6(2)$ mixture in fixed bed packed with DDR zeolite crystals at 298 K. The partial pressures in the bulk gas phase feed mixture are $p_1 = p_2 = 20$ kPa. In these simulations, the bed voidage $\varepsilon = 0.4$, bed length $L = 0.3$ m, the ratio of M-S diffusivities are $Đ_1/Đ_2 = 1333$, the interstitial velocities $v = 0.1$ m s^{-1}, and the contact time $L/v = 3$ s. (a) Diffusional time constant ($Đ_1/r_c^2$) = 0.5 s^{-1}. (b) $Đ_1/r_c^2 = 5 \times 10$ s^{-1}. (c) $Đ_1/r_c^2 = 1.25 \times 10^{-3}$ s^{-1}. (d) $Đ_1/r_c^2 = 2 \times 10$ s^{-1}. The input data and computational details are provided in the Supporting Information.

drawing inspiration from the anti-synergy evidenced in the uptake experiments in Figure 3a.

For anti-synergistic separations, the choice of the particle size is of crucial importance. In order to highlight the influence of particle size, Figure 6 presents the breakthrough simulations for the scenario in which the diffusional time constant ($Đ_1/r_c^2$), is allotted four different values in decreasing order, i.e., increasing zeolite crystallite size. The continuous solid lines are simulations using the Maxwell−Stefan equations, eqs 2 and 3, taking due account of thermodynamic coupling influences. The dashed lines in Figure 6 are the simulations in which thermodynamic coupling effects are ignored, and simplified eq 5 is used to describe the transfer fluxes; these calculations are also representative of LDF approximations. The dashed lines in Figure 6 are the simulations in which thermodynamic coupling effects are ignored and simplified. Equation 5 is used to describe the transfer fluxes; these calculations are also representative of LDF approximations. In Figure 6a, we choose $Đ_1/r_c^2 = 0.5$ s^{-1}; in this case, the diffusional influences are not sufficiently strong to reverse the selectivities. Therefore, the sequence of breakthroughs is dictated by the mixture adsorption equilibrium that favors the alkane.

In Figure 6b,c,d, the values of diffusional constants are (b) $Đ_1/r_c^2 = 6.8 \times 10^{-2}$ s^{-1}, (c) $Đ_1/r_c^2 = 1.7 \times 10^{-2}$ s^{-1}, and (d) $Đ_1/r_c^2 = 1.7 \times 10^{-4}$ s^{-1}. In these three cases, the diffusional influences are strong enough to cause selectivity reversals. The first component to break through is the saturated alkane, which has the higher adsorption strength but significantly lower mobility. With decreasing values of $Đ_1/r_c^2$, the breakthroughs for C_2H_6 occur earlier because the saturated alkane is severely diffusion limited. Concomitantly, the breakthrough of CO_2 also occurs earlier with decreasing intensity ($Đ_1/r_c^2$).

In order to address the question what is the optimum crystallite size?, Figure 7a plots the productivity of purified $C_2H_6(2)$, containing less than 10% CO_2, as a function of the diffusional time constant ($Đ_1/r_c^2$). We note that there is a

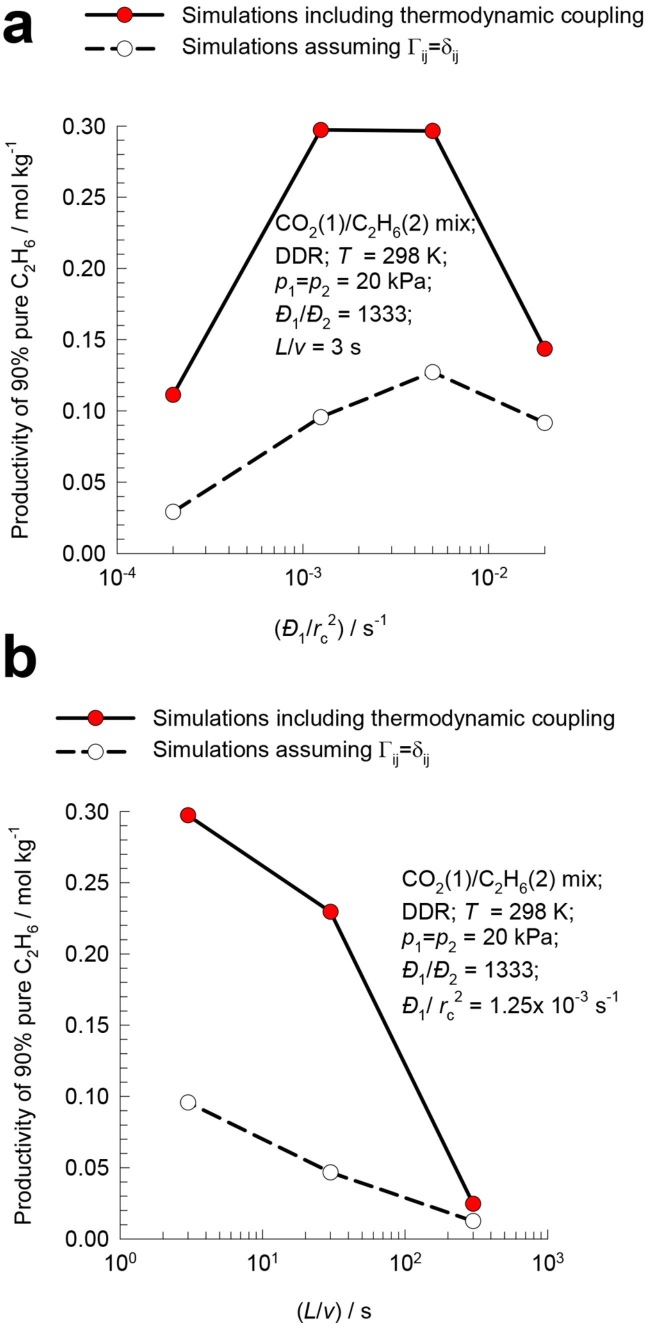

Figure 7. Influence of (a) diffusional time constant ($Đ_1/r_c^2$) and (b) gas−crystal contact time, L/v, on the productivity of purified $C_2H_6(2)$ for the adsorption cycle for the 50/50 $CO_2(1)/C_2H_6(2)$ mixture in a fixed bed packed with DDR zeolite crystals at 298 K. The partial pressures in the bulk gas phase feed mixture are $p_1 = p_2 = 20$ kPa. (a) The productivity of purified $C_2H_6(2)$, containing less than 10% CO_2, plotted as a function of the diffusional time constant ($Đ_1/r_c^2$). (b) The productivity of purified $C_2H_6(2)$ plotted as a function of the gas−crystal contact time, L/v. The dashed lines in (a, b) are productivity calculations in which thermodynamic coupling effects are ignored, and eq 5 is used to describe the transfer fluxes. The input data and computational details are provided in the Supporting Information.

window for values of $Đ_1/r_c^2$ that yield the maximum productivity of the desired product. A further decrease in $Đ_1/r_c^2$, i.e., increasing crystallite size, will reduce the C_2H_6 productivity. The important message is that, for kinetically driven separations to be effective, there is an optimum crystal size, i.e., optimum value of the diffusional time constant ($Đ_1/r_c^2$).

For the optimum crystal size, corresponding to $Đ_1/r_c^2 = 1.25 \times 10^{-3}$ s^{-1}, the productivity of purified ethane decreases with decreasing contact time, L/v; see Figure 7b.

The dashed lines in Figure 7a,b are calculations of the productivities for the scenario in which thermodynamic coupling effects are ignored and simplified eq 5 is invoked; the C_2H_6 productivity values are significantly lowered. The important message to emerge is that the LDF model, which is based on eq 5, will severely underestimate the separation performance in fixed bed adsorbers. A corollary to this finding is that the commonly used LDF model, which invokes eq 5, is of inadequate accuracy for PSA simulations.

For a chosen host material with a specified particle size, and gas−solid contact time, selectivity reversals are feasible only if the ratio of diffusivities is sufficiently high $Đ_1/Đ_2 \gg 1$; simulations to demonstrate this are provided in Figures S33 and S34.

Results entirely analogous to those presented in Figures 5−7 are realized for *n*-hexane/2-methylpentane separations with MFI zeolite (Figures S12) and C_3H_6/C_3H_8 separations with CHA zeolite, KAUST-7, and ZIF-8 (Figures S73, S75, S76, and S83−S89).

As a corollary to the results for breakthrough simulations with varying($Đ_1/r_c^2$ and L/v, we now demonstrate that the breakthrough simulations are uniquely dependent on the product of the diffusional time constant ($Đ_1/r_c^2$) and the gas−particle contact time L/v.

Figure 8a presents transient breakthrough for 2MP/22DMB binary mixtures at 473 K in beds packed with MFI extrudates operating at conditions corresponding to Run 18 of Jolimaître et al.[16] In these sets of simulations, the interstitial velocities are varied such that the contact times are L/v = 42.3, 95.15, 264.3, and 10.57 s; the diffusional constants ($Đ_1/r_c^2$) are adjusted such that $(Đ_1/r_c^2)(L/v) = 5.286 \times 10^{-2}$ and $Đ_1/Đ_2 = 80$. When plotted as a function of $\frac{Q_0 t}{m_{ads}} = \frac{t}{L/v}\frac{\varepsilon}{(1-\varepsilon)\rho}$, all four sets of simulations, portraying diffusion/adsorption synergy, collapse into a unique breakthrough curve.

For anti-synergistic separations, Figure 8 panels b−d present analogous results for transient breakthrough simulations for the adsorption cycle for (b) 50/50 $CO_2(1)/C_2H_6(2)$ mixture separations with DDR, (c) 50/50 C_3H_6/C_3H_8 mixture separations with all-silica CHA, and (d) 50/50 C_3H_6/C_3H_8 mixture separations with ZIF-8. The breakthroughs are uniquely determined by the product $(Đ_1/r_c^2)(L/v)$.

Precisely analogous results are obtained for the adsorption cycle for 50/50 C_3H_6/C_3H_8 mixtures in a fixed-bed adsorber packed with KAUST-7,[8] operating at 298 K and 100 kPa, in which $(Đ_1/r_c^2)(L/v) = 6 \times 10^{-3}$ and $Đ_1/Đ_2 = 100$; see Figure S89.

Figure 8 provides an important tool for interpreting and utilizing the results in laboratory scale equipment for scaling up to commercial units with different particle sizes and contact times; this scaleup should aim for maintaining the same value of $(Đ_1/r_c^2)(L/v)$.

5. ADSORPTION/DESORPTION CYCLES IN PSA OPERATIONS

For the separation of C_3H_6/C_3H_8 mixtures with all-silica CHA, ZIF-8, and KAUST-7, the desired product C_3H_6 is available only in the desorption phase. We highlight some important modelling

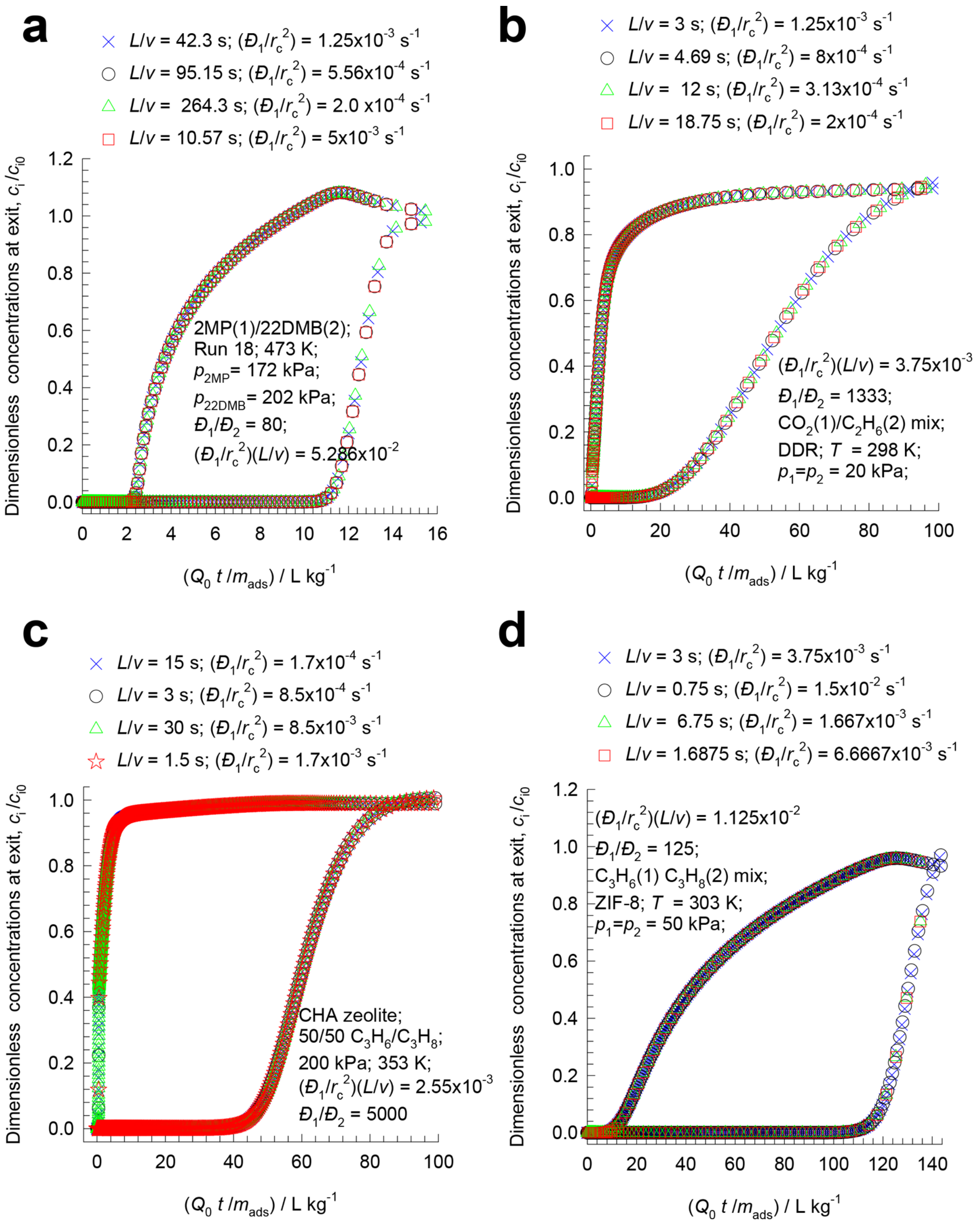

Figure 8. Transient breakthrough simulations for the adsorption cycle for (a) 2MP/22DMB mixtures in MFI extrudates, (b) CO_2/C_2H_6 mixtures in DDR zeolite, (c) C_3H_6/C_3H_8 mixtures in a fixed bed adsorber packed with all-silica CHA, and (d) C_3H_6/C_3H_8 mixtures in a fixed bed adsorber packed with ZIF-8. In these simulations, the bed voidage $\varepsilon = 0.4$, bed length $L = 0.3$ m, and the diffusional time constants and contact times are adjusted such that $(Đ_1/r_c^2)(L/\nu)$ remains the same in all four sets for each host material. The input data and computational details are provided in the Supporting Information.

aspects by employing a simplified 2-step PSA scheme consisting of the adsorption cycle, followed by counter-current vacuum blowdown; see Figure 9. Such a two-step PSA scheme has been employed for ranking C_2H_2-selective MOFs for separation of C_2H_2/CO_2 mixtures.[51,52] For achieving ethyne purities >99%, the best performing MOFs are ZNU-1,[51] Cu^I@UiO-66-$(COOH)_2$,[53] and SOFOUR-TEPE-Zn,[52] which virtually exclude CO_2 from the pores.

Figure 10a shows the transient breakthrough simulations for the adsorption cycle for 50/50 C_3H_6/C_3H_8 mixtures in a fixed bed adsorber packed with CHA, operating at 353 K and 200 kPa. The Maxwell–Stefan diffusivities are $Đ_1/r_c^2 = 1.7 \times 10^{-4}$ s^{-1}, $Đ_1/r_c^2 = 3.4 \times 10^{-8}$ s^{-1}, and $(Đ_1/r_c^2)(L/\nu) = 2.55 \times 10^{-3}$, and $Đ_1/Đ_2 = 5000$. The simulations were carried out with two different model implementations. The black colored lines are simulations based on eqs 2 and 3; the blue colored lines are simulations based on eq 5, in which the thermodynamic correction factors are ignored by invoking $\Gamma_{ij} = \delta_{ij}$, the Kronecker delta. The dimensionless concentrations at the exit of the fixed bed, c_i/c_{i0}, are plotted as a function of time.

In industrial practice, the adsorption cycle will not be carried until bed equilibration. Rather, the adsorption cycle will be

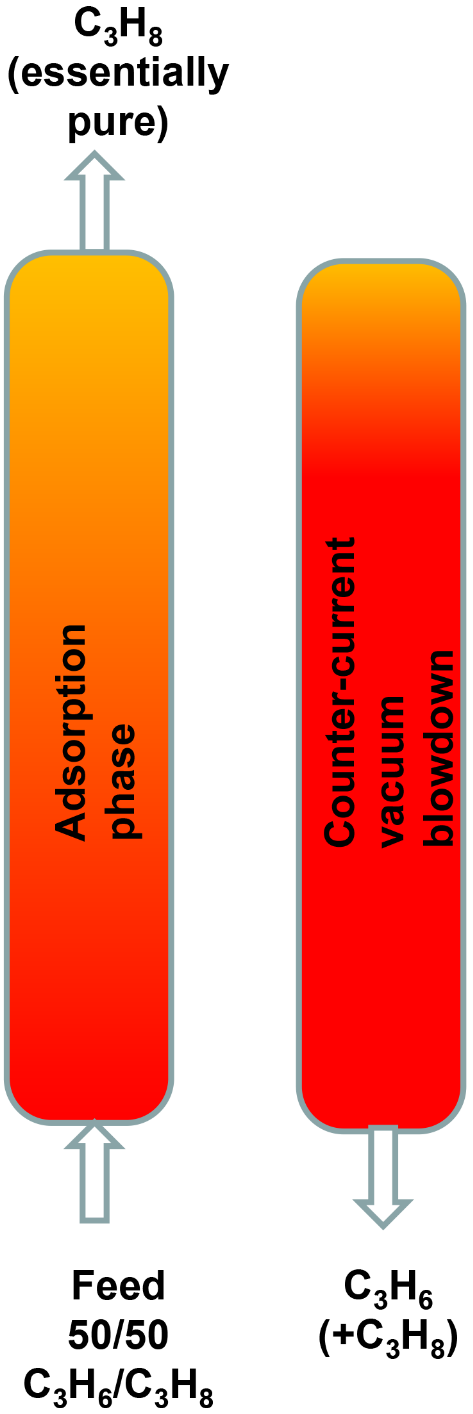

Figure 9. Simplified 2-step PSA process for separating C_3H_6/C_3H_8 mixtures.

terminated just before the alkene breaks through the exit in significant quantities. By application of deep vacuum (at the times 76 and 1160 s, as indicated by the arrows in Figure 10a), both the components remaining in the adsorbed phase within the pores can be recovered. Figure 10b plots the component loadings along the dimensionless distance along the adsorber, z/L, at the termination of the adsorption cycle. For simulations based on eqs 2 and 3, the averaged adsorbed phase loadings are 1.21 and 0.087 mol kg^{-1}, respectively for C_3H_6, and C_3H_8. The corresponding average component loadings are 0.074 and 0.0042 mol kg^{-1}, respectively, for simulations based on eq 5. Taking due account of thermodynamic coupling effects leads to a significantly higher uptake of C_3H_6; this is a direct consequence of uphill diffusion effects (see Figure S71).

Figure 10c plots the number of moles of C_3H_6 and C_3H per kilogram of adsorbent that are recovered in the desorption cycle as a function of time. Inclusion of thermodynamic coupling effects results in the recovery of a significantly larger amount of C_3H_6; concomitantly, a larger amount of the saturated alkane is also recovered. The calculations of the % C_3H_6 in the blowdown product are plotted in Figure 10d. Taking due account of thermodynamic coupling effects, C_3H_6 with 92% purity can be produced in the two-step PSA scheme. Neglect of thermodynamic coupling effects results in a reduced purity of 81%. The important message to emerge is that, for modelling of PSA schemes for adsorption/desorption cycles in PSA schemes, the inclusion of thermodynamic coupling effects is of vital importance.

To attain C_3H_6 purities >99.95%, which are demanded for polymerization feedstocks, we need to operate with multiple beds involving five different steps (cf. Figure S65),[3,12,54,55] consisting of

(i) pressurization with C_3H_6/C_3H_8 feed mixture
(ii) high pressure adsorption separation with withdrawal of purified C_3H_8
(iii) co-current purge with a portion of the product C_3H_6
(iv) co-current blowdown
(v) counter-current vacuum blowdown

A detailed process design exercise, such as that reported by Khalighi et al.[3,12] will be required in order to compare the C_3H_6 productivities of any adsorbent using the 5-step PSA scheme. This 5-step scheme is illustrated for 80/20 $C_2H_4(1)$/$C_2H_6(2)$ mixture separations with Co-gallate pellets in Figure S61.

6. CONCLUSIONS

For mixture separations using microcrystalline adsorbent materials, intracrystalline diffusion influences act either (a) synergistically or (b) anti-synergistically to the adsorption equilibrium. Synergistic influences enhance the adsorption selectivity. Anti-synergistic influences serve to reverse the hierarchy of breakthroughs in fixed bed adsorbers. Such reversals are desirable, for example, for C_3H_6/C_3H_8 mixtures because the diffusional exclusion of the saturated alkane from the pores results in higher purity alkene product in the desorption cycle. Published experimental data on transient mixture uptake into single crystals and mixture breakthroughs in fixed bed adsorbers are analyzed in detail to draw the following set of conclusions.

(1) For transient uptake within crystals, published experimental data (cf. Figure 3) show the more mobile component attains supra-equilibrium loadings during the initial stages of the transience. For quantification of such overshoots, signifying uphill diffusion, we require the use of the M-S diffusion equations using $\partial\mu_i/\partial r$ as driving forces. The overshoots are engendered by the cross-coefficients Γ_{ij} $(i \neq j)$ of the matrix of thermodynamic correction factors. If the thermodynamic factors are ignored; no overshoots are predicted. The simplified eq 5 is not recommended for modelling purposes. Synergistic and anti-synergistic influences are more effective at short contact times, typically, $Đ_1/r_c^2 \ll 1$, and high ratios of diffusivities $Đ_1/Đ_2 \gg 1$.

(2) The experimental breakthroughs of 2MB/2MP/22DMB mixtures are matched by simulations that take proper

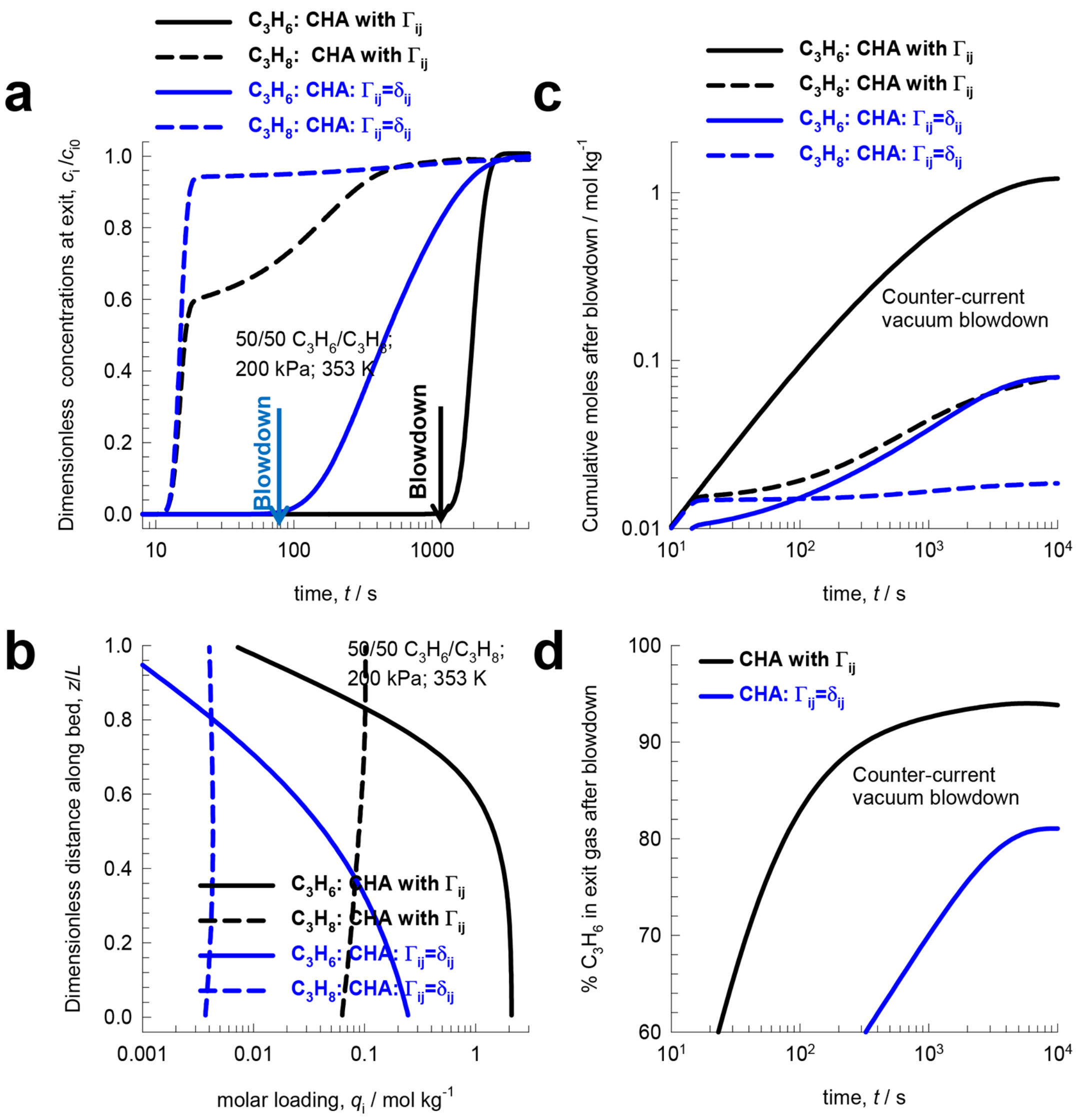

Figure 10. (a) Transient breakthrough simulations for the adsorption cycle for 50/50 C_3H_6/C_3H_8 mixtures in a fixed bed adsorber packed with all-silica CHA operating at 353 K and 200 kPa. (b) Plots of the component loadings along the dimensionless distance, z/L, along the length of the adsorber at the termination of the adsorption cycle. (c) Cumulative values of the number of moles of C_3H_6 and C_3H_8 that are recovered as a function of time. (d) The % C_3H_6 of the exit gas following vacuum blowdown, plotted as a function of time. The black lines are simulations based on eqs 2 and 3; the blue lines are simulations based on eq 5, in which the thermodynamic correction factors are assumed to be described by $\Gamma_{ij} = \delta_{ij}$. The input data and computational details are provided in the Supporting Information.

account of thermodynamic coupling (cf. Figure 4). The simplified eq 5, and the LDF approximation, are not recommended for modelling purposes as they lead to pessimistic estimates of productivities, as witnessed in Figure 7 and Figure 10.

(3) For a given feed mixture and chosen host material, kinetic separations in fixed bed devices are governed by two separate parameters: (a) diffusional time constant, $Đ_1/r_c^2$, and gas−particle contact time, L/v. Broadly speaking, synergistic or anti-synergistic diffusional influences improve with lowering of either of these parameters; see Figure 5b,d. In some scenarios, as illustrated in Figure 7a, there is an optimum range of values of $Đ_1/r_c^2$ for achieving maximum productivities.

(4) The transient breakthroughs, plotted as a function of the modified time parameter $\frac{Q_0 t}{m_{\mathrm{ads}}}$, are uniquely dependent on the product $(Đ_1/r_c^2)(L/v)$; see Figure 8. This finding assists in scaling up from small scale laboratory units to large scale industrial units using different particle sizes, r_c, packed bed lengths, L, and interstitial gas velocities, v.

The exploitation of synergistic diffusional influences in the MFI catalyzed isomerization of n-hexane to mono-branched and di-branched isomers also demands that thermodynamic coupling influences are duly accounted for.[56,57]

■ ASSOCIATED CONTENT

Supporting Information

The Supporting Information is available free of charge at https://pubs.acs.org/doi/10.1021/cbe.3c00057.

(a) Derivation of the Maxwell−Stefan diffusion formulation, (b) computational modelling details of transient mixture uptakes within crystals, and adsorber breakthroughs, (c) structural details of host materials discussed in this article, (d) data on unary isotherm data fits used for IAST calculations for all guest/host combinations, (e) guest diffusivities, and (f) detailed simulation results for transient breakthroughs for several different mixtures (PDF)

AUTHOR INFORMATION

Corresponding Author

Rajamani Krishna − *Van 't Hoff Institute for Molecular Sciences, University of Amsterdam, 1098 XH Amsterdam, The Netherlands;* orcid.org/0000-0002-4784-8530;
Email: r.krishna@contact.uva.nl

Complete contact information is available at:
https://pubs.acs.org/10.1021/cbe.3c00057

Notes

The author declares no competing financial interest.

NOMENCLATURE

Latin Alphabet

c_i	molar concentration of species *i*, mol m^{-3}
c_{i0}	molar concentration of species *i* in fluid mixture at inlet, mol m^{-3}
$Đ_i$	Maxwell−Stefan diffusivity for molecule-wall interaction, $m^2\ s^{-1}$
m_{ads}	mass of adsorbent packed in fixed bed, kg
n	number of species in the mixture, dimensionless
N_i	molar flux of species *i* with respect to framework, mol $m^{-2}\ s^{-1}$
p_i	partial pressure of species *i* in mixture, Pa
p_t	total system pressure, Pa
q_i	component molar loading of species *i*, mol kg^{-1}
$\overline{q}_i$	radial-averaged component loading of species *i*, mol kg^{-1}
Q_0	volumetric flow rate of gas mixture entering fixed bed, $m^3\ s^{-1}$
r	radial direction coordinate, m
r_c	radius of crystallite, m
R	gas constant, 8.314 J $mol^{-1}\ K^{-1}$
S_{ads}	adsorption selectivity, dimensionless
t	time, s
T	absolute temperature, K
u	superficial gas velocity in packed bed, m s^{-1}
v	interstitial gas velocity in packed bed, m s^{-1}

Greek Alphabet

Γ_{ij}	thermodynamic factors, dimensionless
δ_{ij}	Kronecker delta $\delta_{ij}(i = j) = 1$; $\delta_{ij}(i \neq j) = 0$, dimensionless
ε	voidage of packed bed, dimensionless
μ_i	molar chemical potential, J mol^{-1}
ρ	framework density, kg m^{-3}

REFERENCES

(1) Ruthven, D. M.; Farooq, S.; Knaebel, K. S. *Pressure swing adsorption*; VCH Publishers: New York, 1994.

(2) Farooq, S.; Ruthven, D. M. Numerical-Simulation of a Kinetically Controlled Pressure Swing Adsorption Bulk Separation Process Based on a Diffusion-Model. *Chem. Eng. Sci.* **1991**, *46*, 2213−2224.

(3) Khalighi, M.; Chen, Y. F.; Farooq, S.; Karimi, I. A.; Jiang, J. W. Propylene/Propane Separation Using SiCHA. *Ind. Eng. Chem. Res.* **2013**, *52*, 3877−3892.

(4) Krishna, R.; Baur, R. Modelling Issues in Zeolite Based Separation Processes. *Sep. Purif. Technol.* **2003**, *33*, 213−254.

(5) Bloch, E. D.; Queen, W. L.; Krishna, R.; Zadrozny, J. M.; Brown, C. M.; Long, J. R. Hydrocarbon Separations in a Metal-Organic Framework with Open Iron(II) Coordination Sites. *Science* **2012**, *335*, 1606−1610.

(6) Krishna, R. The Maxwell-Stefan Description of Mixture Diffusion in Nanoporous Crystalline Materials. *Microporous Mesoporous Mater.* **2014**, *185*, 30−50.

(7) Krishna, R.; van Baten, J. M. In silico screening of metal-organic frameworks in separation applications. *Phys. Chem. Chem. Phys.* **2011**, *13*, 10593−10616.

(8) Cadiau, A.; Adil, K.; Bhatt, P. M.; Belmabkhout, Y.; Eddaoudi, M. A Metal-Organic Framework−Based Splitter for Separating Propylene from Propane. *Science* **2016**, *353*, 137−140.

(9) Lin, R.-B.; Li, L.; Zhou, H.-L.; Wu, H.; He, C.; Li, S.; Krishna, R.; Li, J.; Zhou, W.; Chen, B. Molecular Sieving of Ethylene from Ethane using a Rigid Metal-Organic Framework. *Nature Materials* **2018**, *17*, 1128−1133.

(10) Böhme, U.; Barth, B.; Paula, C.; Kuhnt, A.; Schwieger, W.; Mundstock, A.; Caro, J.; Hartmann, M. Ethene/Ethane and Propene/Propane Separation via the Olefin and Paraffin Selective Metal−Organic Framework Adsorbents CPO-27 and ZIF-8. *Langmuir* **2013**, *29*, 8592−8600.

(11) Pimentel, B. R.; Lively, R. P. Propylene Enrichment via Kinetic Vacuum Pressure Swing Adsorption Using ZIF-8 Fiber Sorbents. *ACS Appl. Mater. Interfaces* **2018**, *10*, 36323−36331.

(12) Khalighi, M.; Karimi, I. A.; Farooq, S. Comparing SiCHA and 4A Zeolite for Propylene/Propane Separation using a Surrogate-Based Simulation/Optimization Approach. *Ind. Eng. Chem. Res.* **2014**, *53*, 16973−16983.

(13) Liang, B.; Zhang, X.; Xie, Y.; Lin, R.-B.; Krishna, R.; Cui, H.; Li, Z.; Shi, Y.; Wu, H.; Zhou, W.; Chen, B. An Ultramicroporous Metal−Organic Framework for High Sieving Separation of Propylene from Propane. *J. Am. Chem. Soc.* **2020**, *142*, 17795−17801.

(14) Bao, Z.; Wang, J.; Zhang, Z.; Xing, H.; Yang, Q.; Yang, Y.; Wu, H.; Krishna, R.; Zhou, W.; Chen, B.; Ren, Q. Molecular Sieving of Ethane from Ethylene through the molecular Cross-section Size Differentiation in Gallate-based Metal-Organic Frameworks. *Angew. Chem. Int. Ed.* **2018**, *57*, 16020−16025.

(15) Yan, J.; Sheng, L.; Liu, Y.; Zheng, F.; Chen, L.; Zhang, Z.; Yang, Q.; Yang, Y.; Ren, Q.; Bao, Z. Separation of ethylene and ethane using Co-Gallate pellets in a vacuum swing adsorption process. *Sep. Purif. Technol.* **2023**, *319*, No. 124075.

(16) Jolimaître, E.; Ragil, K.; Tayakout-Fayolle, M.; Jallut, C. Separation of Mono- and Dibranched Hydrocarbons on Silicalite. *A.I.Ch.E.J.* **2002**, *48*, 1927−1937.

(17) Schuring, D.; Jansen, A. P. J.; van Santen, R. A. Concentration and chainlength dependence of the diffusivity of alkanes in zeolites studied with MD. *simulations. J. Phys. Chem. B* **2000**, *104*, 941−948.

(18) Krishna, R.; van Baten, J. M. Diffusion of Hydrocarbon Mixtures in MFI Zeolite: Influence of Intersection Blocking. *Chem. Eng. J.* **2008**, *140*, 614−620.

(19) Krishna, R.; Van Baten, J. M. Elucidating Traffic Junction Effects in MFI Zeolite using Kinetic Monte Carlo Simulations. *ACS Omega* **2019**, *4*, 10761−10766.

(20) Krishna, R.; van Baten, J. M. Using Molecular Dynamics Simulations for Elucidation of Molecular Traffic in Ordered Crystalline Microporous Materials. *Microporous Mesoporous Mater.* **2018**, *258*, 151−169.

(21) Jolimaître, E.; Tayakout-Fayolle, M.; Jallut, C.; Ragil, K. Determination of mass transfer and thermodynamic properties of branched paraffins in silicalite by inverse chromatography technique. *Ind. Eng. Chem. Res.* **2001**, *40*, 914−926.

(22) Cavalcante, C. L.; Ruthven, D. M. Adsorption of Branched and Cyclic Paraffins in Silicalite. 2. Kinetics. *Ind. Eng. Chem. Res.* **1995**, *34*, 185−191.

(23) Krishna, R. Highlighting the Influence of Thermodynamic Coupling on Kinetic Separations with Microporous Crystalline Materials. *ACS Omega* **2019**, *4*, 3409−3419.

(24) Krishna, R. Synergistic and Antisynergistic Intracrystalline Diffusional Influences on Mixture Separations in Fixed Bed Adsorbers. *Precision Chemistry* **2023**, *1*, 83−93.

(25) Krishna, R. Describing the Diffusion of Guest Molecules inside Porous Structures. *J. Phys. Chem. C* **2009**, *113*, 19756−19781.

(26) Krishna, R. Diffusion in Porous Crystalline Materials. *Chem. Soc. Rev.* **2012**, *41*, 3099−3118.

(27) Krishna, R. Occupancy Dependency of Maxwell−Stefan Diffusivities in Ordered Crystalline Microporous Materials. *ACS Omega* **2018**, *3*, 15743−15753.

(28) Krishna, R. Diffusing Uphill with James Clerk Maxwell and Josef Stefan. *Curr. Opin. Chem. Eng.* **2016**, *12*, 106−119.

(29) Krishna, R. Thermodynamically Consistent Methodology for Estimation of Diffusivities of Mixtures of Guest Molecules in Microporous Materials. *ACS Omega* **2019**, *4*, 13520−13529.

(30) Binder, T.; Lauerer, A.; Chmelik, C.; Haase, J.; Kärger, J.; Ruthven, D. M. Micro-imaging of transient intracrystalline concentration profiles during two-component uptake of light hydrocarbon - carbon dioxide mixtures by DDR-type zeolites. *Ind. Eng. Chem. Res.* **2015**, *54*, 8997−9004.

(31) Lauerer, A.; Binder, T.; Chmelik, C.; Miersemann, E.; Haase, J.; Ruthven, D. M.; Kärger, J. Uphill Diffusion and Overshooting in the Adsorption of Binary Mixtures in Nanoporous Solids. *Nat. Commun.* **2015**, *6*, No. 7697.

(32) Habgood, H. W. The Kinetics of Molecular Sieve Action. Sorption of Nitrogen-Methane Mixtures by Linde Molecular Sieve 4A. *Canad. J. Chem.* **1958**, *36*, 1384−1397.

(33) Titze, T.; Chmelik, C.; Kärger, J.; van Baten, J. M.; Krishna, R. Uncommon Synergy Between Adsorption and Diffusion of Hexane Isomer Mixtures in MFI Zeolite Induced by Configurational Entropy Effects. *J. Phys. Chem. C* **2014**, *118*, 2660−2665.

(34) Krishna, R. Uphill Diffusion in Multicomponent Mixtures. *Chem. Soc. Rev.* **2015**, *44*, 2812−2836.

(35) Krishna, R. Diffusing Uphill with James Clerk Maxwell and Josef Stefan. *Chem. Eng. Sci.* **2019**, *195*, 851−880.

(36) Majumdar, B.; Bhadra, S. J.; Marathe, R. P.; Farooq, S. Adsorption and Diffusion of Methane and Nitrogen in Barium Exchanged ETS-4. *Ind. Eng. Chem. Res.* **2011**, *50*, 3021−3034.

(37) Yang, R. T. *Adsorbents: Fundamentals and Applications*; John Wiley & Sons, Inc.: Hoboken, New Jersey, 2003.

(38) Krishna, R. Tracing the Origins of Transient Overshoots for Binary Mixture Diffusion in Microporous Crystalline Materials. *Phys. Chem. Chem. Phys.* **2016**, *18*, 15482−15495.

(39) Krishna, R.; Li, S.; van Baten, J. M.; Falconer, J. L.; Noble, R. D. Investigation of slowing-down and speeding-up effects in binary mixture permeation across SAPO-34 and MFI membranes. *Sep. Purif. Technol.* **2008**, *60*, 230−236.

(40) Shafeeyan, M. S.; Wan Daud, W. M. A.; Shamiri, A. A Review of Mathematical Modeling of Fixed-Bed Columns for Carbon dioxide Adsorption. *Chem. Eng. Res. Des.* **2014**, *92*, 961−988.

(41) Ben-Mansour, R.; Habib, M.A.; Bamidele, O.E.; Basha, M.; Qasem, N.A.A.; Peedikakkal, A.; Laoui, T.; Ali, M. Carbon capture by physical adsorption: Materials, experimental investigations and numerical modeling and simulations − A review. *Applied Energy* **2016**, *161*, 225−255.

(42) Li, S.; Deng, S.; Zhao, L.; Zhao, R.; Lin, M.; Du, Y.; Lian, Y. Mathematical modeling and numerical investigation of carbon capture by adsorption: Literature review and case study. *Applied Energy* **2018**, *221*, 437−449.

(43) Zhang, R.; Shen, Y.; Tang, Z.; Li, W.; Zhang, D. A Review of Numerical Research on the Pressure Swing Adsorption Process. *Processes* **2022**, *10*, 812.

(44) Glueckauf, E. Theory of Chromatography. Part 10- Formulae for Diffusion into Spheres and their Application to Chromatography. *Trans. Faraday Soc.* **1955**, *51*, 1540−1551.

(45) Krishna, R. A Maxwell-Stefan-Glueckauf Description of Transient Mixture Uptake in Microporous Adsorbents. *Sep. Purif. Technol.* **2018**, *191*, 392−399.

(46) Krishna, R. Maxwell-Stefan Modelling of Mixture Desorption Kinetics in Microporous Crystalline Materials. *Sep. Purif. Technol.* **2019**, *229*, No. 115790.

(47) Wang, J.; Zhang, Y.; Su, Y.; Liu, X.; Zhang, P.; Lin, R.-B.; Chen, S.; Deng, Q.; Zeng, Z.; Deng, S.; Chen, B. Fine pore engineering in a series of isoreticular metal-organic frameworks for efficient C_2H_2/CO2 separation. *Nat. Commun.* **2022**, *13*, 200.

(48) He, C.; Zhang, P.; Wang, Y.; Zhang, Y.; Hu, T.; Li, L.; Li, J. Thermodynamic and kinetic synergetic separation of CO_2/C_2H_2 in an ultramicroporous metal-organic framework. *Sep. Purif. Technol.* **2023**, *304*, No. 122318.

(49) Krishna, R.; van Baten, J. M. A molecular dynamics investigation of the diffusion characteristics of cavity-type zeolites with 8-ring windows. *Microporous Mesoporous Mater.* **2011**, *137*, 83−91.

(50) Krishna, R.; Van Baten, J. M. Highlighting the Anti-Synergy between Adsorption and Diffusion in Cation-Exchanged Faujasite Zeolites. *ACS Omega* **2022**, *7*, 13050−13056.

(51) Wang, L.; Sun, W.; Zhang, Y.; Xu, N.; Krishna, R.; Hu, J.; Jiang, Y.; He, Y.; Xing, H. Interpenetration symmetry control within ultramicroporous robust boron cluster hybrid MOFs for benchmark purification of acetylene from carbon dioxide. *Angew. Chem. Int. Ed.* **2021**, *60*, 22865−22870.

(52) Liu, X.; Zhang, P.; Xiong, H.; Zhang, Y.; Wu, K.; Liu, J.; Krishna, R.; Chen, J.; Chen, S.; Zeng, Z.; Deng, S.; Wang, J. Engineering Pore Environments of Sulfate-pillared Metal-Organic Framework for Efficient C2H2/CO2 Separation with Record Selectivity. *Adv. Mater.* **2023**, *35*, No. 2210415.

(53) Zhang, L.; Jiang, K.; Yang, L.; Li, L.; Hu, E.; Yang, L.; Shao, K.; Xing, H.; Cui, Y.; Yang, Y.; Li, B.; Chen, B.; Qian, G. Benchmark C_2H_2/CO_2 Separation in an Ultramicroporous Metal−Organic Framework via Copper(I)-Alkynyl Chemistry. *Angew. Chem. Int. Ed.* **2021**, *60*, 15995−16002.

(54) Da Silva, F. A.; Rodrigues, A. E. PropylenePropane Separation by Vacuum Swing Adsorption Using 13X Zeolite. *A.I.Ch.E.J.* **2001**, *47*, 341−357.

(55) Grande, C. A.; Poplow, F.; Rodrigues, A. E. Vacuum pressure swing adsorption to produce polymer-grade polypropylene. *Separ. Sci. Technol.* **2010**, *45*, 1252−1259.

(56) Krishna, R. Exploiting Adsorption/Diffusion Synergy in MFI-Catalyzed Hexane Isomerization Reactor. *Chem. Ing. Technol.* **2023**, *95*, 1794−1799.

(57) Krishna, R.; Baur, R.; Van Baten, J. M. Highlighting Diffusional Coupling Effects in Zeolite Catalyzed Reactions by Combining the Maxwell-Stefan and Langmuir-Hinshelwood Formulations. *React. Chem. Eng.* **2017**, *2*, 324−336.

Supporting Information

Fundamental Insights into Intra-Crystalline Diffusional Influences on Mixture Separations in Fixed Bed Adsorbers

Rajamani Krishna
Van 't Hoff Institute for Molecular Sciences
University of Amsterdam
Science Park 904
1098 XH Amsterdam, The Netherlands
email: r.krishna@contact.uva.nl
ORCID 0000-0002-4784-8530

Contents

1 The Maxwell-Stefan Diffusion Formulation

Within micro-porous crystalline materials, such as zeolites, and metal-organic frameworks (MOFs), the guest molecules exist in the adsorbed phase. The Maxwell-Stefan (M-S) eqs for *n*-component diffusion in porous materials is applied in the following manner[1, 2]

$$\begin{aligned}
-\frac{\partial \mu_1}{\partial r} &= \frac{RT}{Đ_{12}} x_2 \left(u_1 - u_2\right) + \frac{RT}{Đ_{13}} x_3 \left(u_1 - u_3\right) + \ldots + \frac{RT}{Đ_1}\left(u_1\right) \\
-\frac{\partial \mu_2}{\partial r} &= \frac{RT}{Đ_{21}} x_1 \left(u_2 - u_1\right) + \frac{RT}{Đ_{23}} x_3 \left(u_2 - u_3\right) + \ldots + \frac{RT}{Đ_2}\left(u_2\right) \\
&\cdots\cdots\cdots \\
-\frac{\partial \mu_n}{\partial r} &= \frac{RT}{Đ_{n1}} x_1 \left(u_n - u_1\right) + \frac{RT}{Đ_{n2}} x_2 \left(u_n - u_3\right) + \ldots + \frac{RT}{Đ_n}\left(u_n\right)
\end{aligned} \qquad \text{(S1)}$$

The left members of eq (S1) are the negative of the gradients of the chemical potentials, with the units N mol^{-1}; it represents the driving force acting per mole of species 1, 2, 3,..*n*. The u_i represents the velocity of motion of the adsorbate, defined in a reference frame with respect to the framework material. The crystalline framework is considered to be stationary. The term $RT/Đ_i$ is interpreted as the drag or friction coefficient between the guest species *i* and the pore wall. The term $RT/Đ_{ij}$ is interpreted as the friction coefficient for the *i-j* pair of guest molecules. The multiplier $x_i = q_i / q_t$ where q_i is the molar loading of adsorbate, and q_t is the *total* mixture loading $q_t = \sum_{i=1}^{n} q_i$. We expect the friction to be dependent on the number of molecules of *j* relative to that of component *i*.

An important, persuasive, argument for the use of the M-S formulation for mixture diffusion is that the M-S diffusivity $Đ_i$ in mixtures can be estimated using information on the loading dependence of the corresponding unary diffusivity values. Put another way, the M-S diffusivity .$Đ_i$. can be estimated from experimental data on *unary* diffusion in the porous material.

The M-S diffusivity $Đ_{ij}$ has the units m^2 s^{-1} and the physical significance of an *inverse* drag coefficient. The magnitudes of the M-S diffusivities $Đ_{ij}$ do not depend on the choice of the mixture reference velocity because eq (S1) is set up in terms of velocity differences. At the molecular level, the $Đ_{ij}$ reflect how the facility for transport of species *i* *correlates* with that of species *j*; they are also termed *exchange coefficients*.

The Maxwell-Stefan diffusion formulation (S1) is consistent with the theory of irreversible thermodynamics. The Onsager Reciprocal Relations imply that the M-S pair diffusivities are symmetric

$$Đ_{ij} = Đ_{ji} \tag{S2}$$

We define N_i as the number of moles of species *i* transported per m^2 of crystalline material per second

$$N_i \equiv \rho q_i u_i \tag{S3}$$

where . ρ . is the framework density with units of kg m^{-3}. Multiplying both sides of eq (S1) by ρq_i, the M-S equations for *n*-component diffusion in zeolites, MOFs, and ZIFs take the form [3-5]

$$-\rho \frac{q_i}{RT}\frac{\partial \mu_i}{\partial r} = \sum_{\substack{j=1 \\ j \neq i}}^{n} \frac{x_j N_i - x_i N_j}{Đ_{ij}} + \frac{N_i}{Đ_i}; \qquad i = 1, 2, ..n \tag{S4}$$

The fluxes N_i in eqs (S4) are defined in terms of the moles transported per m^2 of the *total surface of crystalline material.*

1.1 Thermodynamic correction factors

At thermodynamic equilibrium, the chemical potential of component *i* in the bulk fluid mixture equals the chemical potential of that component in the adsorbed phase. For the bulk fluid phase mixture we have

$$\frac{1}{RT}\frac{\partial \mu_i}{\partial r} = \frac{\partial \ln f_i}{\partial r} = \frac{1}{f_i}\frac{\partial f_i}{\partial r}; \qquad i = 1, 2, ..n \tag{S5}$$

In eq (S5), f_i represent the partial fugacities in the bulk fluid phase mixture. The chemical potential gradients $\partial \mu_i / \partial r$ can be related to the gradients of the molar loadings, q_i, by defining thermodynamic correction factors Γ_{ij}

$$\frac{q_i}{RT}\frac{\partial \mu_i}{\partial r} = \sum_{j=1}^{n} \Gamma_{ij}\frac{\partial q_j}{\partial r}; \quad \Gamma_{ij} = \frac{q_i}{f_i}\frac{\partial f_i}{\partial q_j}; \qquad i,j = 1,....n \tag{S6}$$

The thermodynamic correction factors Γ_{ij} can be calculated by differentiation of the model describing mixture adsorption equilibrium. Generally speaking, the Ideal Adsorbed Solution Theory (IAST) of Myers and Prausnitz[6] is the preferred method for estimation of mixture adsorption equilibrium.

In some special case, the mixed-gas Langmuir model

$$\frac{q_i}{q_{i,sat}} = \theta_i = \frac{b_i f_i}{1+\sum_{i=1}^{n} b_i f_i}; \quad i = 1,2,...n \tag{S7}$$

may be of adequate accuracy. Analytic differentiation of eq (S7) yields

$$\Gamma_{ij} = \delta_{ij} + \left(\frac{q_{i,sat}}{q_{j,sat}}\right)\left(\frac{\theta_i}{\theta_V}\right); \qquad i,j = 1,2\ldots n \tag{S8}$$

where the fractional vacancy θ_V is defined as

$$\theta_V = 1 - \theta_t = 1 - \sum_{i=1}^{n} \theta_i \tag{S9}$$

The elements of the matrix of thermodynamic factors Γ_{ij} can be calculated explicitly from information on the component loadings q_i in the adsorbed phase; this is the persuasive advantage of the use of the mixed-gas Langmuir model. By contrast, the IAST does not allow the calculation of Γ_{ij} explicitly from knowledge on the component loadings q_i in the adsorbed phase; a numerical procedure is required.

In the scenario in which correlation effects are of negligible importance, eqs (S4) simplify to yield

$$N_i = -\rho Đ_i \frac{q_i}{RT}\frac{\partial \mu_i}{\partial r} \tag{S10}$$

Combining eqs (S4), (S5), and (S6) we get

$$N_i = -\rho Đ_i \sum_{j=1}^{n} \Gamma_{ij}\frac{\partial q_j}{\partial r}; \qquad i = 1,2..n \tag{S11}$$

Furthermore, if thermodynamic correction factors are also ignored, eq (S11) reduces to a set of uncoupled equations

$$N_i = -\rho Đ_i \frac{\partial q_i}{\partial r}; \qquad i = 1, 2..n \tag{S12}$$

Watch also the video presentation titled **Diffusion in Micropores** on YouTube

https://www.youtube.com/@rajamanikrishna250/videos

1.2 M-S formulation for binary mixture diffusion

For binary mixture diffusion inside microporous crystalline materials the Maxwell-Stefan equations (S4) are written

$$\begin{aligned} -\rho \frac{q_1}{RT}\frac{\partial \mu_1}{\partial r} &= \frac{x_2 N_1 - x_1 N_2}{Đ_{12}} + \frac{N_1}{Đ_1} \\ -\rho \frac{q_2}{RT}\frac{\partial \mu_2}{\partial r} &= \frac{x_1 N_2 - x_2 N_1}{Đ_{12}} + \frac{N_2}{Đ_2} \end{aligned} \tag{S13}$$

The first members on the right hand side of Eq (S13) are required to quantify slowing-down effects that characterize binary mixture diffusion.[7-9] There is no experimental technique for direct determination of the exchange coefficients $Đ_{12}$, that quantify molecule-molecule interactions.

In two-dimensional matrix notation, eq (S6) take the form

$$\begin{pmatrix} \frac{q_1}{RT}\frac{\partial \mu_1}{\partial r} \\ \frac{q_2}{RT}\frac{\partial \mu_2}{\partial r} \end{pmatrix} = [\Gamma] \begin{pmatrix} \frac{\partial q_1}{\partial r} \\ \frac{\partial q_2}{\partial r} \end{pmatrix} \tag{S14}$$

For the mixed-gas Langmuir model, eq (S7), we can derive simple analytic expressions for the four elements of the matrix of thermodynamic factors:[10]

$$\begin{bmatrix} \Gamma_{11} & \Gamma_{12} \\ \Gamma_{21} & \Gamma_{22} \end{bmatrix} = \frac{1}{1-\theta_1-\theta_2} \begin{bmatrix} 1-\theta_2 & \frac{q_{1,sat}}{q_{2,sat}}\theta_1 \\ \frac{q_{2,sat}}{q_{1,sat}}\theta_2 & 1-\theta_1 \end{bmatrix} = \begin{bmatrix} 1+b_1 f_1 & \frac{q_{1,sat}}{q_{2,sat}} b_1 f_1 \\ \frac{q_{2,sat}}{q_{1,sat}} b_2 f_2 & 1+b_2 f_2 \end{bmatrix} \tag{S15}$$

where the fractional occupancies, θ_i, are defined by eq (S7).

Let us define the square matrix $[B]$

$$[B]=\begin{bmatrix} \frac{1}{\text{Đ}_{1}}+\frac{x_{2}}{\text{Đ}_{12}} & -\frac{x_{1}}{\text{Đ}_{12}} \\ -\frac{x_{2}}{\text{Đ}_{12}} & \frac{1}{\text{Đ}_{2}}+\frac{x_{1}}{\text{Đ}_{12}} \end{bmatrix}; \quad [B]^{-1}=\frac{1}{1+\frac{x_{1}\text{Đ}_{2}}{\text{Đ}_{12}}+\frac{x_{2}\text{Đ}_{1}}{\text{Đ}_{12}}}\begin{bmatrix} \text{Đ}_{1}\left(1+\frac{x_{1}\text{Đ}_{2}}{\text{Đ}_{12}}\right) & \frac{x_{1}\text{Đ}_{1}\text{Đ}_{2}}{\text{Đ}_{12}} \\ \frac{x_{2}\text{Đ}_{1}\text{Đ}_{2}}{\text{Đ}_{12}} & \text{Đ}_{2}\left(1+\frac{x_{2}\text{Đ}_{1}}{\text{Đ}_{12}}\right) \end{bmatrix} \tag{S16}$$

In proceeding further, it is convenient to define a 2×2 dimensional square matrix $\left[\Lambda\right]$:

$$\left[\Lambda\right]=\begin{bmatrix} \frac{1}{\text{Đ}_{1}}+\frac{x_{2}}{\text{Đ}_{12}} & -\frac{x_{1}}{\text{Đ}_{12}} \\ -\frac{x_{2}}{\text{Đ}_{12}} & \frac{1}{\text{Đ}_{2}}+\frac{x_{1}}{\text{Đ}_{12}} \end{bmatrix}^{-1}=\frac{1}{1+\frac{x_{1}\text{Đ}_{2}}{\text{Đ}_{12}}+\frac{x_{2}\text{Đ}_{1}}{\text{Đ}_{12}}}\begin{bmatrix} \text{Đ}_{1}\left(1+\frac{x_{1}\text{Đ}_{2}}{\text{Đ}_{12}}\right) & \frac{x_{1}\text{Đ}_{1}\text{Đ}_{2}}{\text{Đ}_{12}} \\ \frac{x_{2}\text{Đ}_{1}\text{Đ}_{2}}{\text{Đ}_{12}} & \text{Đ}_{2}\left(1+\frac{x_{2}\text{Đ}_{1}}{\text{Đ}_{12}}\right) \end{bmatrix} \tag{S17}$$

Eq (S13) can be re-cast into 2-dimensional matrix notation

$$\begin{gathered} \left(N\right)=-\rho[\Lambda][\Gamma]\frac{\partial\left(q\right)}{\partial r}; \\ \begin{pmatrix} N_{1} \\ N_{2} \end{pmatrix}=-\frac{\rho}{1+\frac{x_{1}\text{Đ}_{2}}{\text{Đ}_{12}}+\frac{x_{2}\text{Đ}_{1}}{\text{Đ}_{12}}}\begin{bmatrix} \text{Đ}_{1}\left(1+\frac{x_{1}\text{Đ}_{2}}{\text{Đ}_{12}}\right) & \frac{x_{1}\text{Đ}_{1}\text{Đ}_{2}}{\text{Đ}_{12}} \\ \frac{x_{2}\text{Đ}_{1}\text{Đ}_{2}}{\text{Đ}_{12}} & \text{Đ}_{2}\left(1+\frac{x_{2}\text{Đ}_{1}}{\text{Đ}_{12}}\right) \end{bmatrix}\begin{bmatrix} \Gamma_{11} & \Gamma_{12} \\ \Gamma_{21} & \Gamma_{22} \end{bmatrix}\begin{pmatrix} \frac{\partial q_{1}}{\partial r} \\ \frac{\partial q_{2}}{\partial r} \end{pmatrix} \end{gathered} \tag{S18}$$

The elements of $\left[B\right]$ can be obtained by inverting the matrix $\left[\Lambda\right]$:

$$\begin{bmatrix} B_{11} & B_{12} \\ B_{21} & B_{22} \end{bmatrix}=\begin{bmatrix} \frac{1}{\text{Đ}_{1}}+\frac{x_{2}}{\text{Đ}_{12}} & -\frac{x_{1}}{\text{Đ}_{12}} \\ -\frac{x_{2}}{\text{Đ}_{12}} & \frac{1}{\text{Đ}_{2}}+\frac{x_{1}}{\text{Đ}_{12}} \end{bmatrix}=[\Lambda]^{-1} \tag{S19}$$

A 2×2 dimensional Fick diffusivity matrix $\left[D\right]$ is defined as the product of $\left[\Lambda\right]$ and the matrix of thermodynamic correction factors $\left[\Gamma\right]$:

$$
[D]=[B]^{-1}[\Gamma]=\frac{1}{1+\frac{x_1 Đ_2}{Đ_{12}}+\frac{x_2 Đ_1}{Đ_{12}}}\begin{bmatrix} Đ_1\left(1+\frac{x_1 Đ_2}{Đ_{12}}\right) & \frac{x_1 Đ_1 Đ_2}{Đ_{12}} \\ \frac{x_2 Đ_1 Đ_2}{Đ_{12}} & Đ_2\left(1+\frac{x_2 Đ_1}{Đ_{12}}\right) \end{bmatrix}\begin{bmatrix} \Gamma_{11} & \Gamma_{12} \\ \Gamma_{21} & \Gamma_{22} \end{bmatrix}
$$

$$
(N)=-\rho[D]\frac{\partial(q)}{\partial r} \tag{S20}
$$

1.3 Negligible correlations scenario for M-S diffusivities

For values of $Đ_1/Đ_{12} \rightarrow 0$, and $Đ_2/Đ_{12} \rightarrow 0$, the contribution of the first right member of M-S Eq (S13) can be ignored and correlations can be considered to be of negligible importance; we derive

$$
\frac{Đ_1}{Đ_{12}} \rightarrow 0; \quad \frac{Đ_2}{Đ_{12}} \rightarrow 0; \quad \begin{bmatrix} \Lambda_{11} & \Lambda_{12} \\ \Lambda_{21} & \Lambda_{22} \end{bmatrix} \rightarrow \begin{bmatrix} Đ_1 & 0 \\ 0 & Đ_2 \end{bmatrix}
$$

$$
\begin{bmatrix} D_{11} & D_{12} \\ D_{21} & D_{22} \end{bmatrix}=\begin{bmatrix} Đ_1 & 0 \\ 0 & Đ_2 \end{bmatrix}\begin{bmatrix} \Gamma_{11} & \Gamma_{12} \\ \Gamma_{21} & \Gamma_{22} \end{bmatrix}
$$

$$
\begin{pmatrix} N_1 \\ N_2 \end{pmatrix}=-\rho\begin{bmatrix} D_{11} & D_{12} \\ D_{21} & D_{22} \end{bmatrix}\begin{pmatrix} \frac{\partial q_1}{\partial r} \\ \frac{\partial q_2}{\partial r} \end{pmatrix} \tag{S21}
$$

Eq (S21) is valid, as a first approximation, for diffusion in cage-type zeolites with 8-ring windows (CHA, LTA, DDR, ERI) and ZIF-8; see earlier publications.[4, 11-17] For all of the guest/host combinations considered in this article, the use of eq (S21) is justified.

When correlation effects are negligible, the diffusional coupling effects are solely traceable to mixture adsorption thermodynamics, embodied in the matrix $[\Gamma]$.

If the mixed-gas Langmuir model is used to describe mixture adsorption equilibrium, the matrix of thermodynamic correction factors is given by Eq (S15). Combining eqs (S15)., and (S21) we obtain the flux expression

$$\begin{pmatrix} N_1 \\ N_2 \end{pmatrix} = -\rho \begin{bmatrix} Đ_1 & 0 \\ 0 & Đ_2 \end{bmatrix} \frac{1}{1-\theta_1-\theta_2} \begin{bmatrix} 1-\theta_2 & \frac{q_{1,sat}}{q_{2,sat}}\theta_1 \\ \frac{q_{2,sat}}{q_{1,sat}}\theta_2 & 1-\theta_1 \end{bmatrix} \begin{pmatrix} \frac{\partial q_1}{\partial r} \\ \frac{\partial q_2}{\partial r} \end{pmatrix} \tag{S22}$$

Eq (S22) is essentially equivalent to the flux relation used by Habgood[18] to model transient overshoots in the loading of N_2 during transient uptake of N_2/CH_4 in LTA-4A zeolite. These flux relations (S22) are also incorporated into the models for describing the transient breakthroughs in fixed bed adsorbers by Ruthven, Farooq, Knaebel, and co-workers.[19-22]

1.4 Ignoring thermodynamic coupling effects

In the Henry regime of adsorption, i.e. at low component loading, thermodynamic correction factors may be adequately described by $\Gamma_{ij} = \delta_{ij}$, the Kronecker delta.

$$\begin{bmatrix} \Gamma_{11} & \Gamma_{12} \\ \Gamma_{21} & \Gamma_{22} \end{bmatrix} = \begin{bmatrix} 1 & 0 \\ 0 & 1 \end{bmatrix}; \quad \begin{pmatrix} N_1 \\ N_2 \end{pmatrix} = -\rho \begin{bmatrix} Đ_1 & 0 \\ 0 & Đ_2 \end{bmatrix} \begin{pmatrix} \frac{\partial q_1}{\partial r} \\ \frac{\partial q_2}{\partial r} \end{pmatrix} \tag{S23}$$

Indeed, the major objective of this article is to demonstrate the inadequacy of Eq (S23) to model transient mixture uptake in microporous crystals, and transient breakthroughs in fixed bed adsorbers.

2 IAST calculations of mixture adsorption equilibrium

2.1 Brief outline of theory

Within microporous crystalline materials such as zeolites and metal-organic frameworks (MOFs), the guest molecules exist in the adsorbed phase. The Gibbs adsorption equation in differential form is

$$A d\pi = \sum_{i=1}^{n} q_i d\mu_i \tag{S24}$$

The quantity A is the surface area per kg of framework, with units of m^2 per kg of the framework of the crystalline material; q_i is the molar loading of component i in the adsorbed phase with units moles per kg of framework; μ_i is the molar chemical potential of component i. The spreading pressure π has the same units as surface tension, i.e. N m^{-1}.

The chemical potential of any component in the adsorbed phase, μ_i, equals that in the bulk fluid phase. If the partial fugacities in the bulk fluid phase are f_i, we have

$$d\mu_i = RTd\ln f_i \tag{S25}$$

where R is the gas constant (= 8.314 J mol^{-1} K^{-1}).

Briefly, the basic equation of Ideal Adsorbed Solution Theory (IAST) theory of Myers and Prausnitz[6] is the analogue of Raoult's law for vapor-liquid equilibrium, i.e.

$$f_i = P_i^0 x_i; \quad i = 1, 2, \ldots n \tag{S26}$$

where x_i is the mole fraction in the adsorbed phase

$$x_i = \frac{q_i}{q_1 + q_2 + \ldots q_n} \tag{S27}$$

and P_i^0 is the pressure for sorption of every component i, which yields the same spreading pressure, π for each of the pure components, as that for the mixture:

$$\frac{\pi A}{RT}=\int_0^{P_1^0}\frac{q_1^0(f)}{f}df=\int_0^{P_2^0}\frac{q_2^0(f)}{f}df=\int_0^{P_3^0}\frac{q_3^0(f)}{f}df=... \tag{S28}$$

where $q_i^0(f)$ is the *pure* component adsorption isotherm. The units of $\frac{\pi A}{RT}\equiv\Phi$, also called the surface potential,[23, 24] are mol kg^{-1}; the surface potential has also been called the adsorption potential in several recent publications.[25-28]

The unary isotherm may be described by say the 1-site Langmuir isotherm

$$q^0\left(f\right)=q_{sat}\frac{bf}{1+bf};\quad \theta=\frac{bf}{1+bf} \tag{S29}$$

where we define the fractional *occupancy* of the adsorbate molecules, $\theta=q^0\left(f\right)/q_{sat}$. The superscript 0 is used to emphasize that $q^0\left(f\right)$ relates the *pure component* loading to the bulk fluid fugacity. More generally, the unary isotherms may need to be described by, say, the dual-site Langmuir-Freundlich model

$$q^0(f)=q_{A,sat}\frac{b_Af^{\nu_A}}{1+b_Af^{\nu_A}}+q_{B,sat}\frac{b_Bf^{\nu_B}}{1+b_Bf^{\nu_B}} \tag{S30}$$

Each of the integrals in Eq (S28) can be evaluated analytically:

$$\begin{aligned}\Phi&=\int_{f=0}^{P_i^0}\frac{q^0(f)}{f}df=\frac{q_{A,sat}}{\nu_A}\ln\left(1+b_A\left(P_i^0\right)^{\nu_A}\right)+\frac{q_{B,sat}}{\nu_B}\ln\left(1+b_B\left(P_i^0\right)^{\nu_B}\right)\\ \Phi&=\int_{f=0}^{P_i^0}\frac{q^0(f)}{f}df=\frac{q_{A,sat}}{\nu_A}\ln\left(1+b_A\left(\frac{f_i}{x_i}\right)^{\nu_A}\right)+\frac{q_{B,sat}}{\nu_B}\ln\left(1+b_B\left(\frac{f_i}{x_i}\right)^{\nu_B}\right)\end{aligned} \tag{S31}$$

The right members of eq (S31) is a function of P_i^0. For multicomponent mixture adsorption, each of the equalities on the right side of eq (S28) must be satisfied. These constraints may be solved using a suitable equation solver, to yield the set of values of P_1^0, P_2^0, P_3^0,.. P_n^0, all of which satisfy eq (S28). The corresponding values of the integrals using these as upper limits of integration must yield the same value of the surface potential $\frac{\pi A}{RT}\equiv\Phi$ for each component; this ensures that the obtained solution is the correct one.

The adsorbed phase mole fractions x_i are then determined using eq (S26):

$$x_i = \frac{f_i}{P_i^0}; \quad i = 1,2,...n \tag{S32}$$

The applicability of eq (S32) mandates that all of the adsorption sites within the microporous material are equally accessible to each of the guest molecules, implying a homogeneous distribution of guest adsorbates within the pore landscape, with no preferential locations of any guest species. The circumstances in which this mandate is not fulfilled are highlighted in recent works.[26-29]

A further key assumption of the IAST is that the enthalpies and surface areas of the adsorbed molecules do not change upon mixing. If the total mixture loading is q_t, the area covered by the adsorbed mixture is $\frac{A}{q_t}$ with units of m^2 (mole mixture)$^{-1}$. Therefore, the assumption of no surface area change due to mixture adsorption translates as $\frac{A}{q_t} = \frac{Ax_1}{q_1^0\left(P_1^0\right)} + \frac{Ax_2}{q_2^0\left(P_2^0\right)} + \cdots \frac{Ax_n}{q_n^0\left(P_n^0\right)}$; the total mixture loading is $q_t = q_1 + q_2 ... + q_n$ is calculated from

$$\frac{1}{q_t} = \frac{x_1}{q_1^0(P_1^0)} + \frac{x_2}{q_2^0(P_2^0)} + ... + \frac{x_n}{q_n^0(P_n^0)} \tag{S33}$$

in which $q_1^0(P_1^0)$, $q_2^0(P_2^0)$,… $q_n^0(P_n^0)$ are determined from the unary isotherm fits, using the sorption pressures for each component P_1^0, P_2^0, P_3^0,.. P_n^0 that are available from the solutions to eqs (S28), and (S31). The occurrence of molecular clustering and hydrogen bonding should be expected to applicability of eq (S33) because the surface area occupied by a molecular cluster is different from that of each of the un-clustered guest molecules in the adsorbed phase.

The entire set of eqs (S26) to (S33) need to be solved numerically to obtain the loadings, q_i of the individual components in the mixture.

Watch also the presentation titled **The IAST for Mixture Adsorption Equilibrium** on YouTube https://www.youtube.com/@rajamanikrishna250/videos

3 Transient breakthroughs in fixed bed adsorbers

We first analyze the transient uptake of mixtures within a spherical micro-porous crystalline particle. Watch also the video presentation titled **Transient Breakthrough Simulations** on YouTube

https://www.youtube.com/@rajamanikrishna250/videos

3.1 Transient uptake inside microporous crystals

The radial distribution of molar loadings, q_i, within a spherical crystallite, of radius r_c, is obtained from a solution of a set of differential equations describing the uptake

$$\rho \frac{\partial q_i(r,t)}{\partial t} = -\frac{1}{r^2}\frac{\partial}{\partial r}\left(r^2 N_i\right) \tag{S34}$$

The intra-crystalline fluxes N_i, in turn, are related to the radial gradients in the molar loadings by Eq (S18), or the simplified Eq (S21) for the negligible correlations scenario. At time $t = 0$, i.e. the initial conditions, the molar loadings $q_i(r,0)$ at all locations r within the crystal are uniform (zero loadings). For all times $t \geq 0$, the exterior of the crystal is brought into contact with a bulk gas mixture at partial pressures p_{i0} that is maintained constant till the crystal reaches thermodynamic equilibrium with the surrounding gas mixture. At any time t, the component loadings at the surface of the particle $q_i(r_c,t) = q_i^*$ is in equilibrium with the bulk phase gas mixture with partial pressures p_{i0}. In the general case, the component loadings are calculated using the Ideal Adsorbed Solution Theory (IAST) of Myers and Prausnitz.[6] Alternatively, in some cases, the mixed-gas Langmuir eq (S7) may be of sufficient accuracy. An important advantage of the use of the mixed-gas Langmuir model is that the matrix of the thermodynamic correction factors can be determined explicitly using Eq (S15).

At time *t*, during the transient approach to thermodynamic equilibrium, the spatial-averaged component loading within the crystallites of radius r_c is calculated using

$$\overline{q}_i(t) = \frac{3}{r_c^3}\int_0^{r_c} q_i(r,t) r^2 dr \tag{S35}$$

Summing eq (S35) over all *n* species in the mixture allows calculation of the *total average* molar loading of the mixture within the crystallite

$$\overline{q}_t(t,z) = \sum_{i=1}^{n} \overline{q}_i(t,z) \tag{S36}$$

The spatial-averaged $\overline{q}_i(t)$ and $\overline{q}_t(t,z)$ can be compared directly with experimental transient uptake data.

For *n*-component transient uptake, the set of eqs (S18), (S34), and (S35), and (S36) need to be solved numerically using robust computational techniques. Eqs (S34) are first subjected to finite volume discretization. One of two strategies can be adopted: (a) equi-volume discretization, or (b) equi-distant discretization; see Figure S2. The choice of the discretization scheme used is crucially important in obtaining accurate, converged results. The choice of equi-volume slices is needed when the gradients of the loadings are particularly steep nearer to $r = r_c$. For either strategy, about 20 – 150 slices were employed in the simulations presented in this work, depending on the guest/host combination. Combination of the discretized partial differential eqs (S34) along with algebraic equations describing mixture adsorption equilibrium (IAST or mixed-gas Langmuir model), results in a set of differential-algebraic equations (DAEs), which are solved using BESIRK.[30] BESIRK is a sparse matrix solver, based on the semi-implicit Runge-Kutta method originally developed by Michelsen,[31] and extended with the Bulirsch-Stoer extrapolation method.[32] Use of BESIRK improves the numerical solution efficiency in solving the set of DAEs. The evaluation of the sparse Jacobian required in the numerical algorithm is largely based on analytic expressions.[10] Further details of the numerical procedures used in this work, are provided by

Krishna and co-workers;[10, 33-35] interested readers are referred to our website that contains the numerical details.[33]

3.2 Geddes model for transient uptake inside microporous crystals

If the matrix of Fick diffusivities, $[D]=[B]^{-1}[\Gamma]$, defined by either eq (S20), or eq (S21) may be considered to be loading-independent during the entire duration of the equilibration process, it is possible to obtained an analytic solution for the component loading. The analytic solution, derived first by Geddes[36] to describe diffusion inside spherical vapor bubbles on distillation trays, is expressed as

$$\frac{\left(q^* - \overline{q}(t)\right)}{\left(q^* - q_0\right)} = \frac{6}{\pi^2}\sum_{m=1}^{\infty}\frac{\exp(-m^2\pi^2\frac{D}{r_c^2}t)}{m^2};$$
$$\left(q^* - \overline{q}(t)\right) = Q\left(q^* - q_0\right); \tag{S37}$$
$$Q = \frac{6}{\pi^2}\sum_{m=1}^{\infty}\frac{\exp(-m^2\pi^2\frac{D}{r_c^2}t)}{m^2}$$

Equation (S37) holds when (a) the initial loadings at all locations r within the crystal are uniform, i.e. $q(r,0) = q_0$, and (b) for all times $t \geq 0$, the exterior of the crystal is brought into contact with a bulk fluid mixture at a bulk pressure $p(r_c,t)$, and molar loading, q^*, that is maintained constant till the crystal reaches thermodynamic equilibrium with the surrounding fluid mixture.

Figure S1a shows the experimental data for transient adsorption and desorption profiles for C_2H_6 in LTA-4A zeolite. The adsorption branch can be fitted with $D_i/r_c^2 = 1.1\times10^{-3}$ s^{-1}, while the desorption branch yields a lower value $D_i/r_c^2 = 6\times10^{-4}$ s^{-1}. The continuous solid lines are the solutions to Eq (S37). The asymmetry in the adsorption and desorption kinetics is not easy to interpret on the basis of the Fick formulation.

Watch also the video presentation titled **Unary Diffusivities in Micropores** on YouTube

https://www.youtube.com/@rajamanikrishna250/videos

For a fundamental understanding of the observed asymmetry, we turn to the Maxwell-Stefan formulation that uses chemical potential gradients as the driving forces $N_i = -\rho Đ_i \frac{q_i}{RT}\nabla\mu_i$ where the M-S diffusivity, $Đ_i$, is inter-related to the Fick diffusivity by $D_i = Đ_i \Gamma_i$; $\Gamma_i \equiv \frac{q_i}{f_i}\frac{\partial f_i}{\partial q_i}$.The thermodynamic correction factor, Γ_i, can be obtained by differentiation of the adsorption isotherm that relates the molar loadings to the bulk fluid phase pressure, or fugacity, surrounding the crystals. For the simplest case of a single-site Langmuir isotherm $\frac{q_i}{q_{i,sat}} = \theta_i = \frac{b_i f_i}{1+b_i f_i}$, the thermodynamic correction factor, Γ_i, is $\Gamma_i = \frac{1}{1-q_i/q_{i,sat}} = \frac{1}{1-\theta_i}$. The inverse thermodynamic factor, $1/\Gamma_i$, decreases linearly with fractional occupancy (cf. Figure S1b; the unary isotherm fit is provided in Table S1). Figure S1b shows the simulations of the transient uptake using the numerical solution to the M-S equations. Both the adsorption and desorption cycles can be fitted with $Đ_i/r_c^2$ = 2×10^{-4} s^{-1}. This implies that that the asymmetry in the adsorption and desorption transience have their origin in the characteristics of $1/\Gamma_i$; the slower desorption kinetics is attributable to the decrease in $1/\Gamma_i$ during the desorption phase.

3.3 LDF model for transient uptake inside microporous crystals

In the Linear Driving Force (LDF) model of Glueckauf, [37] the simplified eq (S12) is invoked and, furthermore, the solution to the set of partial differential eqs (S34), is obviated by writing the time-derivative of the spatially averaged component loadings as follows

$$\rho \frac{\partial \overline{q}_i(t)}{\partial t} = -\frac{15Đ_i}{r_c^2}\left(q_i^* - \overline{q}_i(t)\right); \quad i = 1,2...n \tag{S38}$$

where q_i^* is the molar loading that is in equilibrium with the bulk fluid mixture surrounding the crystal. Equation (S38) is valid for the condition $\frac{D_i t}{r_c^2} > 0.1$, along with the assumption $\frac{\partial \overline{q}_i(t)}{\partial t} \approx \frac{\partial q_i^*}{\partial t}$. The LDF model predicts that each component will approach equilibrium following

$$\frac{\left(q_i^* - \overline{q}_i(t)\right)}{\left(q_i^* - q_i(r_c,0)\right)} = \exp(-\frac{15Đ_i}{r_c^2}t); \quad i = 1,2...n \tag{S39}$$

Equation (S39) implies that the approach to equilibrium for each species will be monotonous, i.e. without overshoots. The failure of the LDF for kinetic separations is due to the fact that for synergistic and anti-synergistic diffusion influences to be effective, we must have $\frac{Đ_i t}{r_c^2} < 0.1$.

Watch also the video presentation titled **The LDF Model for Intra-particle Diffusion** and **LDF vs Maxwell-Stefan in PSA** on YouTube

https://www.youtube.com/@rajamanikrishna250/videos

3.4 Modelling transient breakthroughs in fixed bed

We describe below the simulation methodology used to perform transient breakthrough calculations for fixed bed adsorbers (see schematics in Figure S2, and Figure S3). The simulation methodology is the same as used in our earlier publications.[3, 5, 38, 39] For an *n*-component gas mixture flowing through a fixed bed maintained under isothermal, isobaric, conditions, the molar concentrations in the gas phase at any position and instant of time are obtained by solving the following set of partial differential equations for each of the species *i* in the gas mixture[3, 10, 19, 33]

$$-D_{ax}\frac{\partial^2 c_i(t,z)}{\partial z^2} + \frac{\partial c_i(t,z)}{\partial t} + \frac{\partial\left(v(t,z)c_i(t,z)\right)}{\partial z} + \frac{\left(1-\varepsilon\right)}{\varepsilon}\rho\frac{\partial \overline{q}_i(t,z)}{\partial t} = 0; \quad i = 1,2,...n \tag{S40}$$

In eq (S40), t is the time, z is the distance along the adsorber, ρ is the framework density, ε is the bed voidage, D_{ax} is the axial dispersion coefficient, v is the interstitial gas velocity, and $\overline{q}_i(t,z)$ is the *spatially averaged* molar loading within the crystallites of radius r_c, monitored at position z, and at time t. The time $t = 0$, corresponds to the time at which the feed mixture is injected at the inlet to the fixed bed. Prior to injection of the feed, it is assumed that an inert, non-adsorbing, gas flows through the fixed bed. In this model described by eq (S40), the effects of all mechanisms that contribute to axial mixing are lumped into a single effect axial dispersion coefficient D_{ax}. Ruthven et al.[19] state that more detailed models that include radial dispersion are generally not necessary. They also make the following remark "when mass transfer resistance is significantly greater than axial dispersion, one may neglect the axial dispersion term and assume plug flow". This is the situation that manifests for kinetically controlled separations, the focus of the present article. Consequently, all of the analysis and breakthrough simulations were carried out using the plug flow assumption.

The term $\frac{\partial \overline{q}_i(t,z)}{\partial t}$ in eq (S40) is determined by solving the set of eqs (S34), and (S35), and (S36). At any time *t*, and position *z*, the component loadings at the outer surface of the particle $q_i(r_c,t,z)$ is in equilibrium with the bulk phase gas mixture with partial pressures $p_i(t,z)$ in the bulk gas mixture. In the general case, the component loadings $q_i(r_c,t,z)$ are calculated using the Ideal Adsorbed Solution Theory (IAST) of Myers and Prausnitz.[6] Alternatively, in some cases, the mixed-gas Langmuir eq (S7) may be of sufficient accuracy.

If the value of $Đ_i/r_c^2$ is large enough to ensure that intra-crystalline gradients are absent and the entire crystallite particle can be considered to be in thermodynamic equilibrium with the surrounding bulk gas phase at that time *t*, and position *z* of the adsorber

$$\overline{q}_i(t,z) = q_i(t,z) \tag{S41}$$

The *interstitial* gas velocity is related to the *superficial* gas velocity by

$$v = \frac{u}{\varepsilon} \tag{S42}$$

In all of the simulations reported in this article, the entire bed of crystalline particles is considered to be devoid of adsorbates at time *t* = 0, i.e. we have the initial condition

$$t = 0; \quad q_i(0,z) = 0 \tag{S43}$$

Eq (S43) is relevant to the operation of the transient breakthrough experiments on a laboratory scale, but are not truly reflective of industrial operations.

At time, $t = 0$, the inlet to the adsorber, $z = 0$, is subjected to a step input of the n-component gas mixture and this step input is maintained till the end of the adsorption cycle when steady-state conditions are reached.

$$t \geq 0; \quad p_i(0,t) = p_{i0}; \quad u(0,t) = u_0 \tag{S44}$$

where $u_0 = v_0 \varepsilon$ is the superficial gas velocity at the inlet to the adsorber.

Besides, the breakthrough simulations with a step-input, we also carried out simulations for a packed bed adsorber with injection of a short duration pulse of the mixture of reactants. presents a schematic of a packed bed reactor with pulse input of feed gas mixture. For simulation of pulse chromatographic reactors, we use the corresponding set of inlet conditions

$$0 \leq t \leq t_0; \quad p_i(0,t) = p_{i0}; \quad u(0,t) = u_0 \tag{S45}$$

where the time for duration of the pulse is t_0.

Typically, the adsorber length is divided into 100 slices, and each spherical crystallite was discretized into 20 - 150 equi-volume slices. The results thus obtained were confirmed to be of adequate accuracy. Combination of the discretized partial differential equations (PDEs) along with the algebraic equations describing mixture adsorption equilibrium (IAST, or mixed-gas Langmuir model, as appropriate), results in a set of differential-algebraic equations (DAEs), which are solved using BESIRK.[30] BESIRK is a sparse matrix solver, based on the semi-implicit Runge-Kutta method originally developed by Michelsen,[31] and extended with the Bulirsch-Stoer extrapolation method.[32] Use of BESIRK improves the numerical solution efficiency in solving the set of DAEs. The evaluation of the sparse Jacobian required in the numerical algorithm is largely based on analytic expressions.[10] Further details of the numerical procedures used in this work, are provided by Krishna and co-workers;[10, 33-35] interested readers are referred to our website that contains the numerical details.[33]

Watch also the video presentation titled **Transient Breakthrough Simulations** on YouTube

https://www.youtube.com/@rajamanikrishna250/videos

For *most* of the simulations reported in this article we choose the following: adsorber length, L = 0.3 m; cross-sectional area, A = 1 m^2; superficial gas velocity in the bed, u_0 = 0.04 m s^{-1}; voidage of the packed bed, ε = 0.4. Also, the total pressures is assumed to be constant along the length of the fixed bed. Please note that since the superficial gas velocity is specified, the specification of the cross-sectional area of the tube, A, is not relevant in the simulation results presented. The total volume of the bed is $V_{bed} = LA$. The volume of zeolite or MOF used in the simulations is $V_{ads} = LA(1-\varepsilon)$ = 0.18 m^3. If ρ is the framework density, the mass of the adsorbent in the bed is $m_{ads} = \rho LA(1-\varepsilon)$ kg. It is important to note that the volume of adsorbent, V_{ads}, includes the pore volume of the adsorbent material. In these breakthrough simulations we use the same volume of adsorbent in the breakthrough apparatus, i.e. (1 - ε) A L = 0.18 m^3 = 180 L.

The transient breakthrough data for the dimensionless concentrations at the exit of the fixed bed, c_i/c_{i0}, are plotted as a function of a modified time parameter defined by

$$\begin{aligned}&\frac{\left(Q_0 = \text{flow rate m}^3\text{ s}^{-1}\right)\times\left(\text{time in s}\right)}{\left(\text{kg MOF packed in tube}\right)} = \frac{Q_0 t}{m_{ads}} = \text{m}^3\text{ kg}^{-1}\\ &= \frac{\left(u_0 \text{A}\right)\times\left(t\right)}{(1-\varepsilon)\times\left(L\text{ m}\right)\times\left(A\text{ m}^2\right)\times\left(\rho\text{ kg m}^{-3}\right)} = \frac{u_0 t \varepsilon}{(1-\varepsilon)\varepsilon\times L\times\rho}\end{aligned} \tag{S46}$$

The theoretical justification for the use of this modified time parameter is the shock-wave model, as described in previous works.[38, 40]

Alternatively, we may present the data on transient breakthroughs for the adsorption cycle using the molar flow rates *entering* the adsorber

$$\frac{\left(F_0 = \text{flow rate mol s}^{-1}\right)\times\left(\text{time in s}\right)}{\left(\text{kg MOF packed in tube}\right)} = \frac{F_0 t}{m_{ads}} = \text{mol kg}^{-1} \tag{S47}$$

3.5 Comparison of breakthrough experimental data with breakthrough simulations

We describe below how we compare experimental data on transient breakthroughs with breakthrough simulations using the methodology outlined in the foregoing section.

The following data are usually provided in the published literature on the breakthrough experiments.

Inside diameter of tube of diameter: d.

Effective length of packed column: L.

The mass of the crystallites in the packed tube: m_{ads}.

The crystal framework density ρ kg m^{-3}.

Total pressure, p_t, and temperature, T at which the experiments are conducted.

Composition of entering gas phase mixture.

The total flow rate of the gas mixture at the entrance to the tube Q_0, usually expressed in units of mL min^{-1} at STP or at actual total pressure, p_t, and temperature, T. We may convert the data to determine Q_0 in units of m^3 s^{-1} at total pressure, p_t, and temperature, T.

We calculate $\left(1-\varepsilon\right)=\dfrac{m_{ads}/\rho}{\pi d^2 L/4}$ and $\varepsilon=1-\dfrac{m_{ads}/\rho}{\pi d^2 L/4}$.

The superficial gas velocity at the inlet to the adsorber $u=\dfrac{Q_0}{\pi d^2/4}$.

The interstitial velocity $v=\dfrac{u}{\varepsilon}=\dfrac{Q_0}{\left(\pi d^2/4\right)\left(1-\dfrac{m_{ads}/\rho}{\pi d^2 L/4}\right)}$.

$$\left(Đ_1/r_c^2\right)\left(L/v\right)\ ;\quad \left(1-\varepsilon\right)=\frac{m_{ads}/\rho}{\pi d^2 L/4}$$

$$\frac{v r_c^2}{L}=\frac{Q_0 r_c^2}{\left(\pi d^2/4\right)L\varepsilon}=\frac{Q_0 r_c^2\left(1-\varepsilon\right)}{\left(m_{ads}/\rho\right)\varepsilon}$$

$$\left(Đ_1/r_c^2\right)\left(L/v\right)=\left(Đ_1/r_c^2\right)\frac{m_{ads}}{Q_0\rho}\frac{\varepsilon}{(1-\varepsilon)}$$

$$\frac{Q_0 t}{m_{ads}}=\frac{t}{L/v}\frac{\varepsilon}{(1-\varepsilon)\rho}$$

$$\left(L/v\right)=\frac{m_{ads}}{Q_0\rho}\frac{\varepsilon}{(1-\varepsilon)}$$

The IAST model calculations for mixture adsorption equilibria are calculated using the unary isotherms that are commonly fitted with the dual-site Langmuir-Freundlich model

$$q = q_{A,sat} \frac{b_A p^{\nu_A}}{1 + b_A p^{\nu_A}} + q_{B,sat} \frac{b_B p^{\nu_B}}{1 + b_B p^{\nu_B}} \tag{S48}$$

The only other parameter that is required for performing the simulations are the values of $Đ_i / r_c^2$. For "open" structures such as M2(dobdc) and M2(*m*-dobdc), with channel dimensions of the order of 11 Å, the diffusional influences are usually of negligible importance and eq (S41) may be invoked. Alternatively, the values of $Đ_i / r_c^2$ may be chosen to match the essential distended characteristics of the experimental breakthroughs.

Watch also the presentation titled **Evaluating MOFs using Breakthrough Experiments** on YouTube https://www.youtube.com/@rajamanikrishna250/videos

3.6 List of Tables for Transient breakthroughs in fixed bed adsorbers

Table S1. Langmuir parameters for adsorption of C_2H_6 in LTA-4A at 298 K.

	$\frac{q_{sat}}{\text{mol kg}^{-1}}$	$\frac{b}{\text{Pa}^{-1}}$
C_2H_6	2.53	1.0E-02

3.7 List of Figures for Transient breakthroughs in fixed bed adsorbers

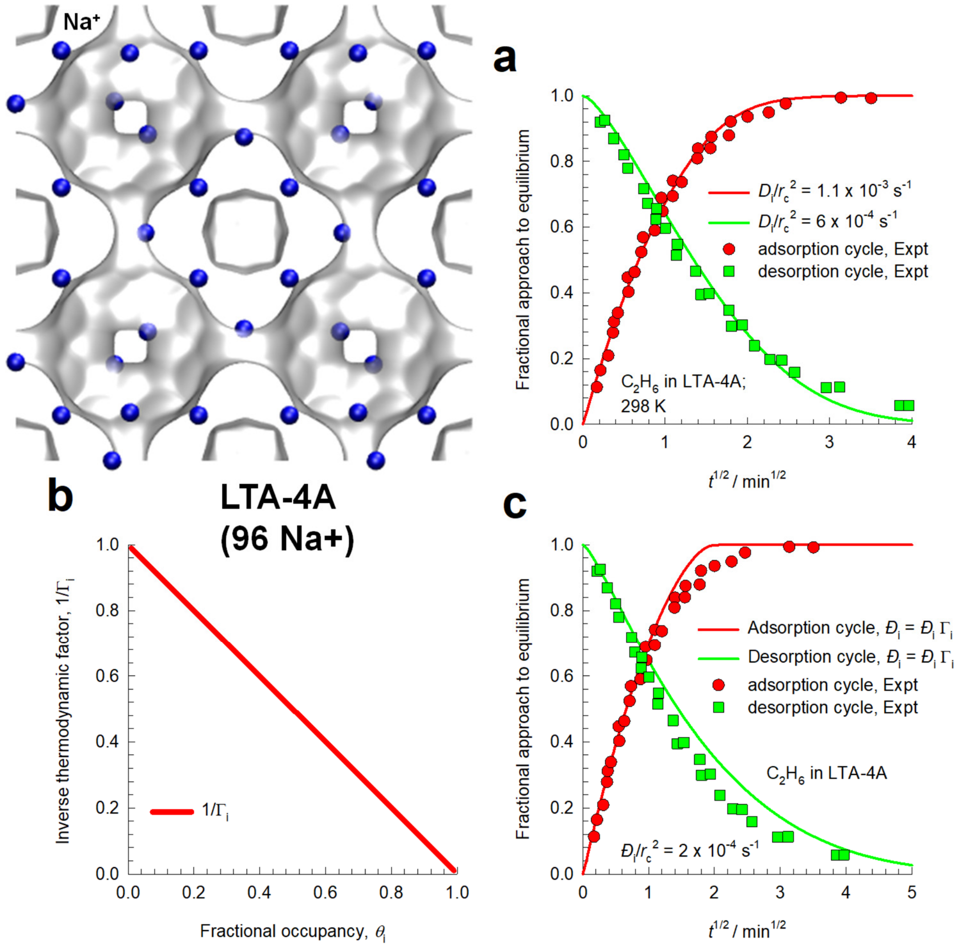

Figure S1. (a) Transient adsorption and desorption profiles for C_2H_6 in LTA-4A zeolite at 298 K. Experimental data of Garg and Ruthven.[41] The continuous solid lines are the solutions to the Geddes model for transient uptake. (b) Variation of the inverse thermodynamic correction factor with fractional occupancy. (c) Transient adsorption and desorption profiles for C_2H_6 in LTA-4A zeolite at 298 K. The continuous solid lines are the numerical solutions to the Maxwell-Stefan model for transient uptake, including the influence of the thermodynamic correction factor.

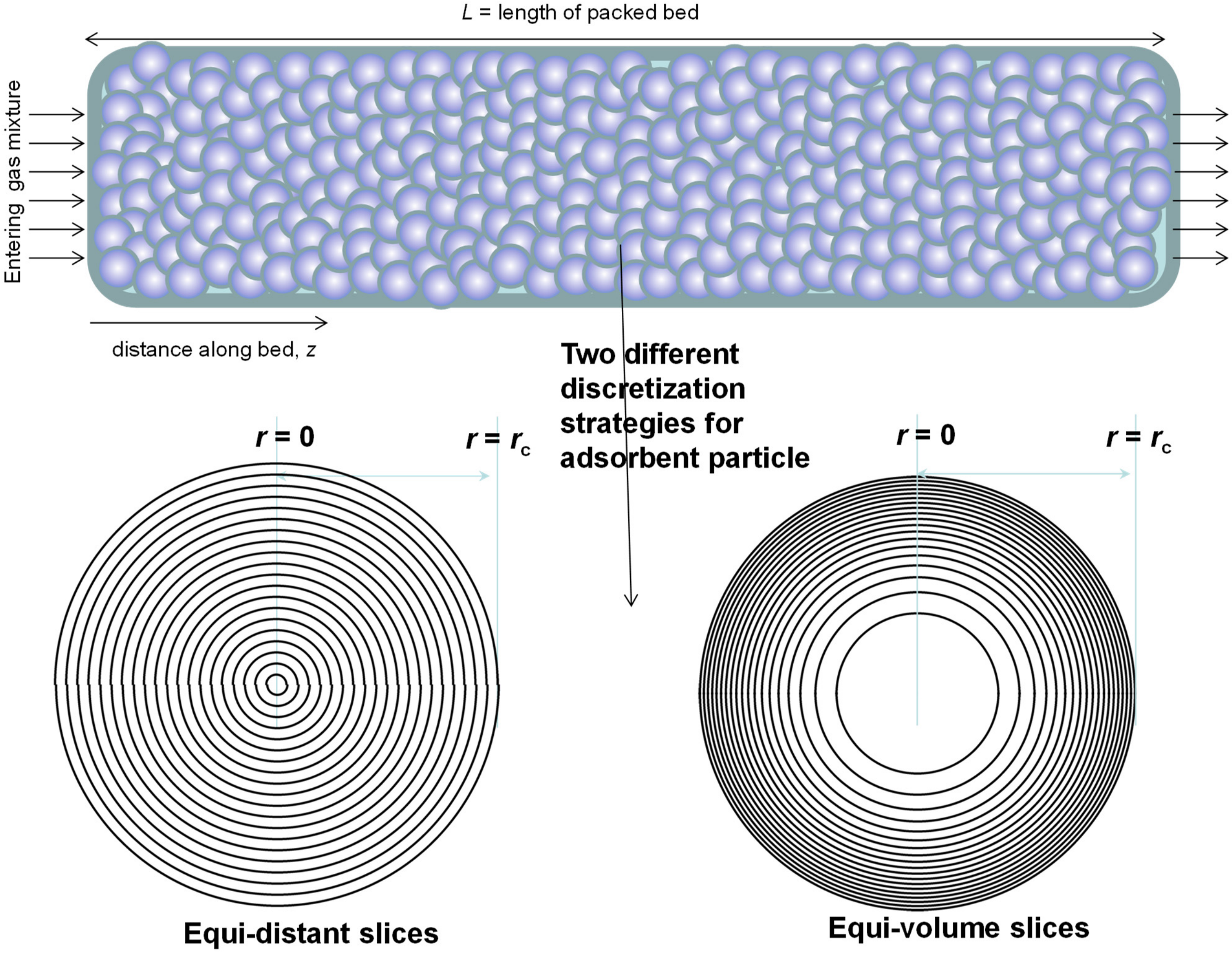

Figure S2. Two different discretization schemes for a single spherical crystallite.

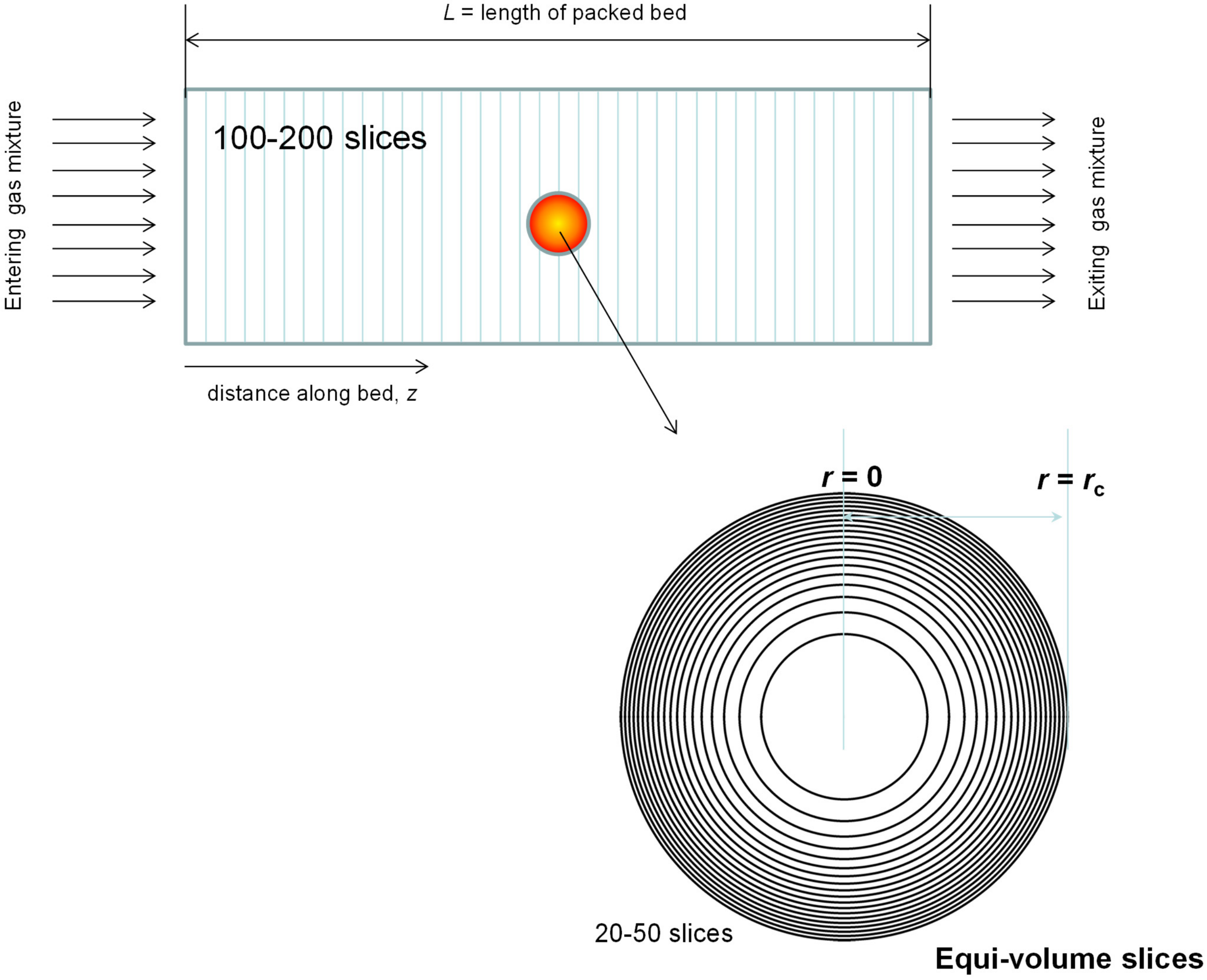

Figure S3. Discretization scheme for fixed bed adsorber.

4 Separation of hexane isomers

4.1 Background on hexane isomers separation

The separation of hexane isomers, n-hexane (nC6), 2-methylpentane (2MP), 3-methylpentane (3MP), 2,2 dimethylbutane (22DMB), and 2,3 dimethylbutane (23DMB) is required for production of high-octane gasoline. The values of the Research Octane Number (RON) increases with the degree of branching; Table S2 lists the Research Octane Numbers (RON) of C5, C6 and C7 alkanes.[42] The di-branched isomers (22DMB, 23DMB) have significantly higher RON values than that of the linear isomer (nC6), and mono-branched isomers (2MP, 3MP). The RON values are: nC6 = 30, 2MP = 74.5, 3MP = 75.5, 22DMB = 94, 23DMB = 105. Therefore, di-branched isomers are preferred products for incorporation into the high-octane gasoline pool.[3, 43, 44] Table S2 also lists the boiling points of alkane isomers. Due to the small differences in boiling points, distillation is energy intensive.

Currently, the separation of hexane isomers is performed using LTA-5A zeolite that operates on the principle of molecular sieving; see Figure S4. Linear nC6 can hop from one cage to the adjacent cage through the 4 Å windows of LTA-5A, but branched alkanes are largely excluded. An improved separation scheme, pictured in Figure S5, would require an adsorbent that would separate the di-branched isomers 22DMB and 23DMB from the nC6, 2MP, and 3MP; this would allow the low-RON components to be recycled back to the isomerization reactor. The separation of 22DMB and 23DMB from the remaining isomers is a difficult task because it requires distinguishing molecules on the *degree* of branching; such a separation is not feasible with the currently used LTA-5A. Typically, in such a processing scheme the aim would be to produce a product stream from the separation step with RON value > 92. This requirement of 92+ RON implies that the product stream will contain predominantly the di-branched isomers 22DMB and 23DMB, while allowing a small proportion of 2MP and 3MP to be incorporated into the product stream. Sharp separations between mono- and di- branched isomers is not a strict requirement.

4.2 Configurational-entropy effects in MFI zeolite

According to a patent granted to Universal Oil Products (UOP) for separation of hexane isomers,[45-47] the desired separation of hexane isomers as portrayed in Figure S5 is achievable with a variety of materials; see the pulse chromatographic separation data as presented in the UOP patents, and reproduced in Figure S6. The UOP patent states:

"The adsorbent may be silicalite, ferrierite, zeolite Beta, MAPO-31, SAPO-31, SAPO-11, zeolite X ion exchanged with alkaline cations, alkaline earth cations, or a mixture thereof, and zeolite Y ion exchanged with alkaline cations…."

Even though a vast number of zeolites are named in the patent, a careful examination of the separation performance of all zeolites[3, 39, 48] reveals the pulse chromatographic separation data in Figure S6 is obtained with MFI (silicalite) zeolite. MFI zeolite (also called silicalite-1) has a topology consisting of a set of intersecting straight channels, and zig-zag (or sinusoidal) channels of approximately 5.5 Å size. The pore landscapes and structural details are provided in Figure S7, and Figure S8. This chromatographic pulse data clearly shows the potential of MFI zeolite to separate a mixture of hexane isomers into three different fractions consisting of linear, mono-branched, and di-branched isomers. The separation relies essentially on configurational entropy effects. Figure S9 shows the computational snapshots for nC6, 2MP, 3MP, and 22DMB within the intersecting channels of MFI zeolite. The linear nC6 can locate anywhere along the straight and zig-zag channels; the linear isomer is not "configurationally challenged". Mono-branched 2MP, 3MP, and di-branched 22DMB prefer to locate at the intersections of MFI, because these are too bulky to locate within the channels; these branched isomers are subject to a configurational "penalty".

Watch the presentation **Separation of Hexane Isomers** on YouTube

https://www.youtube.com/@rajamanikrishna250/videos

Figure S10a shows the unary isotherms of nC6 and 2MP in MFI zeolite at 300 K. Due to configurational considerations, 2MP molecules prefer to locate at the channel intersections because of the extra "leg room" that is available here. There are four intersection sites per unit cell, and therefore the saturation capacity of 2MP is limited to 4 molecules uc^{-1}, for bulk fugacities ranging to 100 Pa..[48-51] The continuous solid lines are dual-site Langmuir-Freundlich fits; the unary isotherm fit parameters are provided in Table S3. Figure S10b presents CBMC simulations of component loadings of binary 50/50 nC6/2MP mixtures in MFI zeolite at 300 K. At bulk fluid phase fugacities higher than 100 Pa, configurational entropy effects lead to almost total exclusion of 2MP. Figure S10c presents CBMC simulation data on the adsorption selectivity. Figure S10d are the CBMC simulations of the thermodynamic correction factors $\begin{bmatrix} \Gamma_{11} & \Gamma_{12} \\ \Gamma_{21} & \Gamma_{22} \end{bmatrix}$

.

4.3 Transient nC6/2MP uptake in MFI

The transient uptake of nC6(1)/2MP(2) mixtures in microporous crystals of MFI zeolite, exposed to an equimolar $\left(p_1 = p_2\right)$ gas phase mixture at constant total pressure ($p_t = p_1 + p_2$ = 2.6 Pa) have been reported by Titze et al.;[52] see Figure S11a. The transient equilibration of nC6 displays a pronounced overshoot, achieving supraequilibrium loadings during transient equilibration. Titze et al.[52] have established the validity of the uncoupled M-S eqs (S21) to model intra-crystalline fluxes by detailed consideration of correlation effects. The mixture adsorption equilibrium is determined using the IAST; the unary isotherm data are provided in Table S3. The essential features of the transient uptake on nC6/2MP uptake in MFI zeolite can be adequately captured by the flux equation (S21) taking $Đ_1/r_c^2$ = 0.016 s^{-1}; $Đ_2/r_c^2$ = 1.6×10^{-4} s^{-1} $Đ_1/Đ_2$ = 100.[52] The lower diffusivity of the mono-branched isomer 2MP is due to the severe configurational constraints within 5.5 Å sized channels of MFI. The nC6 overshoot is caused by the significant off-diagonal elements of $\left[\Gamma\right]$; the elements of $\left[\Gamma\right]$ are presented in Figure S10d. At a total pressure $p_t = p_1 + p_2$ = 2.6 Pa, the elements of the $\left[\Gamma\right]$ are $\begin{bmatrix} \Gamma_{11} & \Gamma_{12} \\ \Gamma_{21} & \Gamma_{22} \end{bmatrix} = \begin{bmatrix} 4.335 & 2.947 \\ 4.051 & 4.438 \end{bmatrix}$. The

Fick diffusivity matrix is calculated to be $\frac{\begin{bmatrix} D_{11} & D_{12} \\ D_{21} & D_{22} \end{bmatrix}}{r_c^2} = \begin{bmatrix} 693.541 & 471.445 \\ 6.482 & 7.101 \end{bmatrix} \times 10^{-4}$ s^{-1}. If we assume $\Gamma_{ij} = \delta_{ij}$, and invoke eq (S23), the nC6 overshoot disappears; see dashed lines in Figure S11a.[52, 53]

Use of the LDF model, eq (S39) , results in the dashed lines shown in Figure S11b. The results of the LDF model are quite close to those predicted by the use of eq (S23),

4.4 nC6/2MP mixture separations in fixed bed adsorber

Uphill diffusion of nC6 is beneficial to the hexane isomer separations in fixed bed adsorption devices because the desired raffinate phase will be richer in the branched isomers that have high octane numbers. To confirm this expectation, transient breakthrough simulations were performed for separation 50/50 nC6/2MP mixtures at 298 K and total pressure of 10 Pa. Figure S12a plots the dimensionless concentrations at the exit of the adsorber, c_i/c_{i0} , as a function of a modified time parameter defined by $Q_0 t/m_{ads}$. In the three sets of simulations the ratio $Ð_1/Ð_2 = 100$, as determined from the transient uptake experiments of Titze et al.[52] Three different values for the diffusional time constants were chosen $Ð_1/r_c^2$ = $1.6\times10^{-6}, 1.0\times10^{-5}, 1.6\times10^{-2}$ s^{-1}, to investigate the varying degrees of diffusional influences. In practice, stronger diffusional influences are achievable for use of larger sized crystals. Increasing values of $Ð_1/r_c^2$ signify diminishing influences of intra-crystalline transport; indeed for $Ð_1/r_c^2 \to \infty$, there are no diffusional limitations. We note that with decreasing $Ð_1/r_c^2$, i.e. stronger diffusional influences, the breakthroughs take on a more distended character and 2MP exits the adsorber at earlier times. Figure S12b plots the RON of the product gas mixture exiting the adsorber. With stronger diffusion influences, i.e. lower values of $Ð_1/r_c^2$, there is a longer time interval during which product gas with RON= 74.5 can be recovered at the exit; these time intervals are indicated by the colored arrows in Figure S12b.

Schuring et al.[54] have reported experimental data on the self-diffusivities of both nC6 and 2MP in nC6/2MP mixtures. These measurements were made at a total loading that is kept nearly constant at 3.5 molecules per unit cell. Their data, that were measured at 433 K shows that *both* self-diffusivities are reduced with increasing loading of 2MP in the mixture; see Figure S13a. The preferential location of 2MP at the intersections causes blocking of molecular traffic in the intersecting channel system of MFI. MD simulations show that such intersection blocking effects also manifest in nC6/22DMB mixtures.[55] We also note that the linear nC6 has a diffusivity that is about an order of magnitude higher than that of the branched 2MP. MD simulations show that the results such as that in Figure S13a also generally hold for mixtures of n-alkanes and branched alkanes.[55-57]

We now try to get an estimate of the relative values of diffusivities of the branched isomers in MFI. On the basis of the experimental data on diffusivities of hexane isomers reported by Cavalcante and Ruthven[58] and Jolimaître et al,[59] we note that the hierarchy of diffusivities is 2MP ≈ 3MP > > 23DMB > 22DMB; see Arrhenius plots in Figure S13b,c.

4.5 Analysis of Jolimaître experiments on 2MB/2MP/22DMB separations with MFI zeolite

We analyze a set of six experiments reported by Jolimaître et al.[60] for transient breakthrough of both binary and ternary mixtures containing 2-methylbutane (2MB), 2-methylpentane (2MP), and 2,2 dimethylbutane (22DMB) mixtures at 473 K in a fixed bed packed with MFI zeolite. The branched isomers preferentially locate at the channel intersections, that provides extra "leg-room"; see computational snapshots in Figure S9. Per unit cell of MFI zeolite, there are 4 channel intersection sites. The unary isotherms, determined experimentally by Jolimaître et al.[60] , are fitted very well with a 1-site Langmuir model with equal saturation capacities (= 4 molecules per unit cell) for 2MB, 2MP, and 22DMB; see Table S5.

The hierarchy of adsorption strengths, quantified by the Langmuir binding constants, *b*, is 2MB < 2MP > 22DMB, $b_{2MP}/b_{2MB} = 3.08; \quad b_{2MP}/b_{22DMB} = 1.78; \quad b_{22DMB}/b_{2MB} = 1.73$; see Figure S14.

Table 4 of Jolimaître et al.[60] provides data on the unary diffusivities determined from single-component breakthrough curves; see also Figure S13. On the basis of the provided data, we determine the values of the diffusional time constants

$$Đ_{2MB}/r_c^2 = 7.5\times10^{-3} \quad \text{s}^{-1}; Đ_{2MP}/r_c^2 = 5\times10^{-3} \quad \text{s}^{-1}; Đ_{22DMB}/r_c^2 = 6.25\times10^{-5} \quad \text{s}^{-1}$$

The ratios of Maxwell-Stefan (M-S) diffusivities are

$$Đ_{2MB}/Đ_{2MP} = 1.5; \quad Đ_{2MP}/Đ_{22DMB} = 80; \quad Đ_{2MB}/Đ_{22DMB} = 120.$$

For the ternary 2MB/2MP/22DMB mixtures with equal saturation capacities, the matrix of thermodynamic correction factors can be calculated explicitly from the mixed-gas Langmuir model (cf. eq (S8)):

$$[\Gamma] = \frac{1}{1-\theta_1-\theta_2-\theta_3}\begin{bmatrix} 1-\theta_2-\theta_3 & \theta_2 & \theta_3 \\ \theta_1 & 1-\theta_1-\theta_3 & \theta_3 \\ \theta_1 & \theta_2 & 1-\theta_1-\theta_2 \end{bmatrix} \tag{S49}$$

For diffusion of pentane, and hexane isomers in MFI zeolite, we had presented detailed arguments and calculations in our earlier works[3, 52] to demonstrate that the correlation effects are of negligible importance. Therefore, the Maxwell-Stefan flux relations for intra-crystalline transport, eqs (S4) reduce for ternary mixtures to

$$\begin{pmatrix} N_1 \\ N_2 \\ N_3 \end{pmatrix} = -\rho \begin{bmatrix} Đ_1 & 0 & 0 \\ 0 & Đ_2 & 0 \\ 0 & 0 & Đ_3 \end{bmatrix} \frac{1}{1-\theta_1-\theta_2-\theta_3}\begin{bmatrix} 1-\theta_2-\theta_3 & \theta_2 & \theta_3 \\ \theta_1 & 1-\theta_1-\theta_3 & \theta_3 \\ \theta_1 & \theta_2 & 1-\theta_1-\theta_2 \end{bmatrix} \begin{pmatrix} \frac{\partial q_1}{\partial r} \\ \frac{\partial q_2}{\partial r} \\ \frac{\partial q_3}{\partial r} \end{pmatrix} \tag{S50}$$

Figure S15a,b,c,d,e,f present the transient breakthrough experimental data (indicated by colored symbols) of Jolimaître et al.[60] for (a, b) 2MP/22DMB binary mixtures and (c, d, e, f) 2MB/2MP/22DMB ternary mixtures at 473 K. The continuous colored lines are the transient breakthrough simulations in the absence of diffusional influences, i.e. invoking eq. (S41).

For the 2MP/22DMB binary mixtures, the time interval between breakthroughs of 22DMB and 2MP are larger than the time interval anticipated by the breakthrough simulations ignoring diffusional influences. Put another way, the 2MP/22DMP separations are enhanced due to intra-crystalline diffusion influences. This is a clear illustration of adsorption/diffusion synergy enhancing the separations in fixed bed adsorbers. For the 2MB/2MP/22DMB ternary mixtures, the breakthrough simulations ignoring intra-crystalline diffusional influences anticipates the following sequence of breakthroughs 2MB, 22DMB, 2MP, that is dictated by the hierarchy of adsorption strengths; compare the Langmuir b parameters listed in Table S5:

$b_{2MB} = 4.12\times10^{-5} \quad \text{Pa}^{-1}$, $b_{2MP} = 1.27\times10^{-4} \quad \text{Pa}^{-1}$, $b_{22DMB} = 7.12\times10^{-5} \quad \text{Pa}^{-1}$

However, in all the four ternary experiments, the measured breakthroughs follow the sequence 22DMB, 2MB, 2MP. This indicates that the di-branched isomer, 22DMB, with the lowest diffusivity value $Đ_{22DMB}/r_c^2 = 6.25\times10^{-5} \quad \text{s}^{-1}$ breaks through earlier than the mono-branched 2MB, with a significantly higher diffusivity $Đ_{2MB}/r_c^2 = 7.5\times10^{-3} \quad \text{s}^{-1}$. despite have a higher adsorption strength. Clearly, the order of breakthroughs of 2MB and 22DMB are reversed in the experiments, in contrast to the expectation based on adsorption equilibrium. Put another way, diffusional influences cause *anti-synergy* between adsorption and diffusion for 2MB/22DMB mixtures separations in the 2MB/2MP/22DMB ternary mixtures. This anti-synergy is beneficial; earlier breakthrough of 22DMB is desirable because the di-branched isomer 22DMB has the significantly higher value of RON, than the mono-branched 2MB, and 2MP; see Table S2. In other words, diffusional influences are key to the use of MFI zeolite for octane enhancement as it increases the RON productivity.

A further point to note is that the difference in the breakthrough times of 2MP and 22DMB are larger in the experiments than anticipated by the simulations in which diffusional influences are ignored. This implies that diffusional influences cause *synergy* between adsorption and diffusion for 2MPB/22DMB mixtures separations in the 2MB/2MP/22DMB ternary mixtures. This synergy is beneficial.

Summarizing, in the ternary breakthrough experiments both synergistic and anti-synergistic influences are detected; both being beneficial.

In Figure S16a,b,c,d,e,f the experimental data on transient breakthroughs experimental data of Jolimaître et al.[60] for (a, b) 2MP/22DMB binary mixtures and (c, d, e, f) 2MB/2MP/22DMB ternary mixtures at 473 K are compared with transient breakthrough simulations that include diffusional influences. The continuous solid black lines are the breakthrough simulations using M-S flux expression

(S11), including thermodynamic coupling. The important point to stress is that all six breakthrough experimental runs for binary and ternary mixtures can be simulated, reasonably quantitatively, by using the same set of adsorption and diffusion parameters as specified in Table S5.

The dashed lines in Figure S16a,b,c,d,e,f are simulations in which thermodynamic coupling effects are ignored and the simplification $\Gamma_{ij} = \delta_{ij}$ is invoked by use of eq (S12). Though these simulations anticipate the correct hierarchy of breakthroughs as in the experiments, the quantitative agreement is less good than the simulations, in which the thermodynamic coupling influences are duly accounted by use of eq (S11).

Figure S16a,b,c,d present the transient breakthrough experimental data (indicated by colored symbols) of Jolimaître et al.[60] for 2MB/2MP/22DMB ternary mixtures at 473 K, corresponding to Runs 19, 20, 21 and 22, respectively. The continuous solid black lines are the breakthrough simulations using M-S flux expression (S50), including thermodynamic coupling. In all six cases, there is quantitatively good agreement between the experiments and simulations. In all four Runs, the sequence of breakthroughs is 22DMB, 2MB, and 2MP reflecting the combined influences of adsorption and diffusion. The adsorption hierarchy is 2MP > 22DMB > 2MB, whereas the diffusion hierarchy is 2MB > 2MP > > 22DMB. The agreement of the simulation results, that including diffusional limitations along with thermodynamic coupling, with the experiments is good in all four cases.

We analyze the separation of 2MP/22DMB binary mixtures at 473 K in beds packed with MFI extrudates operating at conditions corresponding to Run 18 of Jolimaître et al.[60] Our initial focus is on the adsorption cycle and the influence the particle size, and, consequently, the diffusional time constant, $Đ_1/r_c^2$. For the four sets of simulations presented in Figure S17a, the diffusional time constant is varied $Đ_1/r_c^2$ = $1.25\times10^{-3}, 5.0\times10^{-3}, 1.0\times10^{-2}, 0.1$ s^{-1}, maintaining the ratio $Đ_1/Đ_2 = 80$. With increasing diffusional influences, i.e. decreasing values of $Đ_1/r_c^2$, the time interval between the breakthroughs of 22DMB and 2MP increases; this increase is desirable because it implies that a larger amount of the higher RON product, 22DMB, can be recovered. To emphasize this point, Figure S17b plots the RON of product gas mixture leaving fixed bed adsorber as function of time. Assuming arbitrarily that the desired target is 92+ RON product, we see that decreasing $Đ_1/r_c^2$ beneficial. From a material balance, the productivity of 92+ RON product can be determined; these values are plotted as function of the diffusional time constant $Đ_1/r_c^2$. Larger particle sizes, and stronger diffusional influences result in improved values of 92+ RON productivity.

For any chosen value of the particle size, i.e. chosen value of $\left(Đ_1/r_c^2\right)$, the severity of diffusional influences are also dependent on the contact time between the gas mixture and the adsorbent; this contact time is L/v, where v is the interstitial gas velocity, $v=u/\varepsilon$, L is the length of packed bed, u is the superficial gas velocity, and ε is the bed voidage $\varepsilon=1-\frac{m_{ads}/\rho}{\pi d^2 L/4}$. The superficial gas velocity can be determined from the volumetric gas flow rate at the inlet and the inside diameter of the fixed bed $u=Q_0/\left(\pi d^2/4\right)$. Longer contact times allow the adsorbent particles to equilibrate.

To highlight the influence of L/v, Figure S18a presents four sets of simulations of transient breakthrough for 2MP/22DMB binary mixtures at 473 K in beds packed with MFI extrudates operating at conditions corresponding to Run 18 of Jolimaître et al.[60]; the contact time between the gas mixture and extrudates is varied L/v = $42.3, 79.5, 159, 795$ s, maintaining the ratio $Đ_1/Đ_2=80$. The dimensionless concentrations at the exit of the adsorber, c_i/c_{i0}, are plotted as a function of the modified time parameter $Q_0 t/m_{ads}$. Figure S18b plots the RON of product gas mixture leaving fixed bed adsorber packed with MFI zeolite. With decreasing L/v, there is a larger time interval during which high RON product can be recovered. Figure S18c plots the productivity of 92+ RON product as function of the contact time. The results underscore the benefits of shorter contact times, i.e. stronger diffusional limitations, to achieve desired high RON product.

We now demonstrate that the breakthrough simulations are uniquely dependent on the product of the diffusional time constant $\left(Đ_1/r_c^2\right)$ and the gas-particle contact time L/v. Figure S19 presents transient breakthrough for 2MP/22DMB binary mixtures at 473 K in beds packed with MFI extrudates operating at conditions corresponding to Run 18 of Jolimaître et al.[60] The dimensionless concentrations at the exit of the adsorber, c_i/c_{i0}, are plotted as a function of the modified time parameter Q_0t/m_{ads}. In these sets of simulations the interstitial velocities are varied such that the contact times are L/v = $42.3, 95.15, 264.3, 10.57$ s; the diffusional constants $\left(Đ_1/r_c^2\right)$ are adjusted such that $\left(Đ_1/r_c^2\right)\left(L/v\right) = 5.286\times10^{-2}$; $Đ_1/Đ_2 = 80$.. All these four sets of simulations collapse into a unique breakthrough curve, when plotted as function of $\frac{Q_0t}{m_{ads}} = \frac{t}{L/v}\frac{\varepsilon}{(1-\varepsilon)\rho}$. Figure S35 provides an important tool for interpreting and utlizing the results in laboratory scale equipment for scaling up to commercial units with different particle sizes and contact times.

In order to strengthen the conclusions reached in the foregoing, Figure S20a,b plots the RON calculations of the products exiting the reactor determined from transient breakthrough simulations for Runs 20 and 22 of Jolimaître et al.[60] for 2MB/2MP/22DMB ternary mixtures at 473 K. The continuous red solid lines are the simulations in which the diffusional influences are considered to be negligible. The continuous solid black lines are the breakthrough simulations using M-S flux expression (S11), including thermodynamic coupling. For a target RON of say 92, we can determine the number of moles of product with 92+ RON in the outlet from a material balance. The RON productivities, are higher when diffusional influences are properly accounted for; this is visually evident from the time intervals indicated by the red and black arrows during which 92+ RON product gas can be recovered from the exit of the adsorber.

4.6 Analysis of Peralta experiments for hexane isomers in ZIF-8

Figure S21a,b,c presents the experimental data of Peralta et al.[61] for breakthrough of nC6/3MP, nC6/22DMB, and 3MP/22DMB mixtures in a fixed bed adsorber packed with ZIF-8. The required pure component isotherm data are obtained from the work of Dubbeldam et al.[44] that uses CBMC simulations; Table S6 provides the dual-site Langmuir-Freundlich parameters. For each of the three binary mixtures, two types of transient breakthrough simulations were performed. The dashed lines are simulations in which diffusional influences are ignored, i.e. invoking eq. (S41). The continuous solid lines are simulations in which the diffusional influences are accounted for by taking the following set of values: $Đ_{nC6}/r_c^2 = 4\times10^{-3}$ s^{-1}; $Đ_{3MP}/r_c^2 = 2\times10^{-6}$ s^{-1}; $Đ_{22DMB}/r_c^2 = 8\times10^{-7}$ s^{-1}. In these simulations thermodynamic coupling effects are ignored and the simplification $\Gamma_{ij} = \delta_{ij}$ is invoked by use of eq (S12). There is no real justification for inclusion of thermodynamic coupling effects because the M-S diffusivities $Đ_i$ are fitted to match their breakthrough experiments.

Figure S21a presents the breakthrough simulations for nC6/3MP mixtures. The equilibrium simulations show that nC6 breaks through earlier than 3MP, whereas the experiments show the reverse trend. The experimental breakthroughs can be reproduced nearly quantitatively by introducing diffusional influences, and by choosing the ratio $Đ_{nC6}/Đ_{3MP}$ =1333.

Figure S21b shows the breakthrough simulations for nC6/22DMB mixture. In this case, equilibrium simulations predict the correct hierarchies of breakthrough as in the experiments but the quantitative agreement is poor. A near quantitative agreement in the breakthrough characteristics is obtained by accounting for intra-crystalline diffusion with the ratio $Đ_{nC6}/Đ_{22DMB}$ =5000.

Figure S21c shows the breakthrough simulations for 3MP/22DMB mixtures. The experimental breakthroughs are reproduced nearly quantitatively by introducing diffusional limitations and taking the ratio of diffusivities $Đ_{3MP}/Đ_{22DMB}$ =3.75.

The important conclusion that we wish to draw from the simulations of the breakthrough experiments of Peralta et al.[61] is that the separation of alkane isomers using ZIF-8 is dominated by intra-crystalline diffusion. The set of three different breakthroughs can be adequately modeled using the simplified model neglecting thermodynamic coupling.

4.7 List of Tables for Separation of hexane isomers

Table S2. Research Octane Numbers (RON) and boiling points of C5, C6, C7 alkanes.

Alkane		Boiling point/K	Research Octane Number (RON)
nC5	n-pentane	309	61.7
2MB	2-methyl butane	301	93.5
neoP	2,2 dimethyl propane	282.5	98
nC6	n-hexane	341.5	30
2MP	2-methyl pentane	333.1	74.5
3MP	3-methyl pentane	336.5	75.5
22DMB	2,2 dimethyl butane	323.15	94
23DMB	2,3 dimethyl butane	331.2	105
nC7	n-heptane	371.5	0
2MH	2-methyl hexane	363.15	42.4
3MH	3-methyl hexane	365	52
22DMP	2,2 dimethyl pentane	352.15	92.8
23DMP	2,3 dimethyl pentane	362	91.1

Table S3. Dual-site Langmuir-Freundlich parameters for pure component isotherms for hexane isomers in MFI at 300 K. This data is from the Supporting Information of Titze et al.[52] The unary isotherm data are fitted with the dual-Langmuir-Freundlich model

$$\Theta = \Theta_{A,sat} \frac{b_A p^{\nu_A}}{1+b_A p^{\nu_A}} + \Theta_{i,B,sat} \frac{b_B p^{\nu_B}}{1+b_B p^{\nu_B}}$$

	Site A			Site B		
	$\frac{\Theta_{A,sat}}{\text{molecules uc}^{-1}}$.	$\frac{b_A}{\text{Pa}^{-\nu_A}}$	ν_A	$\frac{\Theta_{B,sat}}{\text{molecules uc}^{-1}}$	$\frac{b_B}{\text{Pa}^{-\nu_B}}$	ν_B
nC6	6.6	0.7084	0.83	1.4	16.5765	1.5
2MP	4	4.51	1.05	4	7.92×10^{-6}	1.13

Table S4. Dual-site Langmuir-Freundlich parameters for unary hexane isomers at 433 K in MFI zeolite.

$$\Theta = \Theta_{A,sat}\frac{b_A p^{\nu_A}}{1+b_A p^{\nu_A}} + \Theta_{i,B,sat}\frac{b_B p^{\nu_B}}{1+b_B p^{\nu_B}}$$

The fits are based on CBMC simulation data of Krishna and van Baten.[62]

	Site A			Site B		
	$\frac{\Theta_{A,sat}}{\text{molecules uc}^{-1}}$	$\frac{b_A}{\text{Pa}^{-\nu_A}}$	ν_A	$\frac{\Theta_{B,sat}}{\text{molecules uc}^{-1}}$	$\frac{b_B}{\text{Pa}^{-\nu_B}}$	ν_B
nC6	3.2	2.21×10^{-8}	1.6	4.3	7.42×10^{-4}	1
2MP	4	7.85×10^{-4}	1.03			
3MP	4	4.22×10^{-4}	1.02	1	9.88×10^{-7}	1
22DMB	4	2.55×10^{-4}	1.02			
23DMB	4	4.59×10^{-4}	1.02			

Intra-crystalline diffusion effects are taken into account using the input values as in previous work:[3] $Đ_{nC6}/r_c^2 = 0.002$ s^{-1}; $Đ_{2MP}/Đ_{3MP} = 1$; $Đ_{2MP}/Đ_{22DMB} = 5$; $Đ_{22MB}/Đ_{23DMB} = 1$. The transient breakthrough simulations are based on eq (S11) taking due account of thermodynamic coupling effects.[53, 63]

Table S5. Single-site Langmuir parameters, and M-S diffusivities $Đ_i/r_c^2$, for pure component 2MB, 2MP, and 22DMB at 473 K in MFI zeolite. The parameters are based on the experimental data of Jolimaître et al.[59, 60] All simulations of the breakthrough experiments of Jolimaître et al.[60] were performed for extrudate 2; bed voidage, $\varepsilon = 0.4$; density of extrudate 2, $\rho = 620.8$ kg m^{-3}. The length of the adsorber bed is 0.795 m. The interstitial velocity v varied with each run and were taken from Table 6 of Jolimaître et al.[60] The partial pressures of each of the components 2MB, 2MP, and 22DMB at the inlet to the adsorber are specified using the data provided in Table 6 of Jolimaître et al.[60]

$$q = \frac{q_{sat} bp}{1+bp}.$$

	$\frac{q_{sat}}{\text{mol kg}^{-1}}$	$\frac{b}{\text{Pa}^{-1}}$	$Đ_i/r_c^2$ s^{-1}
2MB	0.693464348	4.12×10^{-5}	0.0075
2MP	0.693464348	1.27×10^{-4}	0.005
22DMB	0.693464348	7.12×10^{-5}	0.0000625

Table S6. Dual-site Langmuir-Freundlich parameters for pure component hexane isomers at 433 K in ZIF-8. $q = \frac{q_{sat,A} b_A p^{\nu A}}{1 + b_A p^{\nu A}} + \frac{q_{sat,B} b_B p^{\nu B}}{1 + b_B p^{\nu B}}$

	Site A			Site B		
	$\frac{q_{A.sat}}{\text{mol kg}^{-1}}$	$\frac{b_A}{\text{Pa}^{-\nu_A}}$	ν_A	$\frac{q_{B.sat}}{\text{mol kg}^{-1}}$	$\frac{b_B}{\text{Pa}^{-\nu_B}}$	ν_B
nC6	2.8	8.53×10^{-5}	1.07	0.44	5.59×10^{-5}	0.59
2MP	2.8	1.06×10^{-4}	1.04	1.0	8.08×10^{-6}	0.64
3MP	2.8	9.81×10^{-5}	1.07	1.2	2.98×10^{-5}	0.58
22DMB	1.82	1.09×10^{-4}	1.0	1.1	1.55×10^{-7}	1.34
23DMB	2.4	1.18×10^{-4}	1.06	0.6	1.11×10^{-4}	0.76

4.8 List of Figures for Separation of hexane isomers

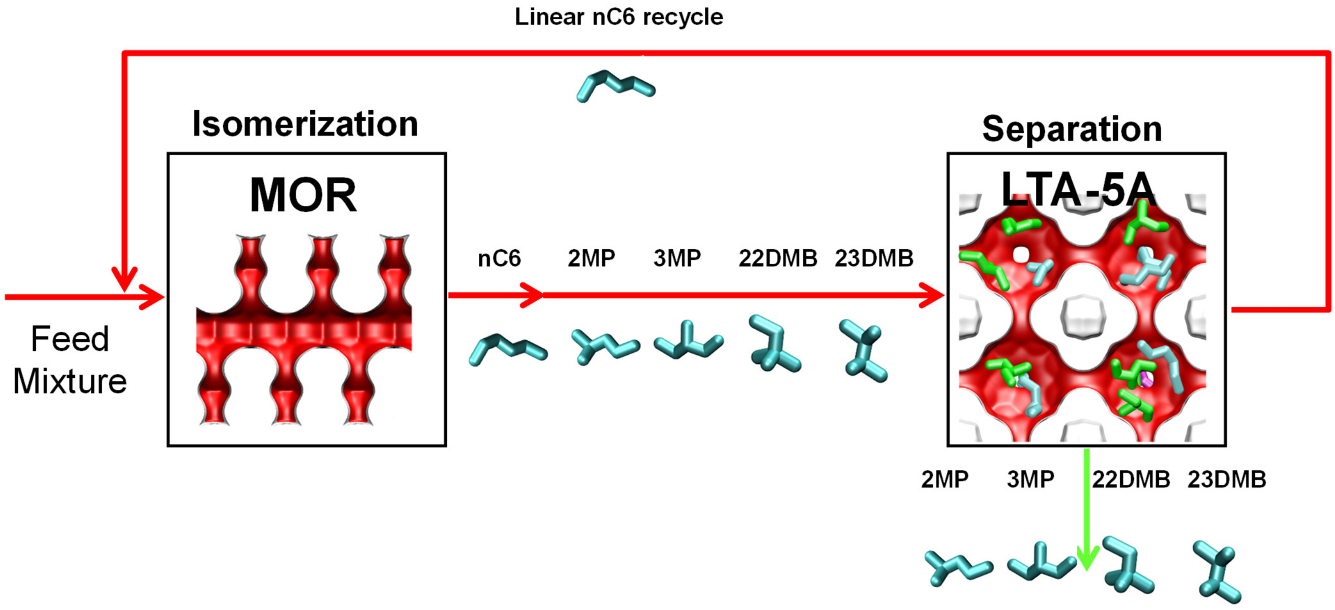

Figure S4. Currently employed processing scheme for nC6 isomerization and subsequent separation step using LTA-5A zeolite.

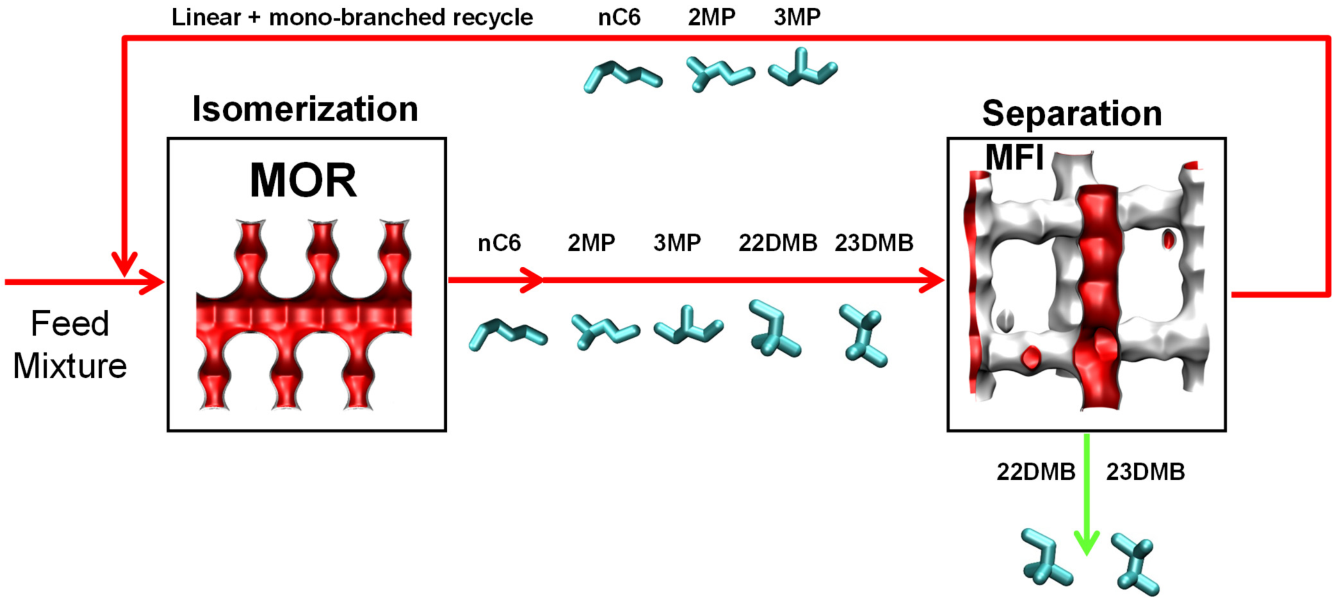

Figure S5. Improved processing scheme for the nC6 isomerization process using MFI zeolite in the separation step.

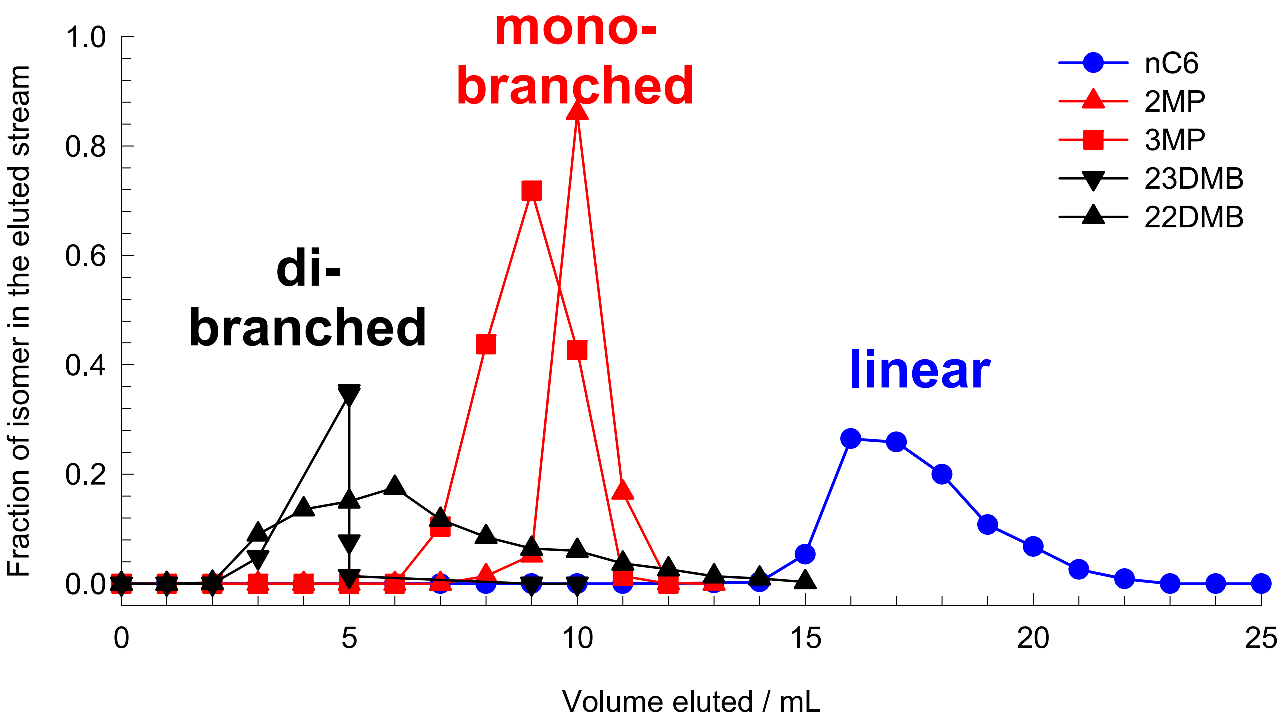

Figure S6 Pulsed chromatographic separation of hexane isomers as reported in the patents assigned to Universal Oil Products (UOP).[45-47]

MFI pore landscape

	MFI
a /Å	20.022
b /Å	19.899
c /Å	13.383
Cell volume / Å^3	5332.025
conversion factor for [molec/uc] to [mol per kg Framework]	0.1734
conversion factor for [molec/uc] to [kmol/m^3]	1.0477
ρ [kg/m3]	1796.386
MW unit cell [g/mol(framework)]	5768.141
ϕ, fractional pore volume	0.297
open space / Å^3/uc	1584.9
Pore volume / cm^3/g	0.165
Surface area /m^2/g	487.0
DeLaunay diameter /Å	5.16

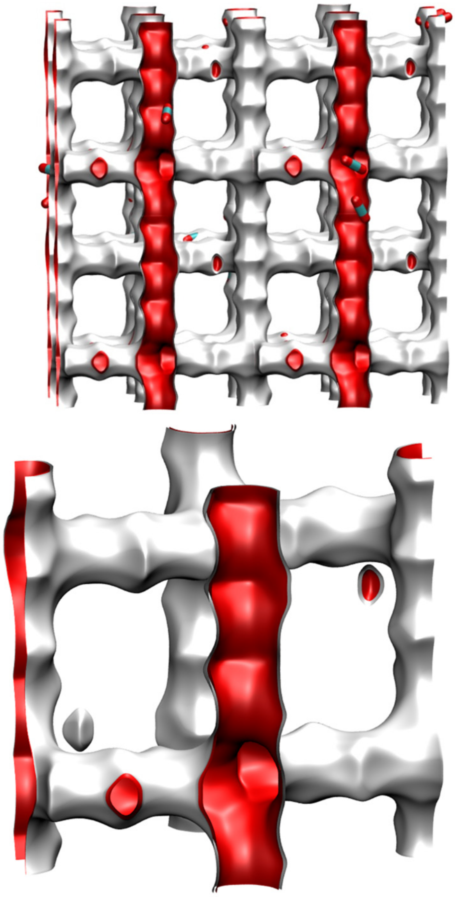

Figure S7. Structural details and pore landscape for MFI zeolite.

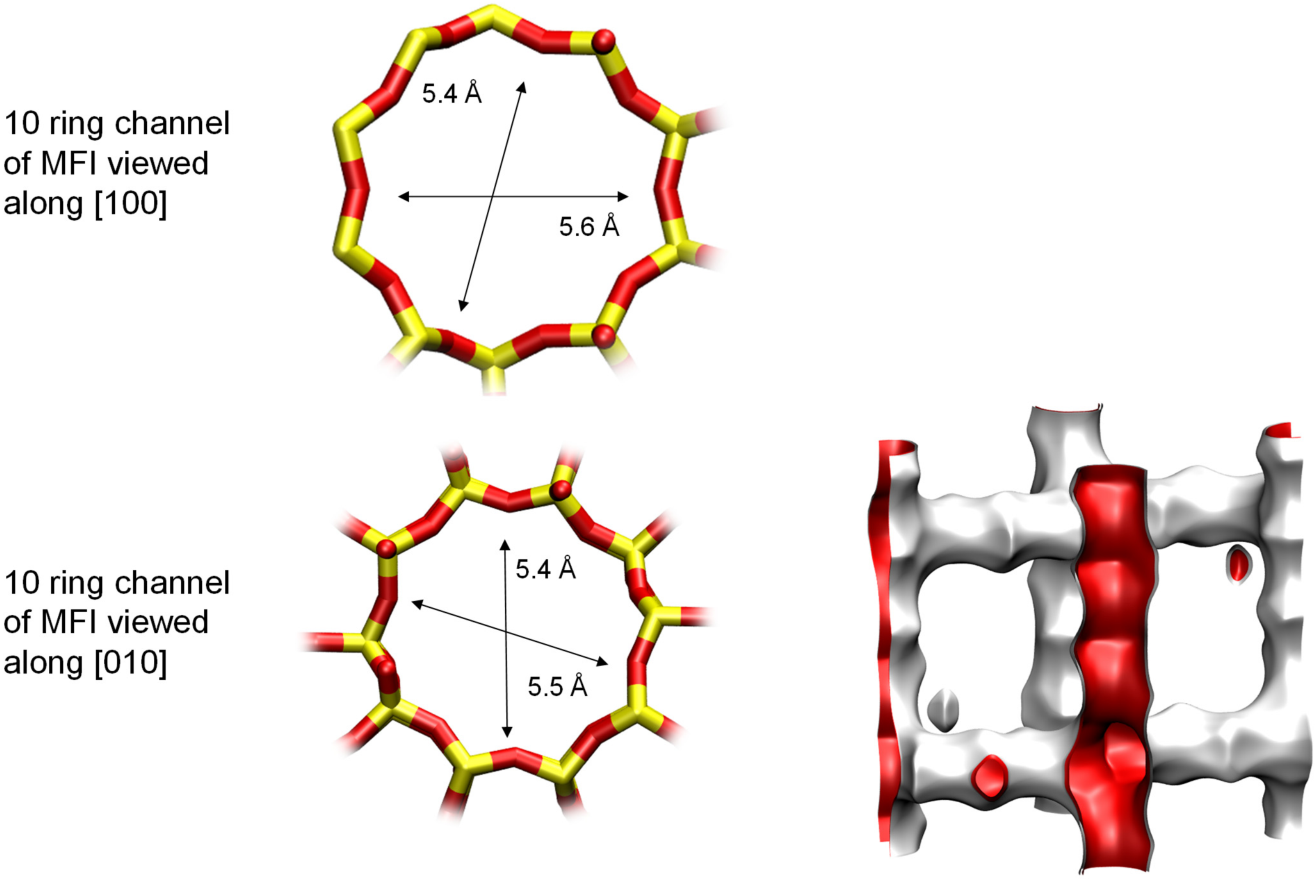

Figure S8. Structural details and pore landscape for MFI zeolite.

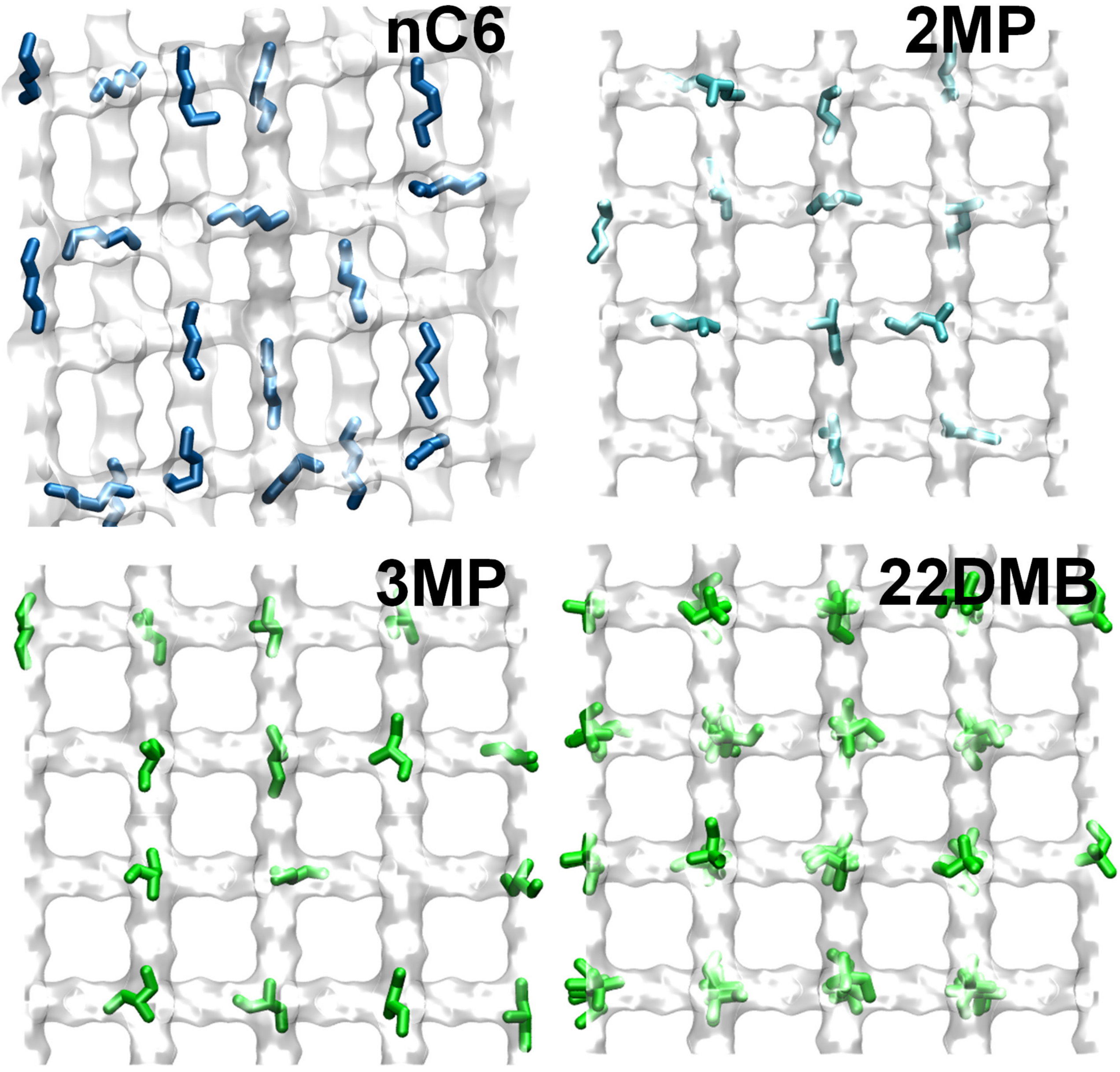

Figure S9. Computational snapshots showing the location of nC6, 2MP, 3MP, and 22DMB within the intersecting channel topology of MFI zeolite.

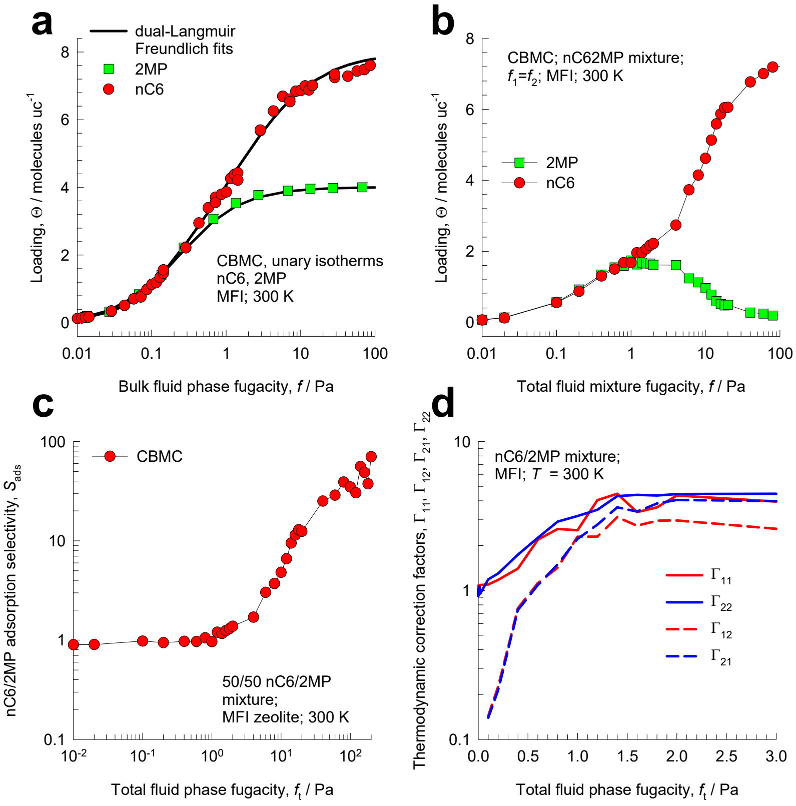

Figure S10. (a) CBMC simulations[52] of unary isotherms of nC6 and 2MP in MFI zeolite at 300 K. The continuous solid lines are dual-site Langmuir-Freundlich fits; the unary isotherm fit parameters are provided in Table S3. (b, c, d) CBMC simulations[52] of (b) component loadings of binary 50/50 nC6/2MP mixtures in MFI zeolite at 300 K, (c) adsorption selectivity, and (d) elements of the matrix of thermodynamic correction factors.

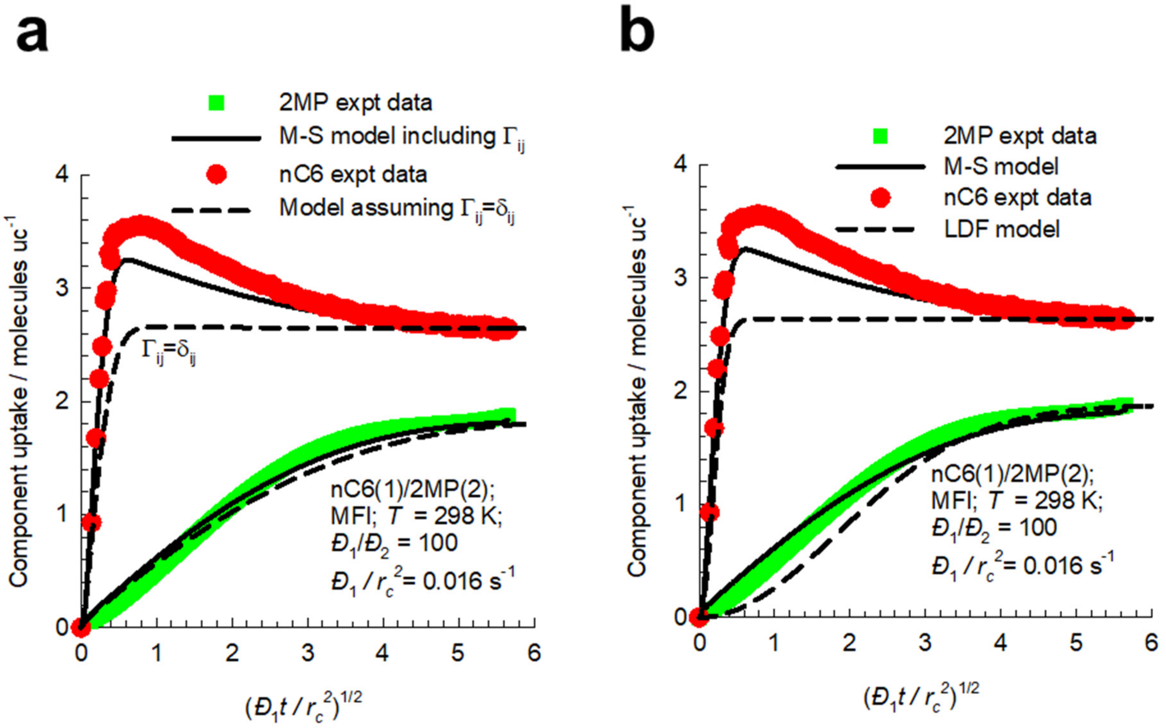

Figure S11. (a, b) Experimental data of Titze et al.[52] for Run 1 transient uptake of nC6/2MP mixtures in MFI zeolite. Input data simulation of Run 1: $Đ_1/r_c^2$ = 0.016 s^{-1}; $Đ_2/r_c^2$ = 1.6×10^{-4} s^{-1}; $t = 0$; $p_1(r_c,t) = p_2(r_c,t)$ = 0 Pa; $t \geq 0$; $p_1(r_c,t) = p_2(r_c,t)$ = 1.3 Pa. The isotherm data are provided in Table S3. The continuous solid lines in (a,b) are the numerical solutions for transient uptake using the M-S diffusion eq (S21). The dashed lines in (a) are the solutions invoking the simplified eq (S23), Use of the LDF model, eq (S39) , results in the dashed lines shown in (b).

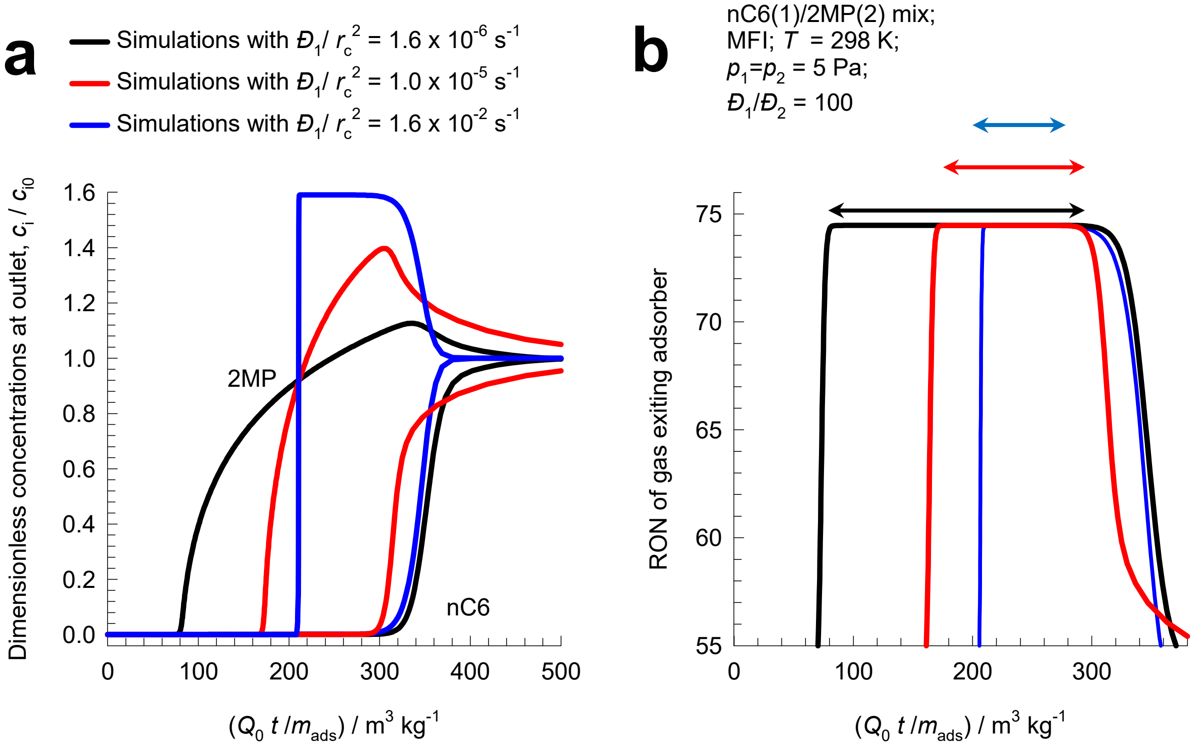

Figure S12. (a) Transient breakthrough for 50/50 nC6(1)/2MP(2) mixtures in MFI zeolite at 298 K and total pressure of 10 Pa. The dimensionless concentrations at the exit of the adsorber, c_i/c_{i0}, are plotted as a function of a modified time parameter defined by $\frac{Q_0 t}{m_{ads}}$. For the three sets of simulations $Đ_1/r_c^2$ = $1.6\times10^{-6}, 1.0\times10^{-5}, 1.6\times10^{-2}$ s^{-1}, maintaining the ratio $Đ_1/Đ_2=100$. (b) RON of product gas mixture leaving fixed bed adsorber packed with MFI zeolite.

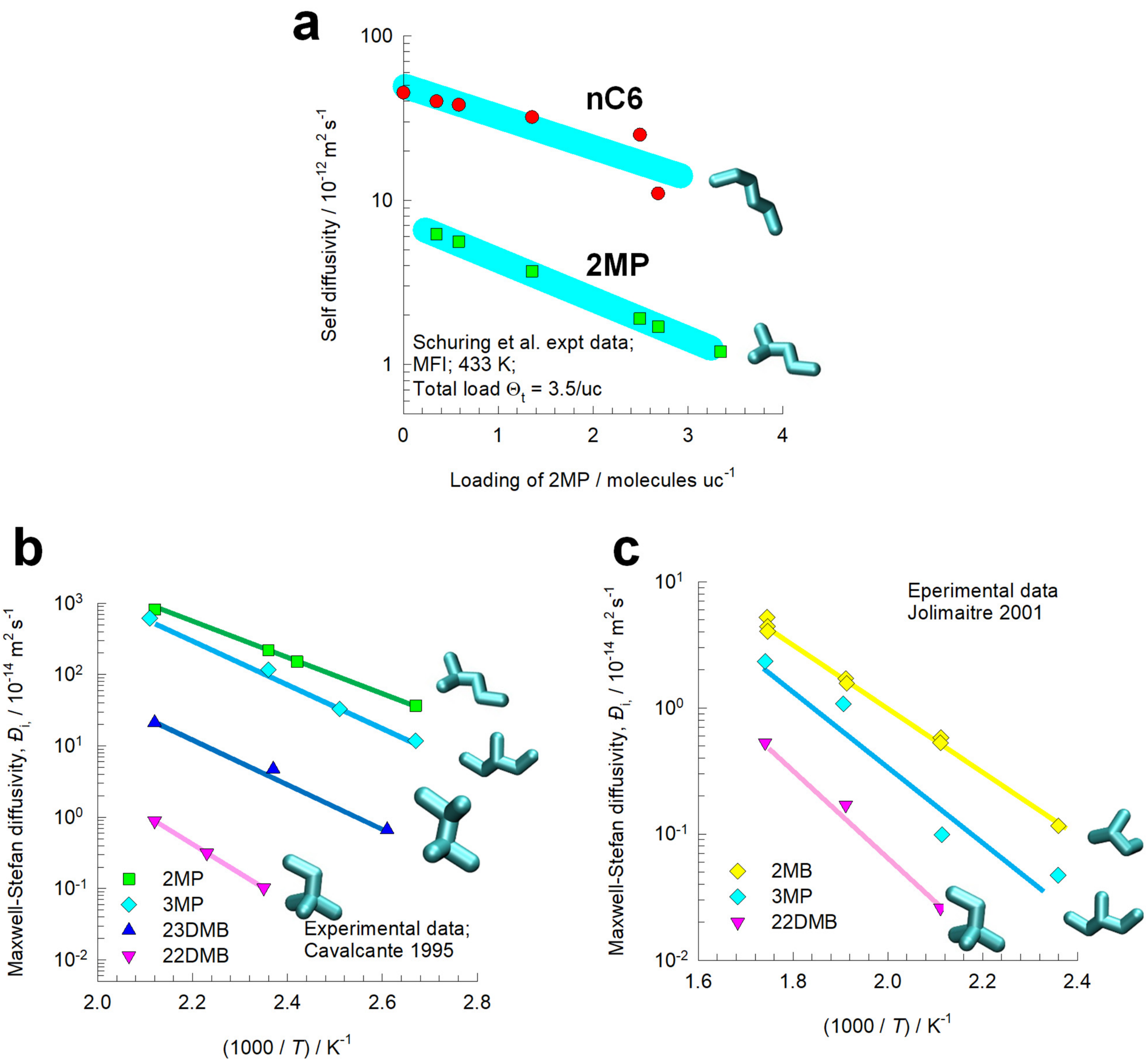

Figure S13. (a) Experimental data[54] on self-diffusivities of nC6 and 2-methylpentane (2MP) as a function of the loading of 2MP, keeping the total loading $\Theta_t = 3.5$/uc. (b, c) Arrhenius plot of diffusivities of 2MB, 2MP, 3MP, 22DMB, and 23DMB in MFI zeolite. The data are re-plotted from the experimental results of (b) Cavalcante and Ruthven,[58] and (c) Jolimaître et al.[59]

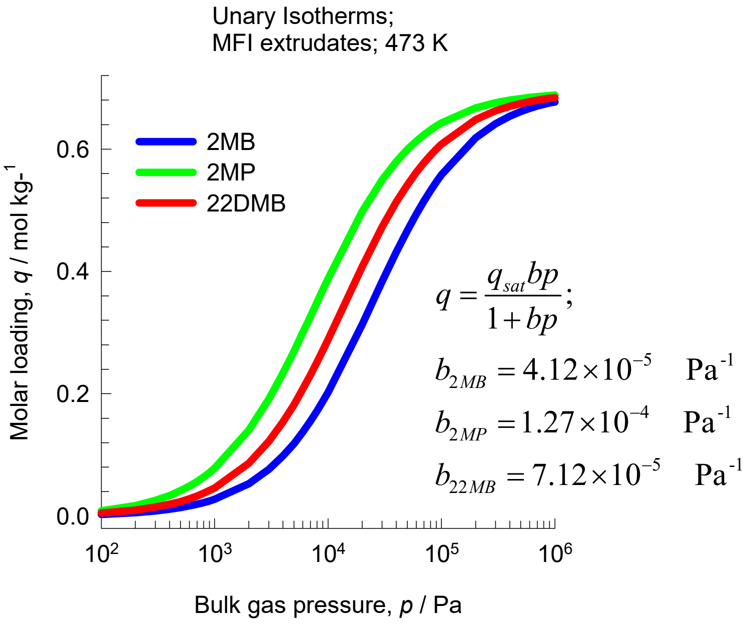

Figure S14. Single-site Langmuir fits of unary isotherms of 2MB, 2MP, and 22DMB at 473 K in MFI extrudates. These fits are based on the experimental isotherm data reported in Figures 4, 5 and 6 of Jolimaître et al.[60] The isotherm fit data are provided in Table S5.

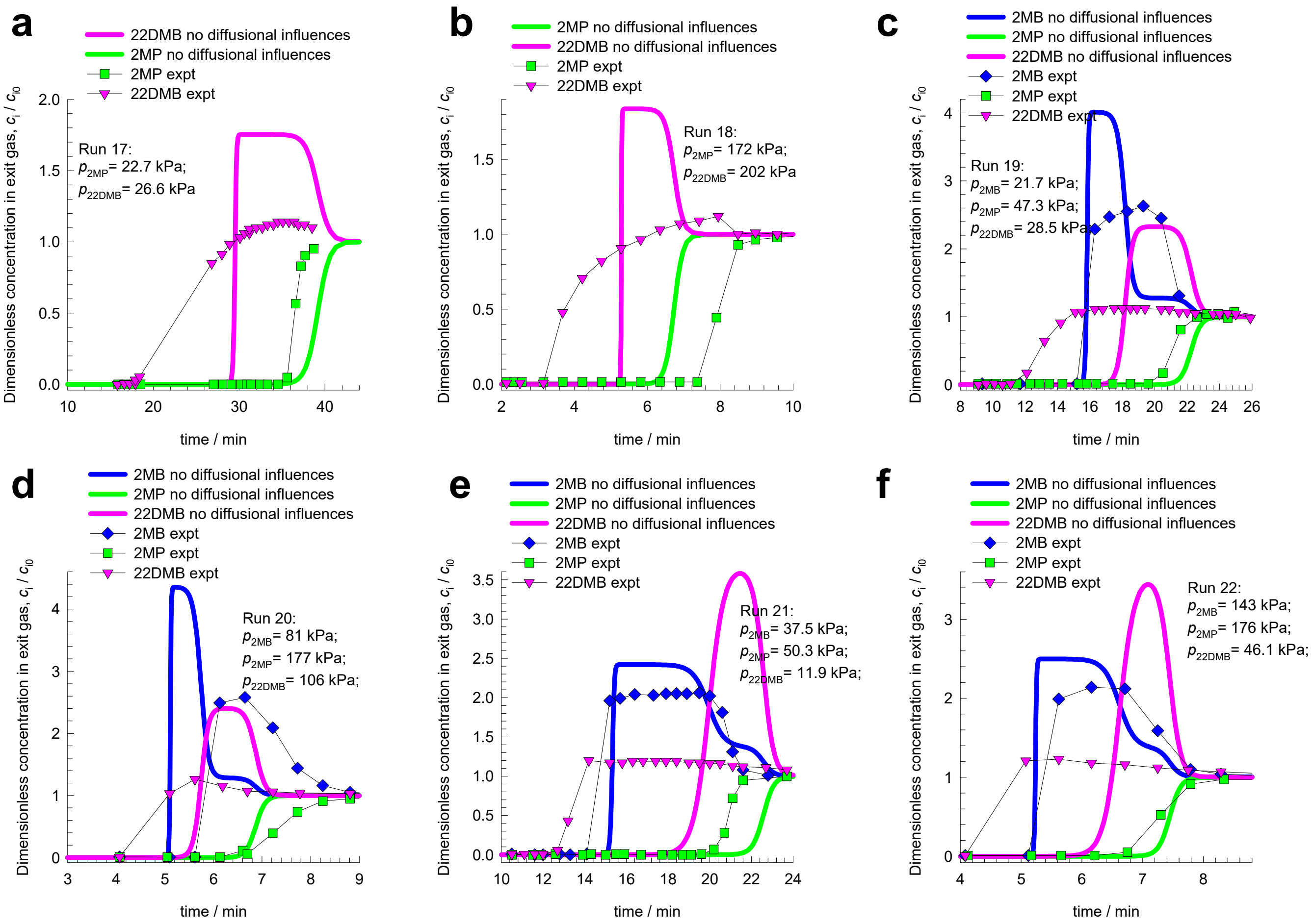

Figure S15. Transient breakthrough experiments of Jolimaître et al.[60] for (a, b) 2MP/22DMB binary mixtures and (c, d, e, f) 2MB/2MP/22DMB ternary mixtures at 473 K. The experimental data correspond to Runs 17, 18, 19, 20, 21, and 22. The continuous colored lines are the simulations in which diffusional influences are ignored. The input data on unary isotherms and M-S diffusivities are provided in Table S5.

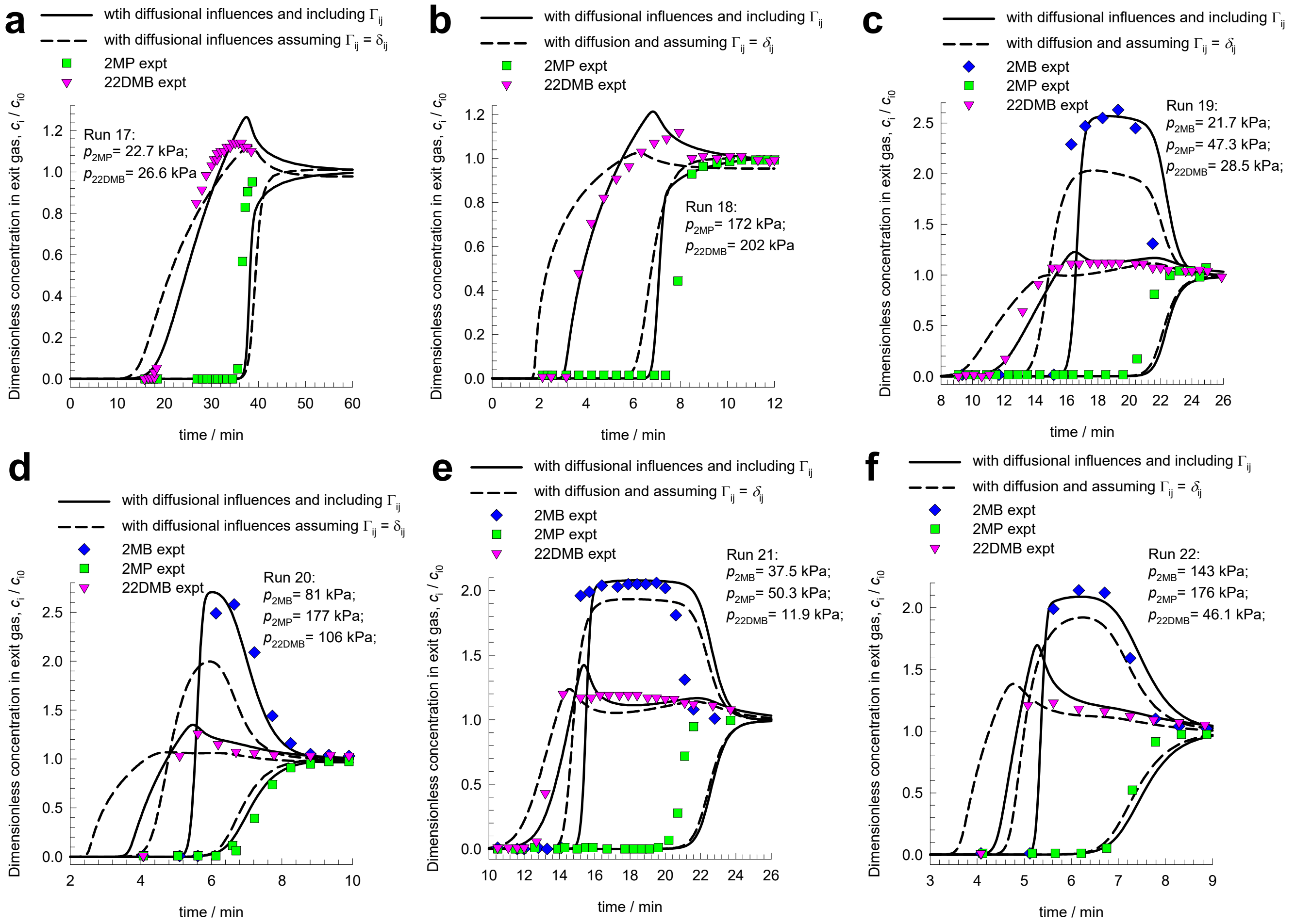

Figure S16. Transient breakthrough experiments of Jolimaître et al.[60] for (a, b) 2MP/22DMB binary mixtures and (c, d, e, f) 2MB/2MP/22DMB ternary mixtures at 473 K. The experimental data correspond to Runs 17, 18, 19, 20, 21, and 22. The continuous solid black lines are the breakthrough simulations using M-S flux expression (S11), including thermodynamic coupling. The dashed lines are simulations in which thermodynamic coupling effects are ignored and the simplification $\Gamma_{ij} = \delta_{ij}$ is invoked by use of eq (S12). The dashed lines are simulations in which the thermodynamic coupling effects are ignored, The input data on unary isotherms and M-S diffusivities are provided in Table S5.

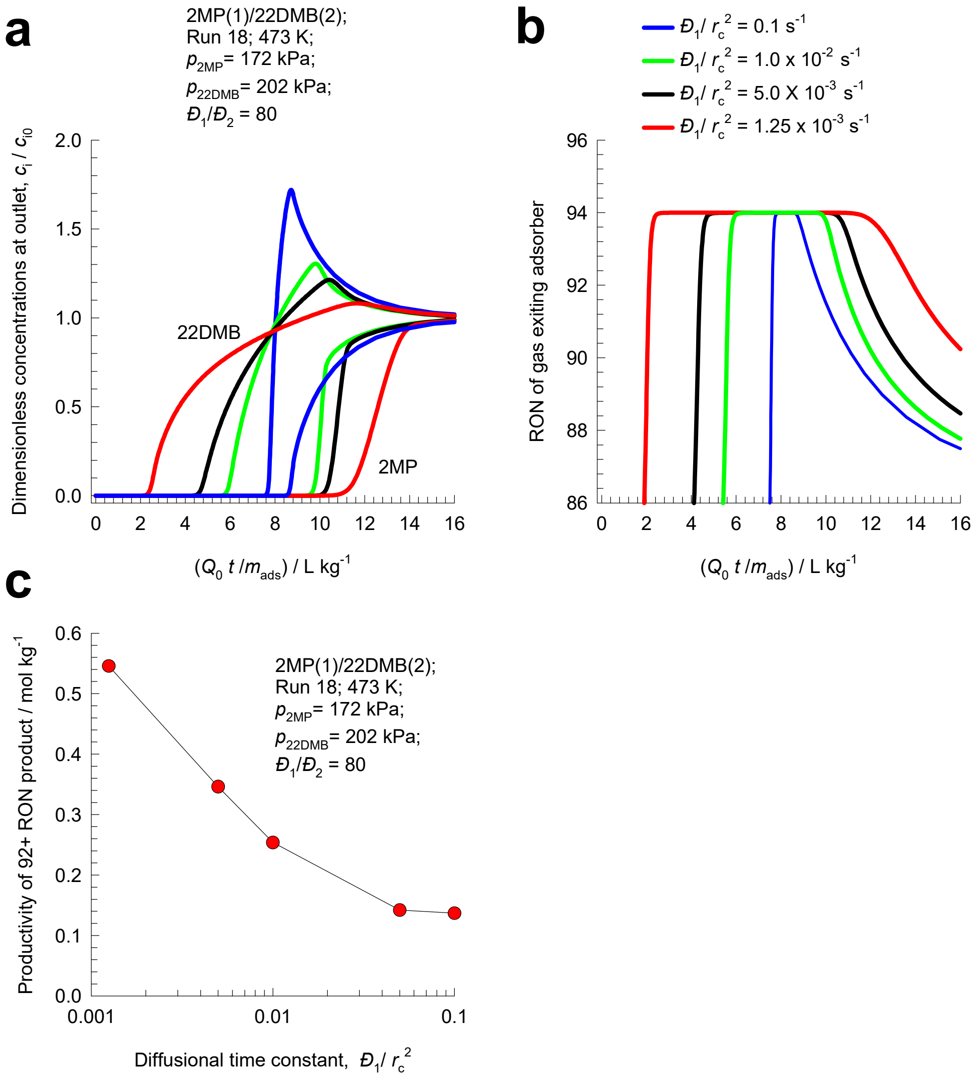

Figure S17. (a) Transient breakthrough for 2MP/22DMB binary mixtures at 473 K in beds packed with MFI extrudates operating at conditions corresponding to Run 18 of Jolimaître et al.[60] The dimensionless concentrations at the exit of the adsorber, c_i/c_{i0}, are plotted as a function of time. For the four sets of simulations, the diffusional time constant is varied $Đ_1/r_c^2 = 1.25\times10^{-3}, 5.0\times10^{-3}, 1.0\times10^{-2}, 0.1$ s^{-1}, maintaining the ratio $Đ_1/Đ_2 = 80$. (b) RON of product gas mixture leaving fixed bed adsorber packed with MFI zeolite. (c) Productivity of 92+ RON, plotted as function of the diffusional time constant.

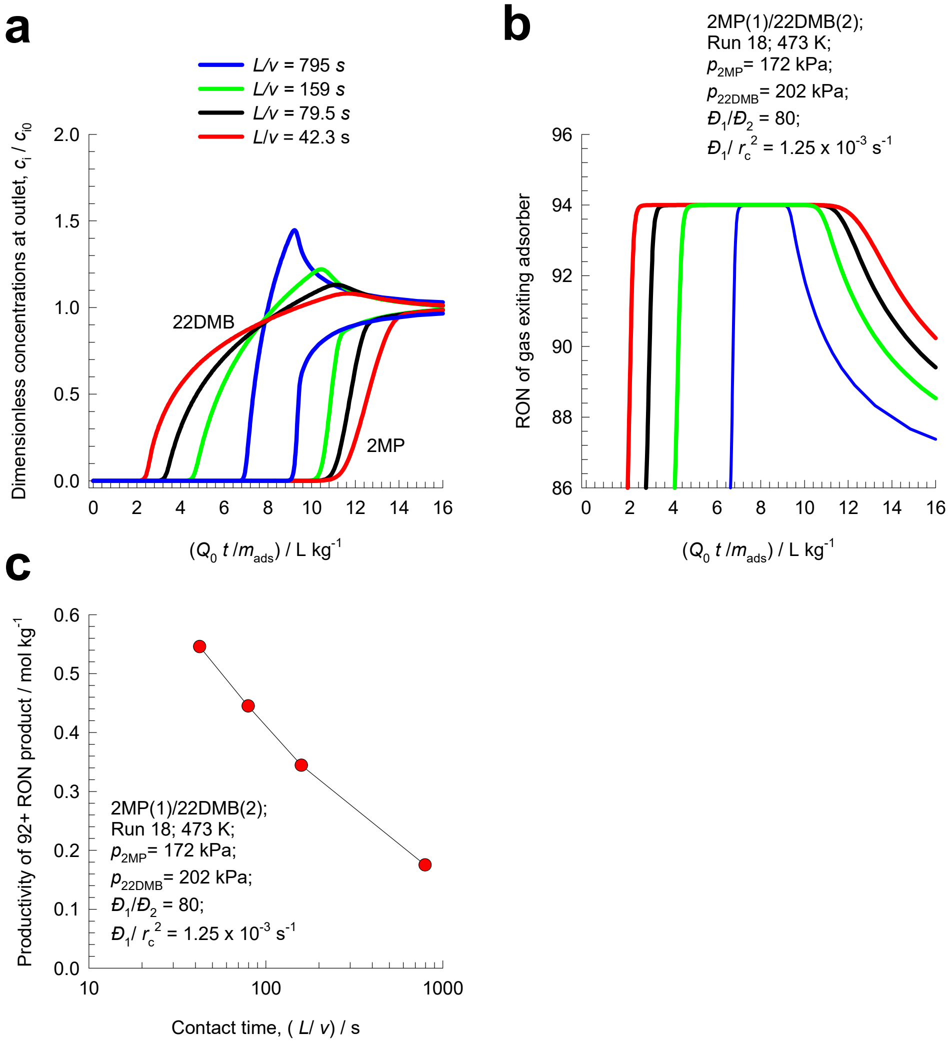

Figure S18. (a) Transient breakthrough for 2MP/22DMB binary mixtures at 473 K in beds packed with MFI extrudates operating at conditions corresponding to Run 18 of Jolimaître et al.[60] The dimensionless concentrations at the exit of the adsorber, c_i/c_{i0} , are plotted as a function of the modified time parameter $Q_0 t/m_{ads}$. For the four sets of simulations, the contact time between the gas mixture and extrudates is varied L/v = 42.3, 79.5, 159, 795 s, maintaining the ratio $Đ_1/Đ_2 = 80$. (b) RON of product gas mixture leaving fixed bed adsorber packed with MFI zeolite. (c) Productivity of 92+ RON, plotted as function of the contact time, L/v .

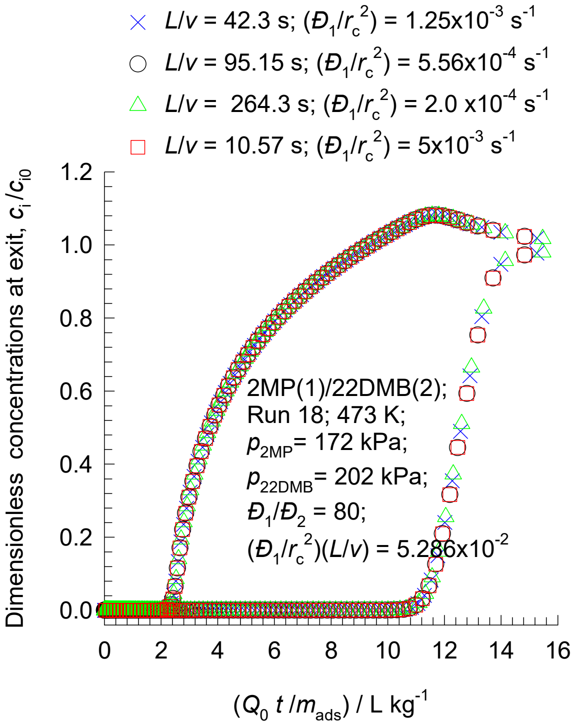

Figure S19. Transient breakthrough for 2MP/22DMB binary mixtures at 473 K in beds packed with MFI extrudates operating at conditions corresponding to Run 18 of Jolimaître et al.[60] The dimensionless concentrations at the exit of the adsorber, c_i/c_{i0}, are plotted as a function of the modified time parameter $Q_0 t/m_{ads}$. In these sets of simulations the interstitial velocities are varied such that the contact times are $42.3, 95.15, 264.3, 10.57$ s; the diffusional constants $\left(Đ_1/r_c^2\right)$ are adjusted such that $\left(Đ_1/r_c^2\right)\left(L/v\right) = 5.286\times10^{-2}$; $Đ_1/Đ_2 = 80$..

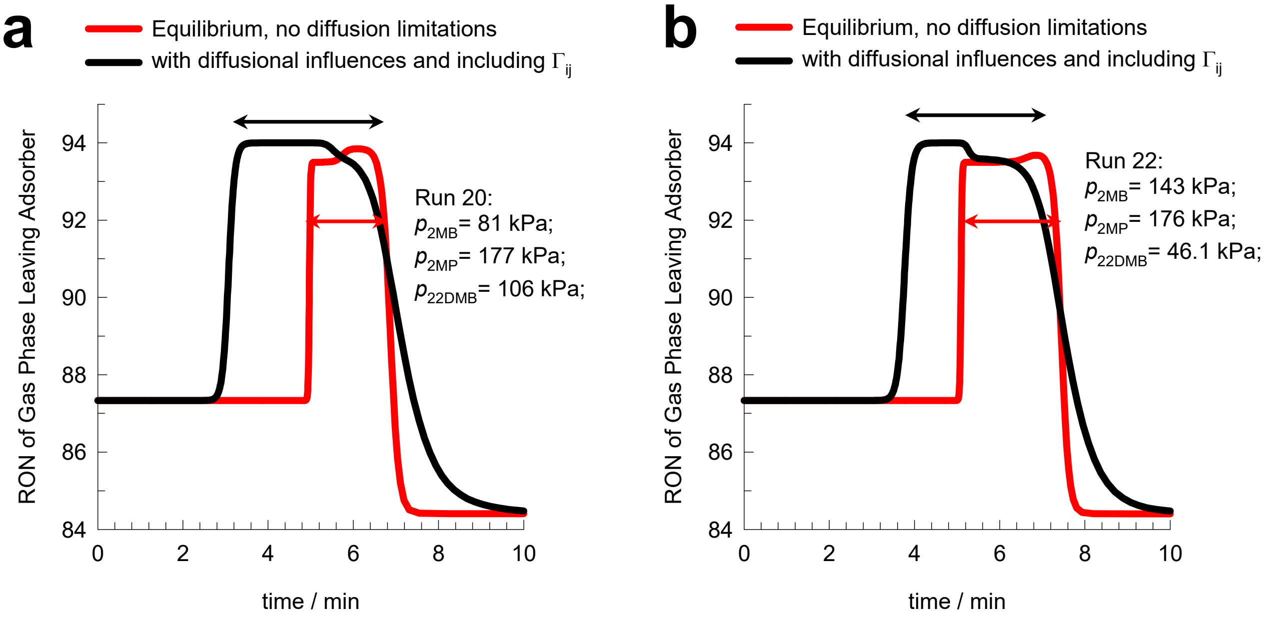

Figure S20. (a, b) The RON calculations of the products exiting the reactor determined from transient breakthrough simulations for Runs 20 and 22 of Jolimaître et al.[60] for 2MB/2MP/22DMB ternary mixtures at 473 K. The continuous red solid lines are the simulations in which the diffusional influences are considered to be negligible. The continuous solid black lines are the breakthrough simulations using M-S flux expression (S11), including thermodynamic coupling. The input data on unary isotherms and M-S diffusivities are provided in Table S5.

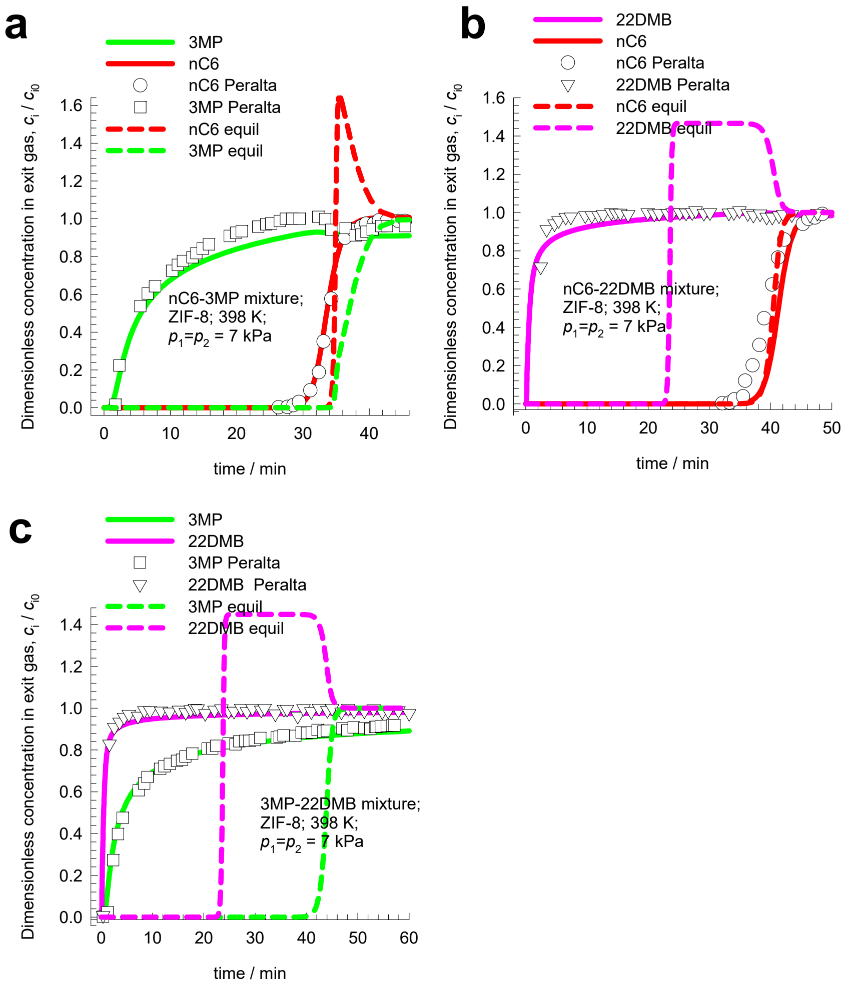

Figure S21. (a, b, c) experimental data of Peralta et al.[61] for breakthrough of (a) nC6/3MP, (b) nC6/22DMB, and (c) 3MP/22DMB mixtures in a fixed bed adsorber packed with ZIF-8. The dashed lines are simulations in which diffusional influences are ignored, i.e. invoking eq. (S41). The continuous solid lines are simulations in which the diffusional influences are accounted for by taking the following set of values: $Đ_{nC6}/r_c^2 = 4\times10^{-3}$ s^{-1}; $Đ_{3MP}/r_c^2 = 2\times10^{-6}$ s^{-1}; $Đ_{22DMB}/r_c^2 = 8\times10^{-7}$ s^{-1}. In these simulations thermodynamic coupling effects are ignored and the simplification $\Gamma_{ij} = \delta_{ij}$ is invoked by use of eq (S12). Table S6 provides the dual-site Langmuir-Freundlich parameters.

5 Separation of CO_2/C_2H_6 mixtures with DDR zeolite

DDR consists of cages of 277.8 Å^3 volume, separated by 3.65 Å × 4.37 Å 8-ring windows; the pore landscapes and structural details are provided in Figure S22, and Figure S23. The guest molecules jump one-at-a-time across the narrow 8-ring windows. Consequently, correlation effects are of negligible importance; the intra-crystalline fluxes N_i, in turn, are related to the radial gradients in the molar loadings by Eq (S21).

Watch also the video presentation titled **Diffusion in DDR Zeolite** on YouTube

https://www.youtube.com/@rajamanikrishna250/videos

5.1 Transient CO_2/C_2H_6 mixture uptake in DDR zeolite

Binder et al.[64] and Lauerer et al.[65] report a set of three mixture uptake experiments with 1:1, 2:1, and 3:1 partial pressure ratios for CO_2 and C_2H_6 in the gas phase.

Experiment 1: 1:1 $CO_2(1)/C_2H_6(2)$ bulk gas mixture at 298 K, p_1 = 20 kPa, p_2 = 20 kPa.

Experiment 2: 2:1 $CO_2(1)/C_2H_6(2)$ bulk gas mixture at 298 K, p_1 = 40 kPa, p_2 = 20 kPa.

Experiment 3: 3:1 $CO_2(1)/C_2H_6(2)$ bulk gas mixture at 298 K, p_1 = 60 kPa, p_2 = 20 kPa.

The data on the unary isotherms of CO_2 and C_2H_6 at 298 K are provided in Figure 36, Chapter 4 of the PhD dissertation of Binder.[66] The unary isotherms for both CO_2, and C_2H_6 can be described adequately by a single-site Langmuir isotherm

$$q_i = \frac{q_{i,sat} b_i p_i}{1 + b_i p_i} \tag{S51}$$

The single-site Langmuir parameters are provided in Table S7. Figure S25a provides a comparison of unary isotherm data with single-site Langmuir fits using the parameters reported in Table S7. The fits are of good accuracy.

Figure 3 of Binder et al.[64] presents IAST calculations for binary mixture adsorption with constant CO_2 partial pressures of p_1 = 20, 40, and 60 kPa for experiments (1), (2), and (3), respectively. The partial pressures of C_2H_6 ethane in the gas phase is varied. The IAST calculations of Binder et al.[64] are shown as symbols in Figure S25b. For the conditions of the Binder/Lauerer experiments,[64, 65] a good prediction of the mixture adsorption equilibrium is also provided by the mixed-gas Langmuir model. To demonstrate this, the calculations using the mixed-gas Langmuir model, eq (S7) are presented as the continuous solid lines in Figure S25b. For the range of experiments, the mixed-gas Langmuir model is in very good agreement with IAST calculations.

Since we have established the accuracy of the mixed-gas Langmuir model to describe CO_2/C_2H_6 mixture adsorption equilibrium in DDR, Figure S25c,d,e presents the calculations using (S8) for the elements of the matrix of thermodynamic correction factors Γ_{ij}, using expressed as a function of total mixture loading, q_t, for (c) 1:1, (d) 2:1, and (e) 3:1 ratios of partial pressures in the gas phase. In these calculations the total gas pressure, p_t, was varied from 1 to 100 kPa. The off-diagonal elements Γ_{12}, and Γ_{21} become increasingly important with increasing loadings. This implies that thermodynamic coupling effects are of particular importance for the uptake of CO_2(1) from CO_2(1)/C_2H_6(2) gas mixtures.

Both of the guest molecules CO_2, and C_2H_6 jump length-wise across the 8-ring windows of DDR zeolite. The cross-sectional dimension of CO_2 is smaller than that of C_2H_6 (see Figure S24), and therefore the intra-crystalline M-S diffusivity of CO2 is significantly higher than that of C_2H_6. The diffusivity input values of $Đ_1/r_c^2$, and $Đ_2/r_c^2$ are taken from earlier work[5]:

Experiment 1: $Đ_1/r_c^2 = 0.125$ s^{-1}; $Đ_2/r_c^2 = 9.38\times10^{-5}$ s^{-1}; $Đ_1/Đ_2 = 1333$.

Experiment 2: $Đ_1/r_c^2 = 9.375\times10^{-3}$ s^{-1}; $Đ_2/r_c^2 = 9.38\times10^{-5}$ s^{-1}; $Đ_1/Đ_2 = 100$.

Experiment 3: $Đ_1/r_c^2 = 6.25\times10^{-3}$ s^{-1}; $Đ_2/r_c^2 = 1.25\times10^{-4}$ s^{-1}; $Đ_1/Đ_2 = 50$.

Figure S26(a,b,c) show the experimental data of Binder et al.[64] and Lauerer et al.[65] (indicated by symbols) for spatial-averaged transient uptake of (a) 20/20 (b) 40/40, and (c) 60/20 CO_2(1)/C_2H_6(2) gas mixtures within crystals of DDR zeolite at 298 K. The continuous solid lines are simulations of the transient uptake using the flux relations (S21). The Maxwell-Stefan model captures the overshoots in CO_2 loadings with good accuracy for all three cases. The overshoots in the CO_2 uptake signal the phenomenon of uphill diffusion, engendered by thermodynamic coupling.[5, 67] In order to confirm that thermodynamic coupling effects are responsible for the overshoots, we also performed transient uptake in which the thermodynamic correction factors are assumed to be described by $\Gamma_{ij} = \delta_{ij}$, the Kronecker delta. The dashed lines in Figure S26(a,b,c) represent the simulation results based on Eq (S23); with this simplified model, no overshoots in the CO_2 uptake are experienced. An important consequence of thermodynamic coupling effects is that supraequilibrium loadings of CO_2 are realized during the early transience. We now investigate the consequence of thermodynamic coupling and uphill diffusion on CO_2/C_2H_6 mixture separations in a fixed bed adsorber packed with DDR adsorbent.

5.2 Analysis of CO_2/C_2H_6 uptake using eigenvalues and eigenvectors

We now proceed to analyze the three sets of experimental data in more detail in order to gain more fundamental insights.

For 20/20 $CO_2(1)/C_2H_6(2)$ gas mixtures within crystals of DDR zeolite at 298 K, at a total pressure $p_t = p_1 + p_2$ = 40 kPa, the elements of the $[\Gamma]$ are $\begin{bmatrix} \Gamma_{11} & \Gamma_{12} \\ \Gamma_{21} & \Gamma_{22} \end{bmatrix} = \begin{bmatrix} 1.208 & 0.324 \\ 0.849 & 2.32 \end{bmatrix}$. The Fick diffusivity matrix is calculated to be $\dfrac{\begin{bmatrix} D_{11} & D_{12} \\ D_{21} & D_{22} \end{bmatrix}}{r_c^2} = \begin{bmatrix} 1510 & 404.44 \\ 0.796 & 2.175 \end{bmatrix} \times 10^{-4} \quad s^{-1}$.

The continuous solid lines in Figure S27a,b are the numerical solutions for transient uptake using the M-S diffusion eq (S21). The dashed lines in (a) are the solutions invoking the simplified eq (S23), Use of the LDF model, eq (S39) , results in the dashed lines shown in (b).

5.3 Separating CO_2/C_2H_6 mixtures in fixed bed adsorber packed with DDR zeolite

The separation of CO_2/C_2H_6 is relevant in the context of natural gas processing. Current technologies for CO_2/C_2H_6 separations use extractive distillation because of CO_2/C_2H_6 azeotrope formation.[68] Another alternative is to combine distillation technology with membrane separations; for this purpose cross-linked polyethylene oxide (XLPEO) membranes have demonstrated to have good separation potential.[1, 69, 70] The Binder/Lauerer uptake experiments suggest the possibility of diffusion-selective purification of ethane by selective removal of CO_2 present as impurities in mixtures with ethane.

To demonstrate the concept of diffusion-selective separations, we carried out transient breakthrough simulations in a fixed bed adsorber packed with crystallites of DDR.

Figure S28a,b show the transient breakthrough simulations for 50/50 CO_2/C_2H_6 mixtures through fixed bed adsorber packed with DDR crystals operating at 298 K, and total pressure p_t = 40 kPa. In Figure S28a, the dimensionless concentrations c_i/c_{i0} exiting the fixed bed are plotted as a function of $\frac{\left(Q_0 = \text{flow rate L s}^{-1}\right)\times\left(\text{time in s}\right)}{\left(\text{kg MOF packed in tube}\right)} = \frac{Q_0 t}{m_{ads}} = \text{L kg}^{-1}$ as the x-axis. The y-axis in Figure S28b is the % C_2H_6 at the adsorber outlet. The continuous solid lines are simulations taking due account of intra-crystalline diffusion along with thermodynamic coupling influences using eq (S21) with parameters: $Đ_1/r_c^2$ = 0.00125 s^{-1}; $Đ_1/Đ_2$ = 1333.

We note that C_2H_6 breaks through earlier and can be recovered in purified form during the early stages of the transient operations, prior to the breakthrough of CO_2. The dashed lines in Figure S28a,b are the simulations in which thermodynamic coupling effects are ignored and eq (S23) is used to describe the transfer fluxes. In this scenario, the breakthrough of CO_2 occurs earlier and therefore the productivity of purified C_2H_6 is lower. If we assume that the target purity of C_2H_6 is 90%, we can determine the moles of 90%+ pure C_2H_6 produced from a material balance on the adsorber. Expressed per kg of DDR zeolite in the packed bed, the respective productivities are 0.2973 mol kg^{-1}, and 0.0957 mol kg^{-1}, respectively. Ignoring thermodynamic coupling effects severely underestimates the separation performance.

For kinetic separations the choice of the particle size is of crucial importance. In order to highlight the influence of particle size, Figure S29 presents the breakthrough simulations for the scenario in which the diffusional time constant $\left(Đ_1/r_c^2\right)$, is allotted four different values in decreasing order, i.e. increasing zeolite crystallite size; the ratio of M-S diffusivities $Đ_1/Đ_2$ = 1333. The continuous solid lines are simulations taking due account of thermodynamic coupling influences using eq (S21) The dashed lines are the simulations in which thermodynamic coupling effects are ignored and eq (S23) is used to describe the transfer fluxes. In Figure S29a we choose $\left(Đ_1/r_c^2\right) = 0.5$ s $^{-1}$; in this case the diffusional influences are not sufficiently strong to reverse the selectivities. Therefore, the sequence of breakthroughs is dictated by mixture adsorption equilibrium that favors the alkane.

Figure S29b,c,d present the breakthrough simulation results for increasing crystal sizes: (b) $\left(Đ_1/r_c^2\right) = 6.8\times10^{-2}$ s $^{-1}$. (c) $\left(Đ_1/r_c^2\right) = 1.7\times10^{-2}$ s $^{-1}$. (d) $\left(Đ_1/r_c^2\right) = 1.7\times10^{-4}$ s $^{-1}$. In these cases, the first component to break through is the saturated alkane that has the higher adsorption strength but significantly lower mobility. We note that the breakthroughs for C_2H_6 occurs earlier because the saturated alkane is severely diffusion limited. Concomitantly, the breakthrough of CO_2 also occurs earlier with decreasing $\left(Đ_1/r_c^2\right)$.

In order to address the question: what is the optimum crystallite size?, Figure S30a plots the % C_2H_6 at the adsorber outlet is plotted as a function of the modified time parameter $\frac{Q_0 t}{m_{ads}} = \text{L kg}^{-1}$ for three different values of $\left(Đ_1/r_c^2\right)$. If the target purity is set at > 90%, the productivity of purified C_2H_6 may be determined from a material balance. In Figure S30b the productivity of purified C_2H_6(2), containing less than 10% CO_2, plotted as a function of the diffusional time constant $\left(Đ_1/r_c^2\right)$. We note that there is a narrow window for values of $\left(Đ_1/r_c^2\right)$ that yields the maximum productivity of the desired product. Further decrease in $\left(Đ_1/r_c^2\right)$, i.e. increasing crystallite size, will reduce the productivity. The important message is that for kinetically driven separations to be effective there is an optimum crystal size, i.e. optimum value of the diffusional time constant, $\left(Đ_1/r_c^2\right)$. The dashed lines in Figure S30b are the values of the productivities in the scenario wherein thermodynamic coupling effects are ignored and eq (S23) is used to describe the transfer fluxes; in this scenario, the productivities are severely underestimated.

Watch also the video presentations titled **Particle Size Effects in Kinetic Separations,** and **Diffusional Time Constants & Contact Times** on YouTube

https://www.youtube.com/@rajamanikrishna250/videos

For any chosen value of the crystal size, i.e. chosen value of $\left(Đ_1/r_c^2\right)$, the severity of diffusional influences are also dependent on the contact time between the gas mixture and the crystallites; this contact time is L/v, where v is the interstitial gas velocity. To illustrate this influence, Figure S31a,b,c,d present transient breakthrough simulations for the adsorption cycle for 50/50 CO_2/C_2H_6 mixtures through fixed bed adsorber packed with DDR crystals operating at 298 K, and total pressure p_t = 40 kPa for (a) $L/v = 600 \quad \text{s}$, (b) $L/v = 300 \quad \text{s}$, (c) $L/v = 30 \quad \text{s}$, and (d) $L/v = 3 \quad \text{s}$. The continuous solid lines are simulations taking due account of thermodynamic coupling influences using eq (S21) The dashed lines are the simulations in which thermodynamic coupling effects are ignored and eq (S23) is used to describe the transfer fluxes. Selectivity reversals in favor of CO_2 occur only for contact times shorter than $L/v = 300 \quad \text{s}$. We note that the shorter the contact time, the more severe is the influence of diffusional limitations. With decreasing contact times, the breakthroughs of C_2H_6 occur earlier, resulting in improved separations.

Figure S32a plots the % C_2H_6 at the adsorber outlet is plotted as a function of the modified time parameter $\frac{Q_0 t}{m_{ads}} = \text{L kg}^{-1}$ for three different values of L/v. If the target purity is set at > 90% , the productivity of purified C_2H_6 may be determined from a material balance. In b the productivity of purified C_2H_6(2), containing less than 10% CO_2, plotted as a function of the contact time L/v. We note that the productivity of purified C_2H_6 decreases with increasing values of the contact time L/v.The dashed lines in Figure S32b are the values of the productivities in the scenario wherein thermodynamic coupling effects are ignored and eq (S23) is used to describe the transfer fluxes; in this scenario, the productivities are severely underestimated.

For any chosen value of the crystal size, i.e. chosen value of $\left(Đ_1/r_c^2\right)$, and contact time L/v, the sequence of breakthroughs is also dependent on the ratio of Maxwell-Stefan diffusivities $Đ_1/Đ_2$. To highlight this influence, Figure S33 a,b,c,d present transient breakthrough simulations for the adsorption cycle for 50/50 CO_2/C_2H_6 mixtures through fixed bed adsorber packed with DDR crystals operating at 298 K, and total pressure p_t = 40 kPa for (a) $Đ_1/Đ_2 = 10$, (b) $Đ_1/Đ_2 = 100$, (c) $Đ_1/Đ_2 = 500$, and (d) $Đ_1/Đ_2 = 1333$. Selectivity reversals in favor of CO_2 occur only if the ratio $Đ_1/Đ_2 >> 10$.

Figure S34a plots the % C_2H_6 at the adsorber outlet is plotted as a function of the modified time parameter $\frac{Q_0 t}{m_{ads}} = \text{L kg}^{-1}$ for three different values of $Đ_1/Đ_2$. If the target purity is set at > 90% , the productivity of purified C_2H_6 may be determined from a material balance. In Figure S34b the productivity of purified C_2H_6(2), containing less than 10% CO_2, plotted as a function of the ratio of M-S diffusivities $Đ_1/Đ_2$. We note that the productivity of purified C_2H_6 increases with increasing values of the ratio $Đ_1/Đ_2$.

We now demonstrate that the breakthrough simulations are uniquely dependent on the product of the diffusional time constant $\left(Đ_1/r_c^2\right)$ and the gas-particle contact time L/v. Figure S35 presents transient breakthrough simulations for the adsorption cycle for 50/50 CO_2(1)/C_2H_6(2) mixture in fixed bed packed with DDR zeolite crystals at 298 K; the partial pressures in the bulk gas phase feed mixture are $p_1 = p_2 =$ 20 kPa. In these simulations the bed voidage $\varepsilon = 0.4$, bed length $L = 0.3 \quad \text{m}$, The interstitial velocities are varied such that the contact times are $L/v = 3, 4.69, 12, 18.75 \quad \text{s}$; the diffusional constants $\left(Đ_1/r_c^2\right)$ are adjusted such that $\left(Đ_1/r_c^2\right)\left(L/v\right) = 3.75\times10^{-3}$; $Đ_1/Đ_2 = 1333.$. All these four sets of simulations collapse into a unique breakthrough curve, when plotted as function of $\frac{Q_0 t}{m_{ads}} = \frac{t}{L/v}\frac{\varepsilon}{(1-\varepsilon)\rho}$. Figure S35 provides an important tool for interpreting and utlizing the results in laboratory scale equipment for scaling up to commercial units with different particle sizes and contact times.

5.4 Separating CO_2/CH_4 mixtures in fixed bed adsorber packed with DDR zeolite

DDR zeolite is a potent adsorbent for capture of CO_2 from CO_2/CH_4 mixtures. Figure S36a shows the transient breakthrough of 20/80 $CO_2(1)/CH_4(2)$ mixtures through fixed bed adsorber packed with DDR crystals operating at 298 K, and total pressure p_t = 100 kPa. For this separation, there is synergy between adsorption and diffusion; both favor CO_2. In the two sets of simulations the ratio $Đ_1/Đ_2 = 100$. Two different values of the diffusional time constants were chosen $Đ_1/r_c^2 = 2\times10^{-2}, 2$ s^{-1}. In the two sets of simulations the ratio $Đ_1/Đ_2 = 100$. For the case in which diffusional influences are of diminished significance, $Đ_1/r_c^2 = 2$ s^{-1}, the productivity of purified CH_4 is lower.

5.5 Separating $CO_2/C_2H_6/CH_4$ mixtures in fixed bed adsorber packed with DDR zeolite

Figure S36b shows the transient breakthrough of 20/20/60 $CO_2(1)/C_2H_6(2)/CH_4(3)$ mixtures through fixed bed adsorber packed with DDR crystals operating at 298 K, and total pressure p_t = 100 kPa. For separation of this ternary mixture, both synergistic and antisynergistic influences of diffusion are in play. The net result is that both $C_2H_6(2)$, and $CH_4(3)$ can be rejected into the gas phase and recovered during the adsorption cycl.e

5.7 List of Tables for Separation of CO2/C2H6 mixtures with DDR zeolite

Table S7. 1-site Langmuir parameters for CO_2 and C_2H_6 in DDR zeolite at 298 K. These parameters have been fitted from the data scanned from Figure 36, Chapter 4 of the PhD dissertation of Binder.[66] The unary isotherm fit for CH_4 in DDR zeolite at 298 K is based on CBMC simulation data from Krishna and van Baten.[71]

	$\frac{q_{sat}}{\text{mol kg}^{-1}}$	$\frac{b}{\text{Pa}^{-1}}$
CO_2	2.8	1.04E-05
C_2H_6	1.8	6.6E-05
CH_4	2.8	2.0E-06

5.8 List of Figures for Separation of CO2/C2H6 mixtures with DDR zeolite

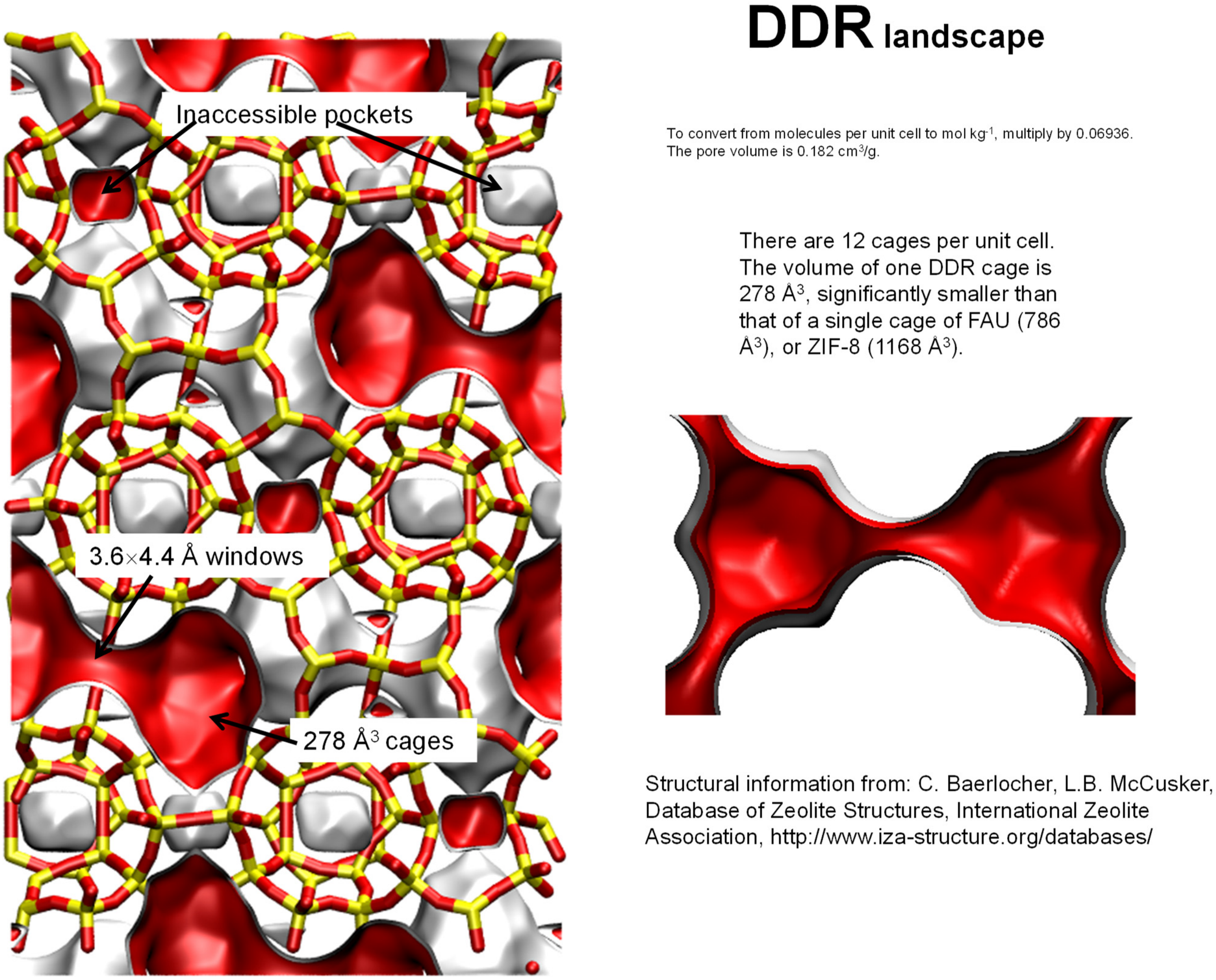

DDR landscape

To convert from molecules per unit cell to mol kg^{-1}, multiply by 0.06936.
The pore volume is 0.182 cm^3/g.

There are 12 cages per unit cell. The volume of one DDR cage is 278 Å^3, significantly smaller than that of a single cage of FAU (786 Å^3), or ZIF-8 (1168 Å^3).

Structural information from: C. Baerlocher, L.B. McCusker, Database of Zeolite Structures, International Zeolite Association, http://www.iza-structure.org/databases/

Figure S22. Pore landscape of all-silica DDR zeolite.

DDR window and pore dimensions

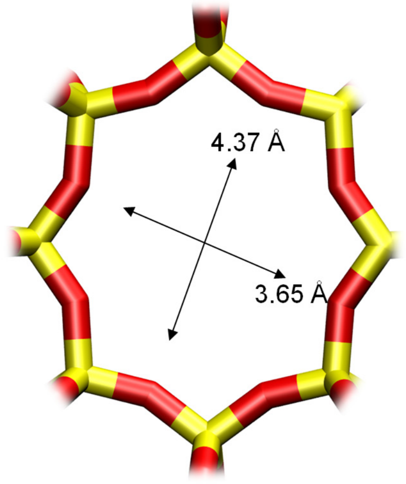

DDR

The window dimensions calculated using the van der Waals diameter of framework atoms = 2.7 Å are indicated above by the arrows.

	DDR
a /Å	24.006
b /Å	13.86
c /Å	40.892
Cell volume / Å^3	13605.72
conversion factor for [molec/uc] to [mol per kg Framework]	0.0693
conversion factor for [molec/uc] to [kmol/m^3]	0.4981
ρ [kg/m3]	1759.991
MW unit cell [g/mol(framework)]	14420.35
ϕ, fractional pore volume	0.245
open space / Å^3/uc	3333.5
Pore volume / cm^3/g	0.139
Surface area /m^2/g	350.0
DeLaunay diameter /Å	3.65

Figure S23. Structural details of all-silica DDR zeolite.

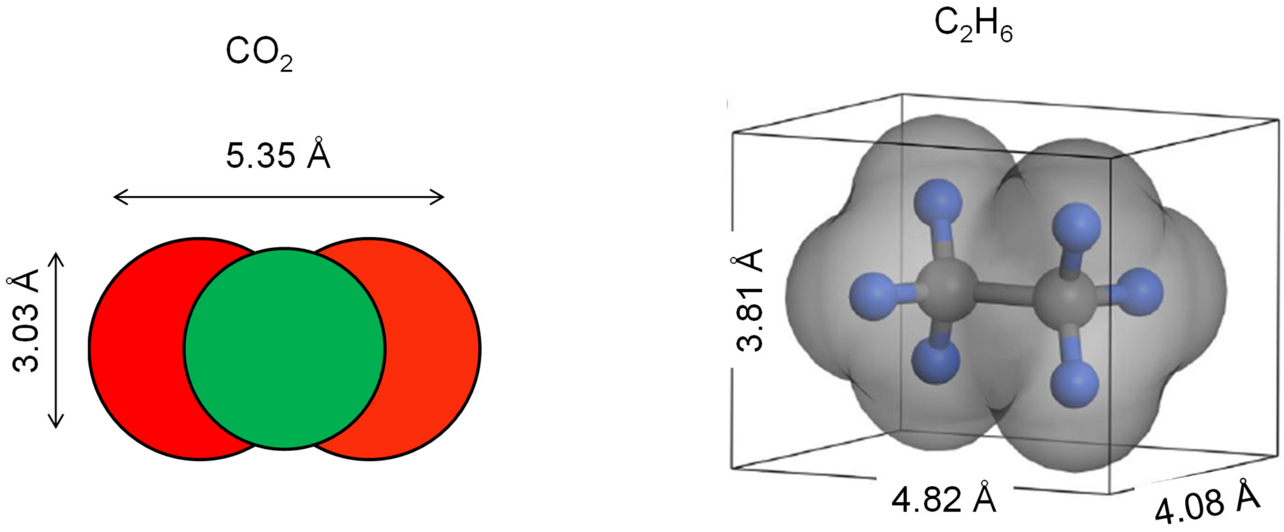

Figure S24. Molecular dimensions of CO_2 and C_2H_6. The molecular dimensions of C_2H_6 are taken from Lin et al.[72]

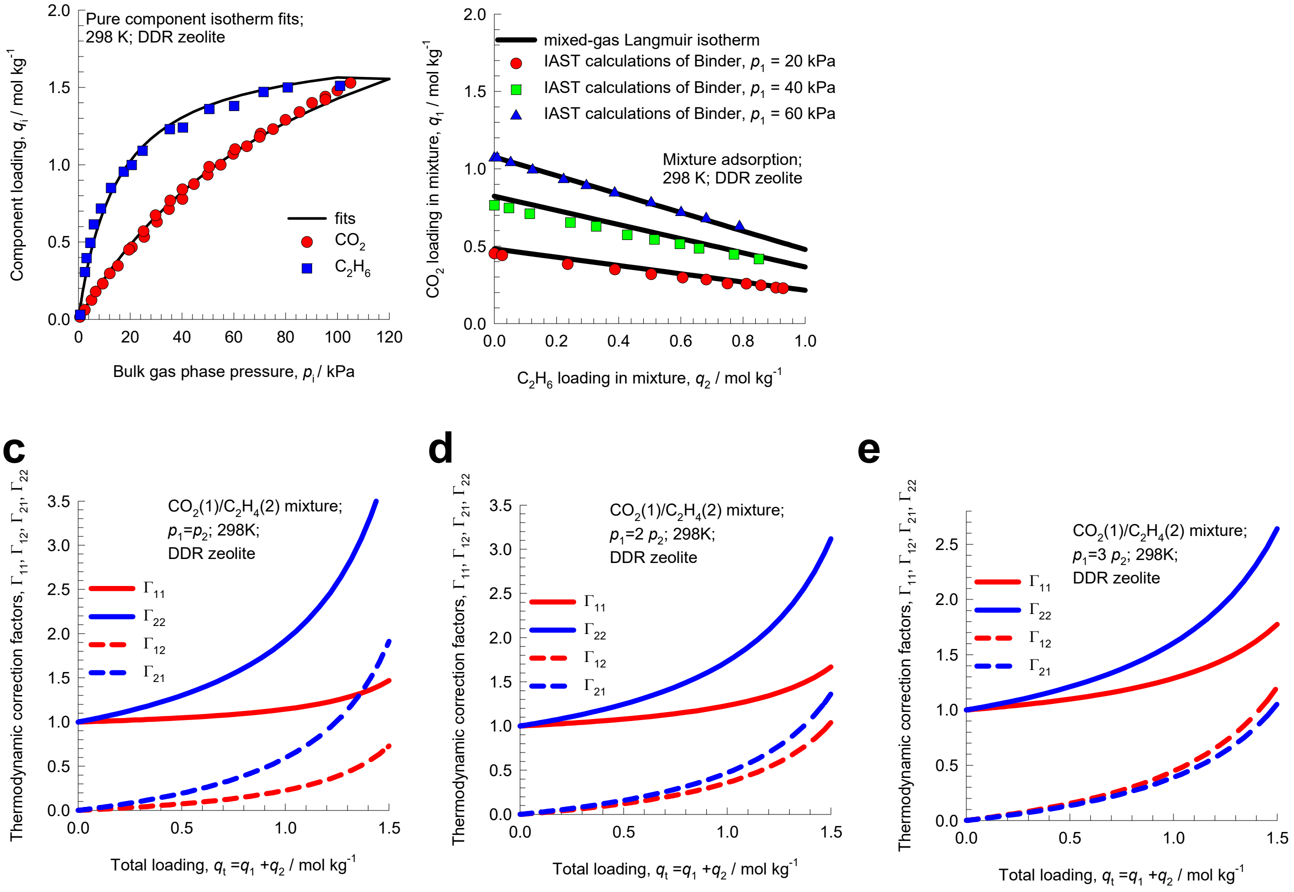

Figure S25. (a) Comparison of unary isotherm data with single-site Langmuir fits using the parameters reported in Table S7. (b) The symbols are scanned from Figure 3 of Binder et al;[64] they represent IAST calculations for binary CO_2 (1)/C_2H_6(2) mixture adsorption in DDR crystals with constant CO_2 partial pressures of p_1 = 20, 40, and 60 kPa for experiments 1, 2, and 3, respectively. The partial pressures of C_2H_6 ethane in the gas phase is varied. The continuous solid lines are our calculations using mixed-gas Langmuir model using the single-site Langmuir parameters reported in in Table S7. (c, d, e) Elements of the matrix of thermodynamic correction factors Γ_{ij} as a function of total mixture loading, q_t, calculated using the mixed-gas Langmuir model for binary CO_2(1)/C_2H_6(2) mixture adsorption in DDR for (c) 20/20 (d) 40/20, and (e) 60/20 ratios of partial pressures in the gas phase.

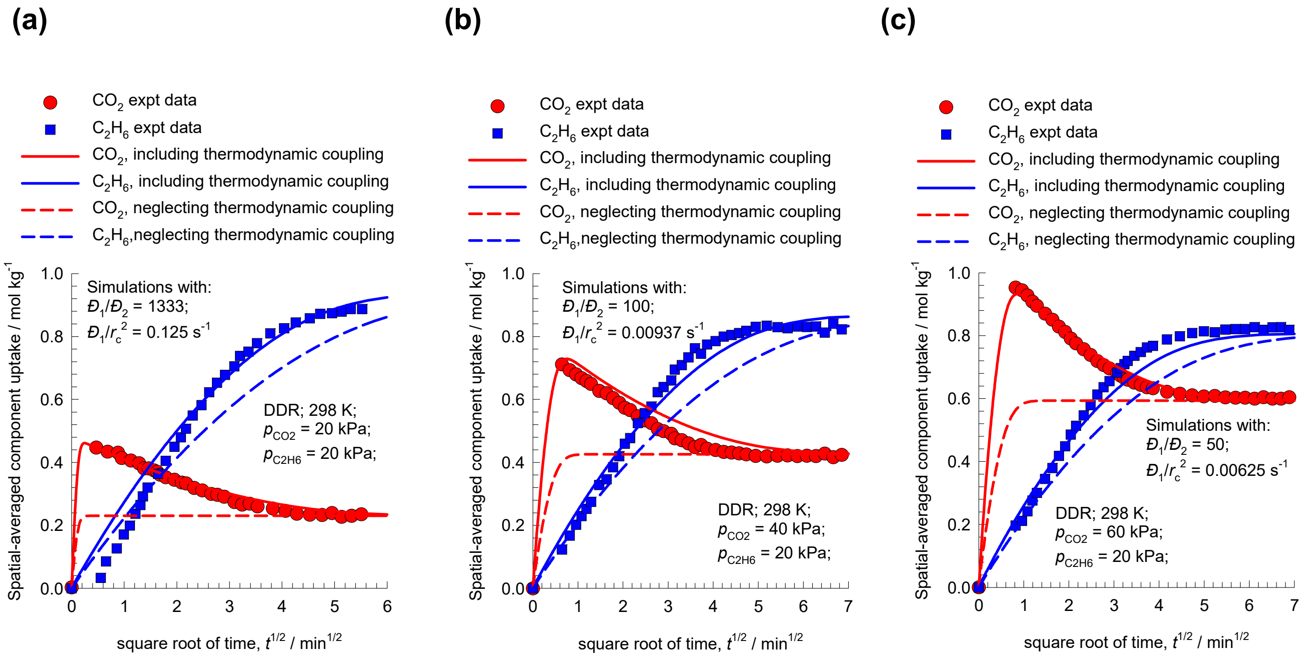

Figure S26. (a, b, c) Experimental data of Binder et al.[64] and Lauerer et al.[65] (indicated by symbols) for spatial-averaged transient uptake of (a) 20/20 (b) 40/20, and (c) 60/20 $CO_2(1)/C_2H_6(2)$ gas mixtures within crystals of DDR zeolite at 298 K. The continuous solid lines are Maxwell-Stefan model simulations based on Eq (S21). The dashed lines are the simulations based on Eq (S23), in which the thermodynamic correction factors are assumed to be described by $\Gamma_{ij} = \delta_{ij}$, the Kronecker delta.

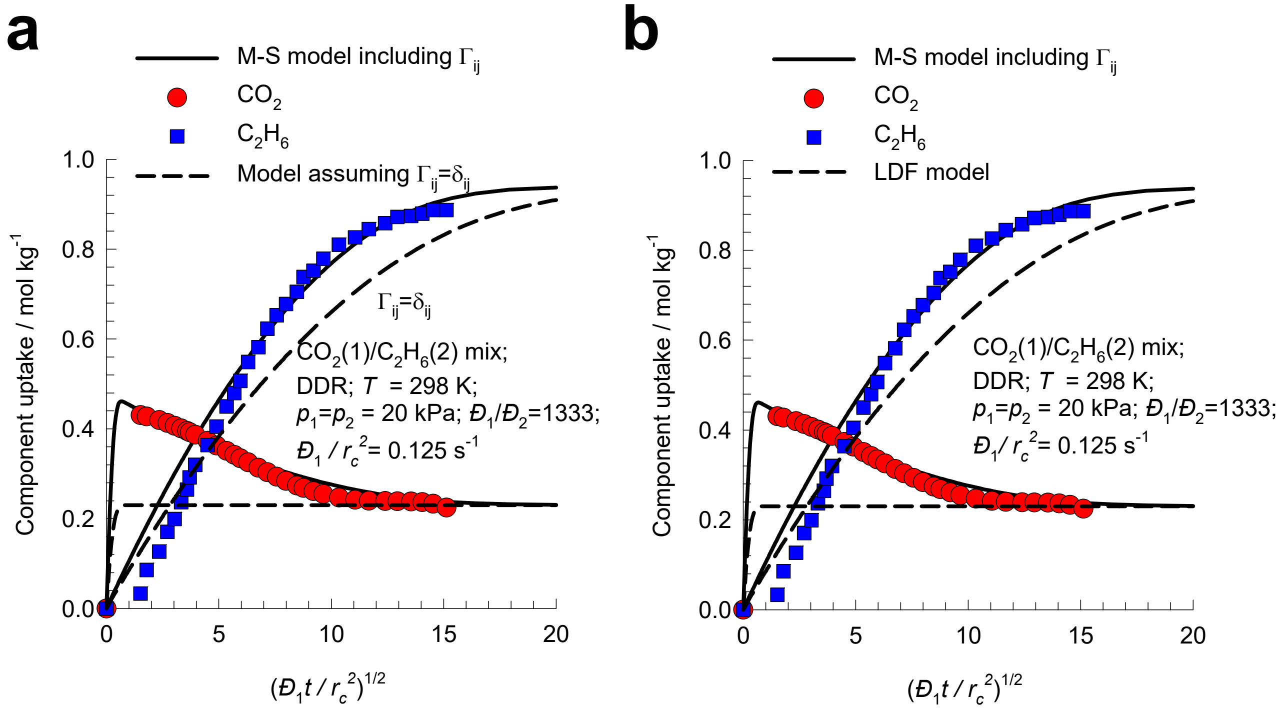

Figure S27. (a, b) Experimental data of Binder et al.[64] and Lauerer et al.[65] (indicated by symbols) for spatial-averaged transient uptake of 20/20 CO_2(1)/C_2H_6(2) gas mixtures within crystals of DDR zeolite at 298 K. The continuous solid lines in (a,b) are the numerical solutions for transient uptake using the M-S diffusion eq (S21). The dashed lines in (a) are the solutions invoking the simplified eq (S23), Use of the LDF model, eq (S39), results in the dashed lines shown in (b).

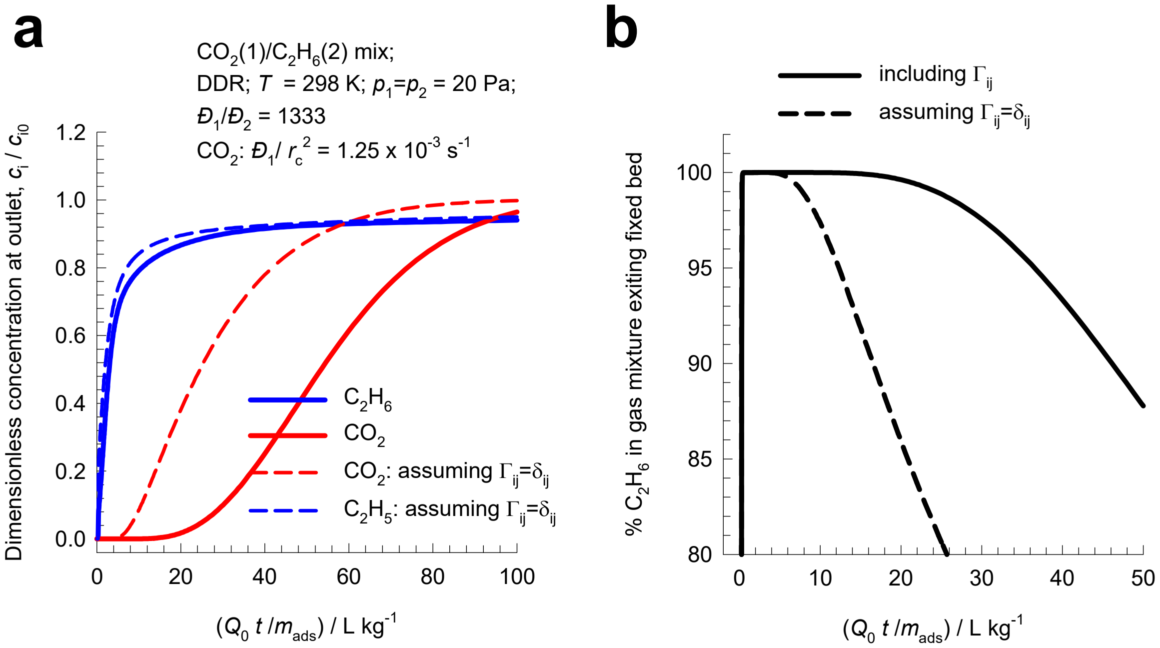

Figure S28. (a,b) Transient breakthrough of 50/50 CO_2(1)/C_2H_6(2) mixture in fixed bed packed with DDR zeolite crystals at 298 K; the partial pressures in the bulk gas phase feed mixture are $p_1 = p_2 = 20$ kPa. In Figure S28a, the dimensionless concentrations c_i/c_{i0} exiting the fixed bed are plotted as a function of $\frac{\left(Q_0 = \text{flow rate L s}^{-1}\right)\times\left(\text{time in s}\right)}{\left(\text{kg MOF packed in tube}\right)} = \frac{Q_0 t}{m_{ads}} = \text{L kg}^{-1}$ as the x-axis. The y-axis in Figure S28b is the % C_2H_6 at the adsorber outlet. The continuous solid lines are simulations taking due account of intra-crystalline diffusion using eq (S21) with parameters: $\left(Đ_1/r_c^2\right) = 1.25\times10^{-3}$ s $^{-1}$; $Đ_1/Đ_2 = 1333$. The dashed lines are the simulations in which thermodynamic coupling effects are ignored and eq (S23) is used to describe the transfer fluxes.

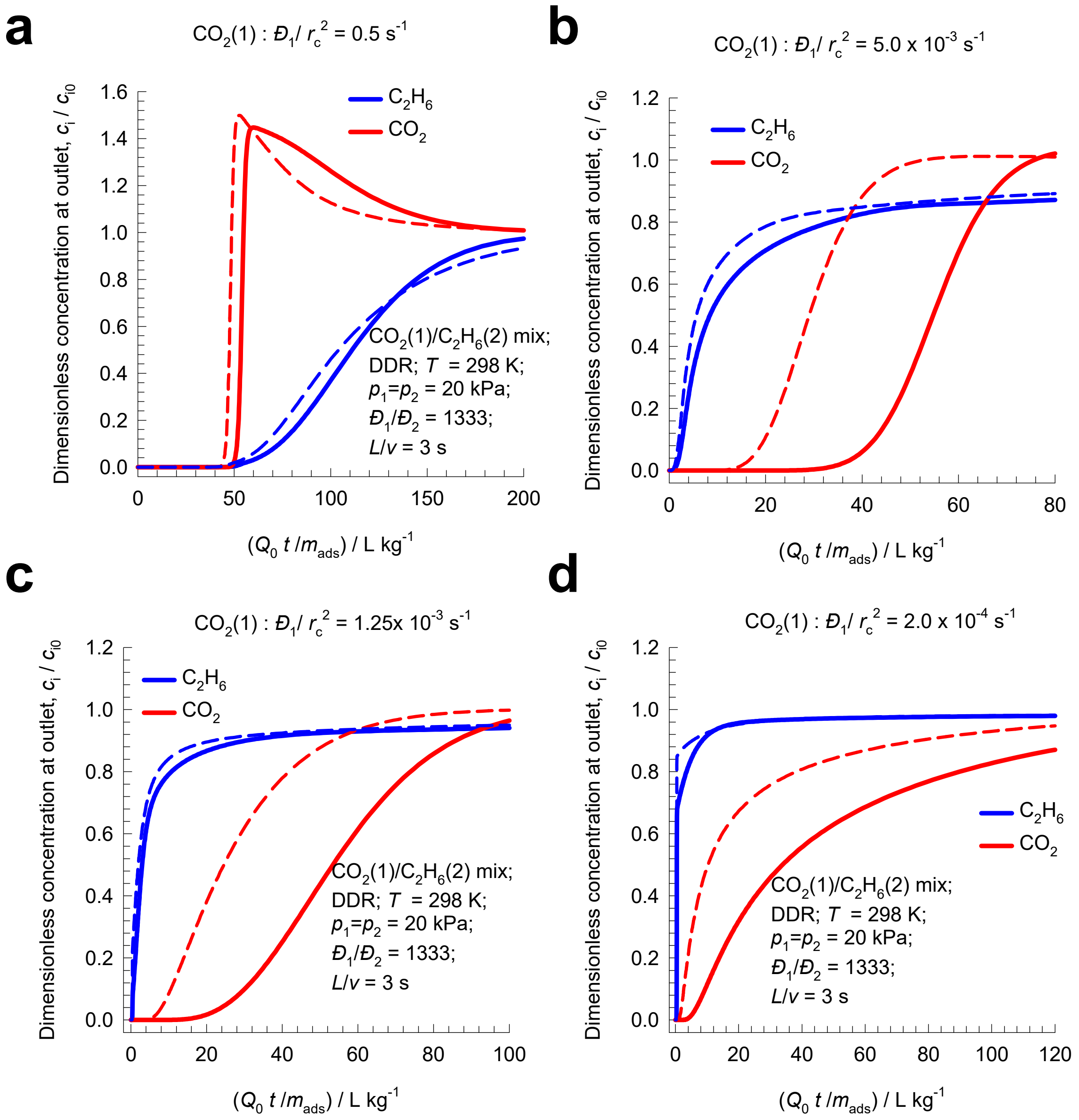

Figure S29. Influence of diffusional time constant $\left(Đ_1/r_c^2\right)$ on transient breakthrough simulations for the adsorption cycle for 50/50 CO$_2$(1)/C$_2$H$_6$(2) mixture in fixed bed packed with DDR zeolite crystals at 298 K; the partial pressures in the bulk gas phase feed mixture are $p_1 = p_2 = 20$ kPa. In these simulations the bed voidage $\varepsilon = 0.4$, bed length $L = 0.3$ m, the ratio of M-S diffusivities are $Đ_1/Đ_2 = 1333$, the interstitial velocities $v = 0.1$ m s^{-1}; the contact time $L/v = 3$ s. (a) Diffusional time constant $\left(Đ_1/r_c^2\right) = 0.5$ s^{-1}. (b) $\left(Đ_1/r_c^2\right) = 5\times10^{-3}$ s^{-1}. (c) $\left(Đ_1/r_c^2\right) = 1.25\times10^{-3}$ s^{-1}. (d) $\left(Đ_1/r_c^2\right) = 2\times10^{-4}$ s^{-1}. The continuous solid lines are simulations taking due account of thermodynamic coupling using eq (S21) with parameters: $\left(Đ_1/r_c^2 \right) = 1.25 \times 10^{-3}$ s $^{-1}$; $Đ_1/Đ_2 = 1333$. The dashed lines are simulations in which thermodynamic coupling effects are ignored and eq (S23) is used to describe the transfer fluxes.

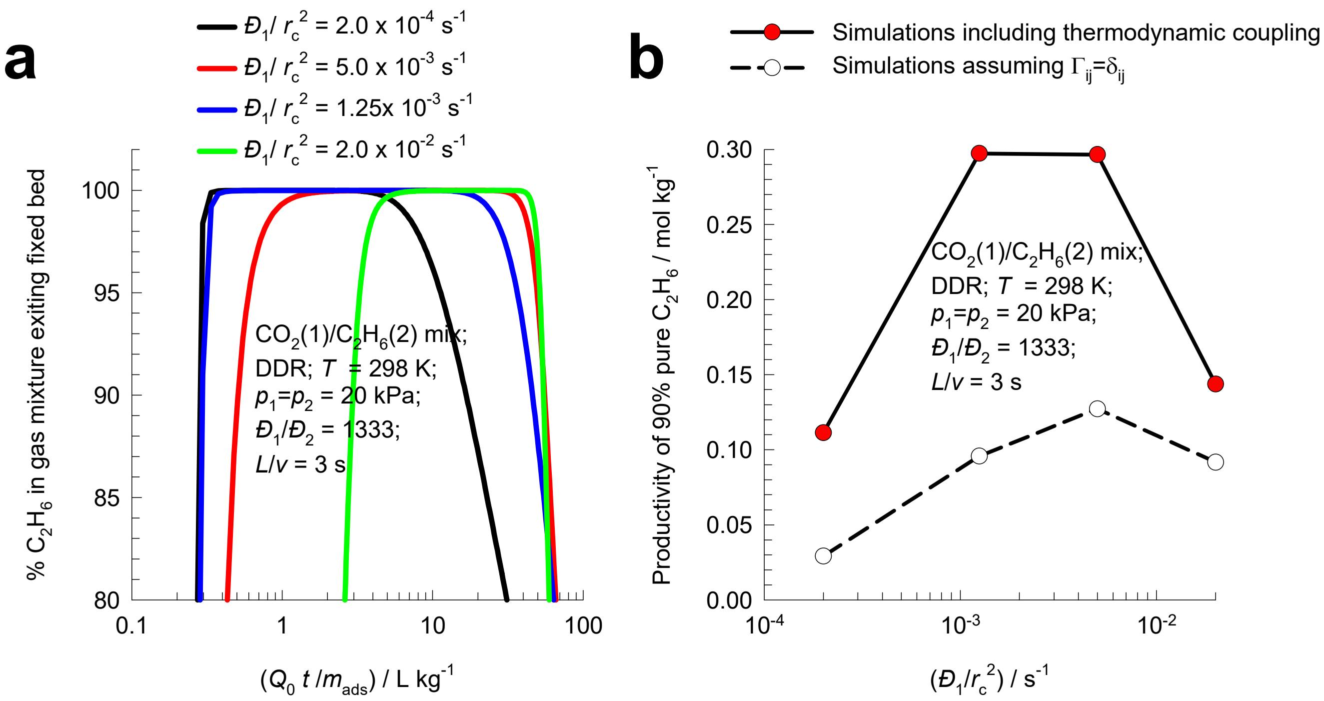

Figure S30. (a, b) Influence of diffusional time constant $\left(Đ_1/r_c^2\right)$ on the productivity of purified C_2H_6(2) for the adsorption cycle for 50/50 CO_2(1)/C_2H_6(2) mixture in fixed bed packed with DDR zeolite crystals at 298 K; the partial pressures in the bulk gas phase feed mixture are $p_1 = p_2 = 20$ kPa. (a) The % C_2H_6 at the adsorber outlet is plotted as a function of $\frac{Q_0 t}{m_{ads}} = \text{L kg}^{-1}$. The continuous solid lines are simulations taking due account of thermodynamic coupling using eq (S21). (b) The productivity of purified C_2H_6(2), containing less than 10% CO_2, plotted as a function of the diffusional time constant $\left(Đ_1/r_c^2\right)$. The dashed line in (b) are productivity calculations in which thermodynamic coupling effects are ignored and eq (S23) is used to describe the transfer fluxes.

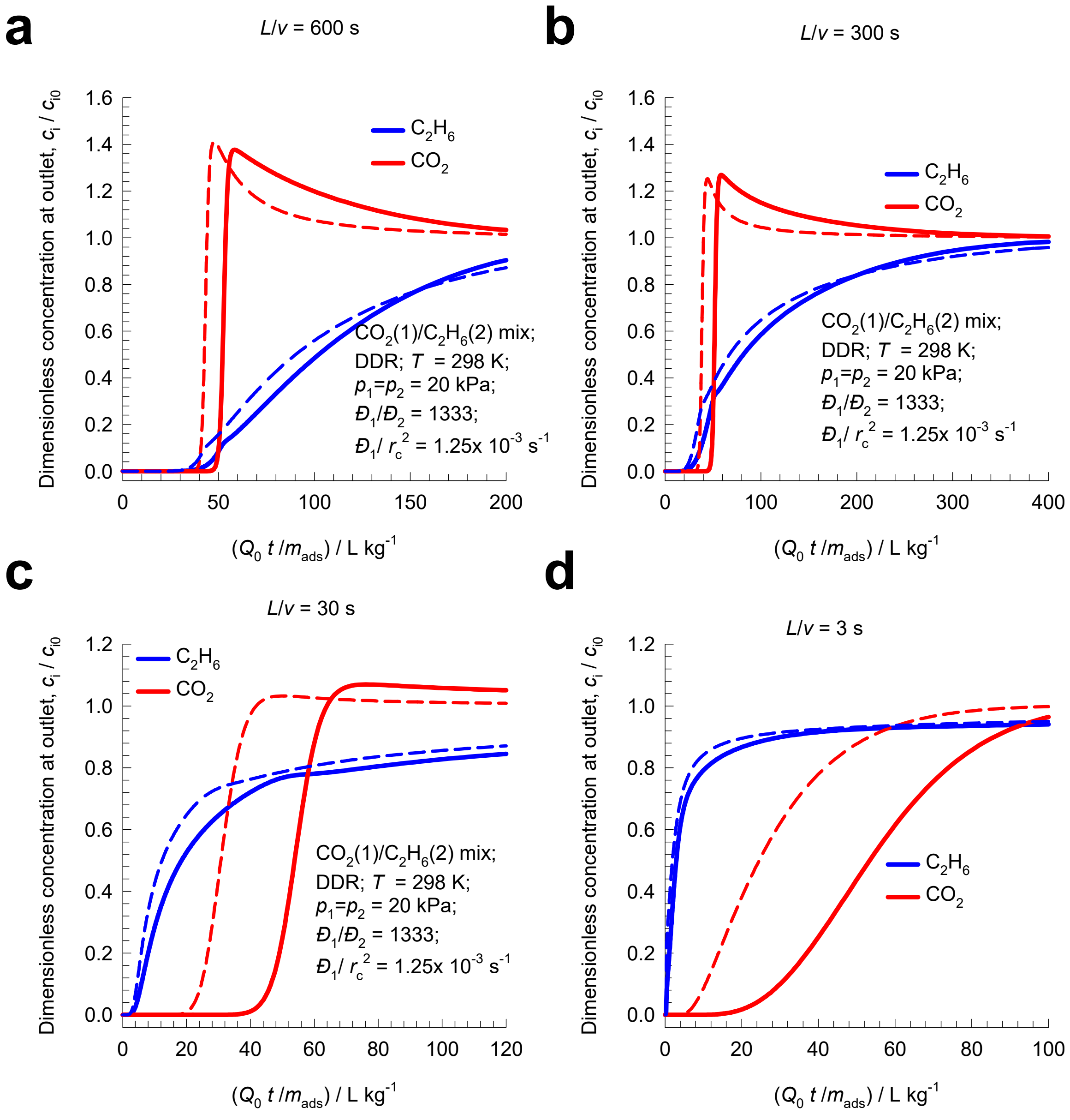

Figure S31. Influence of gas-crystal contact time, L/v, on transient breakthrough simulations for the adsorption cycle for 50/50 $CO_2(1)/C_2H_6(2)$ mixture in fixed bed packed with DDR zeolite crystals at 298 K; the partial pressures in the bulk gas phase feed mixture are $p_1 = p_2 = 20$ kPa. In these simulations the bed voidage $\varepsilon = 0.4$, bed length $L = 0.3$ m, $\left(Đ_1/r_c^2\right) = 1.25\times10^{-3}$ s $^{-1}$, and the ratio of M-S diffusivities are $Đ_1/Đ_2 = 1333$, The interstitial velocities are varied: (a) $L/v = 600$ s, (b) $L/v = 300$ s, (c) $L/v = 30$ s, and (d) $L/v = 3$ s. The continuous solid lines are simulations taking due account of thermodynamic coupling using eq (S21) with parameters: $\left(Đ_1 / r_c^2 \right) = 1.25 \times 10^{-3}$ s $^{-1}$; $Đ_1 / Đ_2 = 1333$. The dashed lines are simulations in which thermodynamic coupling effects are ignored and eq (S23) is used to describe the transfer fluxes.

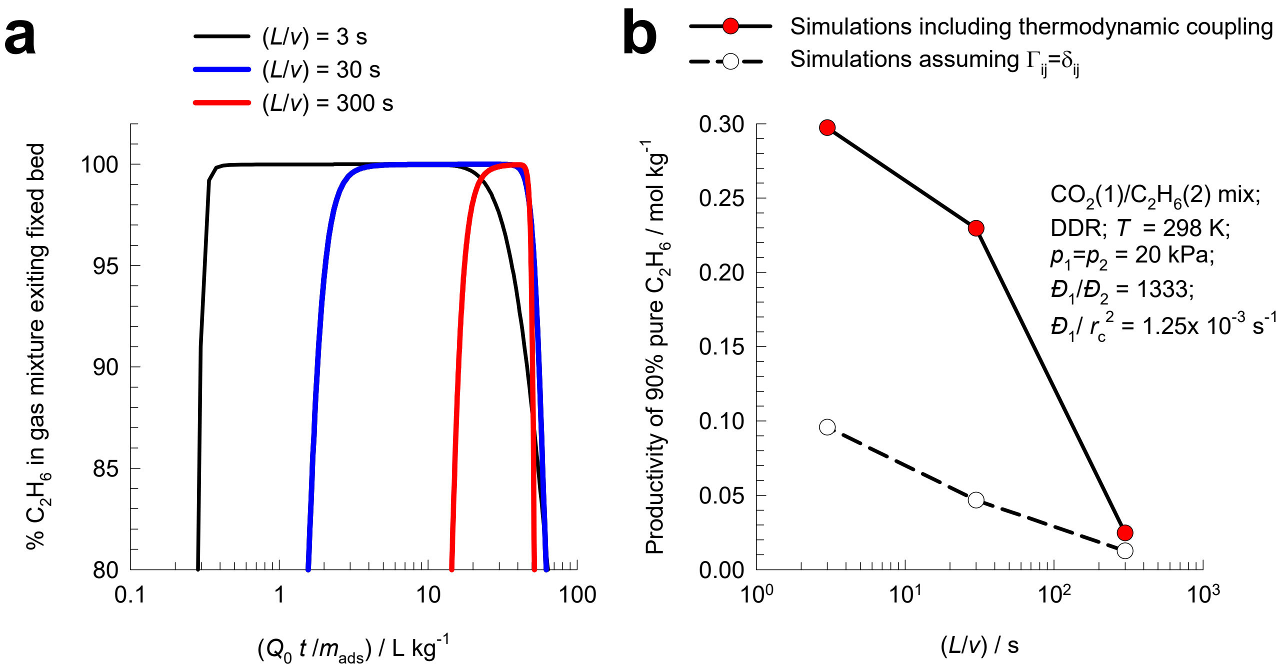

Figure S32. (a, b) Influence of gas-crystal contact time, L/v, on the productivity of purified C_2H_6(2) for the adsorption cycle for 50/50 CO_2(1)/C_2H_6(2) mixture in fixed bed packed with DDR zeolite crystals at 298 K; the partial pressures in the bulk gas phase feed mixture are $p_1 = p_2 = 20$ kPa. (a) The % C_2H_6 at the adsorber outlet is plotted as a function of $\frac{Q_0 t}{m_{ads}} = \text{L kg}^{-1}$. The continuous solid lines are simulations taking due account of thermodynamic coupling using eq (S21). (b) The productivity of purified C_2H_6(2), containing less than 10% CO_2, plotted as a function of the gas-crystal contact time, L/v.The dashed line in (b) are productivity calculations in which thermodynamic coupling effects are ignored and eq (S23) is used to describe the transfer fluxes.

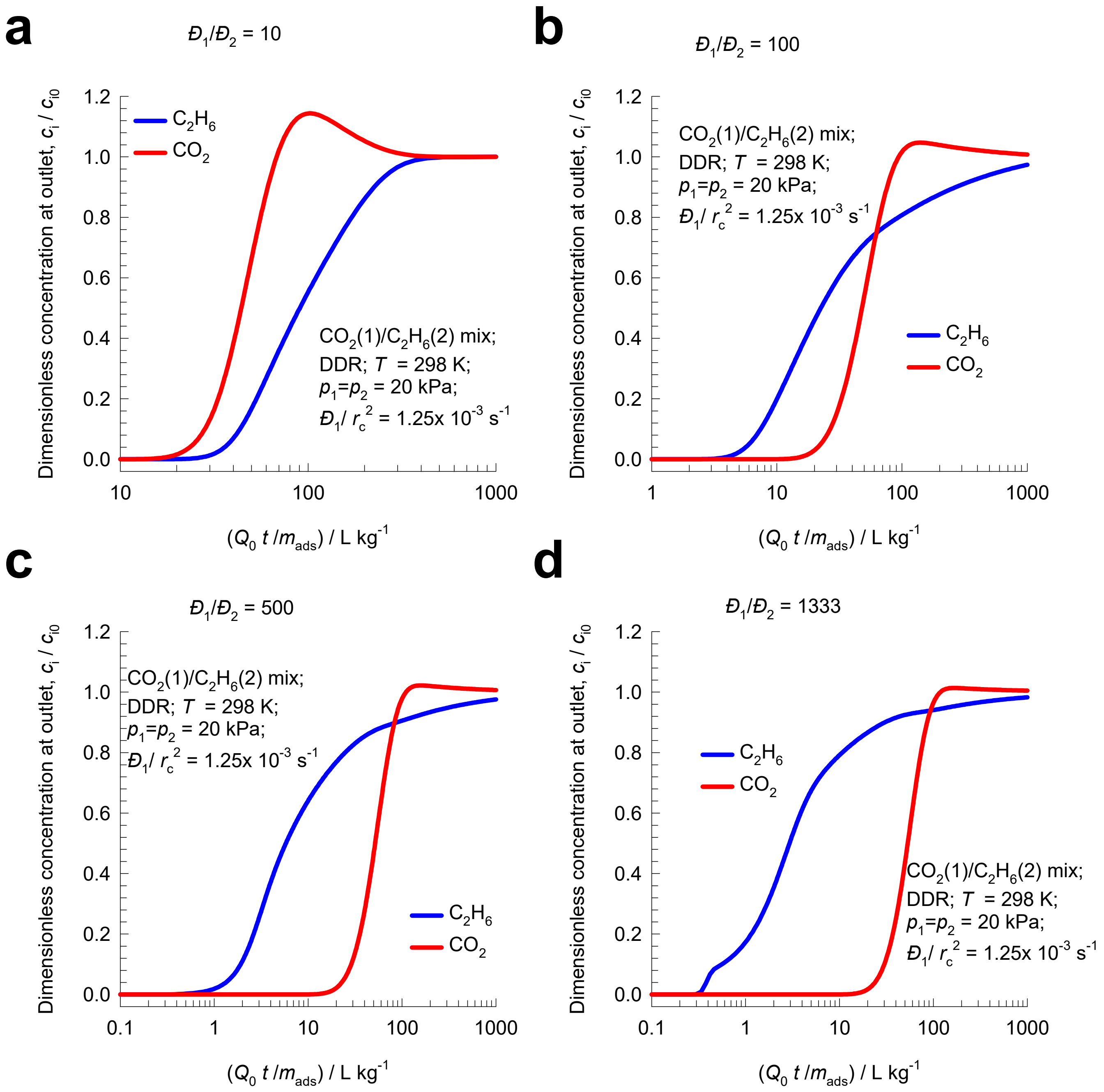

Figure S33. Influence of the ratio of Maxwell-Stefan diffusivities, $Đ_1/Đ_2$, on transient breakthrough simulations for the adsorption cycle for 50/50 $CO_2(1)/C_2H_6(2)$ mixture in fixed bed packed with DDR zeolite crystals at 298 K; the partial pressures in the bulk gas phase feed mixture are $p_1 = p_2 = 20$ kPa. In these simulations the bed voidage $\varepsilon = 0.4$, bed length $L = 0.3$ m, the ratio of M-S diffusivities are

$Đ_1/Đ_2=1333$, the interstitial velocities $v=0.1$ m s^{-1}; $\left(Đ_1/r_c^2\right)=1.25\times10^{-3}$ s $^{-1}$ the contact time $L/v=3$ s. The ratio of Maxwell-Stefan diffusivities is varied: $Đ_1/Đ_2=10,100,500,1333$.

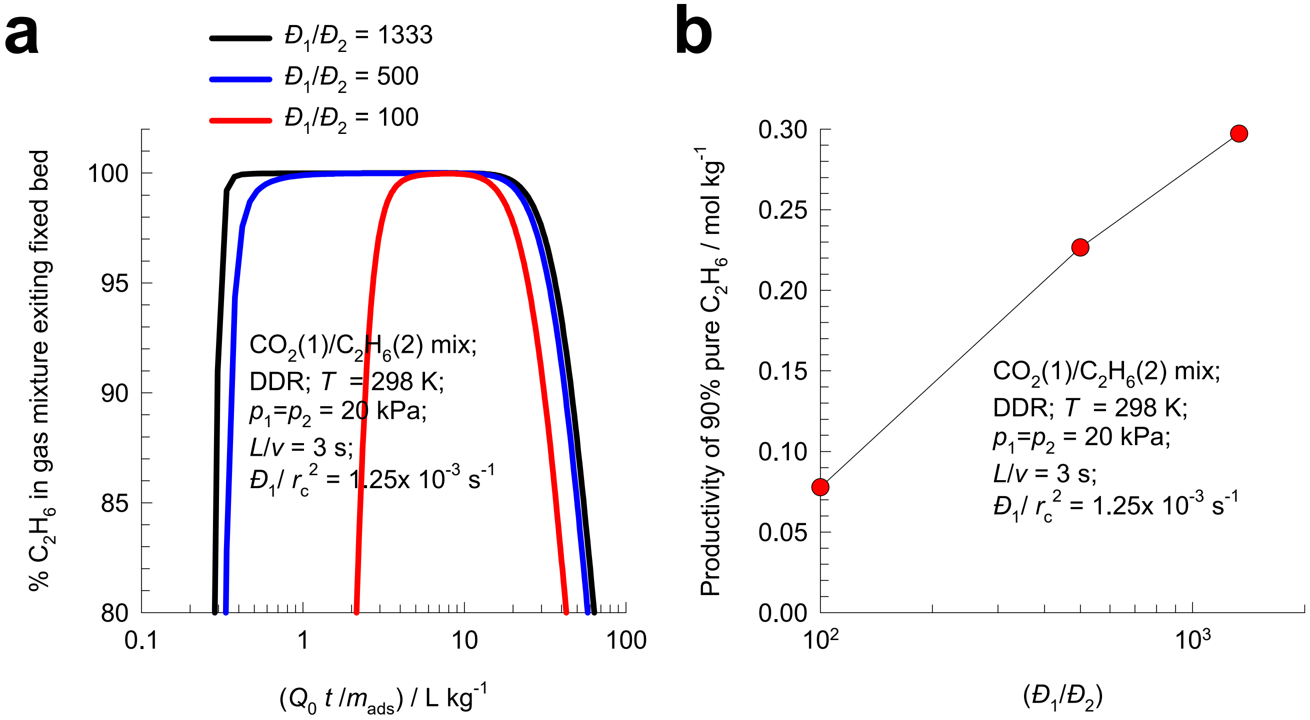

Figure S34. (a, b) Influence of the ratio of Maxwell-Stefan diffusivities, $Đ_1/Đ_2$, on the productivity of purified C_2H_6(2) for the adsorption cycle for 50/50 CO_2(1)/C_2H_6(2) mixture in fixed bed packed with DDR zeolite crystals at 298 K; the partial pressures in the bulk gas phase feed mixture are $p_1 = p_2 = 20$ kPa. (a) The % C_2H_6 at the adsorber outlet is plotted as a function of $\frac{Q_0 t}{m_{ads}} = \text{L kg}^{-1}$. (b) The productivity of purified C_2H_6(2), containing less than 10% CO_2, plotted as ratio of Maxwell-Stefan diffusivities, $Đ_1/Đ_2$.

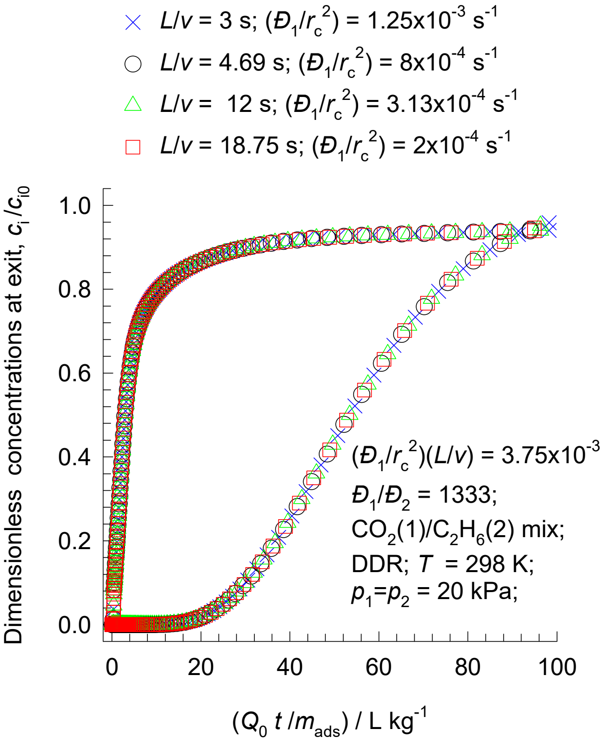

Figure S35. Transient breakthrough simulations for the adsorption cycle for 50/50 $CO_2(1)/C_2H_6(2)$ mixture in fixed bed packed with DDR zeolite crystals at 298 K; the partial pressures in the bulk gas phase feed mixture are $p_1 = p_2 = 20$ kPa. In these sets of simulations the interstitial velocities are varied such that the contact times are $L/v = 3, 4.69, 12, 18.75 \quad \text{s}$; the diffusional constants $\left(Đ_1/r_c^2\right)$ are adjusted such that $\left(Đ_1/r_c^2\right)\left(L/v\right) = 3.75\times10^{-3}$; $Đ_1/Đ_2 = 1333$..

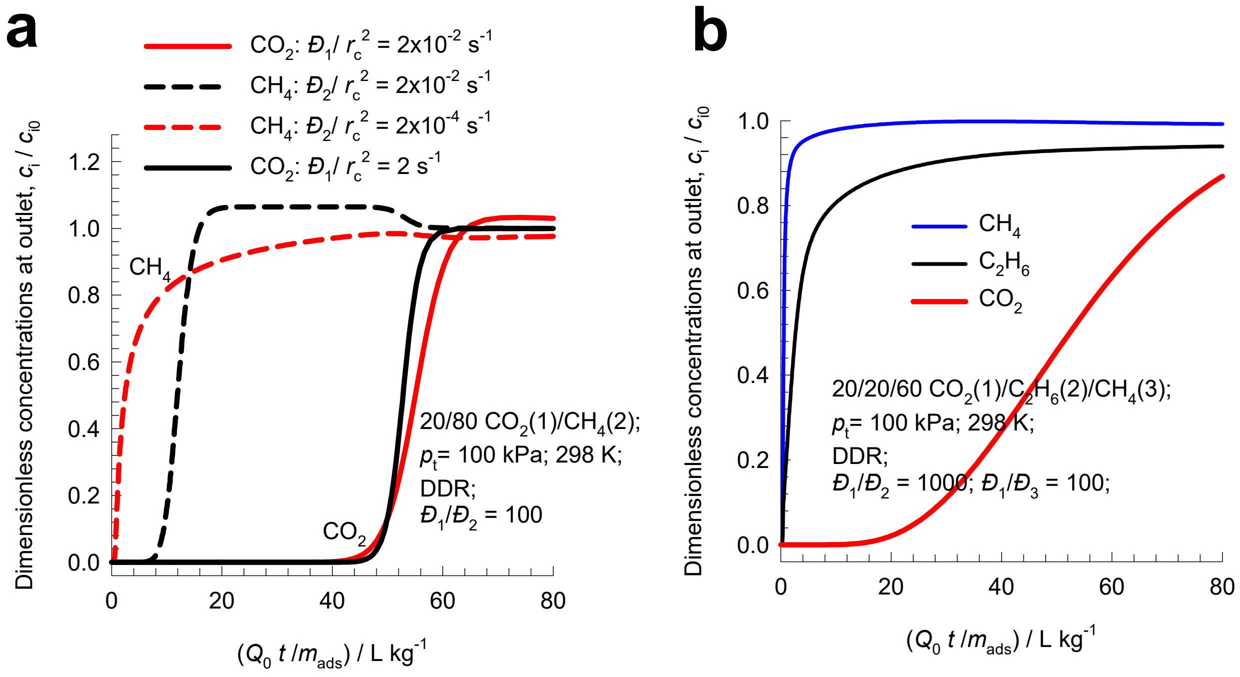

Figure S36. (a) Transient breakthrough of 20/80 $CO_2(1)/CH_4(2)$ mixtures through fixed bed adsorber packed with DDR crystals operating at 298 K, and total pressure p_t = 100 kPa. (b) Transient breakthrough of 20/20/60 $CO_2(1)$/ $C_2H_6(2)/CH_4(3)$ mixtures through fixed bed adsorber packed with DDR crystals operating at 298 K, and total pressure p_t = 100 kPa.

6 Separation of C_2H_2/CO_2 mixtures

Ethyne (C_2H_2) is an important building block in industrial chemical synthesis and also widely used as a fuel in welding equipment. C_2H_2 is commonly manufactured by the partial combustion of CH_4 or comes from cracking of hydrocarbons. In the reactor product, C_2H_2 co-exists with CO_2. Due to the similarity of molecular sizes and shapes (C_2H_2: 3.32 × 3.34 × 5.7 $Å^3$; CO_2: 3.18 × 3.33 × 5.36 $Å^3$), the separation of C_2H_2/CO_2 mixtures is particularly challenging;[73, 74] both molecules possess zero dipole moments and approximately the same quadrupole moment. Since the boiling points of C_2H_2 (189.3 K) and CO_2 (194.7 K) are close, distillation separations need to operate at cryogenic temperatures and high pressures. For separation of $C_2H_2(1)/CO_2(2)$ mixtures, most of the suggested MOFs such as HOF-3,[75] TIFSIX-2-Cu-i,[76] TIFSIX-2-Ni-i,[77] UTSA-74,[78] FJU-90,[79] FeNi-M'MOF,[80] BSF-3,[81] CPL-1-NH_2,[82] ZNU-1,[83] and Cu^I@UiO-66-$(COOH)_2$[84] and are selective to C_2H_2. Consequently, the desired ethyne product can be recovered in the desorption cycle. MOFs that have adsorption selectivity in favor of CO_2 include ZU-610a, [85] Ce(IV)-MIL-140-4F, [86] and Y-bptc[87]. Figure S37a compares experimental data for transient breakthroughs of 50/50 $C_2H_2(1)/CO_2(2)$ mixtures in ZU-610a, [85] Ce(IV)-MIL-140-4F, [86] and Y-bptc[87] operating at 298 K, and total pressure p_t = 100 kPa. The published experimental data for dimensionless concentrations at the exit of the adsorber, c_i/c_{i0} , are plotted as a function of a modified time parameter defined by Q_0t/m_{ads} . The relative productivity values for pure C_2H_2 are indicated by the length of the arrows. This comparison shows that the best separation performance, in terms of C_2H_2 productivity is afforded by the ultra-microporous Y-bptc;[87] we examine further the good separation performance of this MOF.

Figure S37b compares the experimental breakthroughs for Ce(IV)-MIL-140-4F, [86] with simulations ignoring diffusional influences; the unary isotherm data for Ce(IV)-MIL-140-4F are provided in Table

S10. We note that the experiments indicate higher productivity for purified C_2H_2 than the simulations ignoring diffusional influences.

The unary isotherm data for the unary guests in Y-bptc are fitted with the 1-site Langmuir parameter fits; the parameters are specified in Table S8.The adsorption selectivity $S_{ads} \approx 3.75$, in favor of CO_2. Figure S37c compares the experimental breakthroughs for Y-bptc[87] with simulations ignoring diffusional influences. Figure S37d compares the experimental breakthroughs for ZU-610a[85] with simulations ignoring diffusional influences; the unary isotherm data for ZU-610a are provided in Table S9. We note that the experiments indicate higher productivity for purified C_2H_2 than the simulations ignoring diffusional influences. We now quantify the adsorption-diffusion synergy in Y-bptc.

The experimental data on transient unary uptakes of $C_2H_2(1)$, and $CO_2(2)$ mixtures in Y-bptc as reported in the paper by He et al.[87] at a total pressure is 100 kPa are presented in Figure S38. We note that CO_2 attains equilibrium more rapidly than C_2H_2. We have synergy between adsorption and diffusion, both favor CO_2.

Figure S39a presents calculations of the elements of the matrix of thermodynamic correction factors as a function of total bulk gas pressure, p_t, calculated using the mixed-gas Langmuir model for 50/50 $C_2H_2(1)/CO_2(2)$ mixtures adsorption in Y-bptc at 298 K. Figure S39b presents calculations of the ratios Γ_{12}/Γ_{11}, Γ_{21}/Γ_{22} as a function of total bulk gas pressure, p_t, These calculations show that the off-diagonal elements are significant fractions of the diagonal elements. Figure S39c shows simulations of the transient uptake of unary guests $C_2H_2(1)$ and $CO_2(2)$ for Y-bptc crystals exposed to bulk gas pressures of 100 kPa. These unary uptake simulations, with $Đ_1/r_c^2 = 4.25\times10^{-6}\,\Gamma_{ij}$ s^{-1}, and with $Đ_2/r_c^2 = 4.85\times10^{-4}$ s^{-1} are in good agreement with the experimental data on unary uptakes presented in Figure S37b. The diffusion selectivity, determined experimentally from unary uptakes,[87] $Đ_2/Đ_1 \approx 114$, also favors CO_2.

Figure S39d presents simulations of transient uptake of 50/50 $C_2H_2(1)/CO_2(2)$ mixtures in Y-bptc crystals operating at 298 K, and total pressure p_t = 100 kPa. We note that there is an overshoot in the loading of the more mobile CO_2 as it approaches equilibrium.

Figure S40a shows transient breakthrough of 50/50 $C_2H_2(1)/CO_2(2)$ mixtures through fixed bed adsorber packed with Y-bptc crystals operating at 298 K, and total pressure p_t = 100 kPa. The dimensionless concentrations at the exit of the adsorber, c_i/c_{i0}, are plotted as a function of a modified time parameter defined by $Q_0 t/m_{ads}$. For the four sets of simulations $Đ_1/r_c^2$ = $4.25\times10^{-6}, 1.18\times10^{-5}, 4.72\times10^{-5}, 4.25\times10^{-4}$ s^{-1}, maintaining the ratio $Đ_2/Đ_1=114$, as determined experimentally[87]. With lower values of the diffusional constants $Đ_1/r_c^2$, i.e. stronger diffusional influences, the breakthrough of the desired product C_2H_2 occurs earlier, resulting in higher productivity of purified C_2H_2 per kg of adsorbent in bed. In Figure S40b, the productivities of 99%+pure C_2H_2 is plotted as a function of $Đ_1/r_c^2$. We note that with decreasing $Đ_1/r_c^2$ the C_2H_2 productivities increase from 1.05 to 1.35 mol kg^{-1}.

In the sets of breakthrough simulations in Figure S40c we maintain $Đ_1/r_c^2$ = 1.18×10^{-5} s^{-1}, with varying ratios of diffusivities of CO_2 to C_2H_2: $Đ_2/Đ_1 = 200, 114, 50, 10, 2$. We note that with increasing values of $Đ_2/Đ_1$, the C_2H_2 productivities increase from 0.1 to 1.35 mol kg^{-1}; see Figure S40d. We conclude that both $Đ_1/r_c^2$, and $Đ_2/Đ_1$ have a significant impact on the productivities of purified C_2H_2. From the breakthrough experiments of He et al., [87] for Y-bptc, with $Đ_2/Đ_1 = 114$, the C_2H_2 productivity is calculated to be 1.52 mol kg^{-1}, in reasonable agreement with the simulations.

6.1 List of Tables for Separation of C2H2/CO2 mixtures

Table S8. 1-site Langmuir parameters for C_2H_2 and CO_2 in Y-bptc at 298 K. These parameters have been fitted from the data scanned from Figure 2a of He et al.[87]

	$\frac{q_{sat}}{\text{mol kg}^{-1}}$	$\frac{b}{\text{Pa}^{-1}}$
C_2H_2	3.3	6.319E-06
CO_2	3.3	2.374E-05

Table S9. Dual-site Langmuir-Freundlich fits for C_2H_2 and CO_2 in ZU-610a. The readers are altered to the fact that the units of b_A, b_B are not properly reported in Table S4 of Cui et al.[85] The Table below contains the correct parameter values with proper units.

$$q = \frac{q_{sat,A} b_A p^{\nu A}}{1 + b_A p^{\nu A}} + \frac{q_{sat,B} b_B p^{\nu B}}{1 + b_B p^{\nu B}}$$

	Site A			Site B		
	$\frac{q_{A.sat}}{\text{mol kg}^{-1}}$	$\frac{b_A}{\text{Pa}^{-\nu_A}}$	ν_A	$\frac{q_{B.sat}}{\text{mol kg}^{-1}}$	$\frac{b_B}{\text{Pa}^{-\nu_B}}$	ν_B
C_2H_2	0.0368	5.196E-84	28.69	0.184	3.108E-03	0.575
CO_2	0.144	1.690E-16	3.18	2.1	2.040E-05	1

Table S10. Dual-site Langmuir-Freundlich parameter fits for C_2H_2, and CO_2 in Ce(IV)-MIL-140-4F at 298 K. $q = \frac{q_{sat,A} b_A p^{\nu A}}{1 + b_A p^{\nu A}} + \frac{q_{sat,B} b_B p^{\nu B}}{1 + b_B p^{\nu B}}$

	Site A			Site B		
	$\frac{q_{A,sat}}{\text{mol kg}^{-1}}$	$\frac{b_A}{\text{Pa}^{-\nu_A}}$	ν_A	$\frac{q_{B,sat}}{\text{mol kg}^{-1}}$	$\frac{b_B}{\text{Pa}^{-\nu_A}}$	ν_B
C_2H_2	0.35	3.904E-06	1	1.4	1.138E-05	1
CO_2	1.6	2.025E-05	1	1.2	2.104E-19	4.6

6.2 List of Figures for Separation of C2H2/CO2 mixtures

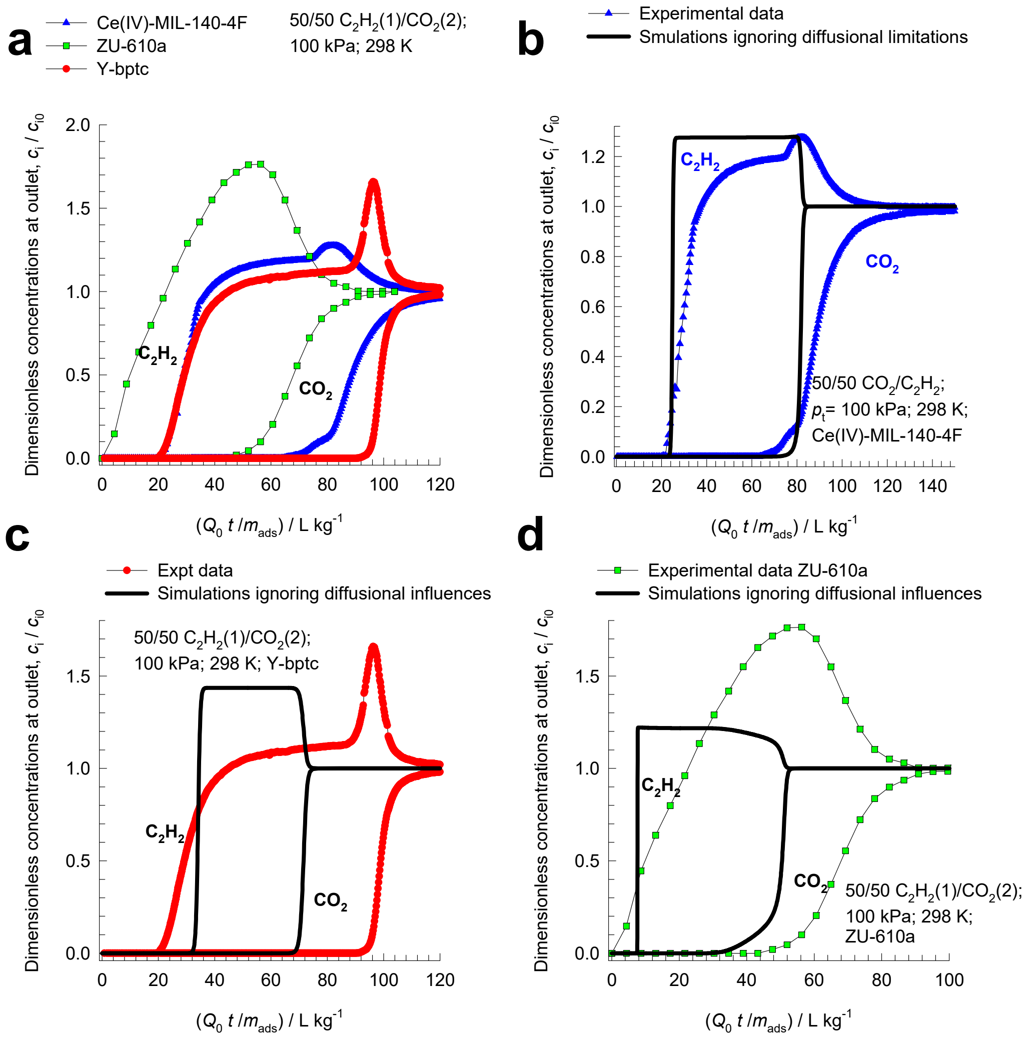

Figure S37. (a) Comparison of experimental data for transient breakthroughs of 50/50 C_2H_2(1)/CO_2(2) mixtures in ZU-610a,[85] Ce(IV)-MIL-140-4F, [86] and Y-bptc[87] operating at 298 K, and total pressure p_t = 100 kPa. The published experimental data for dimensionless concentrations at the exit of the adsorber, c_i/c_{i0}, are plotted as a function of a modified time parameter defined by Q_0t/m_{ads}. (b) Comparison of experimental breakthroughs for Ce(IV)-MIL-140-4F[86] with simulations ignoring diffusional influences. (c) Comparison of experimental breakthroughs for Y-bptc[87] with simulations ignoring diffusional influences. (d) Comparison of experimental breakthroughs for ZU-610a[85] with simulations ignoring diffusional influences.

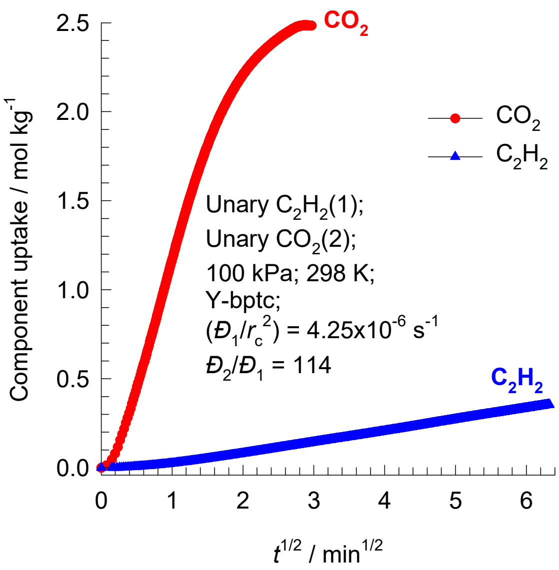

Figure S38. Transient unary uptakes of C$_2$H$_2$(1), and CO$_2$(2) mixtures in Y-bptc; the total pressure is 100 kPa.

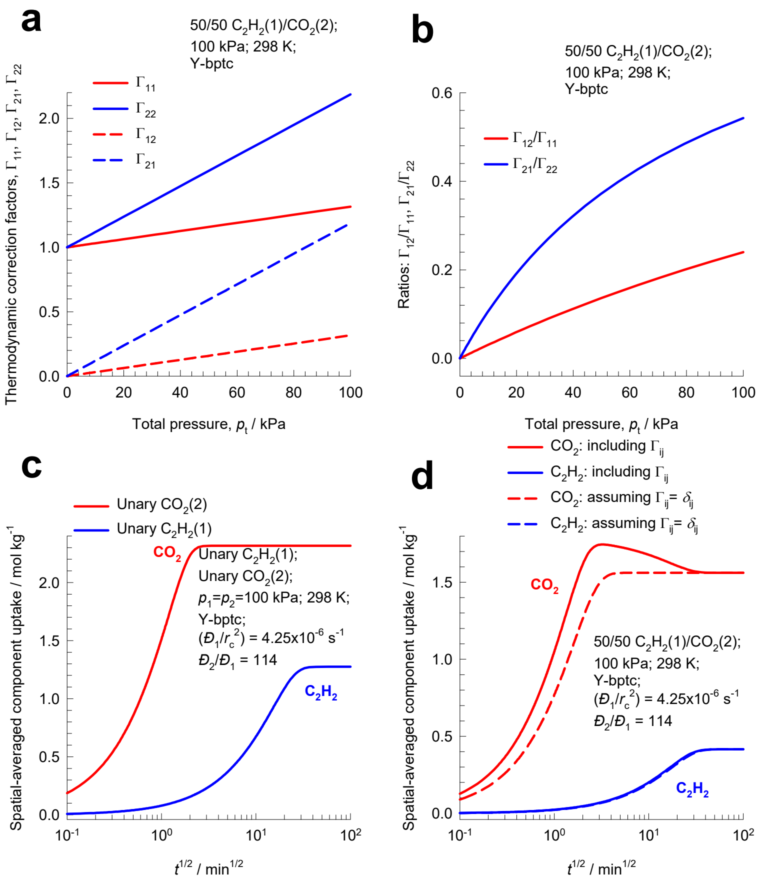

Figure S39. (a) Elements of the matrix of thermodynamic correction factors Γ_{ij} as a function of total bulk gas pressure, p_t, calculated using the mixed-gas Langmuir model for 50/50 C_2H_2(1)/CO_2(2) mixtures adsorption in Y-bptc at 298 K. (b) Calculations of the ratios Γ_{12}/Γ_{11}, Γ_{21}/Γ_{22} as a function of total bulk gas pressure, p_t, (c) Transient uptake of unary guests C_2H_2(1) and CO_2(2) for Y-bptc crystals exposed to bulk gas pressures of 100 kPa for either guests. (d) Transient uptake of 50/50 C_2H_2(1)/CO_2(2) mixtures in Y-bptc crystals operating at 298 K, and total pressure p_t = 100 kPa.

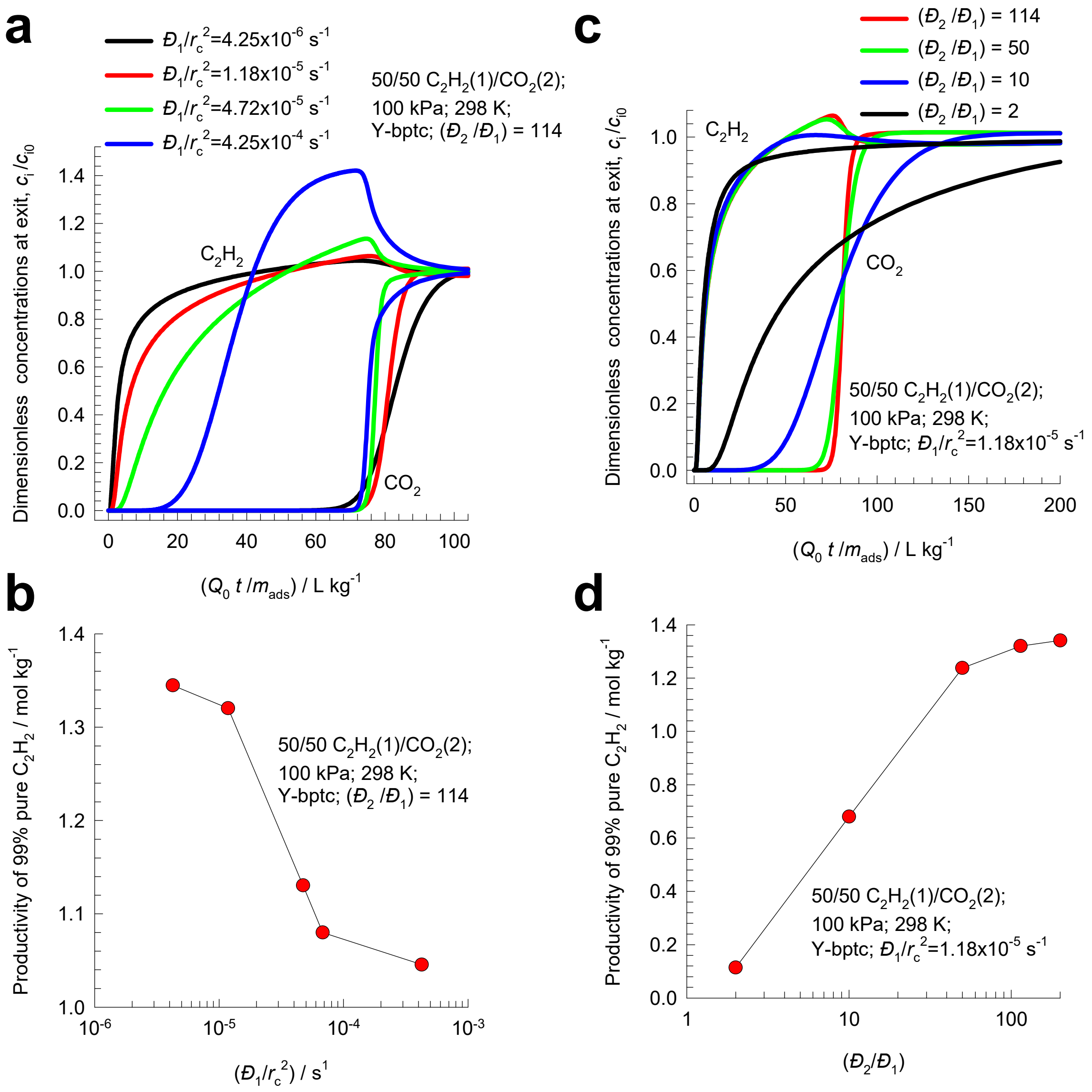

Figure S40. (a, b, c, d) Transient breakthrough of 50/50 C_2H_2(1)/CO_2(2) mixtures through fixed bed adsorber packed with Y-bptc crystals operating at 298 K, and total pressure p_t = 100 kPa. In the sets of simulations in (a, b): $Đ_1/r_c^2 = 4.25\times10^{-6}, 1.18\times10^{-5}, 4.72\times10^{-5}, 4.25\times10^{-4}$ s^{-1}, maintaining the ratio $Đ_2/Đ_1 = 114$. In the sets of simulations in (c, d): $Đ_1/r_c^2 = 1.18\times10^{-5}$ s^{-1}, and the ratio $Đ_2/Đ_1 = 200, 114, 50, 10, 2$. In (a, c), the dimensionless concentrations at the exit of the adsorber, c_i/c_{i0}, are plotted as a function of a modified time parameter defined by $Q_0 t/m_{ads}$. In (b, d), the C_2H_2 productivities are plotted as a function of (b) $Đ_1/r_c^2$, and (d) $Đ_2/Đ_1$.

7 Nitrogen Capture from Natural Gas Streams

Natural gas reserves often contain up to 20% N_2; reduction to values below 4% is required for meeting pipeline specifications.[88] Cryogenic distillation is the economic choice for large capacity wells but for smaller natural gas reserves, PSA separations become more cost-effective, especially because the feed mixtures are available at high pressures.[88, 89] The adsorbent materials in PSA units need to be selective to N_2, but for most available adsorbents, the adsorption selectivity is in favor of CH_4 due to its higher polarizability.

7.1 N_2/CH_4 separations with LTA-4A zeolite

The earliest study demonstrating the possibility of using LTA-4A zeolite, utilizing diffusion selectivities for separating N_2(1)/CH_4(2) mixtures is contained in the classic paper of Habgood.[18] LTA-4A zeolite (also called 4A or NaA zeolite) contains extra-framework cations (containing 96Si, 96 Al, 96 Na^+ per unit cell; Si/Al=1). LTA-4A zeolite consists of cages of 743 Å^3 volume, separated by 4.11 Å × 4.47 Å 8-ring windows. The pore landscape and structural details of LTA-4A zeolite are provided in Figure S41. The Na^+ cations partially block the window sites, leading to low magnitudes of guest diffusivities. The partial blocking of the windows enhances efficacy of kinetic separations, because it significantly enhances the ratio of the diffusivities of mobile and tardier species. Molecules jump one-at-a-time across the windows of LTA-4A. Extensive Molecular Dynamics (MD) simulations have confirmed that correlation effects are of negligible importance for mixture diffusion across cage-type zeolites such as CHA, LTA, DDR, ERI that consist of cages separated by windows in the 3.4 Å – 4.2 Å size range.[7-9, 17] Consequently, the appropriate flux description is provided by eq (S21).

Habgood[18] performed experimental data on transient uptake of N_2(1)/CH_4(2) mixtures in crystallites of LTA-4A; the data measured at 194 K with partial pressures p_1 =50.9 kPa; p_2 = 49.1 kPa are shown in Figure S42a.The experimental data on the spatial averaged component loadings are plotted as a function of the Fourier number, $Đ_1 t / r_c^2$. Nitrogen is a “pencil-like” molecule (4.4 Å × 3.3 Å) that can hop lengthwise across the narrow windows; see computational snapshots in Figure S43. The "spherical" CH_4 (3.7 Å) is much more severely constrained and has a diffusivity that is 21.7 times lower than that of N_2. The adsorption strength of CH_4, as reflected in the Langmuir "*b*" parameter, is higher than that of N_2 by a factor 2.2; see unary isotherm data fits in Table S11. The $N_2(1)/CH_4(2)$ mixture constitutes a combination of more-mobile-less-strongly-adsorbed-N_2 and tardier-more-strongly-adsorbed-CH_4. During the initial stages of the transient uptake, the pores of LTA-4A are predominantly richer in the more mobile N_2, but this is displaced by the more strongly adsorbed, tardier CH_4 molecules at longer times. This results in an overshoot in the N_2 uptake in both the experimental campaigns.

For video animations of the jumping of nitrogen and methane across the narrow windows of LTA-4A, watch **N2/CH4 Separations with LTA-4A** on YouTube

https://www.youtube.com/@rajamanikrishna250/videos

The continuous solid lines in Figure S42a are Maxwell-Stefan model simulations based are simulations based on eq (S22). The Maxwell-Stefan diffusivities used in the simulations are: $Đ_1/r_c^2 = 1.56\times10^{-5}$ s^{-1}; $Đ_1/Đ_2 = 21.7$; these values based on the diffusivity data provided by Habgood.[18] The dashed lines are the simulations based on eq (S23), in which the thermodynamic correction factors are assumed to be described by $\Gamma_{ij} = \delta_{ij}$, the Kronecker delta; in this scenario, no N_2 overshoot is experienced. We conclude that the overshoots in the N_2 uptake, that signal the phenomenon of uphill diffusion,[12, 41] is engendered by thermodynamic coupling effects.

Figure S42b is a plot of the transient uptake selectivity, defined by $\frac{\overline{q}_1(t)/\overline{q}_2(t)}{p_{10}/p_{20}}$ as a function of $\sqrt{Đ_i t/r_c^2}$. As $t\rightarrow\infty$, the uptake selectivity will approach the value of the adsorption selectivity $\frac{q_1^*/q_2^*}{p_{10}/p_{20}}$. From the unary Langmuir isotherm parameters in Table S11, we calculate the equilibrium adsorption selectivity $\frac{q_1^*/q_2^*}{p_{10}/p_{20}} = \frac{b_1}{b_2} = 0.451$. Readers should note that the ratio $\frac{b_1}{b_2}$ should be replaced by the ratio of

Henry constants, $\frac{q_{sat,1}}{q_{sat,2}}\frac{b_1}{b_2}$, in case the saturation capacities of components 1 and 2 are unequal. At short contact times, the transient uptake selectivity is strongly in favor of the more mobile nitrogen. If thermodynamic coupling effects are ignored, and the Maxwell-Stefan diffusivities are assumed to be independent of loading, the following simplified expression can be derived for the transient uptake selectivity as the product of the adsorption equilibrium selectivity and the diffusion selectivity[22, 90]

$$\frac{\overline{q}_1(t)/\overline{q}_2(t)}{p_{10}/p_{20}}=\frac{b_1}{b_2}\sqrt{\frac{Đ_1}{Đ_2}} \tag{S52}$$

Readers should note that the ratio $\frac{b_1}{b_2}$ should be replaced by the ratio of Henry constants, $\frac{q_{sat,1}}{q_{sat,2}}\frac{b_1}{b_2}$, in case the saturation capacities of components 1 and 2 are unequal. We note that the uptake selectivity in favor of nitrogen is significantly enhanced due to the influence of Γ_{ij}.

Based on his experimental results for transient uptake, Habgood filed a patent claiming that natural gas could be upgraded by removing the faster diffusing nitrogen using 4A zeolite and a kinetically controlled separation process at sub-ambient temperatures. We now investigate the consequence of thermodynamic coupling and uphill diffusion on N_2(1)/CH_4(2) mixture separations in a fixed bed adsorber packed with LTA-4A adsorbent.

7.2 Analysis of N_2/CH_4 mixture uptake in LTA-4A

For 40.9/49.1 N_2(1)/CH_4(2) gas mixtures within crystals of LTA-4a zeolite at 194 K, at a total pressure $p_t = p_1 + p_2 = 100$ kPa, the elements of the $[\Gamma]$ are $\begin{bmatrix}\Gamma_{11} & \Gamma_{12}\\ \Gamma_{21} & \Gamma_{22}\end{bmatrix}=\begin{bmatrix}5.785 & 4.785\\ 10.213 & 11.213\end{bmatrix}$. The Fick diffusivity matrix is calculated to be $\frac{\begin{bmatrix}D_{11} & D_{12}\\ D_{21} & D_{22}\end{bmatrix}}{r_c^2}=\begin{bmatrix}90.24 & 74.64\\ 7.353 & 8.073\end{bmatrix}\times 10^{-6} \quad \mathrm{s}^{-1}$.

The continuous solid lines in Figure S44a,b are the numerical solutions for transient uptake using the M-S diffusion eq (S21). The dashed lines in Figure S44a are the solutions invoking the simplified eq (S23), Use of the LDF model, eq (S39), results in the dashed lines shown in Figure S44b.

7.3 Separation of N_2/CH_4 mixtures in fixed bed adsorber

Let us analyze the separations of 20/80 $N_2(1)/CH_4(2)$ mixtures in a fixed bed adsorber using LTA-4A zeolite operating at a total pressure of 100 kPa, and T = 194 K. Figure S45a presents calculations of the elements of the matrix of thermodynamic correction factors Γ_{ij} as a function of total bulk gas pressure, p_t, calculated using the mixed-gas Langmuir model for 20/80 $N_2(1)/CH_4(2)$ mixtures in LTA-4A zeolite at 194 K. Figure S45b presents calculations of the ratios $\Gamma_{12}/\Gamma_{11}, \Gamma_{21}/\Gamma_{22}$ as a function of total bulk gas pressure, p_t,

Figure S46a presents simulations of transient uptake of 20/80 $N_2(1)/CH_4(2)$ mixtures in crystallites of LTA-4A at 194 K with the bulk gas phase maintained at partial pressures p_1 =20 kPa; p_2 = 80 kPa. Nitrogen is a "pencil-like" molecule (4.4 Å × 3.3 Å) that can hop length-wise across the narrow windows; the "spherical" CH_4 (3.7 Å) is much more severely constrained and has a diffusivity that is 21.7 times lower than that of N_2. The adsorption strength of CH_4, as reflected in the Langmuir "b" parameter, is higher than that of N_2 by a factor 2.2; see unary isotherm data fits in Table S11. The $N_2(1)/CH_4(2)$ mixture constitutes a combination of more-mobile-less-strongly-adsorbed-N_2 and tardier-more-strongly-adsorbed-CH_4. The continuous solid lines in Figure S46a are Maxwell-Stefan model simulations based on eq (S21); these simulations display an overshoot in the uptake of the more mobile N_2. The Maxwell-Stefan diffusivities used in the simulations are: $Đ_1/r_c^2$ = 1.56×10^{-5} s^{-1}; $Đ_2/r_c^2$ = 7.2×10^{-9} s^{-1}; these values based on the diffusivity data provided by Habgood.[18] During the initial stages of the transient uptake, the pores of LTA-4A are predominantly richer in the more mobile N_2, but this is displaced by the more strongly adsorbed, tardier CH_4 molecules at longer times. This results in an overshoot in the N_2 uptake during the early stages of the transience. The dashed lines in Figure S46a are the simulations based on eq (S23), in which the thermodynamic correction factors are assumed to be described by $\Gamma_{ij} = \delta_{ij}$, i.e.

$\begin{bmatrix} \Gamma_{11} & \Gamma_{12} \\ \Gamma_{21} & \Gamma_{21} \end{bmatrix} = \begin{bmatrix} 1 & 0 \\ 0 & 1 \end{bmatrix}$; in this scenario, no N_2 overshoot is experienced. We conclude that the overshoots in the N_2 uptake, that signal the phenomenon of uphill diffusion,[12, 41] is engendered by thermodynamic coupling effects.

Figure S46b presents simulations of transient desorption process in which the initial loadings in the zeolite correspond to the final equilibrated loadings Figure S46a, i.e. corresponding to the bulk gas phase maintained at partial pressures p_1 =20 kPa; p_2 = 80 kPa. At time t = 0, the bulk gas phase partial pressures are reduced to the values p_1 =2 kPa; p_2 = 8 kPa. The continuous solid lines in Figure S46b are Maxwell-Stefan model simulations based on eq (S21); these simulations show undershoot in the desorption of the mobile N_2. The dashed lines in Figure S46b are the simulations based on eq (S23), in which the thermodynamic correction factors are assumed to be described by $\Gamma_{ij} = \delta_{ij}$, i.e. $\begin{bmatrix} \Gamma_{11} & \Gamma_{12} \\ \Gamma_{21} & \Gamma_{21} \end{bmatrix} = \begin{bmatrix} 1 & 0 \\ 0 & 1 \end{bmatrix}$; in this scenario, no N_2 undershoot is experienced. We conclude that the undershoot in the N_2 uptake, that signal the phenomenon of uphill diffusion,[12, 41] is engendered by thermodynamic coupling effects.

Overshoots/undershoots during the adsorption/desorption phase of PSA operations have consequences for N_2(1)/CH_4(2) mixture separations in a fixed bed adsorber packed with LTA-4A adsorbent.

Figure S47a show the transient breakthrough simulations for 20/80 N_2(1)/CH_4(2) mixtures through fixed bed adsorber packed with LTA-4A crystals operating at 194 K, and total pressure p_t = 100 kPa. The y-axis is the % CH_4 at the adsorber outlet. The x-axis is $Q_0 t / m_{ads}$, where Q_0 is the volumetric flow rate of the gas mixture at the inlet to the fixed bed at actual temperature and pressure conditions. The continuous black lines are simulations taking due account of intra-crystalline diffusion using eq (S22) with parameters: $Đ_1 / r_c^2 = 1.56 \times 10^{-5}$ s^{-1}; $Đ_1 / Đ_2 = 21.7$. The blue lines are the corresponding simulations based on eq (S23), in which the thermodynamic correction factors are assumed to be described by $\Gamma_{ij} = \delta_{ij}$, the Kronecker delta. For the target CH_4 purity of say 96% we can determine the moles of 96%+ pure CH_4 produced from a material balance on the adsorber. Expressed per kg of LTA-4A zeolite in the packed bed, the respective productivities are 0.93 and 0.11 mol kg^{-1}, with 96%+ purity. Ignoring thermodynamic coupling effects severely underestimates the CH_4 productivity

Having established the importance of including the thermodynamic correction factors in PSA simulations, we proceed to examine the influence of the severity of diffusional limitations. Figure S47b compares the transient breakthrough simulations for 20/80 N_2(1)/CH_4(2) mixtures through fixed bed adsorber packed with LTA-4A for two different scenarios: $Đ_1/r_c^2 = 1.56\times10^{-5}$ s^{-1}; $Đ_1/r_c^2 = 6.09\times10^{-6}$ s^{-1} ; for both scenarios we maintain $Đ_1/Đ_2 = 21.7$, and include the thermodynamic coupling influences. Expressed per kg of LTA-4A zeolite in the packed bed, the respective productivities are 0.93 and 1.62 mol kg^{-1} mol kg^{-1}, with 96%+ purity. More severe diffusional limitations, signified by lower value of $Đ_1/r_c^2$ results in higher CH_4 productivity. Indeed, if the diffusional severity is diminished, kinetic separations are not achievable.

In Figure S47c,d the same sets of data in Figure S47a,b are plotted using the dimensionless concentrations in the gas phase exiting the adsorber, c_i/c_{i0} , as *y*-axes.

7.4 Influence of temperature on kinetic N_2/CH_4 separations

The experimental data and simulations presented in the foregoing section was for a temperature of 194 K. We know examine the influence of increasing temperature on separations of 20/80 N_2(1)/CH_4(2) mixtures using LTA-4A. The unary isotherm data at 194 K and 273 K from the paper by Habgood, [18] combined with the unary isotherm data of Wilkins and Rajendran,[91] measured at 303 K, 323 K, and 343 K were fitted with the temperature-dependent 1-site Langmuir model $q = \frac{q_{sat}bp}{1+b_A p}$; $b = b_0 \exp\left(\frac{E}{RT}\right)$. The fit parameters are provided in Table S12. The goodness of the combined fits is demonstrated in Figure S48 in which the component loadings are plotted against the surface potential $\Phi \equiv \frac{\pi A}{RT} = \int\limits_{f=0}^{P} \frac{q(f)}{f} df = q_{sat} \ln\left(1+bP\right)$; for details of the concept of surface potential refer to Krishna and van Baten.[71]

The diffusivity data for N2(1) and CH4(2) in LTA-4A are reported by Habgood[18] and Wilkins and Rajendran,[91] for a range of temperatures; the combined data set may be fitted with $Đ_1/r_c^2 = A_1 \exp\left(-E_1/RT\right); \quad Đ_2/r_c^2 = A_2 \exp\left(-E_2/RT\right)$ with $A_1 = 38.15$ s^{-1}; $E_1 = 20.86$ kJ mol^{-1} for N2 and $A_2 = 6.418$ s^{-1}; $E_2 = 22.93$ kJ mol^{-1} for CH4.

With the *T*-dependent fits of unary isotherms, and diffusivities we can determine (a) adsorption selectivity, $\frac{b_1}{b_2}$, (b) diffusion selectivity, $\frac{Đ_1}{Đ_2}$, and (c) kinetic selectivity, $\frac{b_1}{b_2}\sqrt{\frac{Đ_1}{Đ_2}}$. These data are plotted in Figure S49 (see left *y*-axis values). We note that all three selectivities decrease, albeit slightly with increasing temperatures. Also plotted on the right *y*-axes in Figure S49 are the values of $Đ_1/r_c^2$. We note there is a significant increase in $Đ_1/r_c^2$ with increasing *T*, implying that the severity of diffusion influences diminishes at higher temperature. Indeed, kinetic separations with LTA-4A are not realizable at temperatures in excess of about 220 K.

Another material that affords kinetic separations of N2(1)/CH4(2) mixtures Ba-RPZ (= Ba exchanged reduced pore Zorite); the unary data on isotherms and diffusivities are presented by Wilkins and Rajendran.[91] The unary isotherm data of Wilkins and Rajendran,[91] measured at three different temperatures may be fitted with the temperature-dependent 1-site Langmuir model $q = \frac{q_{sat} bp}{1 + b_A p}; \quad b = b_0 \exp\left(\frac{E}{RT}\right)$. The fit parameters are provided in Table S13. The goodness of the combined fits is demonstrated in Figure S50 in which the component loadings are plotted against the surface potential $\Phi \equiv \frac{\pi A}{RT} = \int\limits_{f=0}^{P} \frac{q(f)}{f} df = q_{sat} \ln\left(1 + bP\right)$; for details of the concept of surface potential refer to Krishna and van Baten.[71]

The diffusivity data for N2(1) and CH4(2) in Ba-RPZ are reported by Wilkins and Rajendran,[91] for a range of temperatures; the data set were fitted with

$Đ_1/r_c^2 = A_1 \exp\left(-E_1/RT\right)$; $Đ_2/r_c^2 = A_2 \exp\left(-E_2/RT\right)$ with $A_1 = 536.6$ s^{-1}; $E_1 = 25.77$ kJ mol^{-1} for N_2 and $A_2 = 4.498$ s^{-1}; $E_2 = 30.46$ kJ mol^{-1} for CH_4.

With the T-dependent fits of unary isotherms, and diffusivities we can determine (a) adsorption selectivity, $\frac{b_1}{b_2}$, (b) diffusion selectivity, $\frac{Đ_1}{Đ_2}$, and (c) kinetic selectivity, $\frac{b_1}{b_2}\sqrt{\frac{Đ_1}{Đ_2}}$. These data are plotted in Figure S51 (see left y-axis values). We note that all three selectivities decrease with increasing temperatures. Also plotted on the right y-axes in Figure S51b are the values of $Đ_1/r_c^2$. We note there is a significant increase in $Đ_1/r_c^2$ with increasing T, implying that the severity of diffusion influences diminishes at higher temperature. Kinetic separations with Ba-RPZ are not realizable at temperatures in excess of about 273 K.

Figure S52 shows the transient uptake of 20/80 N_2(1)/CH_4(2) mixture in Ba-RPZ crystals operating at 273 K, and total pressure p_t = 100 kPa. The overshoot in the N_2 loading signifies uphill diffusion.

Watch also **N2/CH4 Separations with Ba-RPZ** on YouTube

https://www.youtube.com/@rajamanikrishna250/videos

7.5 N_2/CH_4 separations with Ba-ETS-4

Ba-ETS-4 (ETS = Engelhard Titano-silicate; ETS-4 is also named as CTS-1 = Contracted Titano Silicate -1) with pore size ≈ 3.7 Å effectively exclude the spherical CH_4 molecule (3.7 Å) while allowing entry for the pencil-like nitrogen molecule (4.4 Å × 3.3 Å).[18, 88, 90, 92, 93] The process background is described in detail by Bhadra and Farooq.[88, 94]

Watch also **N2/CH4 Separations with Ba-ETS-4** on YouTube

https://www.youtube.com/@rajamanikrishna250/videos

The transient uptake data of Majumdar et al.[90] for Ba-ETS-4 are shown in Figure S53a,b for (a) 10/90, and (b) 50/50 mixtures show overshoots in the uptake of the more mobile N_2. To confirm these overshoots, we performed transient uptake simulations using the isotherm parameters reported in the thesis of Bhadra;[94] see Table S14. Figure S54a,b presents simulation of transient uptake of 20/80 $N_2(1)/CH_4(2)$ mixture inside crystallite of Ba-ETS-4. The input data on isotherms are taken from Table 3.2 of the PhD thesis of Bhadra.[94] The Maxwell-Stefan diffusivities used in the simulations are: $Đ_1/r_c^2 = 2.8\times 10^{-2}$ s^{-1}; $Đ_2/Đ_2 = 4180$, The surrounding bulk gas mixture is at 283 K, and total pressure p_t = 1 MPa. The *x*-axes represent the Fourier number $Đ_1 t/r_c^2$. The black lines are simulations based on eq (S22). The blue lines are the simulations based on eq (S23), in which the thermodynamic correction factors are described by $\Gamma_{ij} = \delta_{ij}$, the Kronecker delta. Inclusion of thermodynamic coupling effects causes uphill diffusion of N_2, resulting in significantly enhanced N_2/CH_4 uptake selectivities during the early stages of transience.

Let us analyze the separations of 20/80 $N_2(1)/CH_4(2)$ mixture in fixed bed adsorber packed with Ba-ETS-4, operating at 283 K, and total pressure p_t = 1 MPa. Figure S55a,b presents simulation results for transient breakthroughs; the black lines are simulations based on eq (S22). The blue lines are the simulations based on eq (S23) in which the thermodynamic correction factors are assumed to be described by $\Gamma_{ij} = \delta_{ij}$, the Kronecker delta. For the target CH_4 purity of say 96% we can determine the moles of 96%+ pure CH_4 produced from a material balance on the adsorber. Expressed per kg of Ba-ETS-4 in the packed bed, the respective productivities are 3.06 and 1.11 mol kg^{-1}. Ignoring thermodynamic coupling effects severely underestimates the CH_4 productivity.

7.6 List of Tables for Nitrogen Capture from Natural Gas Streams

Table S11. 1-site Langmuir parameters for N_2 and CH_4 in LTA-4A zeolite at 194 K. These parameters have been fitted from the isotherm data scanned from the paper by Habgood[18]

	$\frac{q_{sat}}{\text{mol kg}^{-1}}$	$\frac{b}{\text{Pa}^{-1}}$
N_2	3.6	9.403E-05
CH_4	3.6	2.084E-04

Table S12. Temperature-dependent 1-site Langmuir parameter fits for N_2 and CH_4 in LTA-4A zeolite. $q = \frac{q_{sat} bp}{1+bp}; \quad b = b_0 \exp\left(\frac{E}{RT}\right)$. These parameters have been fitted from the isotherm data at 194 K and 273 K from the paper by Habgood,[18] combined with the unary isotherm data of Wilkins and Rajendran,[91] measured at 303 K, 323 K, and 343 K. For CH_4, the Configurational-Bias Monte Carlo (CBMC) data are also included in the fits.

	$\frac{q_{sat}}{\text{mol kg}^{-1}}$	$\frac{b_0}{\text{Pa}^{-1}}$	$\frac{E}{\text{kJ mol}^{-1}}$
N_2	3.6	4.101E-10	19.9
CH_4	3.6	8.145E-10	20

Table S13. Temperature-dependent 1-site Langmuir parameter fits for N_2 and CH_4 in Ba-RPZ.

$q = \frac{q_{sat} b p}{1 + b_A p}; \quad b = b_0 \exp\left(\frac{E}{RT}\right)$. These parameters have been fitted using the unary isotherm data of Wilkins and Rajendran,[91] measured at three different temperatures.

	Site A		
	$\frac{q_{sat}}{\text{mol kg}^{-1}}$	$\frac{b_0}{\text{Pa}^{-1}}$	$\frac{E}{\text{kJ mol}^{-1}}$
N_2	0.8	5.125E-10	25.5
CH_4	0.8	5.309E-09	22.2

Table S14. Langmuir parameters for adsorption of CH_4, and N_2 in Ba-ETS-4 at 283.15 K. The isotherm parameters are taken from Table 3 of Majumdar et al.[90], and Table 3.2 of the Ph.D. dissertation of Bhadra.[94] The cited parameters are converted to the units that are consistent with the other data presented in our article. For conversion purposes, we use the framework density for BaETS-4 of 1720 kg m^{-3}.

	$\frac{q_{sat}}{\text{mol kg}^{-1}}$	$\frac{b}{\text{Pa}^{-1}}$
N_2	1.4	9.02E-06
CH_4	0.5	9.339E-06

7.7 List of Figures for Nitrogen Capture from Natural Gas Streams

LTA-4A

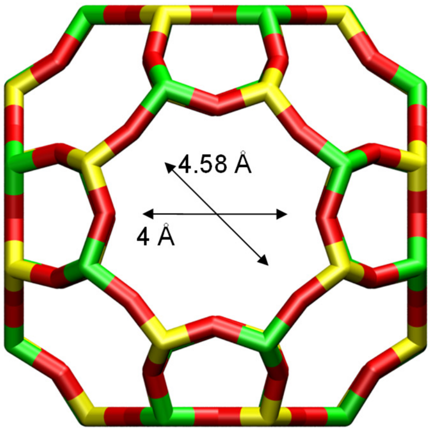

LTA-4A

The window dimension calculated using the van der Waals diameter of framework atoms = 2.7 Å is indicated above by the arrow.

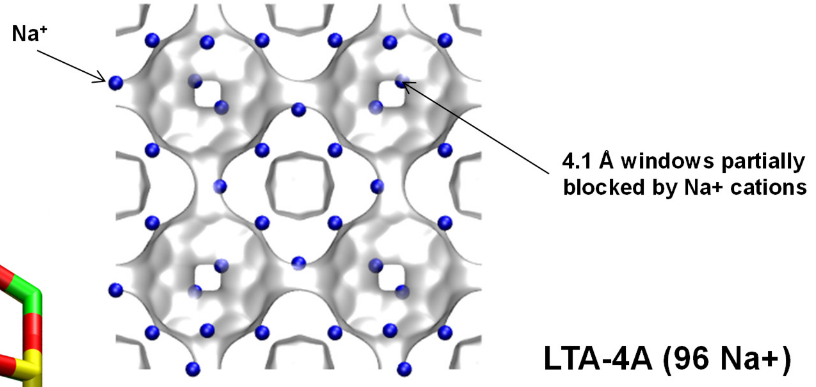

LTA-4A (96 Na+)

	LTA-4A
a /Å	24.555
b /Å	24.555
c /Å	24.555
Cell volume / Å^3	14805.39
conversion factor for [molec/uc] to [mol per kg Framework]	0.0733
conversion factor for [molec/uc] to [kmol/m^3]	0.2991
ρ [kg/m3] (with cations)	1529.55
MW unit cell [g/mol(framework+cations)]	13637.27
ϕ, fractional pore volume	0.375
open space / Å^3/uc	5552.0
Pore volume / cm^3/g	0.245
Surface area /m^2/g	
DeLaunay diameter /Å	4.00

Figure S41. Structural details of LTA-4A zeolite.

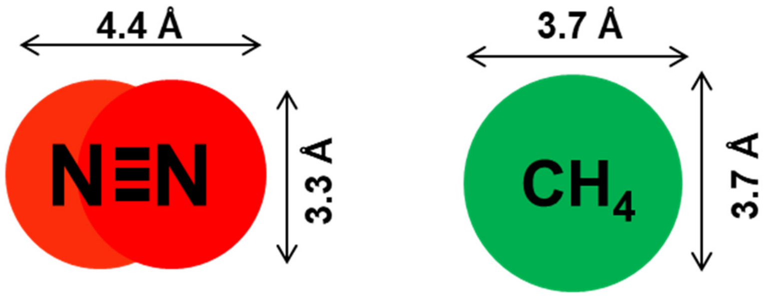

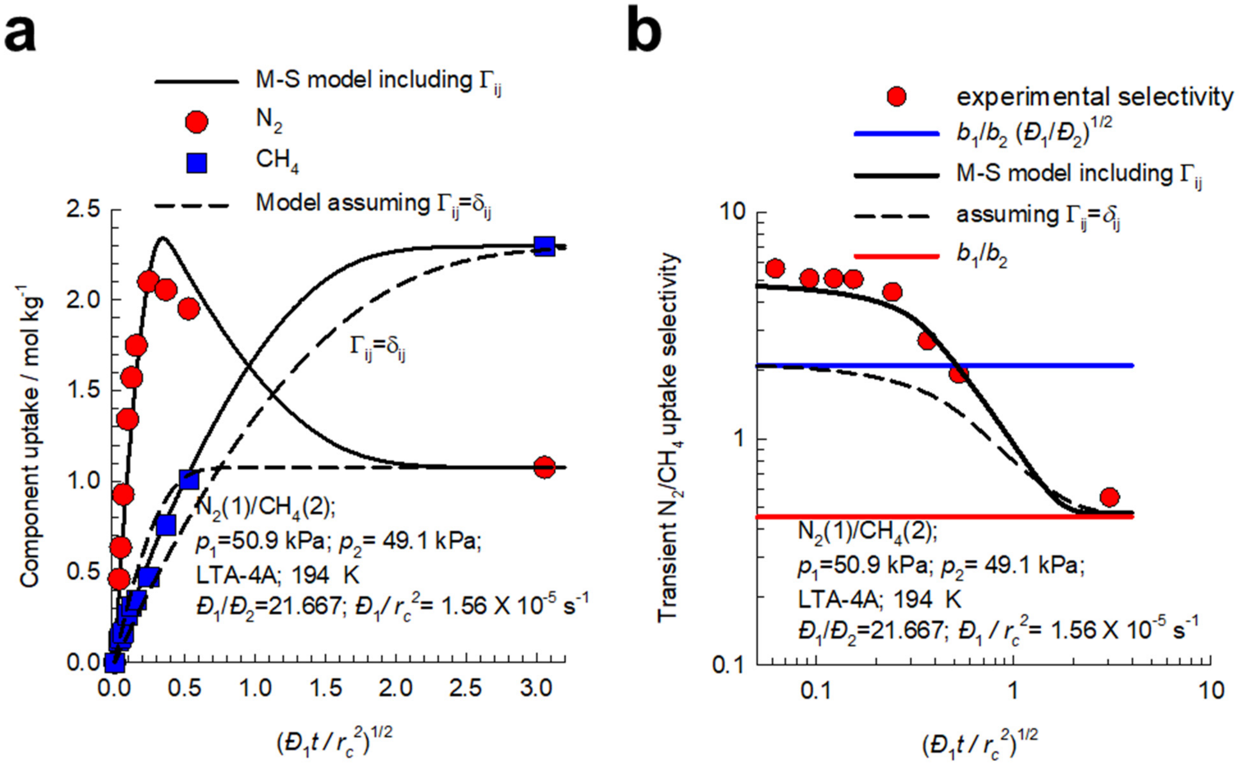

Figure S42. (a, b) Experimental data of Habgood[18] on transient uptakes of $N_2(1)/CH_4(2)$ mixture within LTA-4A crystals, exposed to binary gas mixtures at partial pressures p_1 =50.9 kPa; p_2 = 49.1 kPa. The unary isotherms are provided in Table S11. The continuous solid lines are simulations based on eq (S22). The dashed lines are the simulations based on eq (S23) in which the thermodynamic correction factors are assumed to be described by $\Gamma_{ij} = \delta_{ij}$, the Kronecker delta.

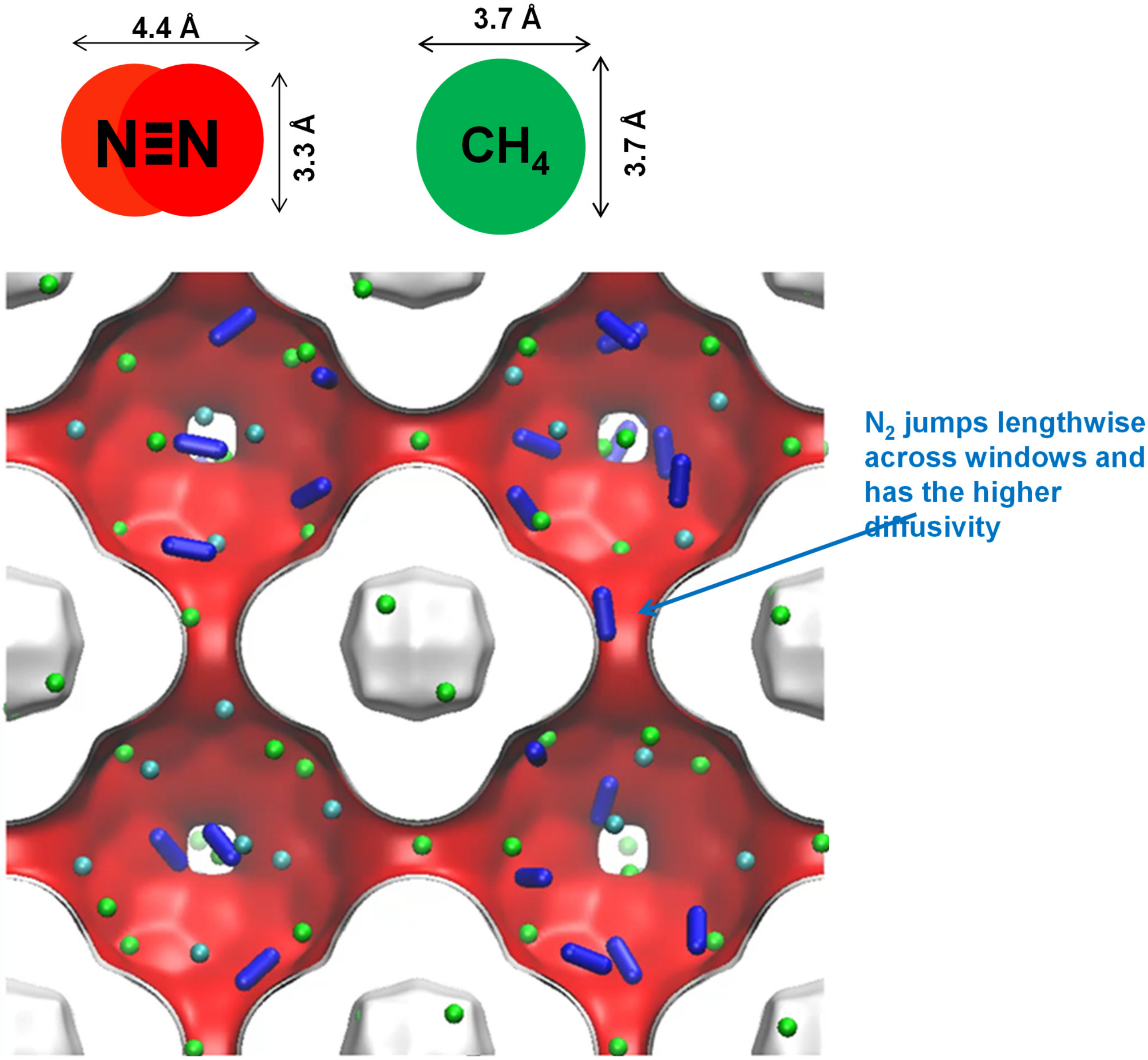

N_2 jumps lengthwise across windows and has the higher diffusivity

Figure S43. Computational snapshot showing that N_2 jumps lengthwise across the 4 Å windows of LTA-4A zeolite.

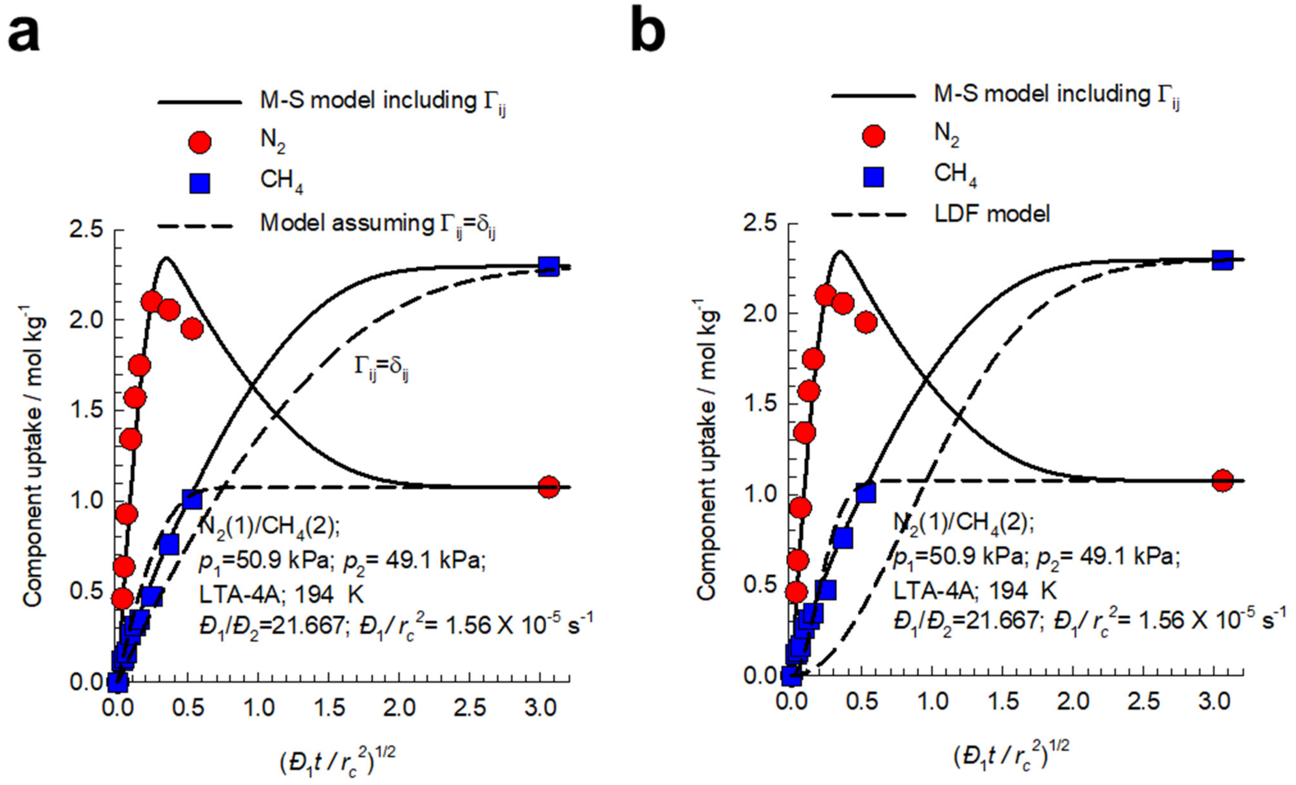

Figure S44. (a, b) Experimental data of Habgood[18] on transient uptakes of $N_2(1)/CH_4(2)$ mixture within LTA-4A crystals, exposed to binary gas mixtures at partial pressures p_1 =50.9 kPa; p_2 = 49.1 kPa. The unary isotherms are provided in Table S11. The continuous solid lines in (a,b) are the numerical solutions for transient uptake using the M-S diffusion eq (S21). The dashed lines in (a) are the solutions invoking the simplified eq (S23), Use of the LDF model, eq (S39) , results in the dashed lines shown in (b).

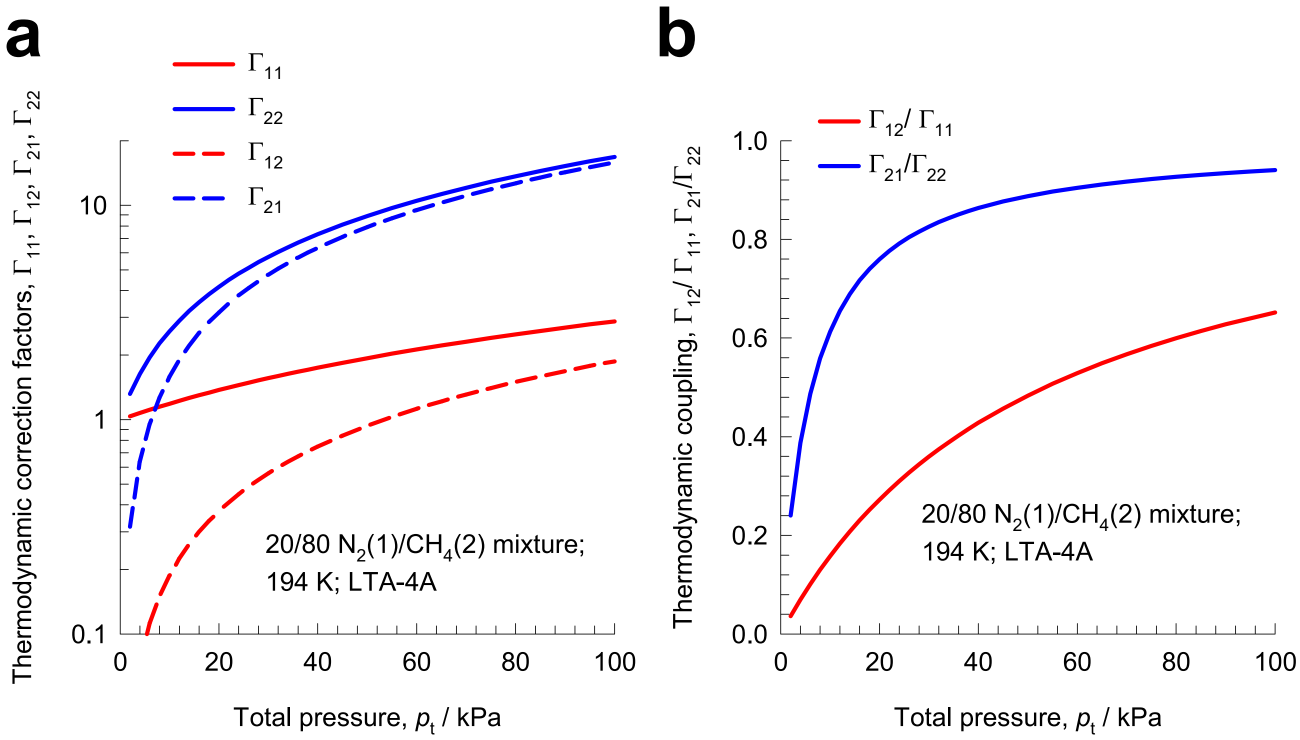

Figure S45. (a) Elements of the matrix of thermodynamic correction factors Γ_{ij} as a function of total bulk gas pressure, p_t, calculated using the mixed-gas Langmuir model for 20/80 N_2(1)/CH_4(2) mixtures adsorption in LTA-4A zeolite at 194 K. (b) Calculations of the ratios Γ_{12}/Γ_{11}, Γ_{21}/Γ_{22} as a function of total bulk gas pressure, p_t,

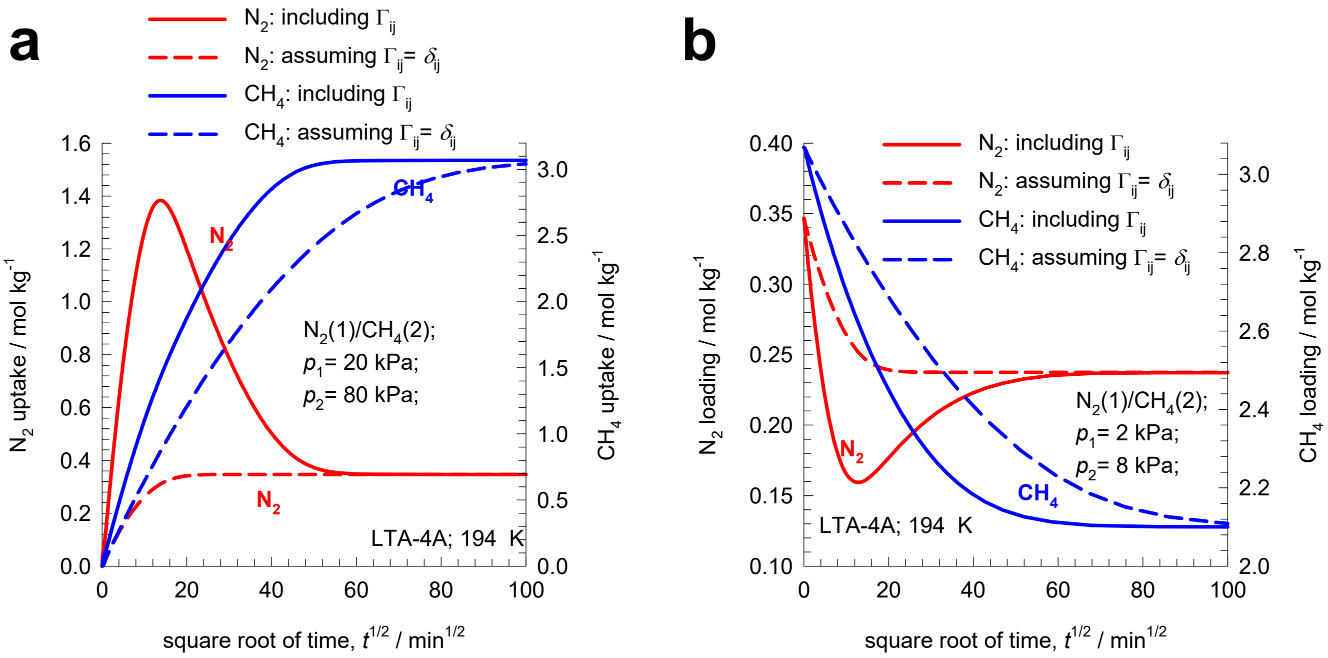

Figure S46. (a) Transient uptake of 20/80 $N_2(1)/CH_4(2)$ mixture within LTA-4A crystals, exposed to binary gas mixtures at 194 K and total pressure in the bulk gas phase p_t = 100 kPa. (b) Transient desorption of $N_2(1)/CH_4(2)$ mixtures in LTA-4A crystals. The initial loadings are those corresponding to the equilibrated loadings in (a). At time t = 0, the bulk gas phase mixture is maintained at p_1 = 2 kPa, and p_2 = 8 kPa. The unary isotherms are provided in Table S11. The continuous solid lines are Maxwell-Stefan model simulations based on Equation (S21). The dashed lines are the simulations based on Equation (S23), in which the thermodynamic correction factors are assumed to be described by $\Gamma_{ij} = \delta_{ij}$, the Kronecker delta. The Maxwell-Stefan diffusivities used in the simulations are: $Đ_1/r_c^2$ = 1.56×10^{-5} s^{-1}; $Đ_2/r_c^2$ = 7.2×10^{-9} s^{-1}.

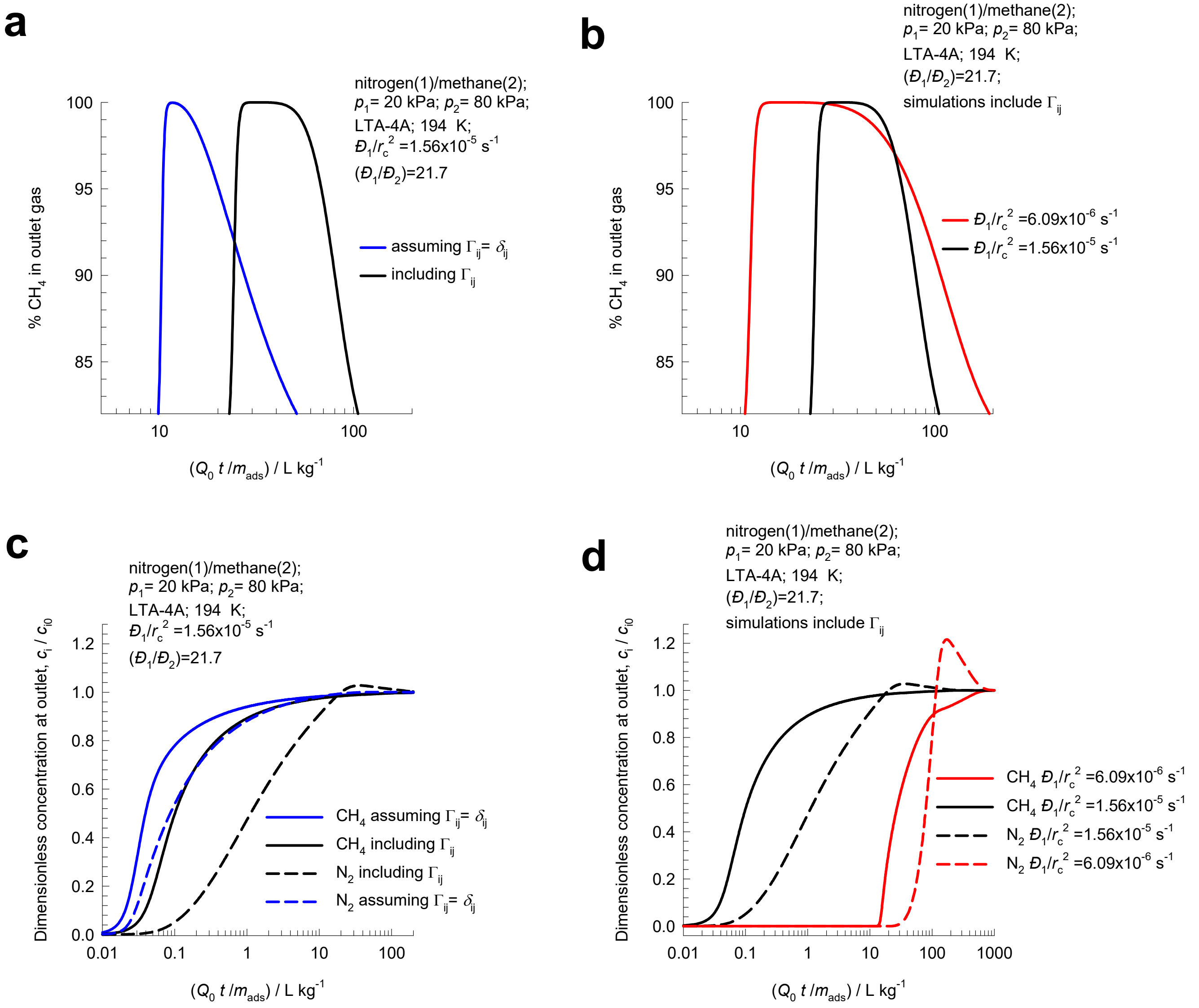

Figure S47. (a, b) Transient breakthrough of 20/80 $N_2(1)/CH_4(2)$ mixture in fixed bed adsorber packed with LTA-4A crystals operating at 194 K, and total pressure p_t = 100 kPa. The *y*-axis is the % CH_4 at the adsorber outlet. The *x*-axis is $Q_0 t/m_{ads}$, where Q_0 is the volumetric flow rate of the gas mixture at the inlet to the fixed bed at actual temperature and pressure conditions. The black lines are simulations based on eq (S22). The blue lines are the simulations based on eq (S23) in which the thermodynamic correction factors are assumed to be described by $\Gamma_{ij} = \delta_{ij}$, the Kronecker delta. In (a) we maintain $Đ_1/r_c^2 = 1.56\times10^{-5}$ s^{-1}; $Đ_1/Đ_2 = 21.7$. In (b) the two simulations (black and red lines) include thermodynamic coupling, and maintain the ratio $Đ_1/Đ_2 = 21.7$; the black and red lines represent two different severities of diffusional influences $Đ_1/r_c^2 = 1.56\times10^{-5}$ s^{-1}; $Đ_1/r_c^2 = 6.09\times10^{-6}$ s^{-1}. In Figure S47c,d the same sets of data in Figure S47a,b are plotted using the dimensionless concentrations in the gas phase exiting the adsorber, c_i/c_{i0}, as *y*-axes.

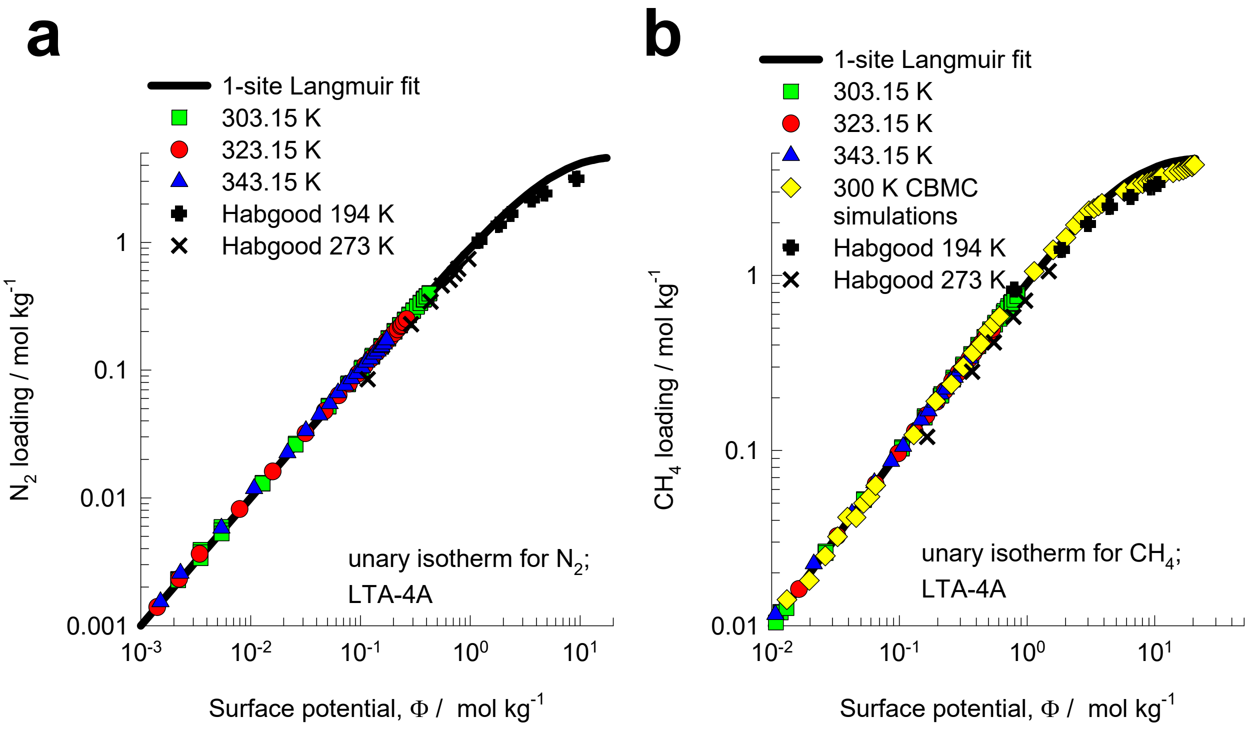

Figure S48. 1-site temperature-dependent Langmuir parameter fits for N_2 and CH_4 in LTA-4A zeolite using the parameters in Table S12. The component loadings are plotted as function of the surface potential Φ ; for details of the concept of surface potential refer to Krishna and van Baten.[71]

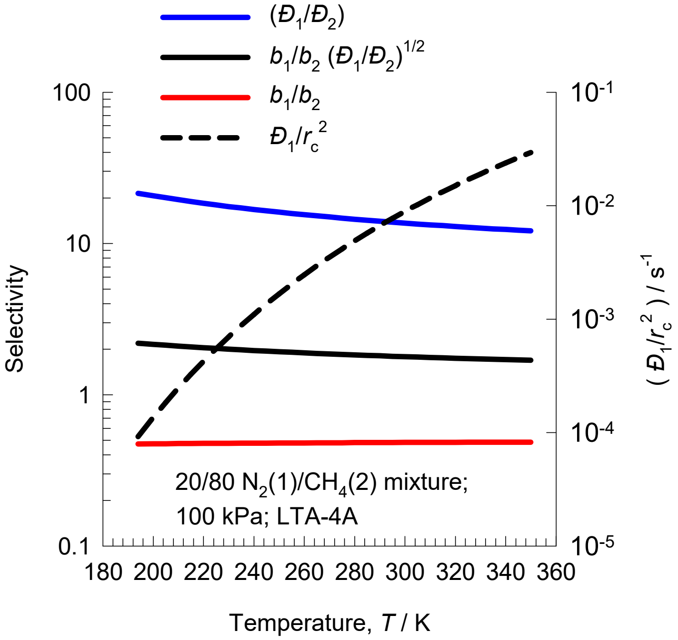

Figure S49. Plot of adsorption selectivity, $\frac{b_1}{b_2}$, diffusion selectivity, $\frac{Đ_1}{Đ_2}$, and kinetic selectivity, $\frac{b_1}{b_2}\sqrt{\frac{Đ_1}{Đ_2}}$ as function of the temperature, *T*, for LTA-4A zeolite. Also plotted on the right *y*-axes are the values of $Đ_1/r_c^2$.

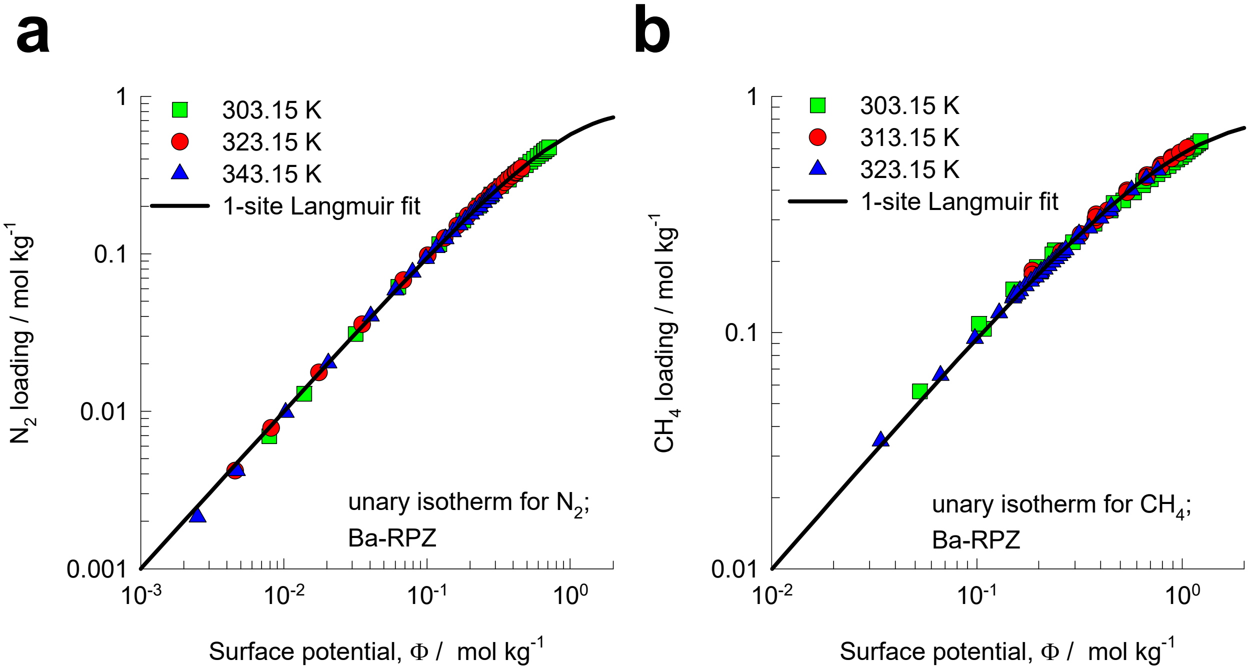

Figure S50. 1-site temperature-dependent Langmuir parameter fits for N_2 and CH_4 in Ba-RPZ using the parameters in Table S13. The component loadings are plotted as function of the surface potential Φ; for details of the concept of surface potential refer to Krishna and van Baten.[71]

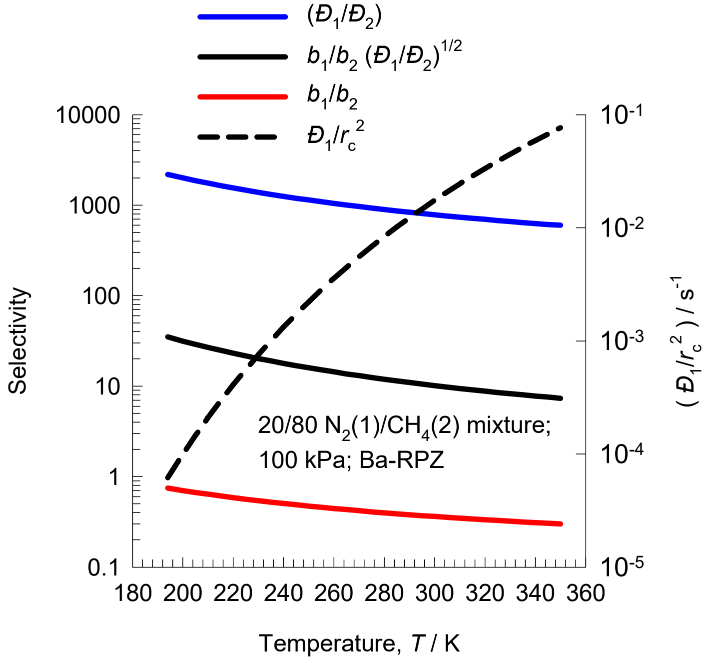

Figure S51. Plot of adsorption selectivity, $\frac{b_1}{b_2}$, diffusion selectivity, $\frac{Đ_1}{Đ_2}$, and kinetic selectivity, $\frac{b_1}{b_2}\sqrt{\frac{Đ_1}{Đ_2}}$ as function of the temperature, T, for Ba-RPZ. Also plotted on the right y-axes are the values of $Đ_1/r_c^2$.

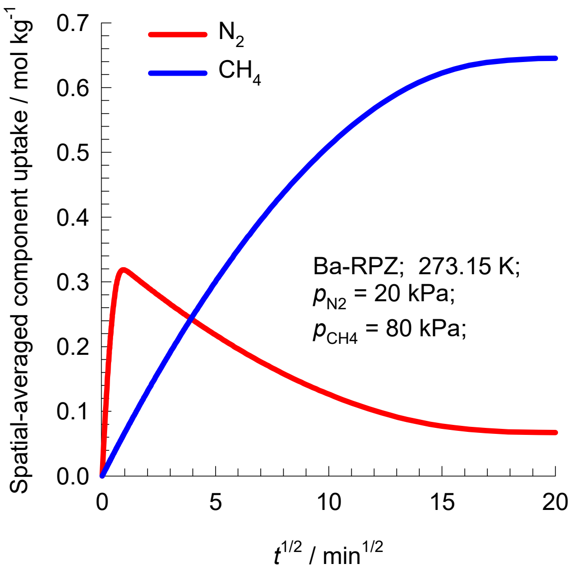

Figure S52. Transient uptake of 20/80 $N_2(1)/CH_4(2)$ mixture in Ba-RPZ crystals operating at 273 K, and total pressure p_t = 100 kPa.

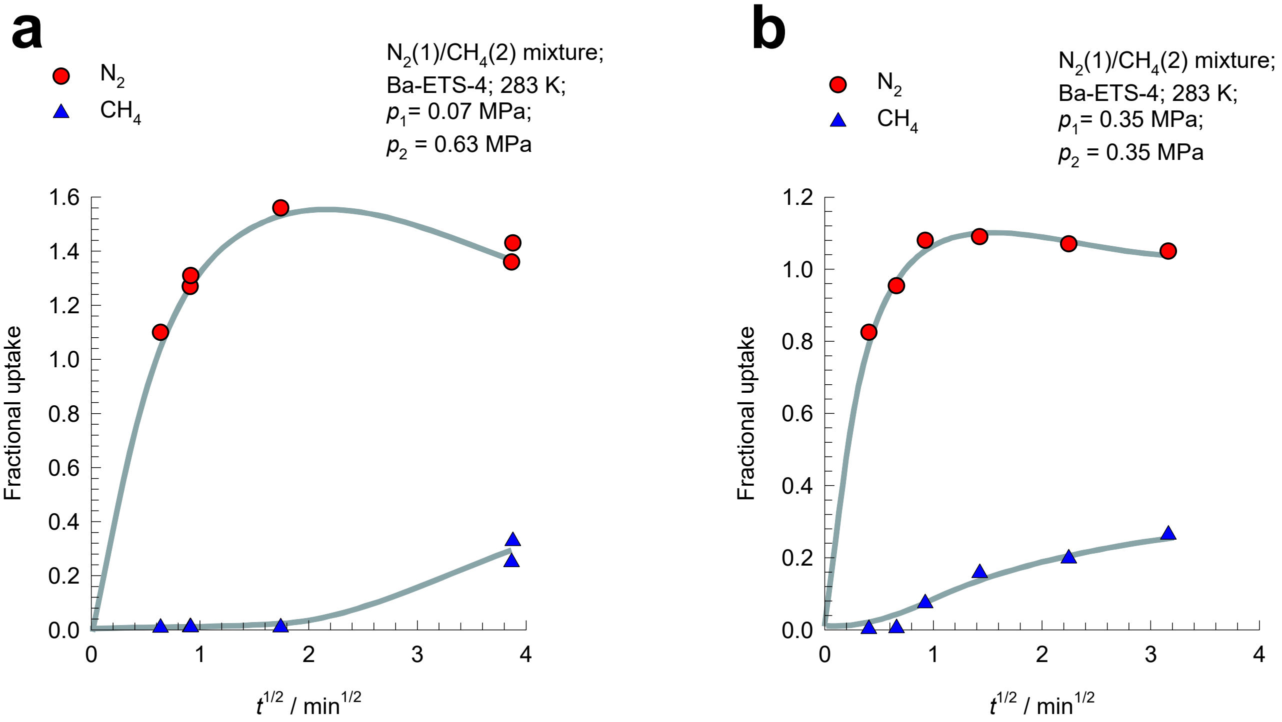

Figure S53. (a, b) The transient uptake data of Majumdar et al.[90] for Ba-ETS-4 for (a) 10/90, and (b) 50/50 mixtures in Ba-ETS-4 at 283 K and 0.7 MPa. Note that the *y*-axes are plotted in terms of fractional uptake.

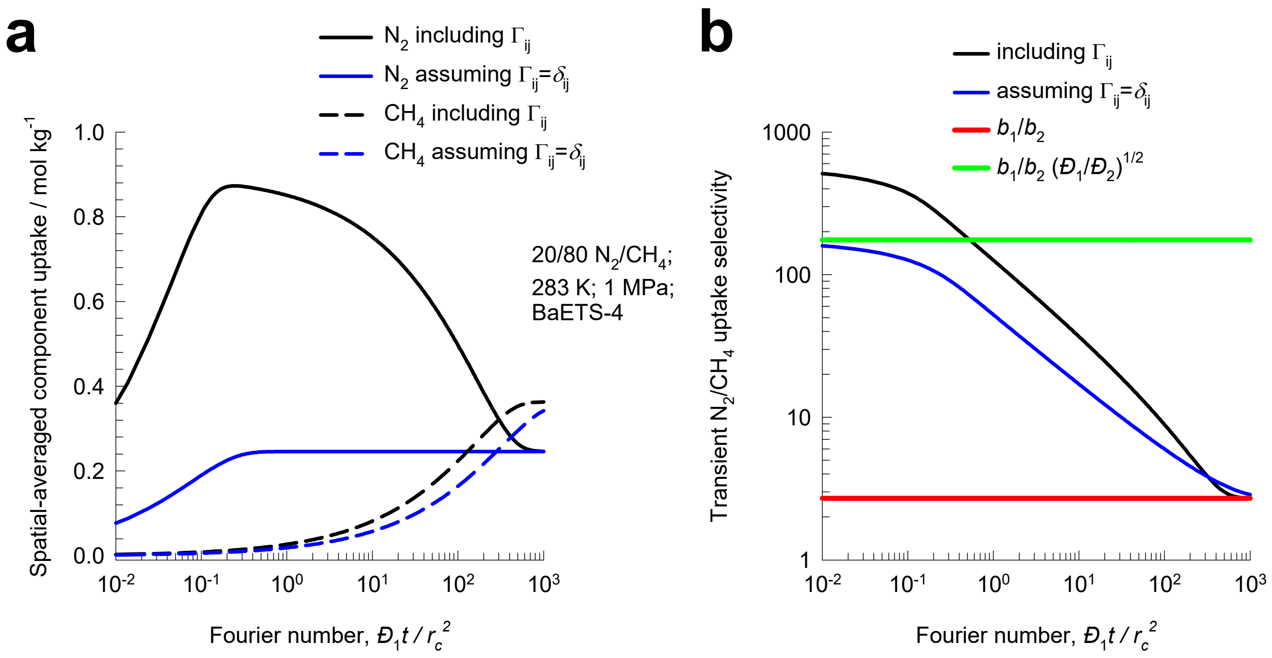

Figure S54. (a, b) Transient uptake of 20/80 $N_2(1)/CH_4(2)$ mixture inside crystallite of Ba-ETS-4. The surrounding bulk gas mixture is at 283 K, and total pressure p_t = 1 MPa. The *x*-axes represent the Fourier number $Đ_1 t/r_c^2$. The black lines are simulations based on eq (S22). The blue lines are the simulations based on eq (S23) in which the thermodynamic correction factors are assumed to be described by $\Gamma_{ij} = \delta_{ij}$, the Kronecker delta.

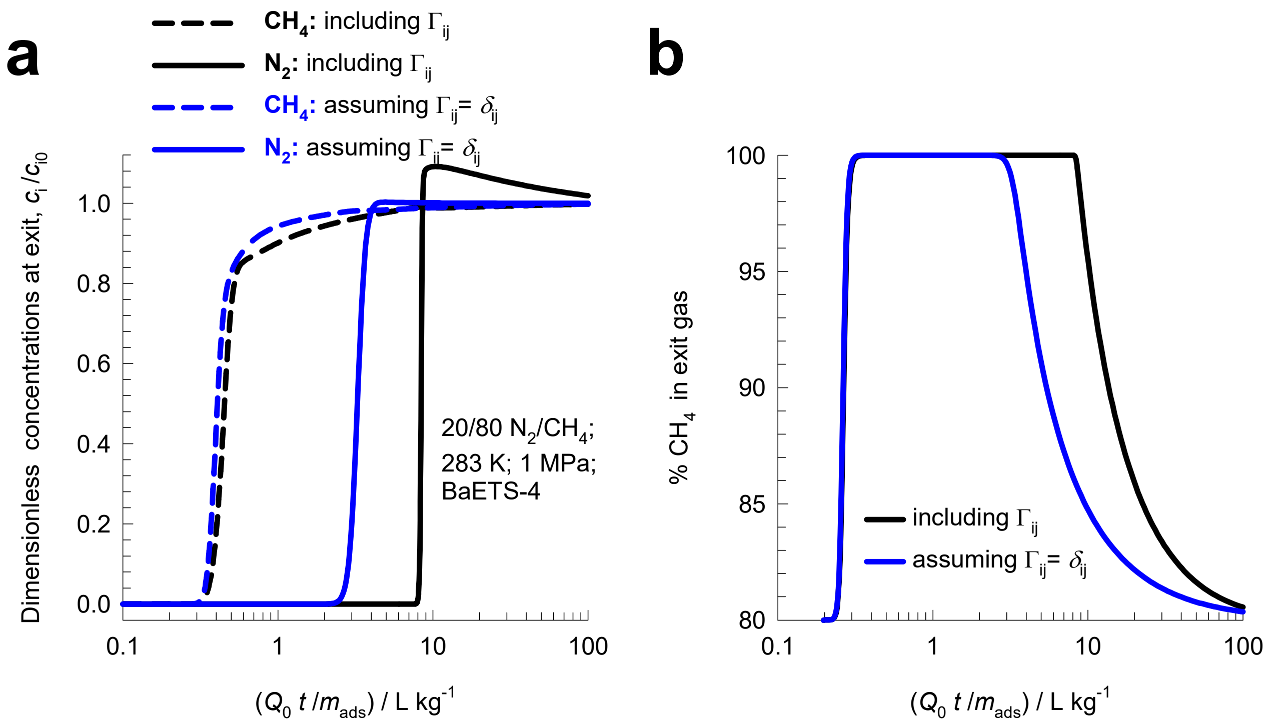

Figure S55. (a, b) Ttransient breakthroughs of 20/80 N_2(1)/CH_4(2) mixture in fixed bed adsorber packed with Ba-ETS-4, operating at 283 K, and total pressure p_t = 1 MPa. The *x*-axes are $Q_0 t / m_{ads}$, where Q_0 is the volumetric flow rate of the gas mixture at the inlet to the fixed bed at actual temperature and pressure conditions. The *y*-axis in (b) is the % CH_4 at the adsorber outlet. The black lines are simulations based on eq (S22). The blue lines are the simulations based on eq (S23) in which the thermodynamic correction factors are assumed to be described by $\Gamma_{ij} = \delta_{ij}$, the Kronecker delta.

8 Kinetic Separations of Alkene/Alkane Mixtures

Ethene is an important chemical used as feedstock in manufacture of polymers such as polyethene, polyvinyl chloride, polyester, polystyrene as well as other organic chemicals. Propene is mostly used to make polypropylene, which accounts for nearly two-thirds of global propylene consumption. Other outlets include acrylonitrile, propylene oxide, a number of alcohols, cumene and acrylic acid. Propene is a by-product from the steam cracking of liquid feedstocks such as naphtha and liquefied petroleum gas (LPG), as well as off-gases produced in fluid catalytic cracking (FCC) units in refineries.

Key processing steps in preparing feedstocks for polymer production are the separations of ethene/ethane, and propene/propane mixtures.

The boiling points are below ambient temperatures: ethane (184.5 K), ethene (169.4 K), propane (231.3 K), propene (226 K). Due to the small differences in the boiling points, the separations of ethene/ethane, and propene/propane mixtures have low relative volatilities, in the range of 1.1 – 1.2. These separations are traditionally carried out by distillation columns that operate at high pressures and low temperatures. The purity requirement of the alkenes as feedstocks to polymerization reactors is 99.95%, and consequently the distillation columns are some of the largest and tallest distillation columns used in the petrochemical industries with about 150 - 200 trays, and operating at reflux ratios of about 15. Distillation is energy intensive, and adsorptive separations offer an attractive, energy-efficient, alternative.

Watch also the presentation titled **Alkene/Alkane Separations with MOFs** and **C_2H_4/C_2H_6 Separations with Co-Gallate,** on YouTube

https://www.youtube.com/@rajamanikrishna250/videos

Figure S56a,b,c presents data on the polarizabilities, dipole moments, and quadrupole moments of C_2H_4, C_2H_6, C_3H_6, and C_3H_8. C_3H_8 has a significantly large dipole moment. Each of the unsaturated alkenes C_2H_4, and C_3H_6 possesses a pi-bond, and the preferential adsorption of the alkene from the corresponding alkane with the same number of C atoms can be achieved by choosing zeolitic adsorbents with extra-framework cations, or MOFs with unsaturated "open" metal sites.[95] All of the atoms of C_2H_4 lie on the same plane, and its dipole moment is zero; however it does possess a quadrupole moment.

It is to be noted that the polarizability of the alkane (C_2H_6, C_3H_8) is slightly higher than that of the corresponding alkene (C_2H_4, C_3H_6). The unary adsorption isotherms in ZIF-8, that does not contain extra-framework cations or unsaturated metal atoms show that the alkane is slightly more strongly adsorbed than the corresponding alkene.

For production of alkene feedstocks of 99.95%+ purity required for polymerization reactors, cryogenic distillation columns operated at high pressures and high reflux ratios are commonly employed for large scale separations of C_2H_4/C_2H_6, and C_3H_6/C_3H_8 mixtures. Many MOF developments have targeted alkene/alkane separations with the objective of eventually supplanting the energy-intensive distillation technologies.[72, 95-100] Each of the unsaturated alkenes C_2H_4, and C_3H_6 possesses a π-bond, and the preferential adsorption of the alkene from the corresponding alkane with the same number of C atoms can be achieved by choosing zeolitic adsorbents with extra-framework cations (e.g. LTA-4A, LTA-5A,[101-103] and NaX (= 13X) zeolites[101, 104]), or MOFs with unsaturated "open" metal sites[95, 105] (e.g. M_2(dobdc)[95, 105] [M = Mg, Mn, Co, Ni, Zn, Fe; dobdc^{4-} = 2,5- dioxido-1,4-benzenedicarboxylate], M_2(*m*-dobdc) [106] [M = Mn, Fe, Co, Ni; *m*-dobdc^{4-} = 4,6-dioxido-1,3-benzenedicarboxylate] and CuBTC[107]).

Figure S57a,b shows the experimental data on the adsorption/desorption cycles for separation of (a) 50/50 C_2H_4/C_2H_6, and (b) 50/50 C_3H_6/C_3H_8 mixtures in a fixed bed adsorber packed with Fe_2(dobdc)[95] and operating at 318 K. Bloch et al.[95] have established that each alkene molecule attaches *side-on* to an Fe(II) atom in the framework. The alkene/alkane selectivities are about 15. For a certain interval of time (indicated by yellow bar), the saturated alkanes of high purity can be recovered.

The desorption cycle is initiated by nitrogen purge. During the early stages of desorption (indicated by cyan colored bars), it is evident that the product gas mixture contains significantly more than about 0.5% alkanes. Polymer grade alkenes with purities >99.95%, **cannot** be recovered from the **cumulative**

desorbed gas mixture. This is due to the presence of finite amounts of saturated alkane at the termination of the adsorption cycle. Generally speaking, the attainment of high alkene purities in the desorption cycle is only possible if the saturated alkanes are virtually excluded from the pores. This objective is met with NbOFFIVE-1-Ni (= KAUST-7),[96] UTSA-280,[72] ZIF-8,[108] CHA zeolite,[22, 109] or Co-gallate,[98, 110] that almost completely exclude the saturated alkane from the pores due to strong diffusional limitations.

8.1 Kinetic Separations of C_2H_4/C_2H_6 mixtures using Co-gallate

Figure S58 compares the experimental data on transient breakthroughs for separation of C_2H_4/C_2H_6 mixtures in a fixed bed adsorber packed with: UTSA-280,[72] Co-gallate,[98] and Fe_2(dobdc).[95] The dimensionless concentrations at the exit of the fixed bed, c_i/c_{i0}, are plotted as a function of $Q_0 t/m_{ads}$, where Q_0 is the volumetric flow rate of the gas mixture at the inlet to the fixed bed, expressed in L s^{-1}, at STP conditions. Though Fe_2(dobdc) has significantly higher C_2H_4 uptake capacity, this MOF also adsorb significant amounts of saturated C_2H_6. In the vacuum blowdown step, the presence of the saturated C_2H_6 in the void spaces of the bed is a detrimental factor in the achievement of the desired high-purity C_2H_4 product.

To attain high C_2H_4 purities that are required for polymerization feedstocks, we need to operate with multiple beds involving five different steps, as schematized in Figure S59, [22, 102, 104, 109] consisting of

(i) Pressurization with C_2H_4/C_2H_6 feed mixture

(ii) High pressure adsorption separation with withdrawal of purified C_2H_6

(iii) Co-current purge (rinse) with a portion of the product C_2H_4

(iv) co-current blowdown, and

(v) counter-current vacuum blowdown

A detailed process design exercise, such as that reported by Khalighi et al.[22, 109] will be required in order to compare the C_2H_4 productivities of MOFs using the 5-step PSA scheme. Khalighi et al.[22] points out that the co-current blowdown step may be redundant, and a simplified 4-step scheme is viable.

In order to gain insights into the 5-step PSA scheme for C_2H_4(1)/C_2H_6(2) mixture separations we present simulations of the individual steps in an adsorber packed with Co-gallate pellets operating at 298 K. The unary isotherm data are provided in Table S17 that are adapted from Wu et al.[111] and Yan et al.[112]

The motivation for examining the 5-step PSA scheme for C_2H_4(1)/C_2H_6(2) mixture separations with Co-gallate pellets is the paper by Yan et al.[112] who present simulations of a 4-step PSA scheme using the ASPEN commercial software that incorporates the simple LDF model for modelling diffusion, and not taking account of thermodynamic coupling by essentially invoking $\Gamma_{ij} = \delta_{ij}$, the Kronecker delta. Yan et al.[112] also present experimental data on breakthroughs in a small scale laboratory equipment in order to demonstrate the validity of their ASPEN model for breakthrough simulations. It is instructive to compare the dimensions and operating conditions for the laboratory apparatus with the corresponding parameters for the larger scale commercial unit for which ASPEN PSA simulations are presented; this comparison is presented in Figure S60. The most important difference is that the average contact time between the gas mixture and the Co-gallate pellets is about a factor 10 shorter in the commercial unit. We will demonstrate later on that this implies stronger diffusional influences in the commercial unit.

For 80/20 C_2H_4(1)/C_2H_6(2) mixture separations with Co-gallate pellets, Figure S61 presents simulations of the (a, b) adsorption cycle, (c, d) co-current purge, (e, f) co-current blowdown, and (g, h) counter-current vacuum blowdown. In these simulations, the thermodynamic coupling effects are taken into account, based on eq (S11). The Maxwell-Stefan diffusivities are $Đ_1/r_c^2 = 3\times10^{-4}\ \text{s}^{-1}$; $Đ_2/r_c^2 = 3\times10^{-5}\ \text{s}^{-1}$. The adsorber bed is 0.46 m diameter of packed height 4.61 m. The bed voidage $\varepsilon = 0.571$ and the bulk density of adsorbent is 660 kg m^{-3}. The superficial gas velocity at the bed inlet $u = 0.192\ \text{m s}^{-1}$, and the interstitial gas velocity $v = u/\varepsilon = 0.337\ \text{m s}^{-1}$.

Figure S61a plots gas phase concentrations exiting the adsorption cycle as a function of time, expressed in seconds. The adsorption cycle is terminated at t = 1000 s, just before the unsaturated alkene is about the exit the adsorber. The molar loadings of C_2H_4, and C_2H_6 along the height of the adsorber bed at the end of the adsorption cycle are plotted in Figure S61b.

Figure S61c.d presents the simulations of the co-current purge step in which a portion of the product C_2H_4 is used to "rinse" the contents of the bed in order to desorb the saturated alkane, whose presence in the bed will adversely influence the C_2H_4 product purity in the final vacuum blowdown step. Figure S61c plots of the gas phase concentrations exiting the co-current purge. We note a steady decline in the gas phase concentration of the saturated alkane. The purge gas velocity is arbitrarily chosen to have the same interstitial gas velocity as in the adsorption cycle, i.e. $v = u/\varepsilon = 0.337$ m s^{-1}. The total duration of the co-current purge step is 50 s. Figure S61d plots the component loadings along the dimensionless distance, z/L, along the length of the adsorber at the termination of the co-current purge. The co-current purge has the effect of reducing the adsorbed phase loadings of the saturated alkane.

Figure S61e.f present the simulations of the co-current blowdown step in which exit of the bed is maintained under vacuum, arbitrarily set at 2 Pa, total pressure. The vacuum draw-off rate is arbitrarily chosen to have the same interstitial gas velocity as in the adsorption cycle, i.e. $v = u/\varepsilon = 0.337$ m s^{-1}. Figure S61e plots of the gas phase concentrations exiting the co-current blowdown operation. We note a steady decline in the gas phase concentration of the saturated alkane. The total duration of the co-current blowdown step is 50 s. Figure S61f plots the component loadings along the dimensionless distance, z/L, along the length of the adsorber at the termination of the co-current blowdown. The co-current blowdown has the effect of reducing the adsorbed phase loadings of the saturated alkane.

Figure S61g,h presents the simulations of the counter-current blowdown step in which the exit of the bed is maintained under vacuum, arbitrarily set at 2 Pa, total pressure. Figure S61g plots the gas phase concentrations exiting the counter-current vacuum blowdown. The corresponding cumulative molar loadings of the components exiting the vacuum blowdown phase are plotted in Figure S61h. The recovered C_2H_4 product has a purity of 99.3% and a productivity of 2.2 mol kg^{-1}. With process optimization, the product purity can be made to correspond to the requirements of polymer grade feed stocks.

For 80/20 $C_2H_4(1)/C_2H_6(2)$ mixture separations with Co-gallate pellets, Figure S62 compares the simulations of the adsorption cycle using eq (S11). with simulations in which the thermodynamic coupling influences are ignored by invoking eq (S12), The separations are significantly influenced, in a positive sense, by inclusion of thermodynamic coupling effects.

For our purposes of comparing MOFs for C_2H_4/C_2H_6 mixture separations, it is sufficient to employ a simplified 2-step PSA scheme consisting of the adsorption cycle, followed by counter-current vacuum blowdown, as illustrated in Figure S63 for use of Co-gallate pellets as adsorbent. Figure S63a,b presents the simulations of the adsorption cycle; these simulations are identical to the ones presented earlier in Figure S61a,b. In these simulations, due account is taken of thermodynamic coupling effects. At the termination of the adsorption cycle, at t = 1000 s, the counter-current vacuum blowdown step is initiated.

Figure S63c,d presents the simulations of the counter-current blowdown step in which the exit of the bed is maintained under vacuum, arbitrarily set at 2 Pa, total pressure. Figure S63c plots the gas phase concentrations exiting the counter-current vacuum blowdown. The corresponding cumulative molar loadings of the components exiting the vacuum blowdown phase are plotted in Figure S63d. The recovered C_2H_4 product has a purity of 98.7% and a productivity of 2.04 mol kg^{-1}. We note that both C_2H_4 product purity, and productivity values, are lower than the corresponding ones obtained in the 5-step scheme shown in Figure S61.

Yan et al.[112] present simulations of a 4-step PSA scheme for essentially the same set of conditions as chosen for the simulations presented in Figure S61. Their 4-step excludes the co-current blow-down step, and also ignores the influence of thermodynamic coupling. Their simulations show that the productivity per cycle of purified C_2H_4 product is 1.6 mol kg^{-1}. Their value is significantly lower than the value of 2.2 mol kg^{-1} that is obtainable with 5-step scheme in Figure S61, taking due account of thermodynamic coupling. The significantly lower productivity of C_2H_4 product realized by Yan et al.[112] is primarily ascribable to the adoption of a simplified LDF model, ignoring thermodynamic coupling.

8.2 Kinetic Separations of C_3H_6/C_3H_8 mixtures using CHA zeolite

Figure S64 compares the experimental data on transient breakthroughs for separation of C_3H_6/C_3H_8 mixtures in a fixed bed adsorber packed with: KAUST-7,[96] Co-gallate,[110] LTA-5A,[96] and Ni_2(dobdc).[113] The dimensionless concentrations at the exit of the fixed bed, c_i/c_{i0}, are plotted as a function of Q_0t/m_{ads}, where Q_0 is the volumetric flow rate of the gas mixture at the inlet to the fixed bed, expressed in L s^{-1}, at STP conditions. Though LTA-5A and Ni_2(dobdc) have significantly higher C_3H_6 uptake capacities, these materials also adsorb significant amounts of saturated alkane. In the vacuum blowdown step, the presence of the saturated alkanes in the void spaces of the bed is a detrimental factor in the achievement of the desired high-purity C_3H_6 product.

To attain high C_3H_6 purities that are required for polymerization feedstocks, we need to operate with multiple beds involving five different steps, as schematized in Figure S65, [22, 102, 104, 109] consisting of

(i) Pressurization with C_3H_6/C_3H_8 feed mixture

(ii) High pressure adsorption separation with withdrawal of purified C_3H_8

(iii) Co-current purge with a portion of the product C_3H_6, and

(iv) co-current blowdown, and

(v) counter-current vacuum blowdown

A detailed process design exercise, such as that reported by Khalighi et al.[22, 109] will be required in order to compare the C_3H_6 productivities of MOFs using the 5-step PSA scheme. Khalighi et al.[22] points out that the co-current blowdown step may be redundant, and a simplified 4-step scheme is viable. For our purposes in this article, we employ a simplified 2-step PSA scheme consisting of the adsorption cycle, followed by counter-current vacuum blowdown; see Figure S66. For all the simulations presented in this article, the vacuum blowdown step is performed at a total pressure of 2 Pa.

The recovery of high purity C_3H_6 product in the final vacuum blowdown step is expected to be enhanced if C_3H_8 is (almost) excluded during the high pressure adsorption cycle. Near-total exclusion of C_3H_8 is achievable by kinetically based separations using cage-type zeolites with 8-ring windows. Due to the small cross-section of the propene molecule (see Figure S67), kinetic separations, selective to propene, are possible using all-silica CHA zeolite (all-silica CHA zeolite, also named SiCHA), consists of cages of volume 316 Å^3, separated by 3.8 Å × 4.2 Å 8-ring windows; the pore landscape and structural details are provided in Figure S68, and Figure S69.[22, 114-116]

Ruthven and Reyes[116] compare the ratio of diffusivities of propene to that of propene in CHA with the corresponding values in DDR; see Figure S70. Their data show that CHA is the more effective sieve.

It is to be noted for LTA-4A zeolite,[101, 102] both mixture adsorption and diffusion favor propene, whereas with all-silica CHA zeolite, the adsorption equilibrium is in favor of propane, whereas diffusion favors propene.

Figure S71a,b shows the simulations of transient uptake of 50/50 $C_3H_6(1)/C_3H_8(2)$ mixtures within crystals of all-silica CHA at 353 K. The spatial averaged component loadings are plotted as a function of $\sqrt{t}$. The bulk gas mixture is at a total pressure of 200 kPa. The unary isotherms data are provided in Table S15. The black lines are simulations based on eq (S11). The Maxwell-Stefan diffusivities are $Đ_1/r_c^2 = 1.7\times10^{-4}$ s^{-1}; $Đ_1/Đ_2 = 5000$. The more mobile C_3H_6 exhibits a pronounced overshoot in its approach to thermodynamic equilibrium. The attainment of supra-equilibrium loadings during the initial stages of transience signals the phenomenon of uphill diffusion, and enhanced separation. The blue lines are the simulations based on eq (S12), in which the thermodynamic correction factors are assumed to be described by $\Gamma_{ij} = \delta_{ij}$, the Kronecker delta. In this scenario, no C_3H_6 overshoot is observed indicating that thermodynamic coupling effects are the root cause of uphill diffusion.

Figure S71b is a plot of the transient uptake selectivity, defined by $\frac{\overline{q}_1(t)/\overline{q}_2(t)}{p_{10}/p_{20}}$ as a function of $\sqrt{t}$. As $t \to \infty$, the uptake selectivity will approach the value of the adsorption selectivity $\frac{q_1^*/q_2^*}{p_{10}/p_{20}}$. From the unary Langmuir isotherm parameters Table S15, we calculate the equilibrium adsorption selectivity $\frac{q_1^*/q_2^*}{p_{10}/p_{20}} = \frac{b_1}{b_2} = 0.375$. Readers should note that the ratio $\frac{b_1}{b_2}$ should be replaced by the ratio of Henry constants, $\frac{q_{sat,1}}{q_{sat,2}}\frac{b_1}{b_2}$, in case the saturation capacities of components 1 and 2 are unequal. At short contact times, the transient uptake selectivity is strongly in favor of the more mobile propene. If thermodynamic coupling effects are ignored, and the Maxwell-Stefan diffusivities are assumed to be independent of loading, the following simplified expression can be derived for the transient uptake selectivity as the product of the adsorption equilibrium selectivity and the diffusion selectivity[22, 90]

$$\frac{\overline{q}_1(t)/\overline{q}_2(t)}{p_{10}/p_{20}}=\frac{b_1}{b_2}\sqrt{\frac{Đ_1}{Đ_2}} \tag{S53}$$

Readers should note that the ratio $\frac{b_1}{b_2}$ should be replaced by the ratio of Henry constants, $\frac{q_{sat,1}}{q_{sat,2}}\frac{b_1}{b_2}$, in case the saturation capacities of components 1 and 2 are unequal. In order to appreciate the significance of thermodynamic coupling, Figure S72 presents the calculations of the thermodynamic correction factors Γ_{ij}. We note that at a total pressure of 200 kPa, the cross-coefficients are about 75-90% of the magnitudes of the diagonal elements, indicating that coupling effects cannot be ignored. The green colored line in Figure S71b shows the calculations of the uptake selectivity following the simplified eq (S53), that ignores thermodynamic coupling effects. We note that the uptake selectivity in favor of propene is significantly enhanced due to the influence of Γ_{ij}.

We turn our attention to the separation of 50/50 C_3H_6(1)/C_3H_8(2) mixtures in fixed bed adsorbers packed with crystals of all-silica CHA operating at 353 K and total pressure of 200 kPa. Our initial focus is on the adsorption cycle and the influence of crystallite size in the packed bed. Rather than vary the crystal size, we consider the influence of the diffusional time constant, $Đ_1/r_c^2$; the ratio of M-S diffusivities is held constant $Đ_1/Đ_2=5000$. In these set of simulations the bed voidage $\varepsilon=0.4$, bed length $L=0.3$ m, the interstitial velocities $v=0.02$ m s^{-1}; the contact times are $L/v=15$ s. The x-axis used is

$$
\frac{\left(Q_0 = \text{flow rate m}^3\ \text{s}^{-1}\right)\times\left(\text{time in s}\right)}{\left(\text{kg MOF packed in tube}\right)} = \frac{Q_0 t}{m_{ads}} = \text{m}^3\ \text{kg}^{-1}
$$

$$
= \frac{\left(u_0 \text{A}\right)\times\left(t\right)}{(1-\varepsilon)\times\left(L\ \text{m}\right)\times\left(A\ \text{m}^2\right)\times\left(\rho\ \text{kg m}^{-3}\right)} = \frac{v\varepsilon t}{(1-\varepsilon)\times L\times\rho} = \frac{t}{L/v}\frac{\varepsilon}{(1-\varepsilon)\rho}.
$$

Figure S73a presents the breakthrough simulations for the scenario in which the diffusional time constant $\left(Đ_1/r_c^2\right)\rightarrow\infty$, i.e. diffusional influences are insignificant and eq (S41) can be invoked. In this scenario, the unsaturated C_3H_6 breaks through earlier than the saturated C_3H_8 because the mixture adsorption favors the saturated alkane; see the unary isotherms data that are provided in Table S15.

Figure S73b,c,d present the breakthrough simulation results for increasing crystal sizes: (b) $\left(Đ_1/r_c^2\right)=6.8\times10^{-2}$ s $^{-1}$. (c) $\left(Đ_1/r_c^2\right)=1.7\times10^{-2}$ s $^{-1}$. (d) $\left(Đ_1/r_c^2\right)=1.7\times10^{-4}$ s $^{-1}$. We note that the breakthroughs for C_3H_8 occurs earlier because the saturated is severely diffusion limited. With increasing diffusional influence, i.e. decreasing values of $\left(Đ_1/r_c^2\right)$, the breakthroughs of C_3H_8 occur earlier, resulting in improved separations. The important message is that for kinetically driven separations to be effective there is an optimum crystal size, i.e. optimum value of the diffusional time constant, $\left(Đ_1/r_c^2\right)$.

Watch also the video presentations titled **Particle Size Effects in Kinetic Separations,** and **Diffusional Time Constants & Contact Times** on YouTube

https://www.youtube.com/@rajamanikrishna250/videos

For any chosen value of the crystal size, i.e. chosen value of $\left(Đ_1/r_c^2\right)$, the severity of diffusional influences are also dependent on the contact time between the gas mixture and the crystallites; this contact time is L/v, where v is the interstitial gas velocity. To illustrate this influence, Figure S74a,b,c,d present transient breakthrough simulations for the adsorption cycle for 50/50 C_3H_6/C_3H_8 mixtures in a fixed bed adsorber packed with all-silica CHA operating at 353 K and 200 kPa for (a) $L/v=30000$ s, (b) $L/v=3000$ s, (c) $L/v=300$ s, and (d) $L/v=15$ s. We note that the shorter the contact time, the more severe is the influence of diffusional limitations. With decreasing contact times, the breakthroughs of C_3H_8 occur earlier, resulting in improved separations.

For any chosen value of the crystal size, i.e. chosen value of $\left(Đ_1/r_c^2\right)$, and contact time L/v, the sequence of breakthroughs is also dependent on the ratio of Maxwell-Stefan diffusivities $Đ_1/Đ_2$. To highlight this influence, Figure S75a,b,c,d present transient breakthrough simulations for the adsorption cycle for 50/50 C_3H_6/C_3H_8 mixtures in a fixed bed adsorber packed with all-silica CHA operating at 353 K and 200 kPa for (a) $Đ_1/Đ_2 = 2$, (b) $Đ_1/Đ_2 = 10$, (c) $Đ_1/Đ_2 = 100$, and (d) $Đ_1/Đ_2 = 1000$. We note that selectivity reversals are feasible only if the ratio $Đ_1/Đ_2 > 10$

For a chosen crystal size, the contact time between the gas and crystallite needs to be chosen carefully in order to obtain the optimum separations. In order to underscore this point, Figure S76 presents additional simulation data for contact times of $L/v = 2, 6, 15, 30 \quad \text{s}$, while maintaining the diffusional influences constant $Đ_1/r_c^2 = 1.7 \times 10^{-4}$ s^{-1}; $Đ_1/Đ_2 = 5000$. Figure S76b plots the % C_3H_8 of the exit gas mixture as function of $Q_{des} t \;/ m_{ads}$. We note that when the contact times are progressively lowered, the breakthroughs of the unsaturated C_3H_6 is also concomitantly influenced, with the net result that the separations are worsened. From Figure S76b we must conclude that the optimum contact time is in the range of 15 s to 30 s.

From the results in Figure S74 and Figure S76 we conclude that diffusional influences are influenced by a combination of (a) diffusional time constant, $\left(Đ_1/r_c^2\right)$, and contact time, L/v. We now demonstrate that the product of these two factors $\left(Đ_1/r_c^2\right)\left(L/v\right)$ encompasses diffusional influences, provided the ratio of M-S diffusivities $Đ_1/Đ_2$ remains unaltered.

Figure S77 presents transient breakthrough simulations for the adsorption cycle for 50/50 C_3H_6/C_3H_8 mixtures in a fixed bed adsorber packed with all-silica CHA operating at 353 K and 200 kPa for four sets of values $\left(Đ_1/r_c^2\right)$, and L/v, maintaining the values $\left(Đ_1/r_c^2\right)\left(L/v\right) = 2.55 \times 10^{-3}$. In these simulations the bed voidage $\varepsilon = 0.4$, bed length $L = 0.3$ m. In these sets of simulations, the interstitial velocities are varied such that the contact times are $L/v = 1.5, 3, 15, 30$ s; the M-S diffusivities and contact times are adjusted such that $\left(Đ_1/r_c^2\right)\left(L/v\right) = 2.55\times10^{-3}$; $Đ_1/Đ_2 = 5000$. All four sets of simulations collapse into a unique dependence of the dimensionless concentrations c_i/c_{i0} as function of $\frac{Q_0 t}{m_{ads}} = \mathrm{m}^3\ \mathrm{kg}^{-1} = \frac{t}{L/v}\frac{\varepsilon}{(1-\varepsilon)\rho}$.Figure S77 provides an important tool for interpreting and utlizing the results in laboratory scale equipment for scaling up to commercial units with different particle sizes and contact times.

We now proceed with investigating the influence of thermodynamic coupling on separations in PSA schemes.

In practice, the adsorption cycle will not be carried till bed equilibration. Rather, the adsorption cycle will be terminated just before the alkene breaks through to the exit in significant quantities. We now carryout out separations in a 2-step scheme in which the adsorption cycle, is followed by counter-current vacuum blowdown; see Figure S78.

Figure S78a shows the transient breakthrough simulations for the adsorption cycle for 50/50 C_3H_6/C_3H_8 mixtures in fixed bed adsorber packed with CHA, operating at 353 K and 200 kPa. The Maxwell-Stefan diffusivities are $Đ_1/r_c^2 = 1.7\times10^{-4}\ \mathrm{s}^{-1}$; $Đ_2/r_c^2 = 3.4\times10^{-8}\ \mathrm{s}^{-1}$; $\left(Đ_1/r_c^2\right)\left(L/v\right) = 2.55\times10^{-3}$; $Đ_1/Đ_2 = 5000$. The simulations were carried out with two different model implementations. The black colored lines are simulations based on eq (S11), The blue colored lines are simulations based on eq (S12), in which the thermodynamic correction factors are assumed to be described by $\Gamma_{ij} = \delta_{ij}$, the Kronecker delta. The dimensionless concentrations at the exit of the fixed bed, c_i/c_{i0}, are plotted as a function of time, Transient breakthrough simulations were also performed for the vacuum blowdown operations in a simplified 2-step PSA proces scheme. The vacuum blowdown is conducted at a total pressure of 2 Pa.

By application of deep vacuum (at the times 76 s and 1160 s, as indicated by the arrows in Figure S78a), both the components remaining in the adsorbed phase within the pores can be recovered. Figure S78b plots the component loadings along the dimensionless distance along the adsorber, *z*/*L*, at the termination of the adsorption cycle. For simulations based on eq (S11), the averaged adsorbed phase loadings are 1.21 and 0.087 mol kg^{-1}, respectively for C_3H_6, and C_3H_8. The corresponding average component loadings are 0.074 and 0.0042 mol kg^{-1}, respectively, for simulations based on eq (S12), in which the thermodynamic correction factors are assumed to be described by $\Gamma_{ij} = \delta_{ij}$, the Kronecker delta. Taking due account of thermodynamic coupling effects, leads to a significantly higher uptake of C_3H_6; this is a direct consequence of uphill diffusion effects, witnessed earlier in Figure S71a,b. Figure S78c plots the number of moles of C_3H_6, and C_3H_8 that are recovered as function of time, where the interstitial gas velocity during the desorption cycle is maintained at the value of 0.02 m s^{-1}. Inclusion of thermodynamic coupling effects results in the recovery of a significantly larger amount of C_3H_6; concomitantly, a larger amount of the saturated alkane is also recovered. The calculations of the % C_3H_6 in the blowdown product are plotted in Figure S78d. Taking due account of thermodynamic coupling effects, C_3H_6 with 92% purity can be produced in the 2-step PSA scheme. Neglect of thermodynamic coupling effects results in a reduced purity of 81%.

A different way to demonstrate the importance of thermodynamic coupling on kinetically driven separations is to use pulse chromatography for separation of 50/50 C_3H_6/C_3H_8 mixtures in a fixed bed adsorber packed with all-silica CHA operating at 353 K and 200 kPa. The feed pulse is injected at time t =0 and the pulse duration (see eq (S45)) is 1000 s; this is followed by deep vacuum (total pressure = 2 Pa) Three different model implementations are used in Figure S79a,b,c that plots of the dimensionless concentrations at the exit of the packed bed are plotted as a function of time. In (a) the thermodynamic coupling effects are duly accounted for by use eq (S11). In this model implementation there is clear separation of the guest constituents, and the saturated alkane C_3H_8 (blue) is eluted first, followed by the alkene C_3H_6 (indicated in red). In (b) the pulse chromatographic simulations are based on eq (S12), in which the thermodynamic correction factors are assumed to be described by $\Gamma_{ij} = \delta_{ij}$. In this scenario, the elution of the alkene C_3H_6 (indicated in red) occurs during the same time interval in which the alkane is eluted. In other words, the two components are not clearly separated. In (c) intra-crystalline diffusion effects are ignored and eq (S41) is invoked. In this scenario, the alkene elutes first, and this is followed by the more strongly adsorbed alkane. The input data on the unary isotherm parameters and M-S diffusivities are provided in Table S15.

8.3 Kinetic Separations of C_3H_6/C_3H_8 mixtures using ZIF-8

ZIF-8 has a cage-window SOD (sodalite) topology (see pore landscapes in Figure S80, and Figure S81). The crystallographic size of the windows of ZIF-8 are 3.3 Å, but the windows are flexible. Due to subtle differences in bond lengths and bond angles, the diffusivity of C_3H_6 (1) is significantly higher than that of C_3H_8 (2); Li et al.[117] report the value of the ratio $Đ_1/Đ_2$ = 125 based on the data on pure component uptakes. In ZIF-8, the adsorption strength of the saturated propane is higher than that of propene. From the unary isotherm data in Table S18, the ratio of single-site Langmuir parameter b_2/b_1 = 1.071 at 303 K. In order to appreciate the significance of thermodynamic coupling Figure S82a,b presents the calculations of the thermodynamic correction factors Γ_{ij}. We note that at a total pressure of 200 kPa, the cross-coefficients are about 80% of the magnitudes of the diagonal elements, indicating that coupling effects cannot be ignored.

Figure S82c shows the simulations of transient uptake of 50/50 $C_3H_6(1)/C_3H_8(2)$ mixtures within crystals of ZIF-8 at 303 K. The bulk gas mixture is maintained at partial pressures $p_1 = p_2 = 50$ kPa. The continuous solid lines are Maxwell-Stefan model simulations based on eq (S11). The Maxwell-Stefan diffusivities $Đ_1/r_c^2$ = 1.5×10^{-4} s^{-1}; $Đ_2/r_c^2$ = 1.2×10^{-6} s^{-1}; $Đ_1/Đ_2$ = 125. The more mobile C_3H_6 exhibits a pronounced overshoot in its approach to thermodynamic equilibrium. The attainment of supra-equilibrium loadings during the initial stages of transience signals the phenomenon of uphill diffusion,[12, 41] and enhanced separation. The dashed lines in Figure S82c are the simulations based on eq (S12), in which the thermodynamic correction factors are assumed to be described by $\Gamma_{ij} = \delta_{ij}$, the Kronecker delta. In this scenario, no C_3H_6 overshoot is observed indicating that thermodynamic coupling effects are the root cause of uphill diffusion.

We turn our attention to the separation of 50/50 C_3H_6(1)/C_3H_8(2) mixtures in fixed bed adsorbers packed with crystals of ZIF-8 operating at 353 K and total pressure of 100 kPa. Our initial focus is on the adsorption cycle and the influence of crystallite size in the packed bed. Rather than vary the crystal size, we consider the influence of the diffusional time constant, $Đ_1/r_c^2$; the ratio of M-S diffusivities is held constant $Đ_1/Đ_2=125$. In these set of simulations the bed voidage $\varepsilon = 0.4$, bed length $L = 0.3 \quad \text{m}$, the interstitial velocities $v = 0.1 \quad \text{m s}^{-1}$; the contact times are $L/v = 3 \quad \text{s}$. The *x*-axis used is

$$\frac{Q_0 t}{m_{ads}} = \text{m}^3 \text{ kg}^{-1} = \frac{t}{L/v} \frac{\varepsilon}{(1-\varepsilon)\rho}.$$

Figure S83a presents the breakthrough simulations for the scenario in which the diffusional time constant $\left(Đ_1/r_c^2\right) = 1.5 \text{ s}^{-1}$, i.e. diffusional influences are practically insignificant and in this scenario, the unsaturated C_3H_6 breaks through earlier than the saturated C_3H_8 because the mixture adsorption favors the saturated alkane; see the unary isotherm data are provided in Table S18.

Figure S83b,c,d,e,f present the breakthrough simulation results for increasing crystal sizes: (b) $\left(Đ_1/r_c^2\right) = 1.5\times10^{-2} \text{ s}^{-1}$. (c) $\left(Đ_1/r_c^2\right) = 3.75\times10^{-3} \text{ s}^{-1}$. (d) $\left(Đ_1/r_c^2\right) = 6.0\times10^{-4} \text{ s}^{-1}$, (e) $\left(Đ_1/r_c^2\right) = 2.34\times10^{-4} \text{ s}^{-1}$ (f) $\left(Đ_1/r_c^2\right) = 1.5\times10^{-4} \text{ s}^{-1}$. The continuous solid lines are Maxwell-Stefan model simulations based on eq (S11). The Maxwell-Stefan diffusivities $Đ_1/r_c^2$ = 1.5×10^{-4} s^{-1}; $Đ_2/r_c^2$ = 1.2×10^{-6} s^{-1}; $Đ_1/Đ_2$ = 125. The dashed lines in (c) are the simulations based on eq (S12) in which the thermodynamic correction factors are assumed to be described by $\Gamma_{ij} = \delta_{ij}$, the Kronecker delta. With increasing diffusional influence, i.e. decreasing values of $\left(Đ_1/r_c^2\right)$, the breakthroughs of both C_3H_8 and C_3H_6 occur earlier. Since the ratio $Đ_1/Đ_2=125$, the influence on the breakthrough of the saturated alkane is more severe.

To quantify the diffusional influences on separations, the productivity of purified C_3H_8(2), containing less than 1% C_3H_6, is determined from a material balance from the simulation data. Figure S84 plots the productivity of purified C_3H_8(2) as a function of the diffusional time constant $\left(Đ_1/r_c^2 \right)$.

The important message is that for kinetically driven separations to be effective there is an optimum crystal size, i.e. optimum value of the diffusional time constant, $\left(Đ_1/r_c^2 \right)$. The optimum value of the diffusional time constant $\left(Đ_1/r_c^2 \right) = 3.75\times10^{-3}$ s^{-1}.

For any chosen value of the crystal size, i.e. chosen value of $\left(Đ_1/r_c^2 \right)$, the severity of diffusional influences are also dependent on the contact time between the gas mixture and the crystallites; this contact time is L/v, where v is the interstitial gas velocity. To illustrate this influence, Figure S85a,b,c,d present transient breakthrough simulations for the adsorption cycle for 50/50 C_3H_6/C_3H_8 mixtures in a fixed bed adsorber packed with ZIF-8 operating at 303 K and 100 kPa for (a) $L/v = 30 \quad s$, (b) $L/v = 6 \quad s$, (c) $L/v = 3 \quad s$, and (d) $L/v = 2 \quad s$. The diffusional time constant is maintained at the optimum value $\left(Đ_1/r_c^2 \right) = 3.75\times10^{-3}$ s^{-1}. We note that the shorter the contact time, the more severe is the influence of diffusional limitations. With decreasing contact times, the breakthroughs of C_3H_8 occur progressively earlier, resulting in improved separations.

To quantify the influence of the contact time on separations, the productivity of purified C_3H_8(2), containing less than 1% C_3H_6, is determined from a material balance from the simulation data. Figure S86 plots the productivity of purified C_3H_8(2) as a function of the gas-crystal contact time L/v. Decreasing contact time is beneficial to the attainment of higher productivities.

For any chosen value of the crystal size, i.e. chosen value of $\left(Đ_1/r_c^2 \right)$, and contact time L/v, the sequence of breakthroughs is also dependent on the ratio of Maxwell-Stefan diffusivities $Đ_1/Đ_2$. To highlight this influence, Figure S87a,b,c,d present transient breakthrough simulations for the adsorption cycle for 50/50 C_3H_6/C_3H_8 mixtures in a fixed bed adsorber packed with ZIF-8 operating at 303 K and

100 kPa for (a) $Đ_1/Đ_2 = 1$, (b) $Đ_1/Đ_2 = 2$, (c) $Đ_1/Đ_2 = 125$, and (d) $Đ_1/Đ_2 = 1000$. We note that selectivity reversals are feasible only if the ratio $Đ_1/Đ_2 > 2$.

Figure S88 presents transient breakthrough simulations for the adsorption cycle for 50/50 C_3H_6/C_3H_8 mixtures in a fixed bed adsorber packed with ZIF-8 operating at 303 K and 100 kPa. In these sets of simulations the interstitial velocities are varied such that the contact times are $L/v = 3, 0.75, 6.75, 1.6875 \quad \text{s}$; the diffusional time constants are adjusted such that $\left(Đ_1/r_c^2\right)\left(L/v\right) = 1.125 \times 10^{-2}$; $Đ_1/Đ_2 = 125$. The unary isotherm data are provided in Table S18.All these four sets of simulations collapse into a unique breakthrough curve, when plotted as function of $\frac{Q_0 t}{m_{ads}} = \frac{t}{L/v} \frac{\varepsilon}{(1-\varepsilon)\rho}$. Figure S88 provides an important tool for interpreting and utlizing the results in laboratory scale equipment for scaling up to commercial units with different particle sizes and contact times.

8.4 Kinetic Separations of C_3H_6/C_3H_8 mixtures using KAUST-7

Figure S89 presents transient breakthrough simulations for the adsorption cycle for 50/50 C_3H_6/C_3H_8 mixtures in fixed-bed adsorber packed with KAUST-7,[96] operating at 298 K and 100 kPa. In these simulations the bed voidage $\varepsilon = 0.4$, bed length $L = 0.3 \quad \text{m}$, The interstitial velocities are varied such that the contact times are $L/v = 1.5, 3, 15, 30 \quad \text{s}$; the diffusional time constants times are adjusted such that $\left(Đ_1/r_c^2\right)\left(L/v\right) = 6 \times 10^{-3}$; $Đ_1/Đ_2 = 100$. The unary isotherm data are provided in Table S16. All these four sets of simulations collapse into a unique breakthrough curve, when plotted as function of $\frac{Q_0 t}{m_{ads}} = \frac{t}{L/v} \frac{\varepsilon}{(1-\varepsilon)\rho}$. Figure S89 provides an important tool for interpreting and utlizing the results in laboratory scale equipment for scaling up to commercial units with different particle sizes and contact times.

8.5 List of Tables for Kinetic Separations of Alkene/Alkane Mixtures

Table S15. 1-site Langmuir parameters for C_3H_6, and C_3H_8 in all-silica CHA zeolite at 353 K. These isotherm data are taken from Table 4 of Khalighi et al.[22]

	$\frac{q_{sat}}{\text{mol kg}^{-1}}$	$\frac{b}{\text{Pa}^{-1}}$
C_3H_6	2.9	3×10^{-5}
C_3H_8	2.9	8×10^{-5}

On the basis of the information provided in Table 4 of Khalighi et al.,[22] the Maxwell-Stefan diffusivities are $Đ_1/r_c^2$ = 1.7×10^{-4} s^{-1}; $Đ_2/r_c^2$ = 3.4×10^{-8} s^{-1}; $Đ_1/Đ_2$ = 5000.

Table S16. 1-site Langmuir parameters for C_3H_6, and C_3H_8 in in KAUST-7. These isotherm fit parameters were determined by scanning the experimental data at 298 K as reported in Figures 3b of Cadiau et al.[96]

	$\frac{q_{sat}}{\text{mol kg}^{-1}}$	$\frac{b}{\text{Pa}^{-1}}$
C_3H_6	2.1	2.6×10^{-5}
C_3H_8	2.1	2×10^{-7}

The M-S diffusivities are $Đ_1/r_c^2 = 2\times10^{-3}\ \text{s}^{-1}$; $Đ_2/r_c^2 = 2\times10^{-5}\ \text{s}^{-1}$; $Đ_1/Đ_2 = 100$.

Table S17. 1-site Langmuir parameters for C_2H_4 and C_2H_6 in Co-gallate pellets at 298 K. These parameters have been re-fitted using the DSLF parameters provided in Table S1 of Wu et al.[111]

	$\frac{q_{sat}}{\text{mol kg}^{-1}}$	$\frac{b}{\text{Pa}^{-1}}$
C_2H_4	4	3.449E-05
C_2H_6	0.5	1.441E-05

Table S18. 1-site Langmuir parameters for propene and propane in ZIF-8.[118] The *T*-dependent parameters are obtained by fitting the combined sets of pure component isotherm data of Li et al.[117] and Böhme et al.[108] determined for a variety of temperatures in the range 273 K to 408 K.

$$q = q_{sat}\frac{bp}{1+bp};\; b_A = b_0\exp\left(\frac{E}{RT}\right)$$

	$\frac{q_{sat}}{\text{mol kg}^{-1}}$	$\frac{b_0}{\text{Pa}^{-1}}$	$\frac{E}{\text{kJ mol}^{-1}}$
propene	5.2	4.57×10^{-11}	33.9
propane	5.2	1.39×10^{-10}	31.3

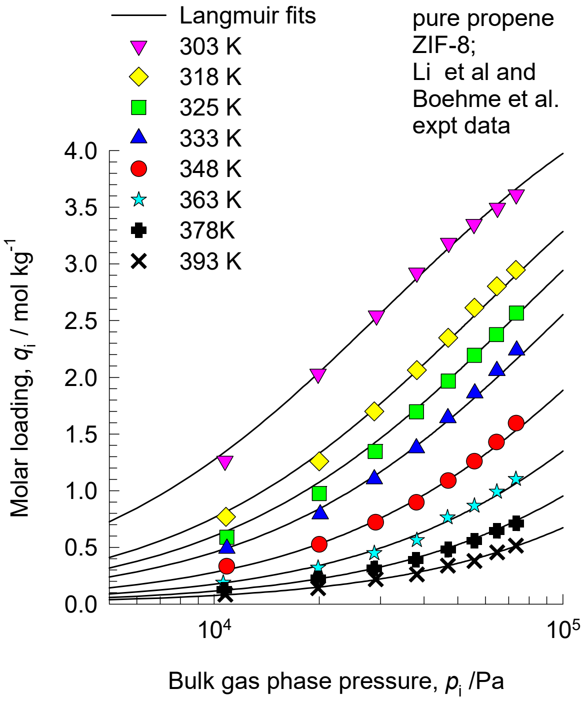

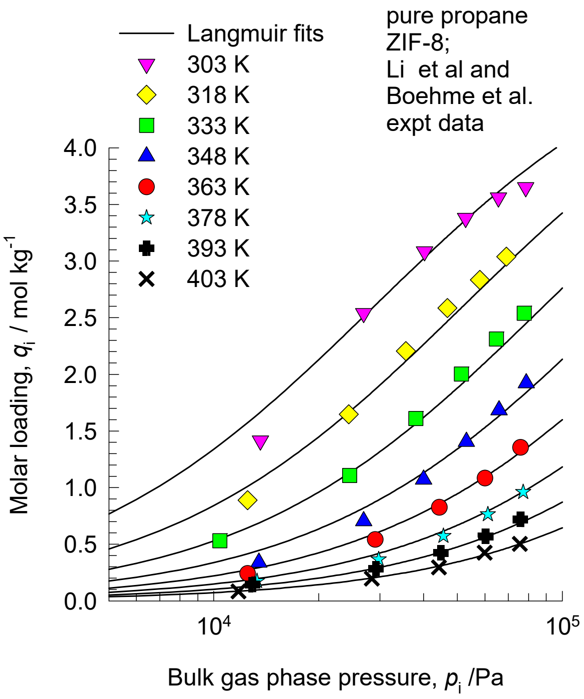

8.6 List of Figures for Kinetic Separations of Alkene/Alkane Mixtures

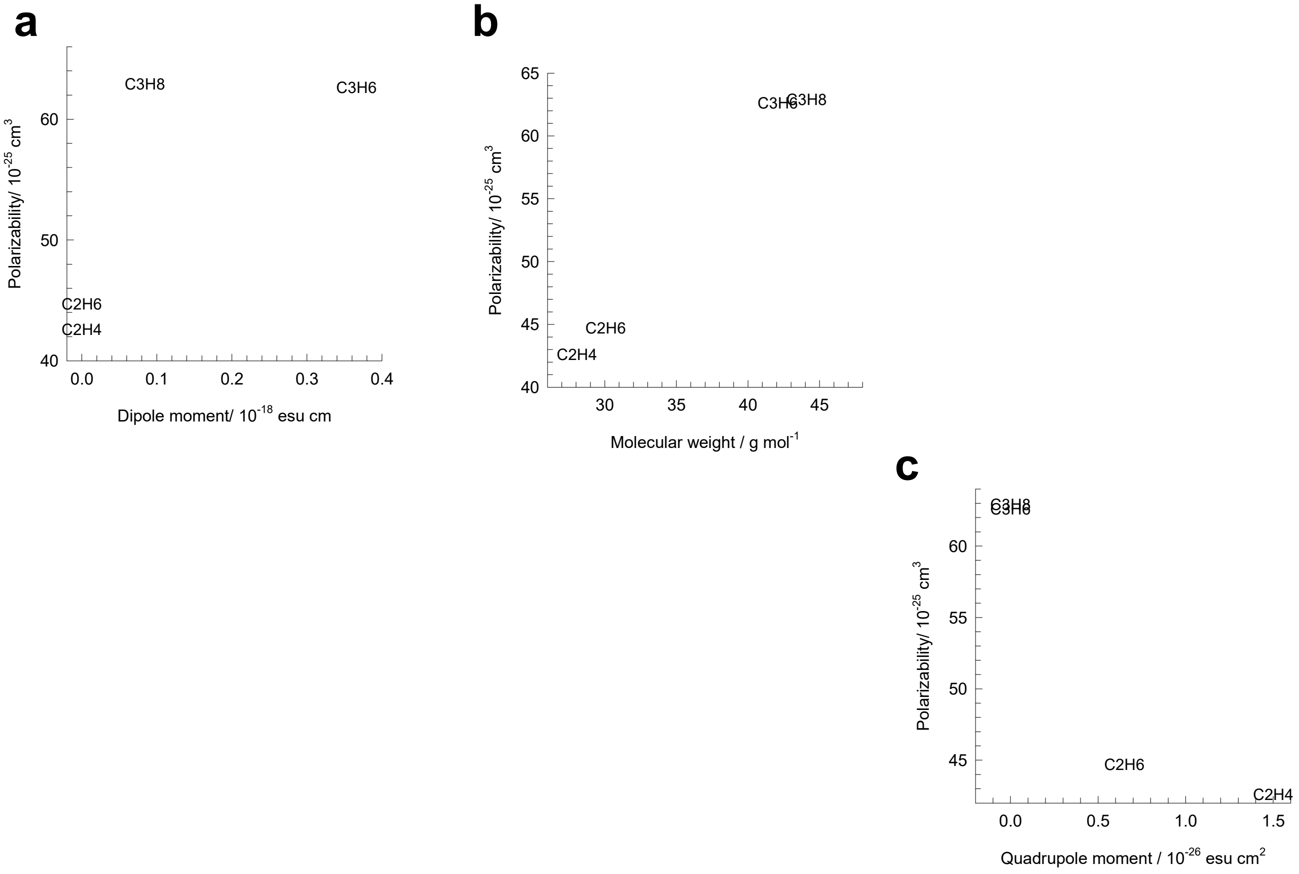

Figure S56. (a, b, c) Polarizabilities, dipole moments, and quadrupole moments of C_2H_4, C_2H_6, C_3H_6, and C_3H_8. The data are taken from Sircar and Myers.[119]

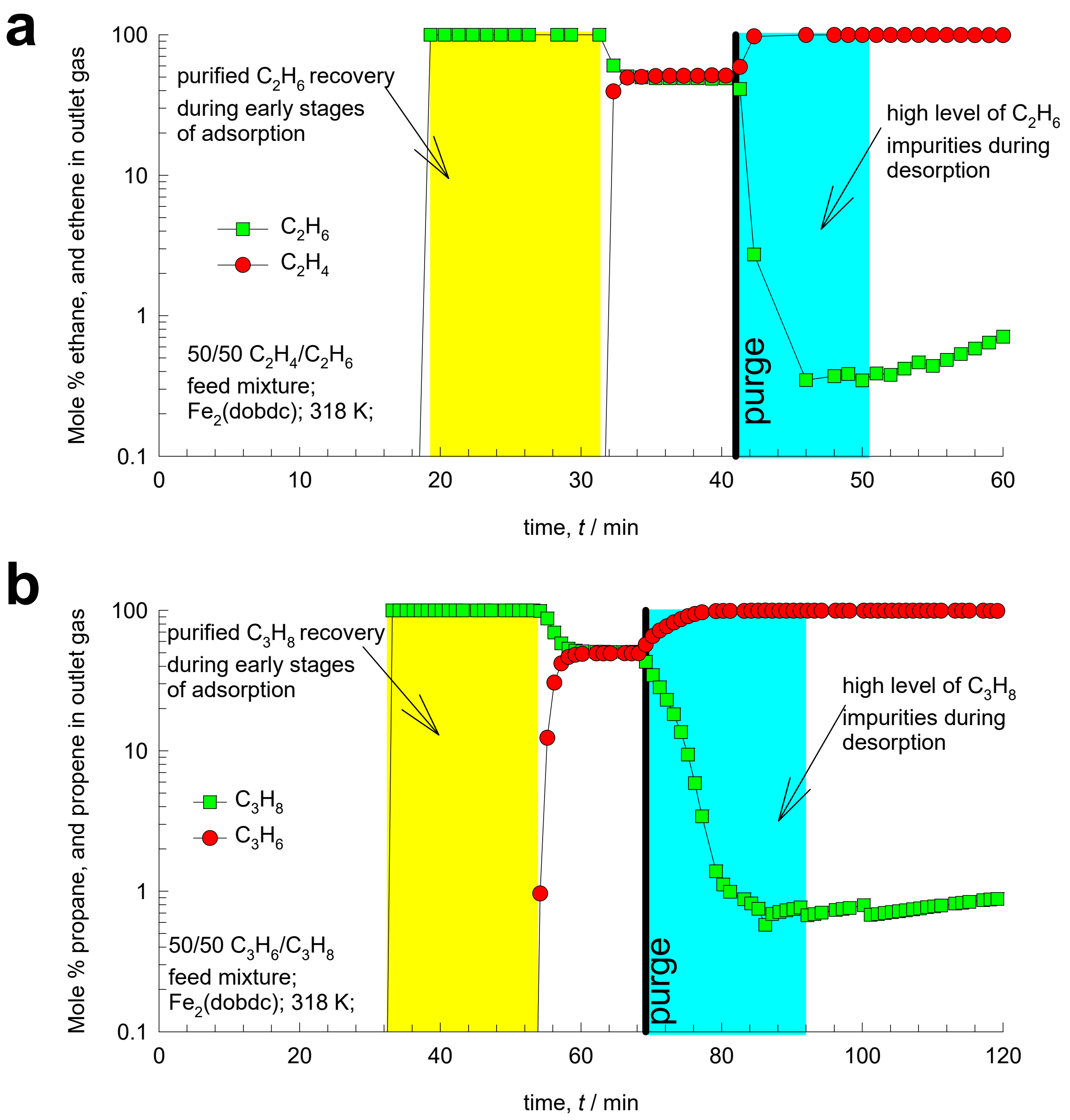

Figure S57. (a, b) Adsorption/desorption cycles for separation of (a) 50/50 C_2H_4/C_2H_6, and (b) 50/50 C_3H_6/C_3H_8 mixtures in a fixed bed adsorber packed with Fe_2(dobdc)[95] and operating at 318 K. The desorption cycle is initiated by nitrogen purge.

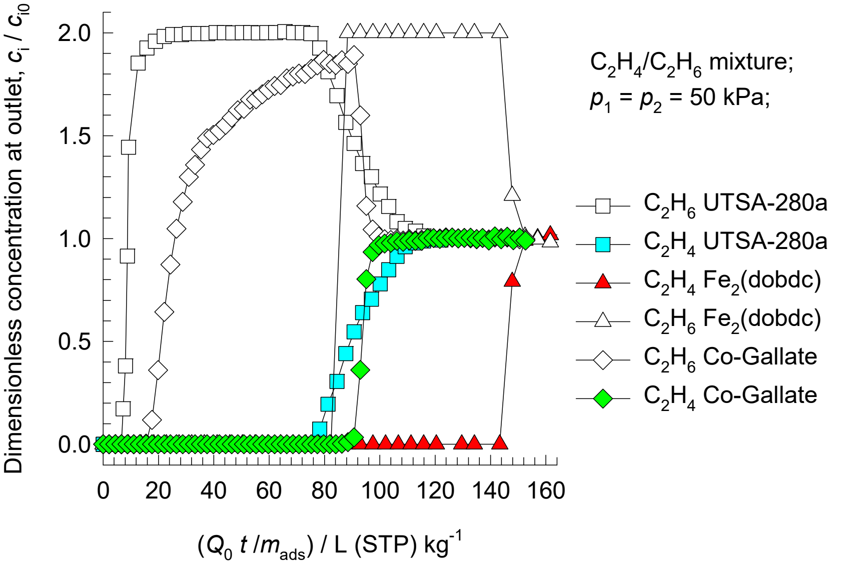

Figure S58. Experimental data on transient breakthroughs for separation of 50/50 C_2H_4/C_2H_6 mixtures in a fixed bed adsorber packed with: UTSA-280,[72] Co-gallate,[98] and Fe_2(dobdc).[95] The dimensionless concentrations at the exit of the fixed bed, c_i/c_{i0} , (open symbols = C_2H_6; filled symbols = C_2H_4) are plotted as a function of Q_0t/m_{ads} , where Q_0 is the volumetric flow rate of the gas mixture at the inlet to the fixed bed, expressed in L s^{-1}, at STP conditions.

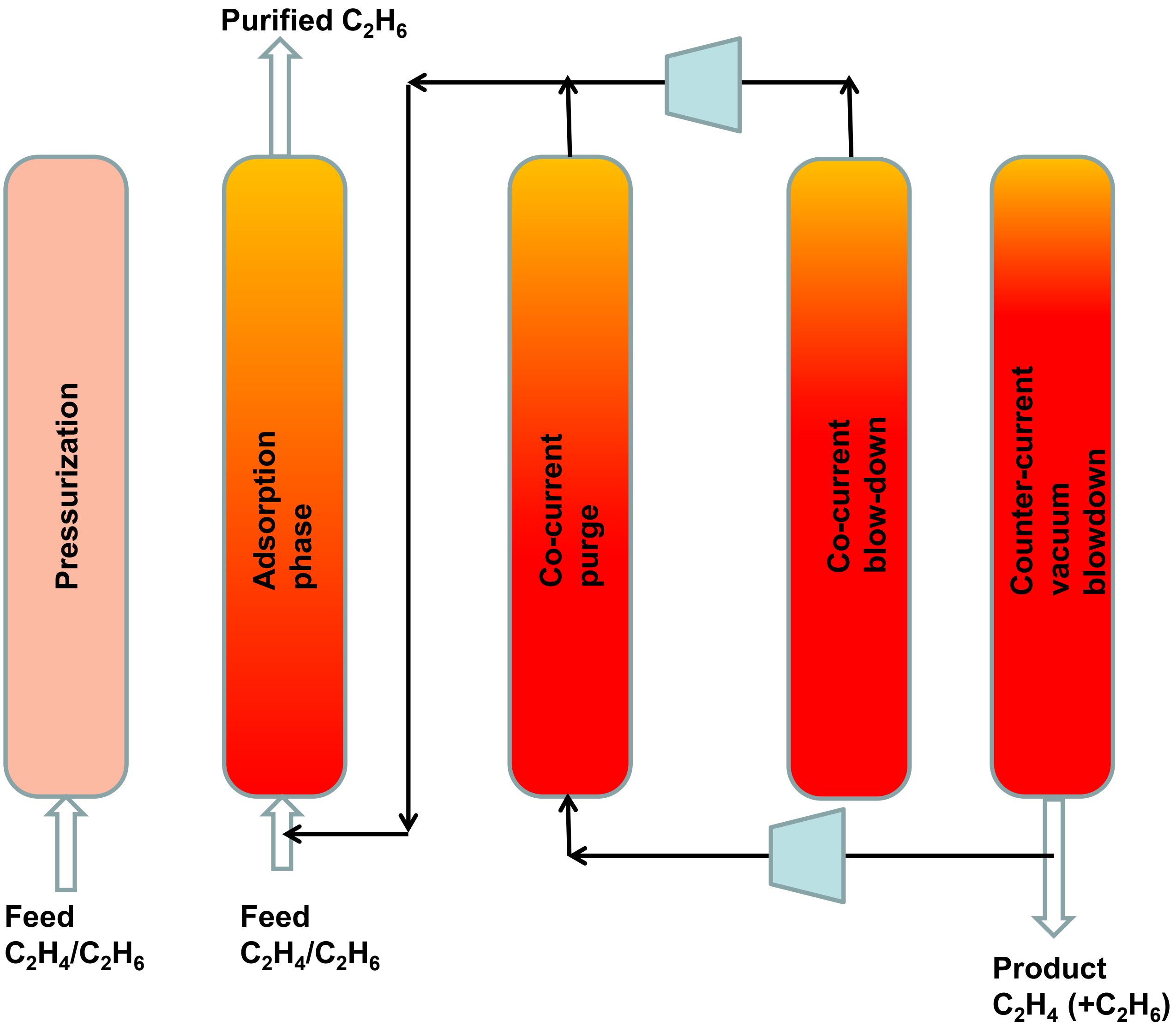

Figure S59. Five-step PSA process for separating C_2H_4/C_2H_6 mixtures.[102, 104, 109]

Laboratory scale breakthrough tube		**Commercial scale unit**
$d = 10 \quad \text{mm}$	**Internal diameter of fixed bed**	$d = 0.46 \quad \text{m}$
$L = 50 \quad \text{mm}$	**Length (height) of fixed bed**	$L = 4.61 \quad \text{m}$
ε=0.57	**Bed voidage**	ε=0.57
$Q_0 = 1 \quad \text{mL min}^{-1}$	**Flow rate at inlet to fixed bed**	$Q_0 = 1.9 \quad \text{m}^3\ \text{min}^{-1}$
$u = 0.2 \quad \text{mm s}^{-1}$	**Superficial gas velocity**	$u = 0.19 \quad \text{m s}^{-1}$
$v = 0.37 \quad \text{mm s}^{-1}$	**Interstitial gas velocity**	$v = 0.34 \quad \text{m s}^{-1}$
$\left(L/v\right) = 130 \quad \text{s}$	**Average contact time**	$\left(L/v\right) = 13.7 \quad \text{s}$
$\left(Đ_1/r_c^2\right) = 2.9\times10^{-4} \quad \text{s}^{-1}$	**Diffusional time constant**	$\left(Đ_1/r_c^2\right) = 2.9\times10^{-4} \quad \text{s}^{-1}$
$\left(Đ_1/r_c^2\right)\left(L/v\right) = 3.8\times10^{-2}$	**Diffusional time constant X contact time**	$\left(Đ_1/r_c^2\right)\left(L/v\right) = 4\times10^{-3}$

Figure S60. Comparison of the dimensions and operating conditions for the laboratory apparatus with the corresponding parameters for the larger scale commercial unit for which ASPEN PSA simulations as reported Yan et al.[112] for C_2H_4(1)/C_2H_6(2) mixtures in a fixed bed adsorber packed with Co-gallate pellets, operating at 298 K and 100 kPa.

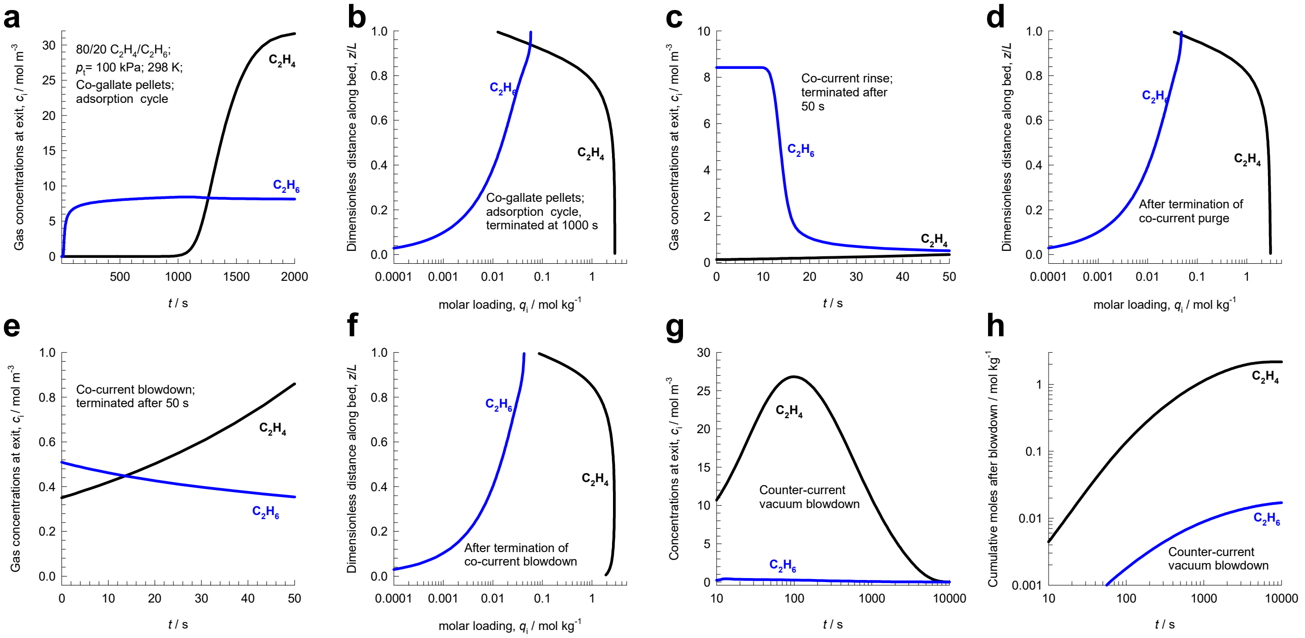

Figure S61. Transient breakthrough simulations for the 5-step PSA scheme for 80/20 $C_2H_4(1)/C_2H_6(2)$ mixtures in a fixed bed adsorber packed with Co-gallate pellets, operating at 298 K and 100 kPa. (a, b) Plots of the (a) gas phase concentrations exiting the adsorption cycle, and (b) component loadings along the dimensionless distance, z/L, along the length of the adsorber at the termination of the adsorption cycle. (c, d) Plots of the (c) gas phase concentrations exiting the co-current purge, and (d) component loadings along the dimensionless distance, z/L, along the length of the adsorber at the termination of the co-current purge. (e, f) Plots of the (e) gas phase concentrations exiting the co-current blowdown, and (d) component loadings along the dimensionless distance, z/L, along the length of the adsorber at the termination of the co-current blowdown. (g, h) Plots of the (g) gas phase concentrations exiting the counter-current vacuum blowdown, and (h) cumulative molar loadings of the components exiting the vacuum blowdown phase. In all these simulations, the thermodynamic coupling effects are taken into account.

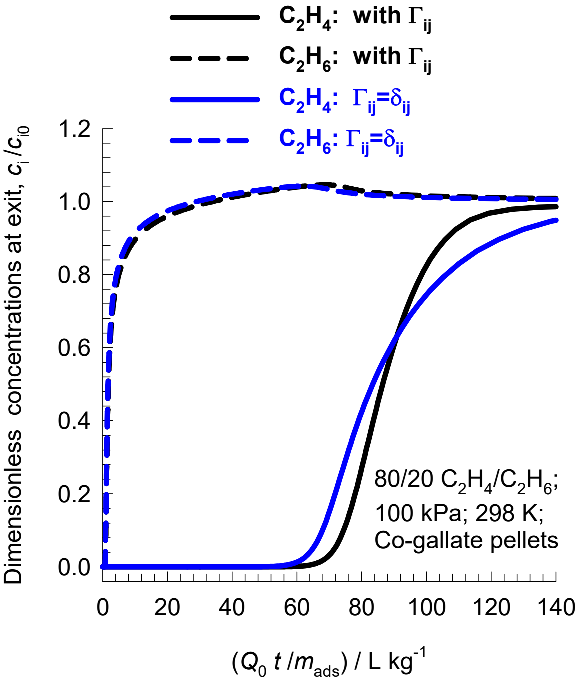

Figure S62. Influence of thermodynamic coupling on the adsorption cycle for 80/20 $C_2H_4(1)/C_2H_6(2)$ mixtures in a fixed bed adsorber packed with Co-gallate pellets, operating at 298 K and 100 kPa.

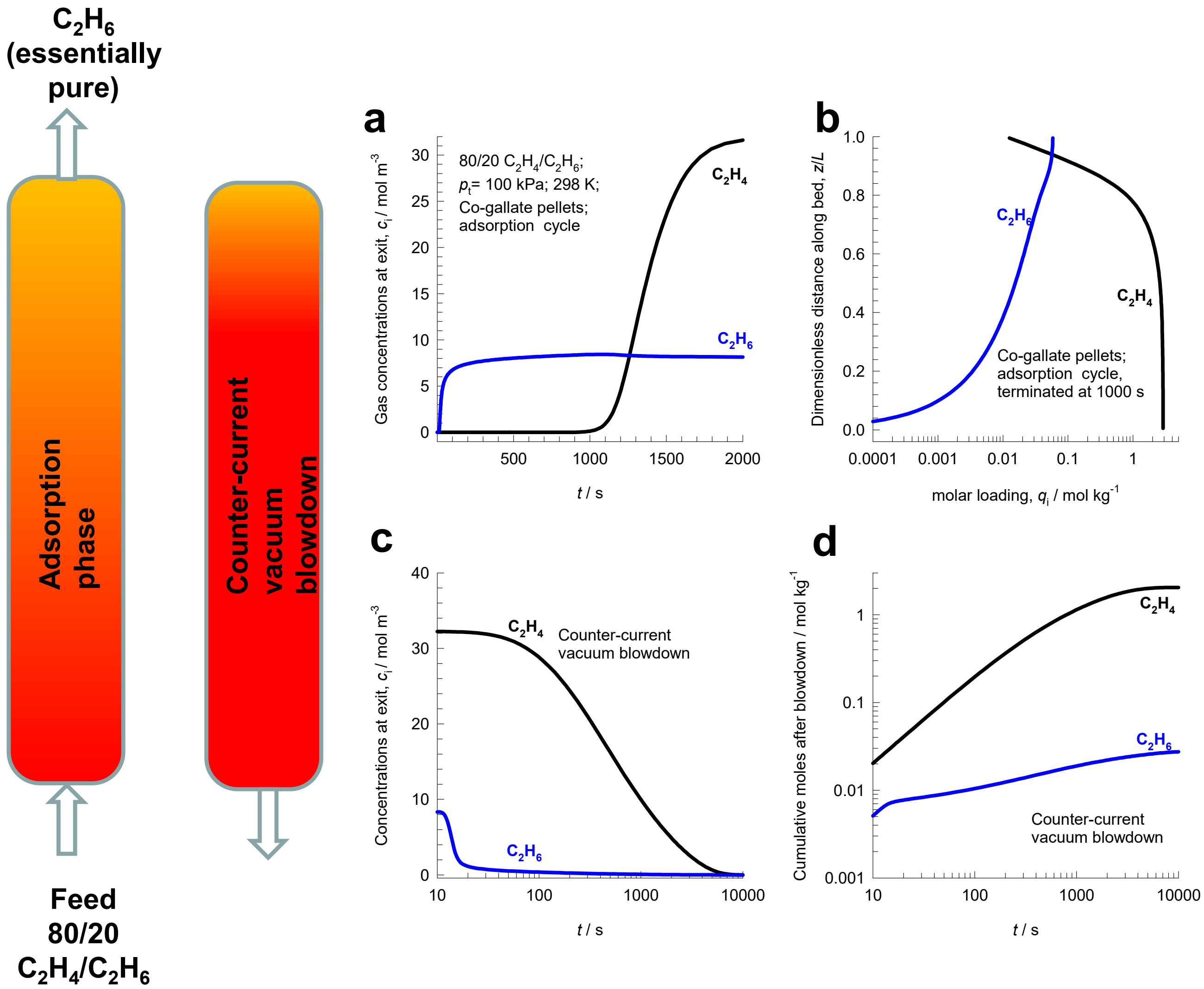

Figure S63. Transient breakthrough simulations for the 2-step PSA scheme for 80/20 C_2H_4(1)/C_2H_6(2) mixtures in a fixed bed adsorber packed with Co-gallate pellets, operating at 298 K and 100 kPa. (a, b) Plots of the (a) gas phase concentrations exiting the adsorption cycle, and (b) component loadings along the dimensionless distance, *z*/*L*, along the length of the adsorber at the termination of the adsorption cycle. (c, d) Plots of the (c) gas phase concentrations exiting the counter-current vacuum blowdown, and (d) cumulative molar loadings of the components exiting the vacuum blowdown phase. In all these simulations, the thermodynamic coupling effects are taken into account.

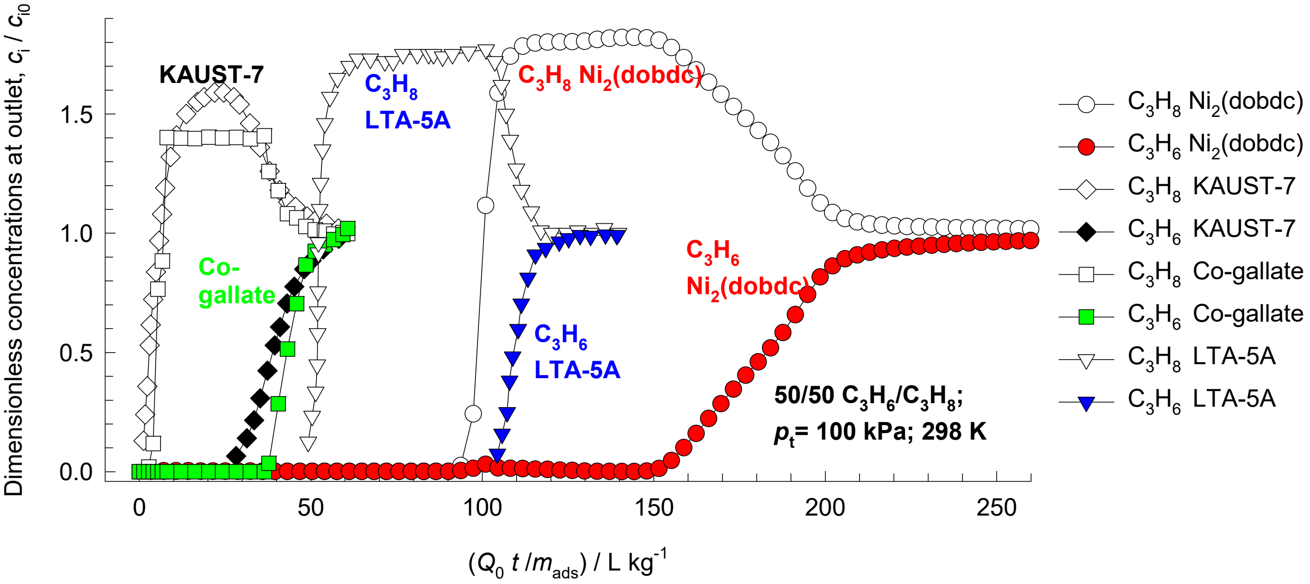

Figure S64. Experimental data on transient breakthroughs for separation of 50/50 C_3H_6/C_3H_8 mixtures in a fixed bed adsorber packed with: KAUST-7,[96] Co-gallate,[110] LTA-5A zeolite,[96] and Ni_2(dobdc).[113] The dimensionless concentrations at the exit of the fixed bed, c_i/c_{i0}, (open symbols = C_3H_8; filled symbols = C_3H_6) are plotted as a function of Q_0t/m_{ads}, where Q_0 is the volumetric flow rate of the gas mixture at the inlet to the fixed bed, expressed in L s^{-1}, at STP conditions.

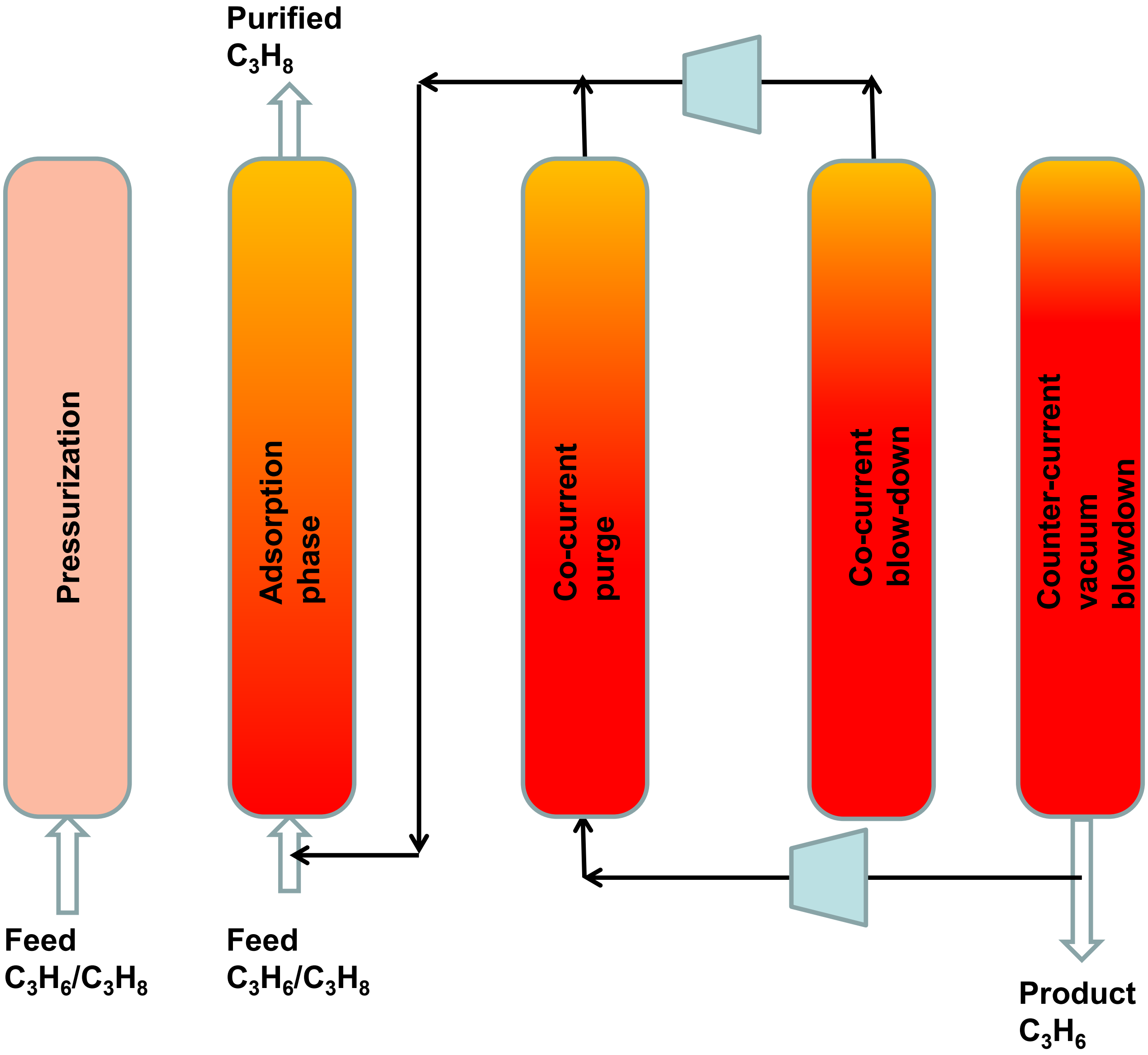

Figure S65. Five-step PSA process for separating C_3H_6/C_3H_8 mixtures.[102, 104, 109]

Figure S66. Simplified 2-step PSA process for separating C_3H_6/C_3H_8 mixtures.

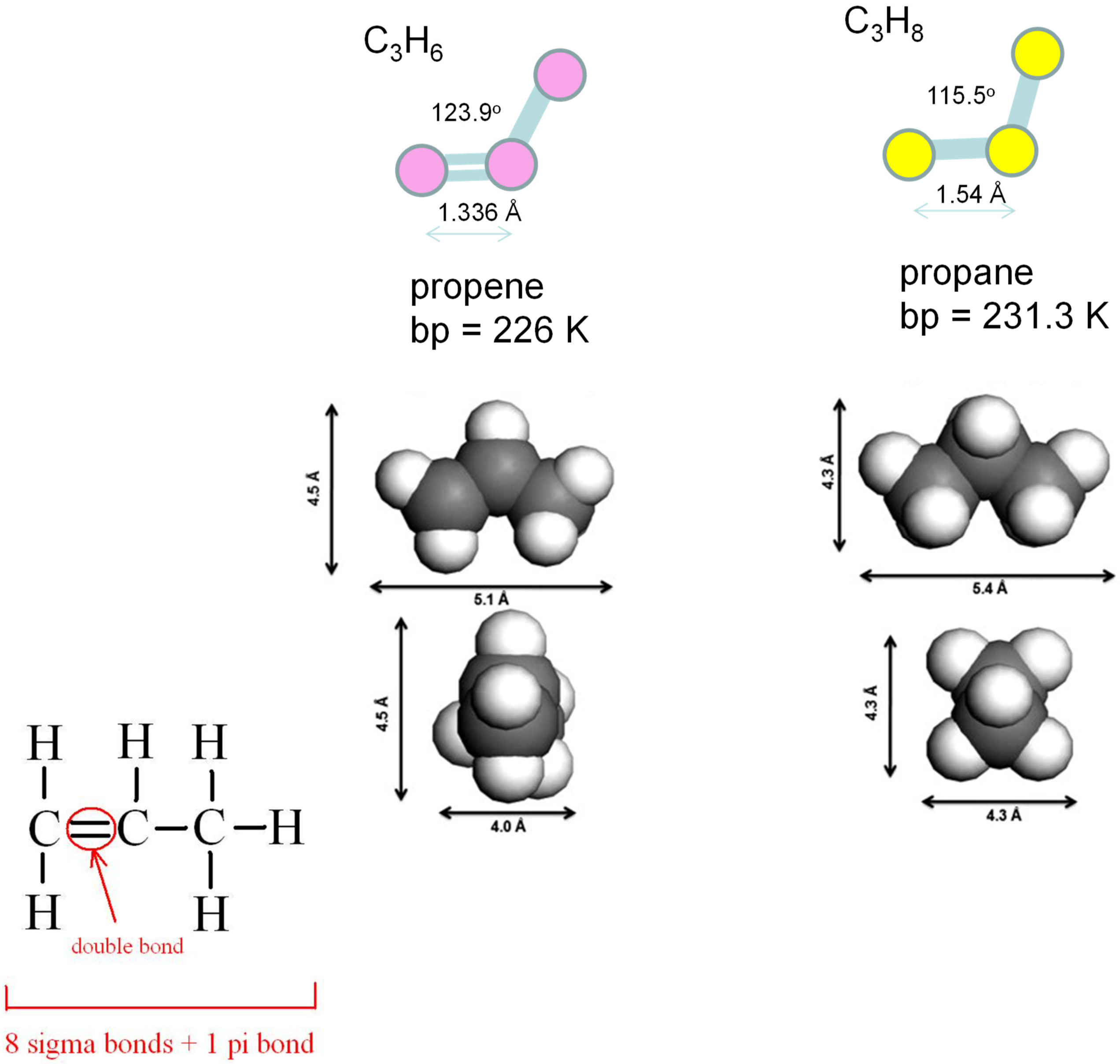

Figure S67. Molecular dimensions of C_3H_6 and C_3H_8, culled from the literature.[120]

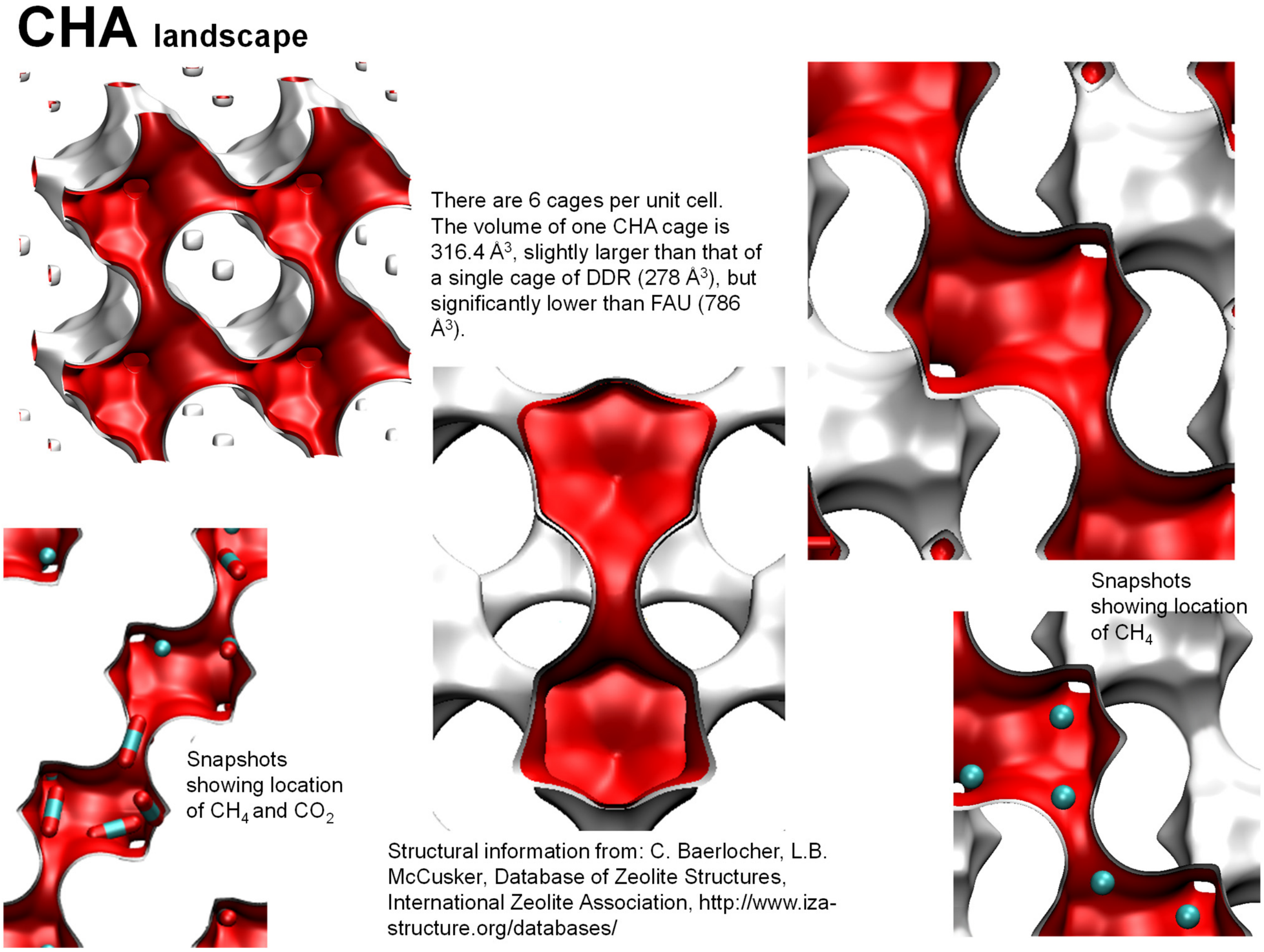

There are 6 cages per unit cell. The volume of one CHA cage is 316.4 Å^3, slightly larger than that of a single cage of DDR (278 Å^3), but significantly lower than FAU (786 Å^3).

Snapshots showing location of CH_4

Snapshots showing location of CH_4 and CO_2

Structural information from: C. Baerlocher, L.B. McCusker, Database of Zeolite Structures, International Zeolite Association, http://www.iza-structure.org/databases/

Figure S68. Pore landscape and structural details of all-silica CHA zeolite, also called SiCHA.

CHA window and pore dimensions

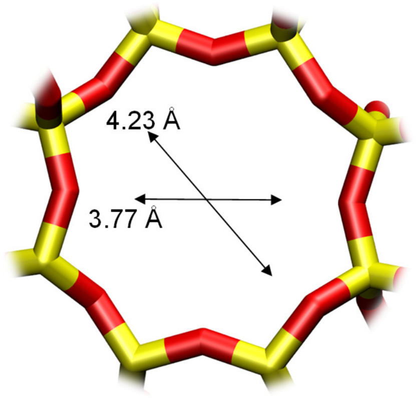

CHA

The window dimensions calculated using the van der Waals diameter of framework atoms = 2.7 Å are indicated above by the arrows.

	CHA
a /Å	15.075
b /Å	23.907
c /Å	13.803
Cell volume / Å^3	4974.574
conversion factor for [molec/uc] to [mol per kg Framework]	0.2312
conversion factor for [molec/uc] to [kmol/m^3]	0.8747
ρ [kg/m3]	1444.1
MW unit cell [g/mol(framework)]	4326.106
ϕ, fractional pore volume	0.382
open space / Å^3/uc	1898.4
Pore volume / cm^3/g	0.264
Surface area /m^2/g	758.0
DeLaunay diameter /Å	3.77

Figure S69. Pore landscape and structural details of all-silica CHA zeolite, also called SiCHA.

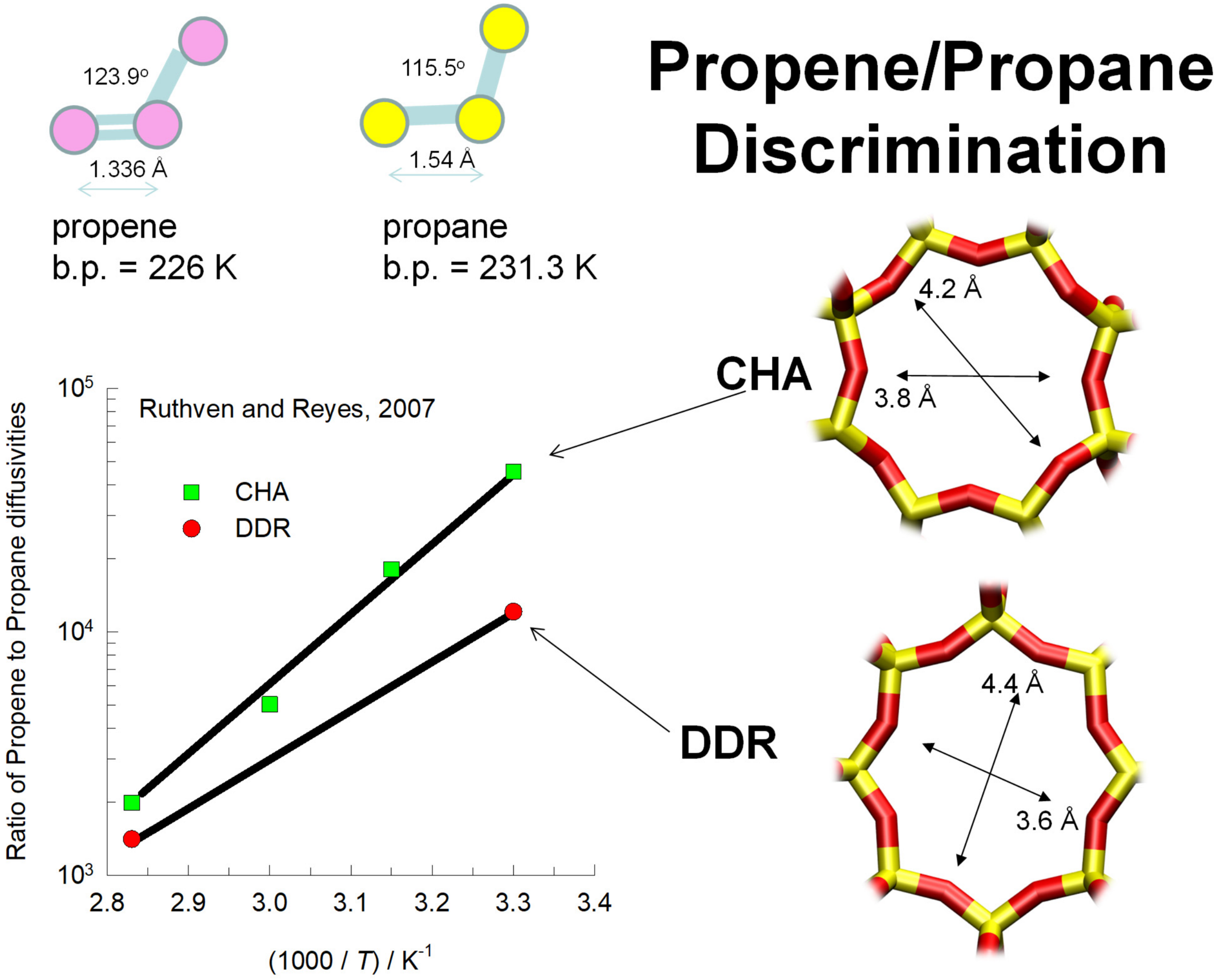

Figure S70. Data of Ruthven and Reyes[116] for the ratio of diffusivities of propene to that of propane in all-silica CHA and DDR zeolites.

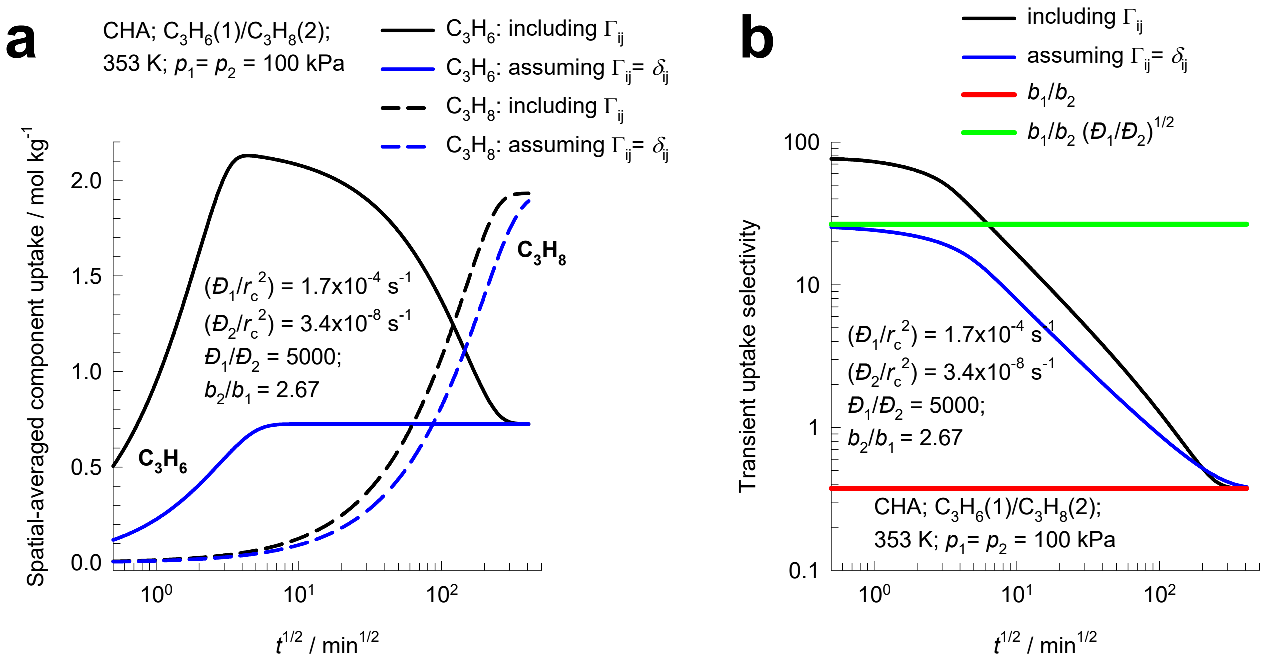

Figure S71. (a) Simulations of transient uptake of 50/50 $C_3H_6(1)/C_3H_8(2)$ mixtures within crystals of all-silica CHA at 353 K, and total pressure of 200 kPa. The spatial averaged component loadings are plotted as a function of $\sqrt{t}$. The black lines are simulations based on eq (S11). The blue lines are simulations based on eq (S12), in which the thermodynamic correction factors are assumed to be described by $\Gamma_{ij} = \delta_{ij}$. (b) Transient uptake selectivity. The unary isotherms and diffusivity data are provided in Table S15.

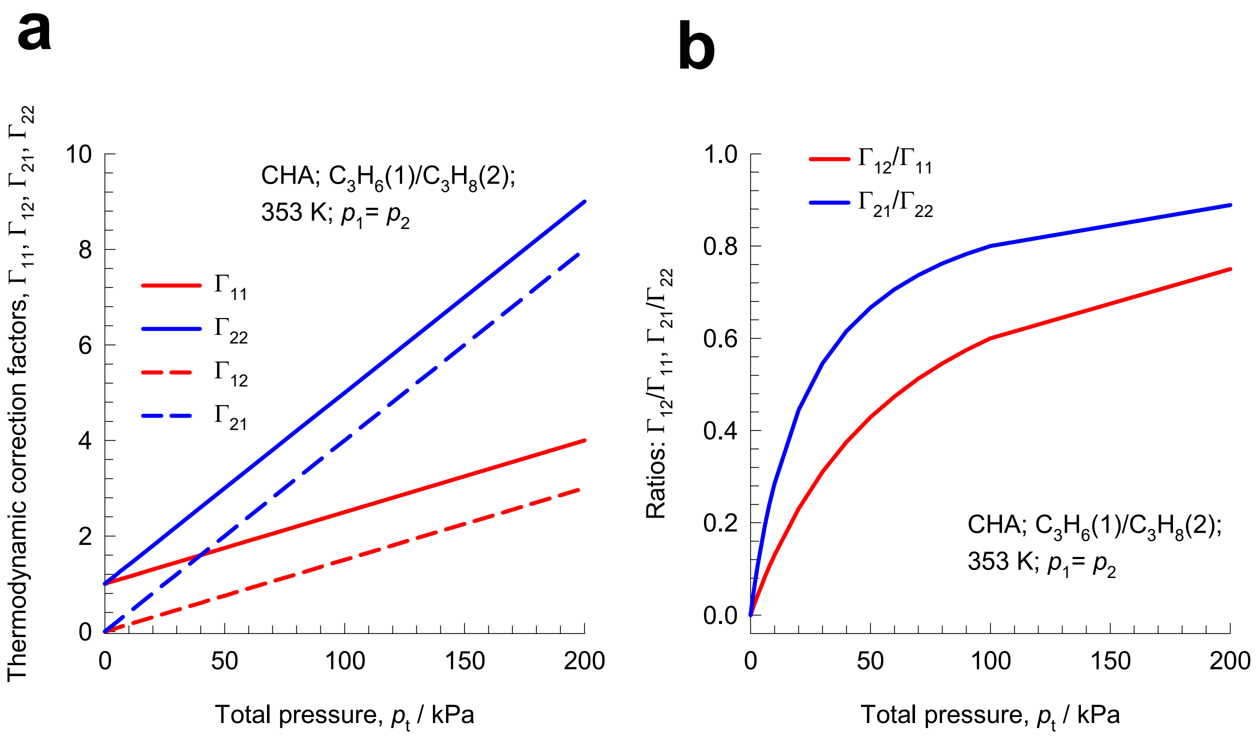

Figure S72. (a) Calculations of the elements of the matrix of thermodynamic factors for 50/50 C_3H_6(1)/C_3H_8(2) mixture adsorption within crystals of all-silica CHA at 353 K (b) Ratios of the off-diagonal elements to the diagonal elements of the matrix of thermodynamic factors.

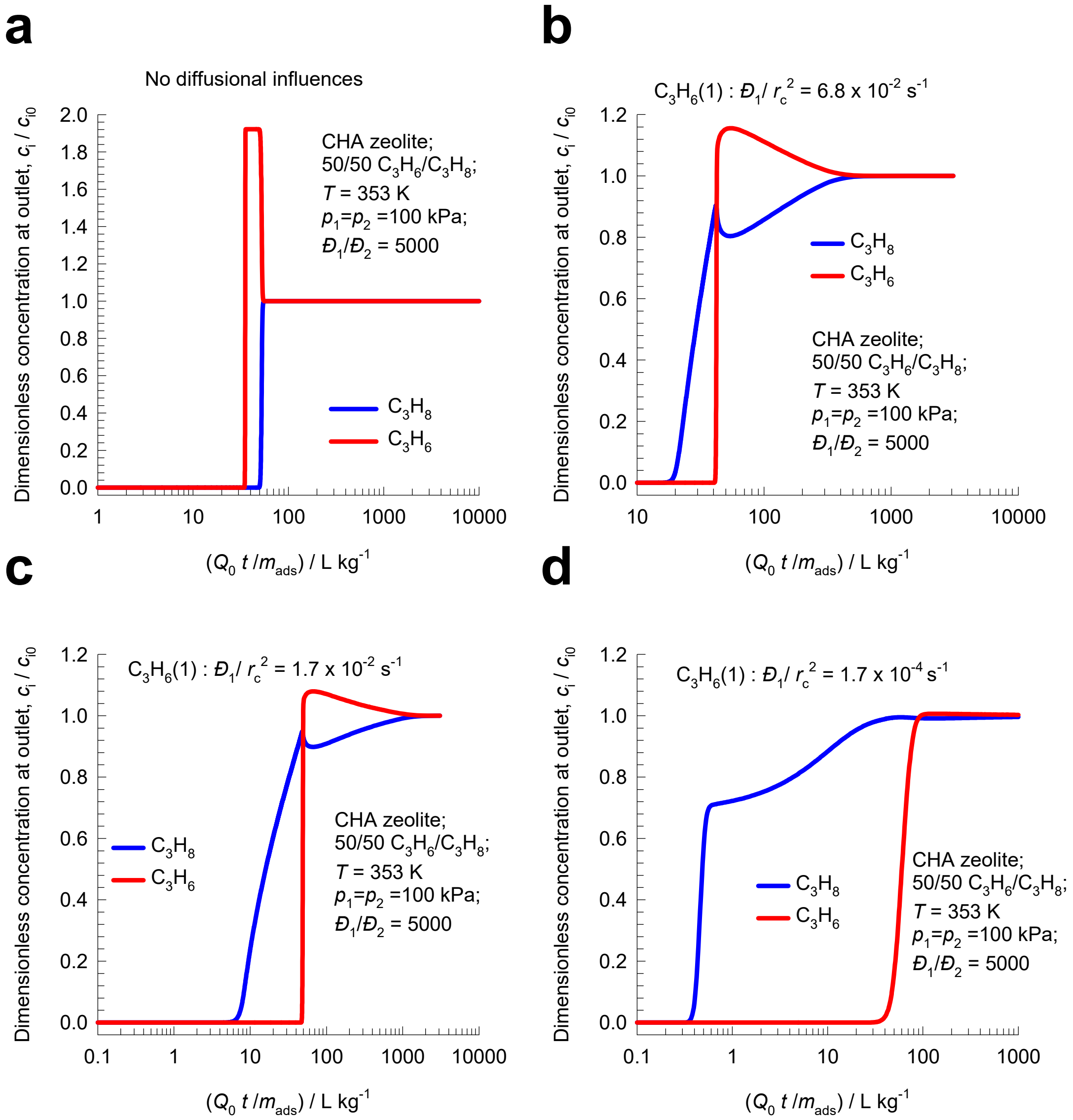

Figure S73. Influence of diffusional time constant $\left(Đ_1/r_c^2\right)$ on transient breakthrough simulations for the adsorption cycle for 50/50 C_3H_6/C_3H_8 mixtures in a fixed bed adsorber packed with all-silica CHA operating at 353 K and 200 kPa. In these simulations the bed voidage $\varepsilon = 0.4$, bed length $L = 0.3$ m, the ratio of M-S diffusivities are $Đ_1/Đ_2 = 5000$, the interstitial velocities $v = 0.02$ m s^{-1}; the contact times are $L/v = 15$ s. (a) Diffusional time constant $\left(Đ_1/r_c^2\right) \to \infty$. (b) $\left(Đ_1/r_c^2\right) = 6.8\times10^{-2}$ s^{-1}. (c) $\left(Đ_1/r_c^2\right) = 1.7\times10^{-2}$ s^{-1}. (d) $\left(Đ_1/r_c^2\right) = 1.7\times10^{-4}$ s^{-1}. The unary isotherms data are provided in Table S15.

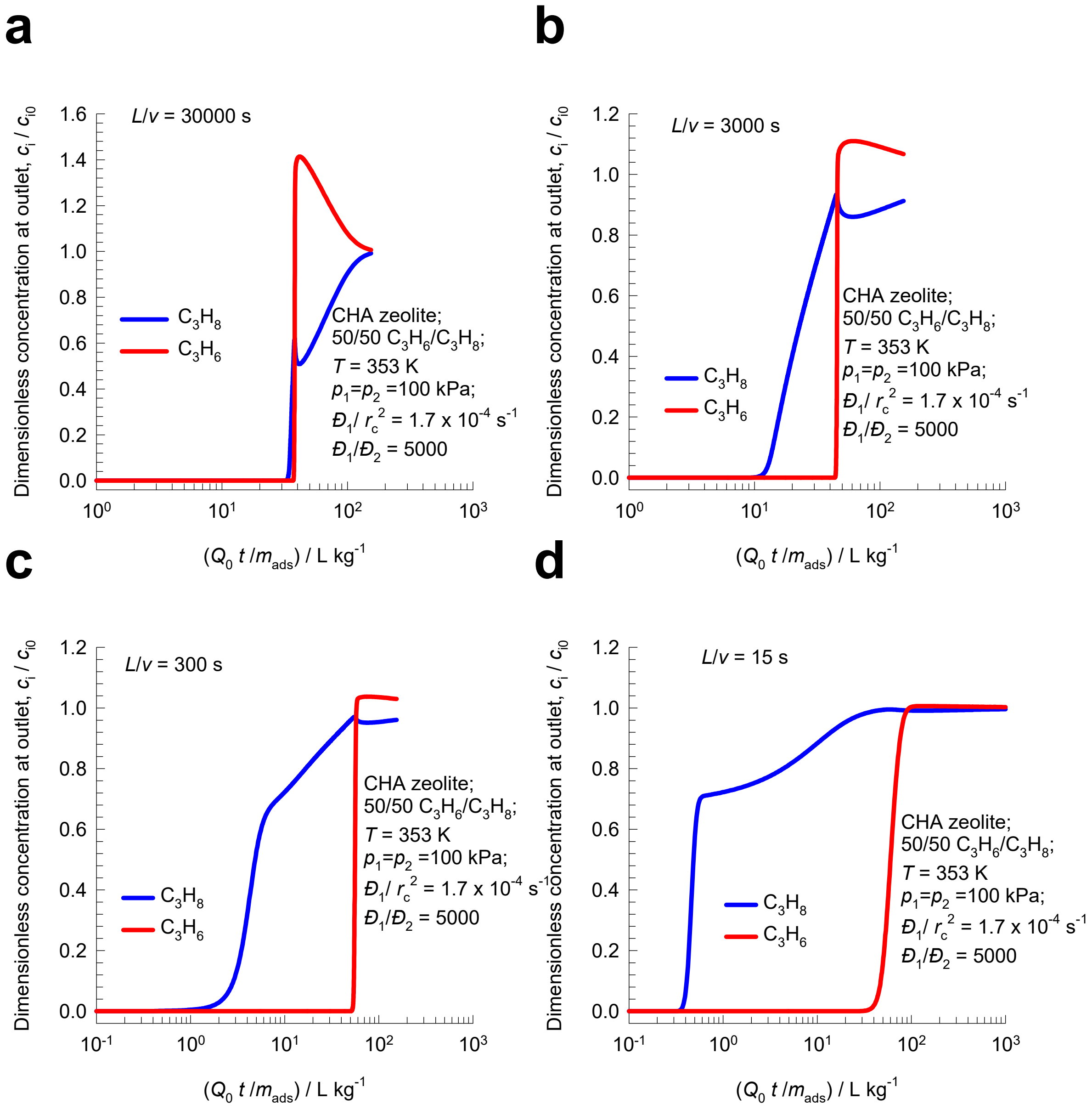

Figure S74. Influence of gas-crystal contact time, L/v, on transient breakthrough simulations for the adsorption cycle for 50/50 C_3H_6/C_3H_8 mixtures in a fixed bed adsorber packed with all-silica CHA operating at 353 K and 200 kPa. In these simulations the bed voidage $\varepsilon = 0.4$, bed length $L = 0.3$ m, the M-S diffusivities are $Đ_1/r_c^2 = 1.7\times10^{-4}$ s^{-1}; $Đ_1/Đ_2 = 5000$. The interstitial velocities are varied: (a) $L/v = 30000$ s, (b) $L/v = 3000$ s, (c) $L/v = 300$ s, and (d) $L/v = 15$ s. The unary isotherm data are provided in Table S15.

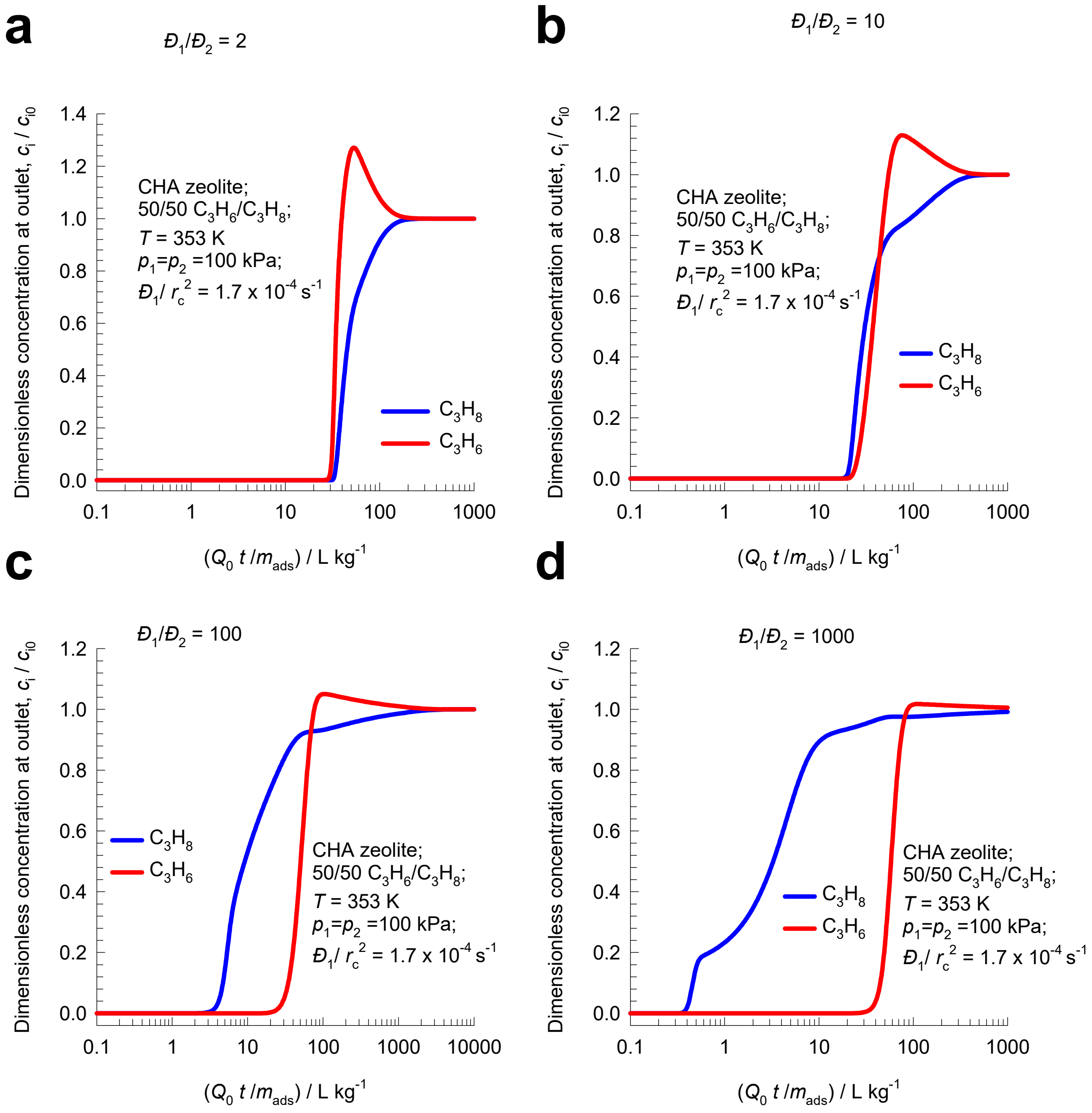

Figure S75. Influence of the ratio of Maxwell-Stefan diffusivities, $Đ_1/Đ_2$, on transient breakthrough simulations for the adsorption cycle for 50/50 C_3H_6/C_3H_8 mixtures in a fixed bed adsorber packed with all-silica CHA operating at 353 K and 200 kPa. In these simulations the bed voidage $\varepsilon = 0.4$, bed length $L = 0.3$ m, the contact time $L/v = 15$ s. The ratio of Maxwell-Stefan diffusivities is varied: $Đ_1/Đ_2 = 2,10,100,1000$. The unary isotherms data are provided in Table S15.

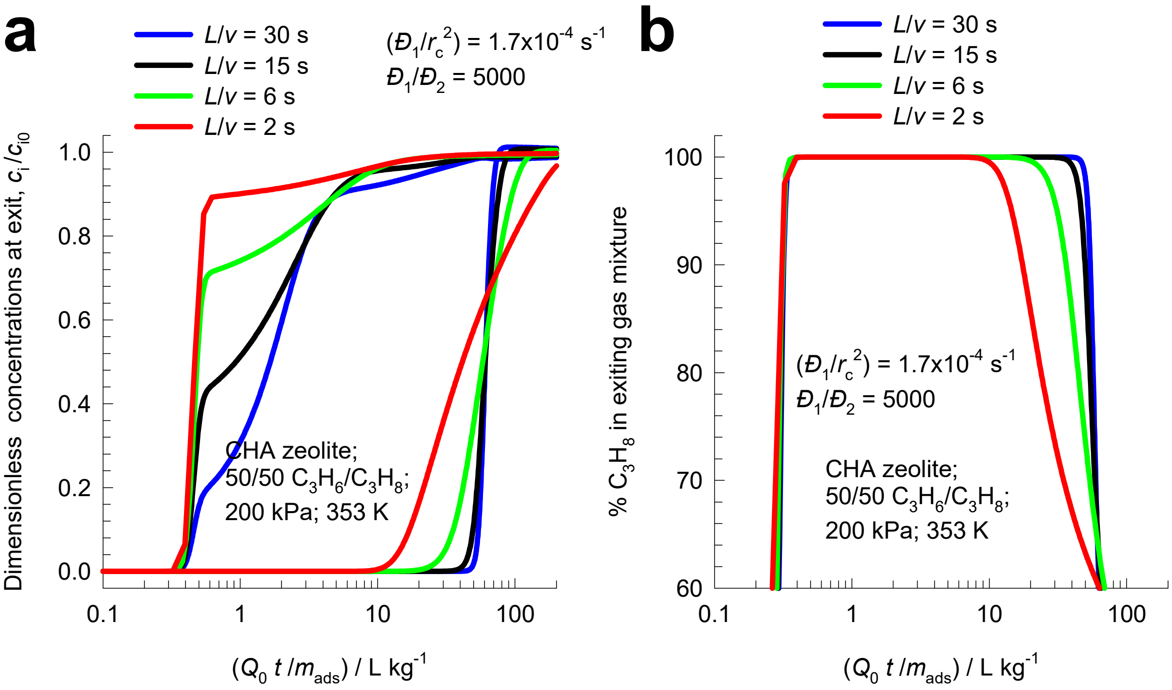

Figure S76. (a, b) Influence of gas-crystal contact time, L/v, on transient breakthrough simulations for the adsorption cycle for 50/50 C_3H_6/C_3H_8 mixtures in a fixed bed adsorber packed with all-silica CHA operating at 353 K and 200 kPa. In these simulations the bed voidage $\varepsilon = 0.4$, bed length $L = 0.3$ m, the M-S diffusivities are $Đ_1/r_c^2 = 1.7\times10^{-4}$ s^{-1}; $Đ_1/Đ_2 = 5000$. The interstitial velocities are varied such that the contact times are $L/v = 2, 6, 15, 30$ s. (b) The % C_3H_8 of the exit gas mixture is plotted as function of $Q_{des} t / m_{ads}$. The unary isotherms data are provided in Table S15.

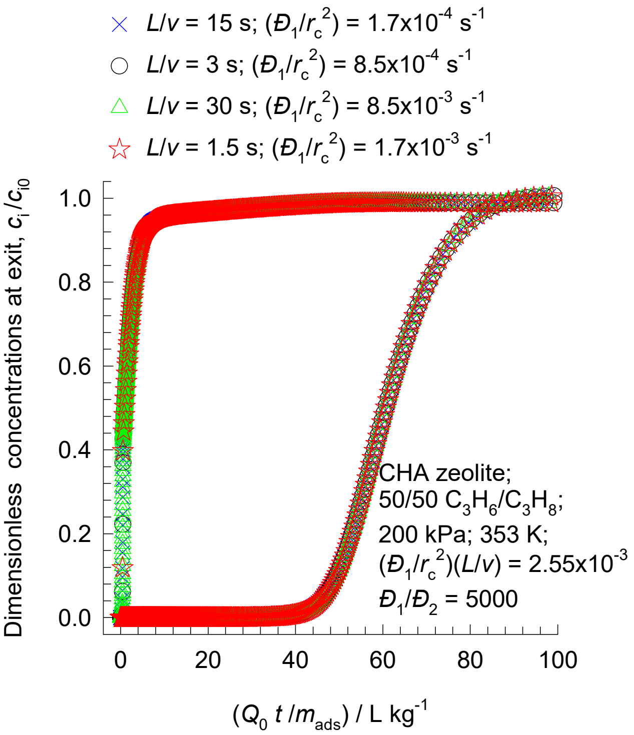

Figure S77. Transient breakthrough simulations for the adsorption cycle for 50/50 C_3H_6/C_3H_8 mixtures in a fixed bed adsorber packed with all-silica CHA operating at 353 K and 200 kPa. In these simulations the bed voidage $\varepsilon = 0.4$, bed length $L = 0.3$ m. In these sets of simulations the interstitial velocities are varied such that the contact times are $L/v = 1.5, 3, 15, 30$ s; the M-S diffusivities and contact times are adjusted such that $\left(Đ_1/r_c^2\right)\left(L/v\right) = 2.55\times10^{-3}$; $Đ_1/Đ_2 = 5000$. The unary isotherms data are provided in Table S15.

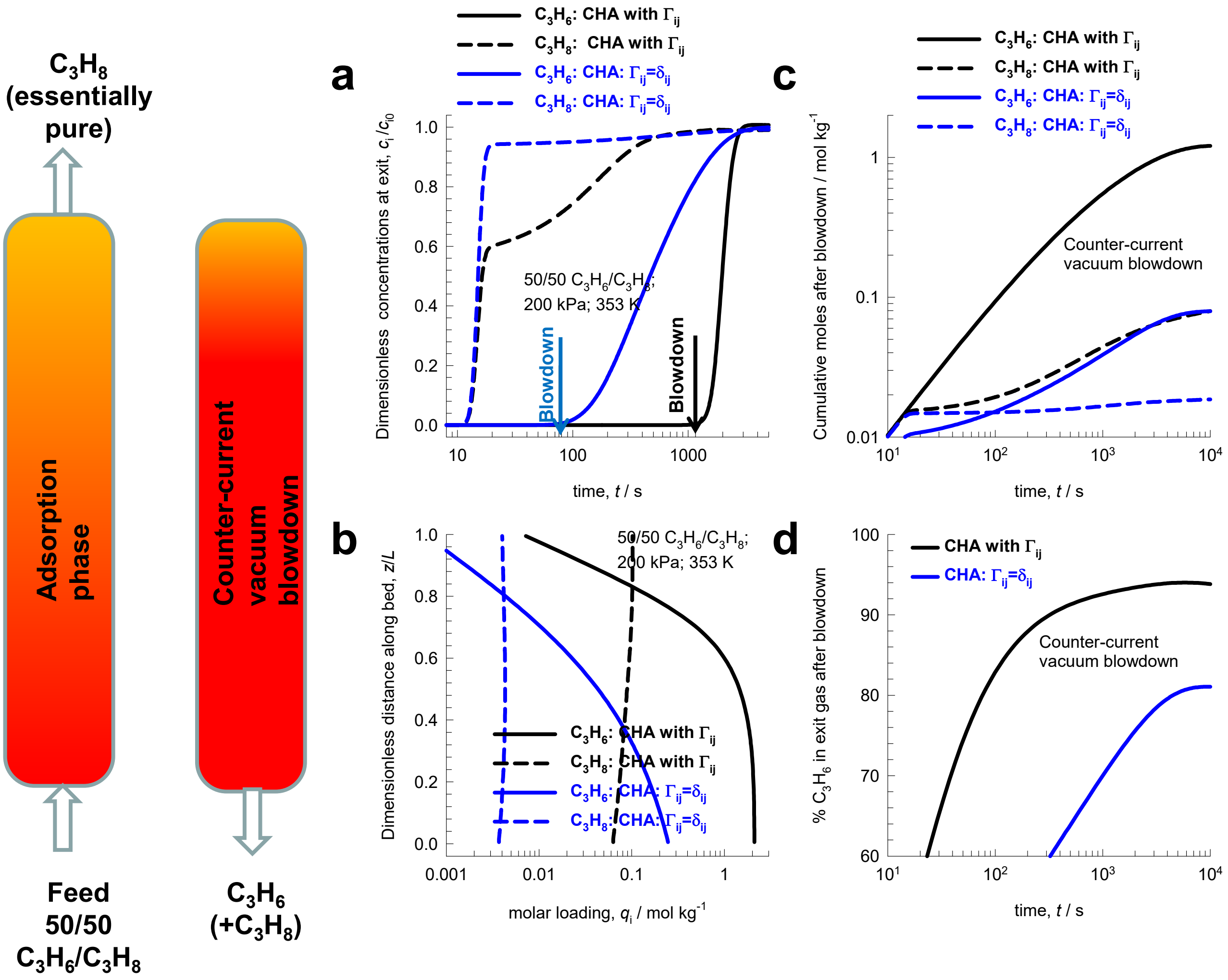

Figure S78. (a) Transient breakthrough simulations for the adsorption cycle for 50/50 C_3H_6/C_3H_8 mixtures in a fixed bed adsorber packed with all-silica CHA operating at 353 K and 200 kPa. (b) Plots of the component loadings along the dimensionless distance, *z*/*L*, along the length of the adsorber at the termination of the adsorption cycle. (c) Cumulative values of the number of moles of C_3H_6 and C_3H_8 that are recovered as function of time. (d) The % C_3H_6 of the exit gas following vacuum blowdown, plotted as function of time. The black lines are simulations based on eq (S11); the blue lines are simulations based on eq (S12), in which the thermodynamic correction factors are assumed to be described by $\Gamma_{ij} = \delta_{ij}$. The input data are provided in Table S15.

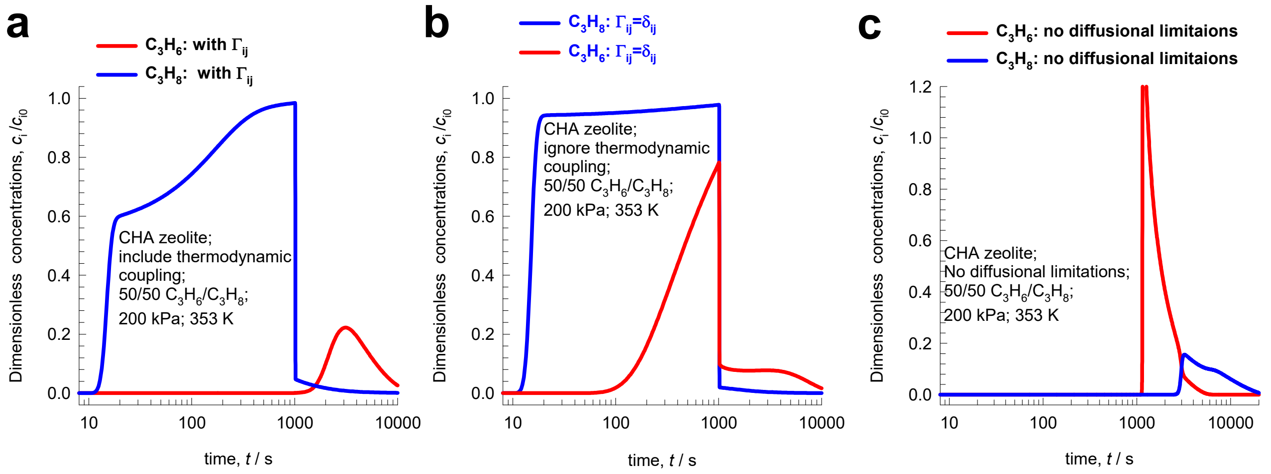

Figure S79. Pulse chromatographic simulations of for separation of 50/50 C_3H_6/C_3H_8 mixtures in a fixed bed adsorber packed with all-silica CHA operating at 353 K and 200 kPa; the feed pulse duration is 1000 s, followed by deep vacuum (2 Pa). Three different model implementations are used in the plots of the dimensionless concentrations at the exit of the packed bed are plotted as a function of time. In (a) the thermodynamic coupling effects are duly accounted for by use eq (S11). In (b) the pulse chromatographic simulations are based on eq (S12) in which the thermodynamic correction factors are assumed to be described by $\Gamma_{ij} = \delta_{ij}$. In (c) intra-crystalline diffusion effects are ignored and eq (S41) is invoked. The input data are provided in Table S15.

ZIF-8 pore landscapes

There are 2 cages per unit cell. To convert from molecules per cage to mol kg^{-1}, multiply by 0.7325.

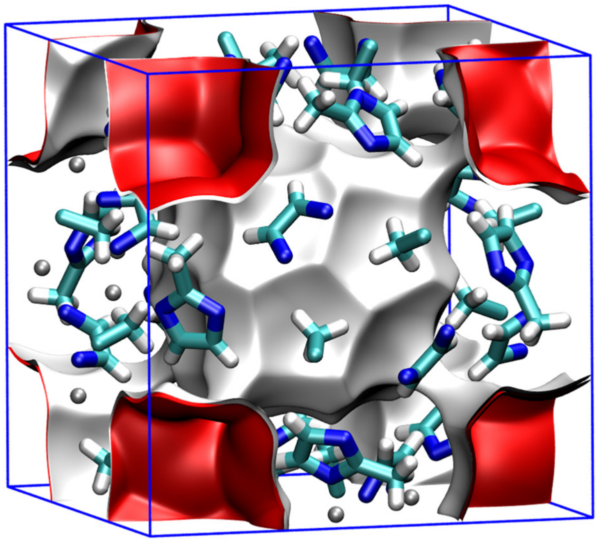

There are 2 cages per unit cell. The volume of one ZIF-8 cage is 1168 Å^3, significantly larger than that of a single cage of DDR (278 Å^3), or FAU (786 Å^3).

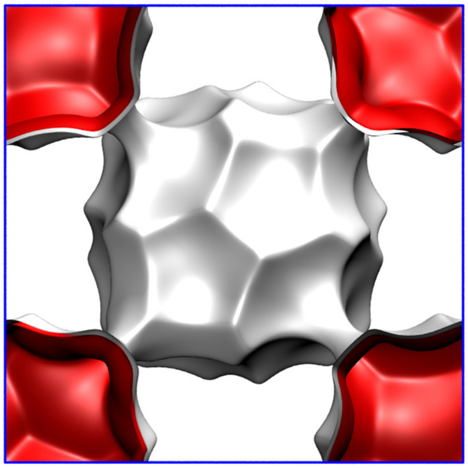

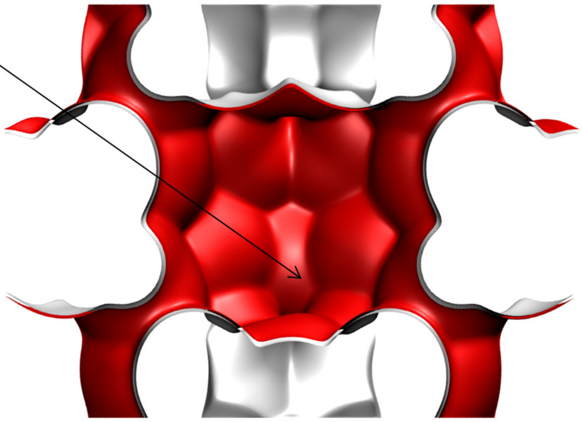

Figure S80. Pore landscape and structural details of ZIF-8.

ZIF-8 dimensions

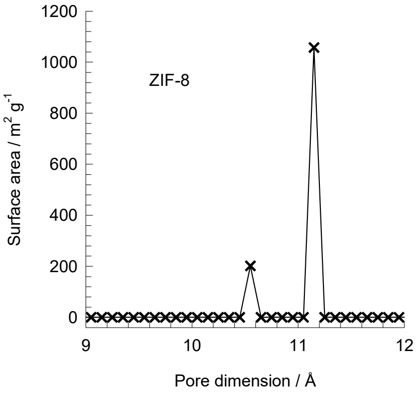

This plot of surface area versus pore dimension is determined using a combination of the DeLaunay triangulation method for pore dimension determination, and the procedure of Düren for determination of the surface area.

	ZIF-8
a /Å	16.991
b /Å	16.991
c /Å	16.991
Cell volume / Å^3	4905.201
conversion factor for [molec/uc] to [mol per kg Framework]	0.3663
conversion factor for [molec/uc] to [kmol/m^3]	0.7106
ρ [kg/m3]	924.253
MW unit cell [g/mol(framework)]	2730.182
ϕ, fractional pore volume	0.476
open space / Å^3/uc	2337.0
Pore volume / cm^3/g	0.515
Surface area /m^2/g	1164.7
DeLaunay diameter /Å	3.26

Figure S81. Pore landscape and structural details of ZIF-8.

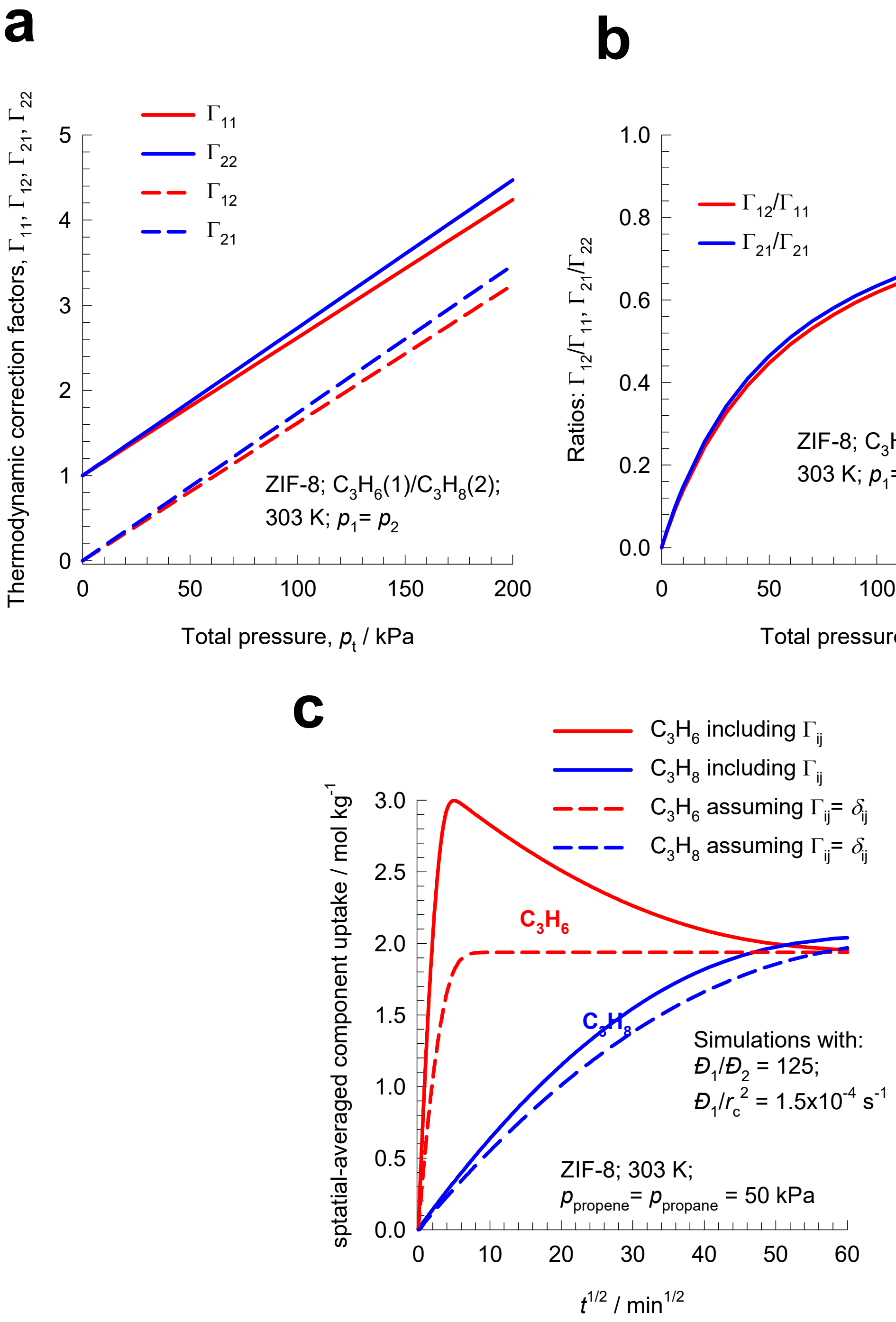

Figure S82. (a) Calculations of the elements of the matrix of thermodynamic factors for 50/50 C_3H_6(1)/C_3H_8(2) mixture adsorption within crystals of all-silica CHA at 353 K (b) Ratios of the off-diagonal elements to the diagonal elements of the matrix of thermodynamic factors. (c) Simulations of transient uptake of 50/50 C_3H_6(1)/C_3H_8(2) mixtures within crystals of ZIF-8 at 303 K; the bulk gas mixture is maintained at partial pressures $p_1 = p_2 = 50$ kPa. The continuous solid lines are Maxwell-Stefan model simulations based on eq (S11). The Maxwell-Stefan diffusivities $Đ_1/r_c^2$ = 1.5×10^{-4} s^{-1}; $Đ_2/r_c^2$ = 1.2×10^{-6} s^{-1}; $Đ_1/Đ_2$ = 125. The dashed lines are the simulations based on eq (S12) in which the thermodynamic correction factors are assumed to be described by $\Gamma_{ij} = \delta_{ij}$, the Kronecker delta. The unary isotherm data are provided in Table S18.

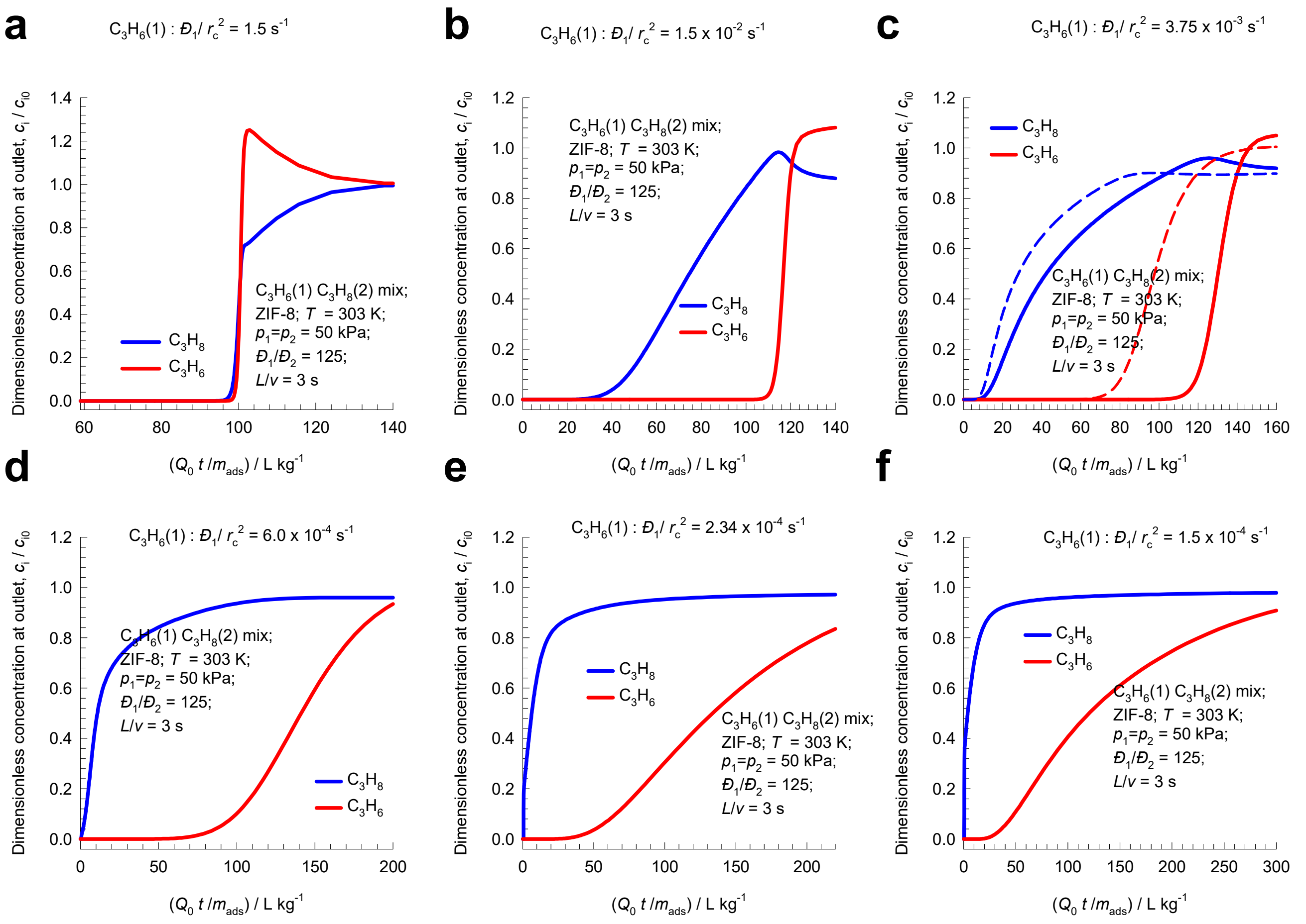

Figure S83. Influence of diffusional time constant $\left(Đ_1/r_c^2\right)$ on transient breakthrough simulations for the adsorption cycle for 50/50 C_3H_6/C_3H_8 mixtures in a fixed bed adsorber packed with ZIF-8 at 303 K operating at 303 K and 100 kPa. In these simulations the bed voidage $\varepsilon = 0.4$, bed length $L = 0.3$ m, the ratio of M-S diffusivities are $Đ_1/Đ_2 = 125$, the interstitial velocities $v = 0.1$ m s^{-1}; the contact times are $L/v = 3$ s. (a) $\left(Đ_1/r_c^2\right) = 1.5$ s^{-1}. (b) $\left(Đ_1/r_c^2\right) = 1.5\times10^{-2}$ s $^{-1}$. (c) $\left(Đ_1/r_c^2\right) = 3.75\times10^{-3}$ s $^{-1}$. (d) $\left(Đ_1/r_c^2\right) = 6.0\times10^{-4}$ s $^{-1}$, (e) $\left(Đ_1/r_c^2\right) = 2.34\times10^{-4}$ s $^{-1}$ (f) $\left(Đ_1/r_c^2\right) = 1.5\times10^{-4}$ s $^{-1}$. The continuous solid lines are Maxwell-Stefan model simulations based on eq (S11).The Maxwell-Stefan diffusivities $Đ_1/r_c^2$ = 1.5×10^{-4} s^{-1}; $Đ_2/r_c^2$ = 1.2×10^{-6} s^{-1}; $Đ_1/Đ_2$ = 125. The dashed lines in (c) are the simulations based on eq (S12) in which the thermodynamic correction factors are assumed to be described by $\Gamma_{ij} = \delta_{ij}$, the Kronecker delta. The unary isotherm data are provided in Table S18.

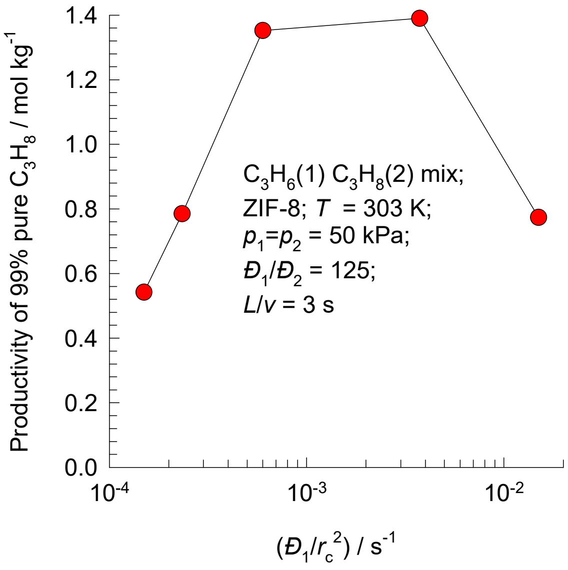

Figure S84. Influence of diffusional time constant $\left(Đ_1/r_c^2\right)$ on the productivity of purified C_3H_8(2) for the adsorption cycle for 50/50 C_3H_6/C_3H_8 mixtures in a fixed bed adsorber packed with ZIF-8 at 303 K operating at 303 K and 100 kPa. The productivity of purified C_3H_8(2), containing less than 1% C_3H_6, plotted as a function of the diffusional time constant $\left(Đ_1/r_c^2\right)$.

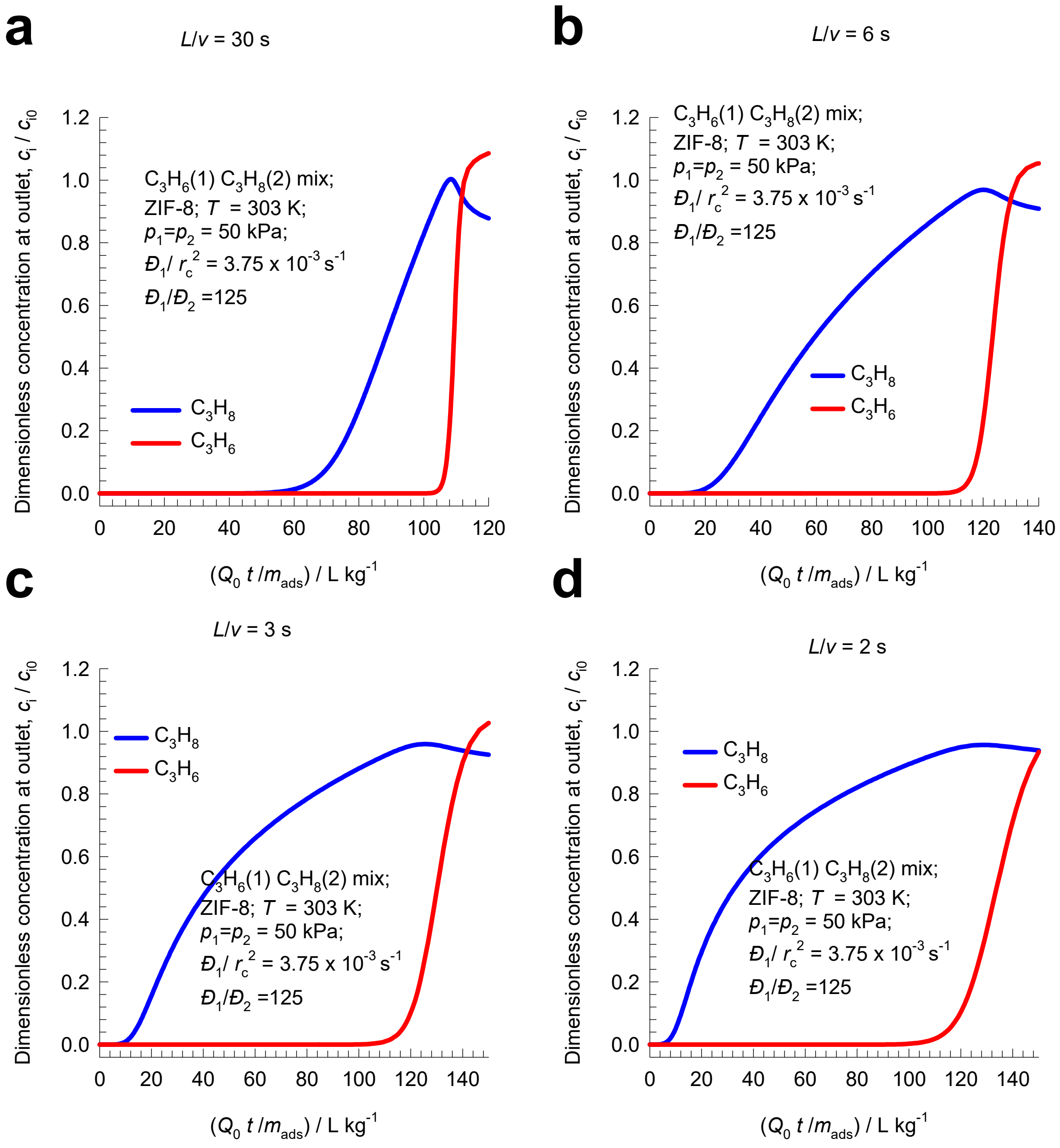

Figure S85. Influence of gas-crystal contact time, L/v, on transient breakthrough simulations for the adsorption cycle for 50/50 C_3H_6/C_3H_8 mixtures in a fixed bed adsorber packed with ZIF-8 operating at 303 K and 100 kPa. In these simulations the bed voidage $\varepsilon = 0.4$, bed length $L = 0.3$ m, the M-S diffusivities are $Đ_1/r_c^2 = 3.75\times10^{-3}$ s^{-1}; $Đ_1/Đ_2 = 125$. The interstitial velocities are varied: (a) $L/v = 30$ s, (b) $L/v = 6$ s, (c) $L/v = 3$ s, and (d) $L/v = 2$ s. The unary isotherm data are provided in Table S18.

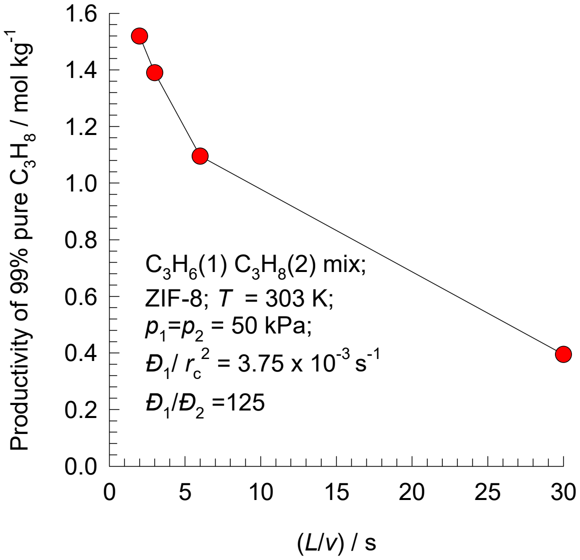

Figure S86. Influence of gas-crystal contact time, L/v, on the productivity of purified C_3H_8(2) for the adsorption cycle for 50/50 C_3H_6/C_3H_8 mixtures in a fixed bed adsorber packed with ZIF-8 at 303 K operating at 303 K and 100 kPa. In these simulations the bed voidage $\varepsilon = 0.4$, bed length $L = 0.3\quad \text{m}$, the M-S diffusivities are $Đ_1/r_c^2 = 3.75\times10^{-3}$ s^{-1}; $Đ_1/Đ_2 = 125$. The productivity of purified C_3H_8(2), containing less than 1% C_3H_6, plotted as a function of gas-crystal contact time, L/v.

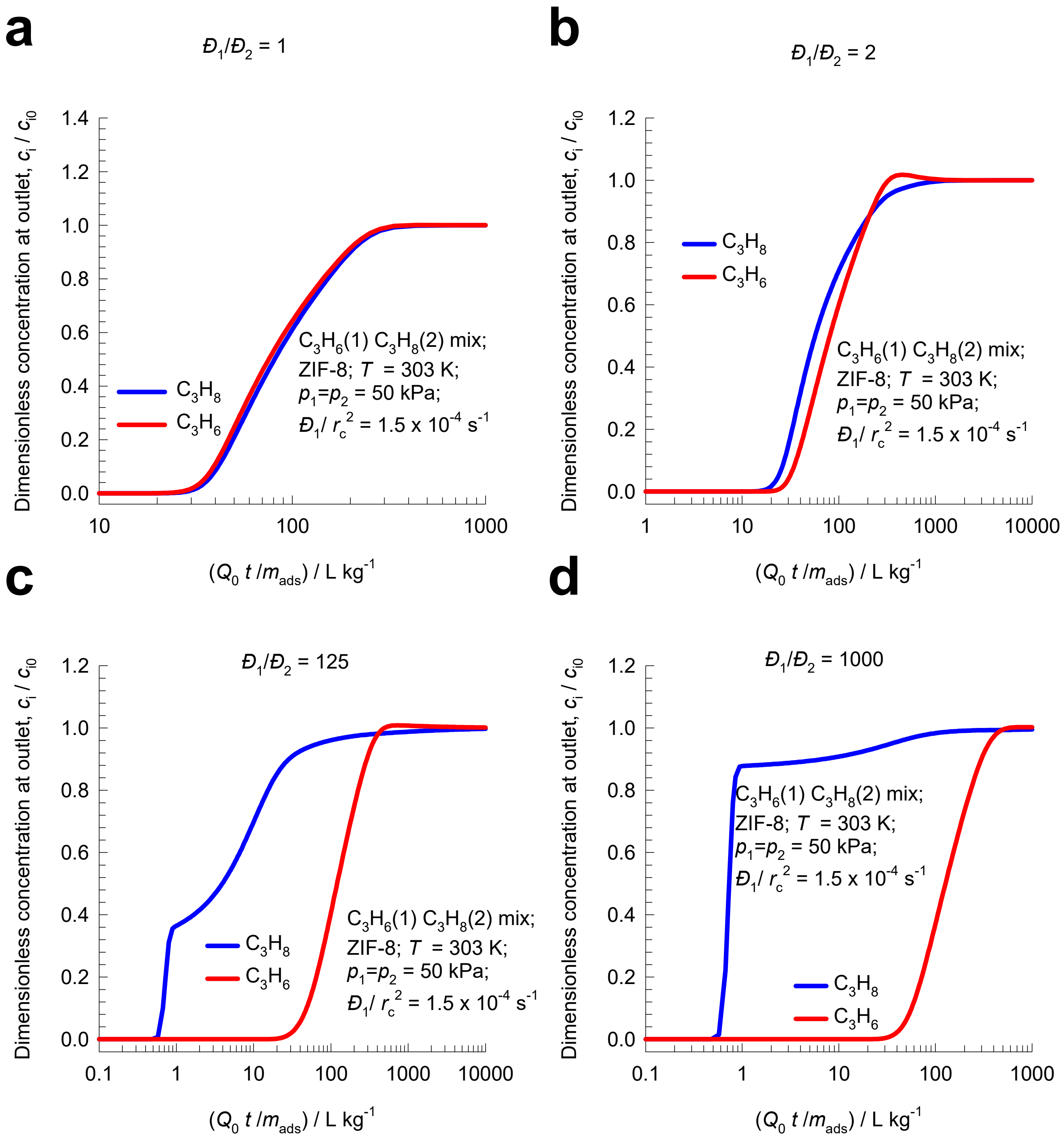

Figure S87. Influence of the ratio of Maxwell-Stefan diffusivities, $Đ_1/Đ_2$, on transient breakthrough simulations for the adsorption cycle for 50/50 C_3H_6/C_3H_8 mixtures in a fixed bed adsorber packed with ZIF-8 operating at 303 K and 100 kPa. In these simulations the bed voidage $\varepsilon = 0.4$, bed length $L = 0.3$ m, the contact time $L/v = 3$ s, $\left(Đ_1/r_c^2\right) = 1.5\times10^{-4}$ s $^{-1}$. The ratio of Maxwell-Stefan diffusivities is varied: $Đ_1/Đ_2 = 1, 2, 125, 1000$. The unary isotherm data are provided in Table S18.

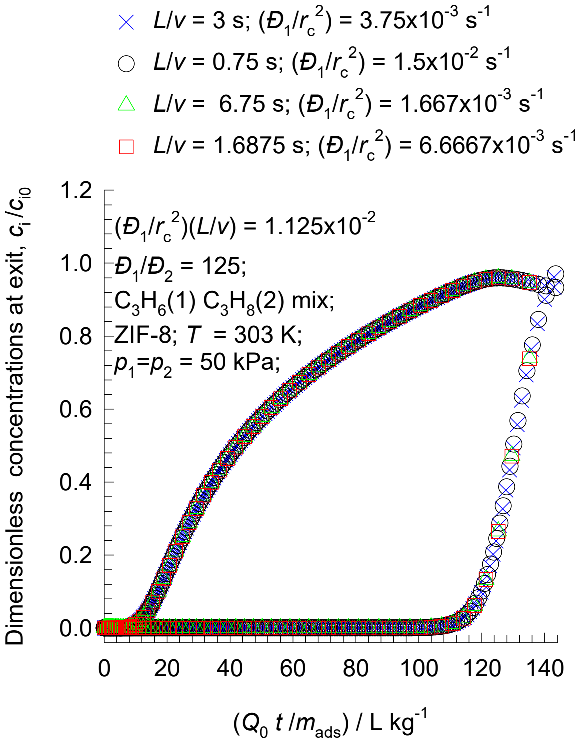

Figure S88. Transient breakthrough simulations for the adsorption cycle for 50/50 C_3H_6/C_3H_8 mixtures in a fixed bed adsorber packed with ZIF-8 operating at 303 K and 100 kPa. In these sets of simulations the interstitial velocities are varied such that the contact times are $L/v = 3, 0.75, 6.75, 1.6875$ s; the diffusional time constants are adjusted such that $\left(Đ_1/r_c^2\right)\left(L/v\right) = 1.125\times10^{-2}$; $Đ_1/Đ_2 = 125$. The unary isotherm data are provided in Table S18.

.

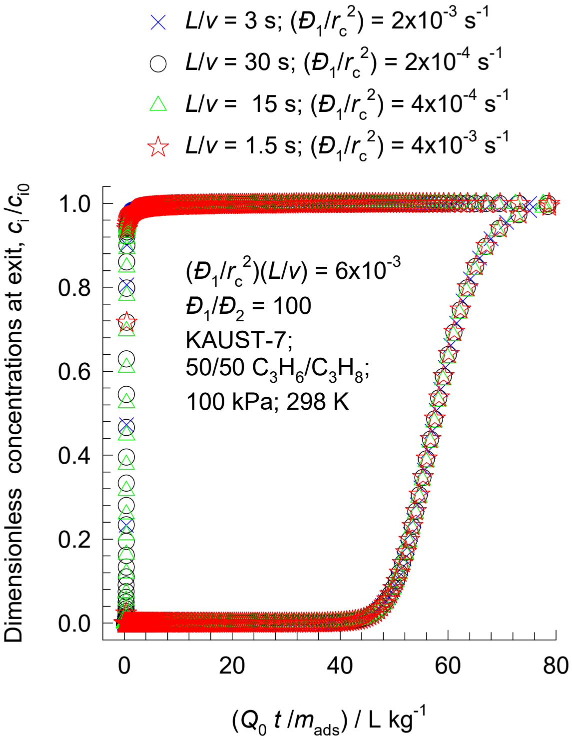

Figure S89. Transient breakthrough simulations for the adsorption cycle for 50/50 C_3H_6/C_3H_8 mixtures in fixed-bed adsorber packed with KAUST-7,[96] operating at 298 K and 100 kPa. In these sets of simulations the interstitial velocities are varied such that the contact times are $L/v = 1.5, 3, 15, 30$ s; the diffusional time constants are adjusted such that $\left(Đ_1/r_c^2\right)\left(L/v\right) = 6\times10^{-3}$; $Đ_1/Đ_2 = 100$. The unary isotherm data are provided in Table S16.

9 Nomenclature

Latin alphabet

b_i	Langmuir parameter, Pa^{-1}
$[B]$	matrix of inverse M-S coefficients, m^{-2} s
c_i	molar concentration of species *i*, mol m^{-3}
c_t	total molar concentration in mixture, mol m^{-3}
c_{i0}	molar concentration of species *i* in fluid mixture at inlet to adsorber, mol m^{-3}
$Đ_i$	Maxwell-Stefan diffusivity for molecule-wall interaction, m^2 s^{-1}
$Đ_{ij}$	M-S exchange coefficient for *n*-component mixture, m^2 s^{-1}
$Đ_{12}$	M-S exchange coefficient for binary mixture, m^2 s^{-1}
$[D]$	Fick diffusivity matrix, m^2 s^{-1}
f_i	partial fugacity of species *i*, Pa
m_{ads}	mass of adsorbent packed in fixed bed, kg
n	number of species in the mixture, dimensionless
L	length of packed bed adsorber, m
N_i	molar flux of species *i* with respect to framework, mol m^{-2} s^{-1}
p_i	partial pressure of species *i* in mixture, Pa
p_t	total system pressure, Pa
q_i	component molar loading of species *i*, mol kg^{-1}
$q_{i,sat}$	molar loading of species *i* at saturation, mol kg^{-1}
q_t	total molar loading in mixture, mol kg^{-1}
$\overline{q}_i(t)$	radial-averaged component loading of species *i*, mol kg^{-1}

Q_0	volumetric flow rate of gas mixture entering fixed bed, m^3 s^{-1}
r	radial direction coordinate, m
r_c	radius of crystallite, m
R	gas constant, 8.314 J mol^{-1} K^{-1}
t	time, s
T	absolute temperature, K
u_i	velocity of motion of adsorbate species *i* with respect to the framework material, m s^{-1}
u	superficial gas velocity in packed bed, m s^{-1}
v	interstitial gas velocity in packed bed, m s^{-1}
x_i	mole fraction of species *i* in adsorbed phase, dimensionless
z	distance along the adsorber, m

Greek alphabet

Γ_{ij}	thermodynamic factors, dimensionless
$[\Gamma]$	matrix of thermodynamic factors, dimensionless
δ_{ij}	Kronecker delta $\delta_{ij}\left(i=j\right)=1;\delta_{ij}\left(i\neq j\right)=0$, dimensionless
ε	voidage of packed bed, dimensionless
θ_i	fractional occupancy of component *i*, dimensionless
θ_t	fractional occupancy of adsorbed mixture, dimensionless
θ_V	fractional vacancy, dimensionless
$[\Lambda]$	matrix of Maxwell-Stefan diffusivities, m^2 s^{-1}
μ_i	molar chemical potential, J mol^{-1}
ν	Freundlich exponent, dimensionless

ρ	framework density, kg m^{-3}

Subscripts

i	referring to component *i*
t	referring to total mixture
sat	referring to saturation conditions

10 References

(1) Krishna, R. Using the Maxwell-Stefan formulation for Highlighting the Influence of Interspecies (1-2) Friction on Binary Mixture Permeation across Microporous and Polymeric Membranes. *J. Membr. Sci.* **2017**, *540*, 261-276. https://doi.org/10.1016/j.memsci.2017.06.062.

(2) Krishna, R. Synergistic and Antisynergistic Intracrystalline Diffusional Influences on Mixture Separations in Fixed Bed Adsorbers. *Precision Chemistry* **2023**, *1*, 83-93. https://doi.org/10.1021/prechem.2c00003.

(3) Krishna, R. The Maxwell-Stefan Description of Mixture Diffusion in Nanoporous Crystalline Materials. *Microporous Mesoporous Mater.* **2014**, *185*, 30-50. https://doi.org/10.1016/j.micromeso.2013.10.026.

(4) Krishna, R.; van Baten, J. M. Maxwell-Stefan modeling of slowing-down effects in mixed gas permeation across porous membranes. *J. Membr. Sci.* **2011**, *383*, 289-300. https://doi.org/10.1016/j.memsci.2011.08.067.

(5) Krishna, R. Tracing the Origins of Transient Overshoots for Binary Mixture Diffusion in Microporous Crystalline Materials. *Phys. Chem. Chem. Phys.* **2016**, *18*, 15482-15495. https://doi.org/10.1039/C6CP00132G.

(6) Myers, A. L.; Prausnitz, J. M. Thermodynamics of Mixed Gas Adsorption. *A.I.Ch.E.J.* **1965**, *11*, 121-130.

(7) Krishna, R. Describing the Diffusion of Guest Molecules inside Porous Structures. *J. Phys. Chem. C* **2009**, *113*, 19756-19781. https://doi.org/10.1021/jp906879d.

(8) Krishna, R. Diffusion in Porous Crystalline Materials. *Chem. Soc. Rev.* **2012**, *41*, 3099-3118. https://doi.org/10.1039/C2CS15284C.

(9) Krishna, R.; van Baten, J. M. Investigating the Influence of Diffusional Coupling on Mixture Permeation across Porous Membranes *J. Membr. Sci.* **2013**, *430*, 113-128.

(10) Krishna, R.; Baur, R. Modelling Issues in Zeolite Based Separation Processes. *Sep. Purif. Technol.* **2003**, *33*, 213-254.

(11) Krishna, R.; van Baten, J. M. Diffusion of alkane mixtures in zeolites. Validating the Maxwell-Stefan formulation using MD simulations. *J. Phys. Chem. B* **2005**, *109*, 6386-6396.

(12) Krishna, R.; van Baten, J. M. Influence of segregated adsorption on mixture diffusion in DDR zeolite. *Chem. Phys. Lett.* **2007**, *446*, 344-349.

(13) Krishna, R.; van Baten, J. M. Insights into diffusion of gases in zeolites gained from molecular dynamics simulations. *Microporous Mesoporous Mater.* **2008**, *109*, 91-108.

(14) Krishna, R.; van Baten, J. M. Segregation effects in adsorption of CO_2 containing mixtures and their consequences for separation selectivities in cage-type zeolites. *Sep. Purif. Technol.* **2008**, *61*, 414-423. https://doi.org/10.1016/j.seppur.2007.12.003.

(15) Krishna, R.; van Baten, J. M. Onsager coefficients for binary mixture diffusion in nanopores. *Chem. Eng. Sci.* **2008**, *63*, 3120-3140.

(16) Krishna, R.; van Baten, J. M. Describing Mixture Diffusion in Microporous Materials under Conditions of Pore Saturation. *J. Phys. Chem. C* **2010**, *114*, 11557-11563.

(17) Krishna, R.; van Baten, J. M. A molecular dynamics investigation of the diffusion characteristics of cavity-type zeolites with 8-ring windows. *Microporous Mesoporous Mater.* **2011**, *137*, 83-91. https://doi.org/10.1016/j.micromeso.2010.08.026.

(18) Habgood, H. W. The Kinetics of Molecular Sieve Action. Sorption of Nitrogen-Methane Mixtures by Linde Molecular Sieve 4A. *Canad. J. Chem.* **1958**, *36*, 1384-1397. https://doi.org/10.1139/v58-204.

(19) Ruthven, D. M.; Farooq, S.; Knaebel, K. S. *Pressure swing adsorption*. VCH Publishers: New York, 1994.

(20) Farooq, S.; Ruthven, D. M. Numerical-Simulation of a Kinetically Controlled Pressure Swing Adsorption Bulk Separation Process Based on a Diffusion-Model. *Chem. Eng. Sci.* **1991**, *46*, 2213-2224.

(21) Farooq, S.; Rathor, M. N.; Hidajat, K. A Predictive Model for a Kinetically Controlled Pressure Swing Adsorption Separation Process. *Chem. Eng. Sci.* **1993**, *48*, 4129-4141.

(22) Khalighi, M.; Chen, Y. F.; Farooq, S.; Karimi, I. A.; Jiang, J. W. Propylene/Propane Separation Using SiCHA. *Ind. Eng. Chem. Res.* **2013**, *52*, 3877-3892. https://doi.org/10.1021/ie3026955.

(23) Siperstein, F. R.; Myers, A. L. Mixed-Gas Adsorption. *A.I.Ch.E.J.* **2001**, *47*, 1141-1159.

(24) Streb, A.; Mazzotti, M. Adsorption for efficient low carbon hydrogen production: part 1—adsorption equilibrium and breakthrough studies for $H_2/CO_2/CH_4$ on zeolite 13X. *Adsorption* **2021**, *27*, 541-558. https://doi.org/10.1007/s10450-021-00306-y.

(25) Krishna, R.; Van Baten, J. M. Using Molecular Simulations to Unravel the Benefits of Characterizing Mixture Permeation in Microporous Membranes in Terms of the Spreading Pressure. *ACS Omega* **2020**, *5*, 32769−32780. https://dx.doi.org/10.1021/acsomega.0c05269.

(26) Krishna, R.; Van Baten, J. M. Elucidation of Selectivity Reversals for Binary Mixture Adsorption in Microporous Adsorbents. *ACS Omega* **2020**, *5*, 9031-9040. https://doi.org/10.1021/acsomega.0c01051.

(27) Krishna, R.; Van Baten, J. M. Using Molecular Simulations for Elucidation of Thermodynamic Non-Idealities in Adsorption of CO_2-containing Mixtures in NaX Zeolite. *ACS Omega* **2020**, *5*, 20535-20542. https://doi.org/10.1021/acsomega.0c02730.

(28) Krishna, R.; Van Baten, J. M. Water/Alcohol Mixture Adsorption in Hydrophobic Materials: Enhanced Water Ingress caused by Hydrogen Bonding. *ACS Omega* **2020**, *5*, 28393-28402. https://doi.org/10.1021/acsomega.0c04491.

(29) Krishna, R.; Van Baten, J. M. Investigating the Non-idealities in Adsorption of CO_2-bearing Mixtures in Cation-exchanged Zeolites. *Sep. Purif. Technol.* **2018**, *206*, 208-217. https://doi.org/10.1016/j.seppur.2018.06.009.

(30) Kooijman, H. A.; Taylor, R. A dynamic nonequilibrium model of tray distillation columns. *A.I.Ch.E.J.* **1995**, *41*, 1852-1863.

(31) Michelsen, M. An efficient general purpose method of integration of stiff ordinary differential equations. *A.I.Ch.E.J.* **1976**, *22*, 594-597.

(32) Bulirsch, R.; Stoer, J. Numerical treatment of ordinary differential equations by extrapolation methods. *Numer. Math.* **1966**, *8*, 1-14.

(33) Krishna, R.; Baur, R. Diffusion, Adsorption and Reaction in Zeolites: Modelling and Numerical Issues. http://krishna.amsterchem.com/zeolite/, University of Amsterdam, Amsterdam, 1 January 2015.

(34) Krishna, R.; van Baten, J. M. Investigating the potential of MgMOF-74 membranes for CO_2 capture. *J. Membr. Sci.* **2011**, *377*, 249-260.

(35) He, Y.; Krishna, R.; Chen, B. Metal-Organic Frameworks with Potential for Energy-Efficient Adsorptive Separation of Light Hydrocarbons. *Energy Environ. Sci.* **2012**, *5*, 9107-9120.

(36) Geddes, R. L. Local efficiencies of bubble-plate fractionators. *Trans. Am. Inst. Chem. Engrs.* **1946**, *42*, 79-105.

(37) Glueckauf, E. Theory of Chromatography. Part 10- Formulae for Diffusion into Spheres and their Application to Chromatography. *Trans. Faraday Soc.* **1955**, *51*, 1540-1551.

(38) Krishna, R. Screening Metal-Organic Frameworks for Mixture Separations in Fixed-Bed Adsorbers using a Combined Selectivity/Capacity Metric. *RSC Adv.* **2017**, *7*, 35724-35737. https://doi.org/10.1039/C7RA07363A.

(39) Krishna, R. Methodologies for Evaluation of Metal-Organic Frameworks in Separation Applications. *RSC Adv.* **2015**, *5*, 52269-52295. https://doi.org/10.1039/C5RA07830J.

(40) Krishna, R. Metrics for Evaluation and Screening of Metal-Organic Frameworks for Applications in Mixture Separations. *ACS Omega* **2020**, *5*, 16987−17004. https://doi.org/10.1021/acsomega.0c02218.

(41) Garg, D. R.; Ruthven, D. M. Effect of the concentration dependence of diffusivity on zeolitic sorption curves. *Chem. Eng. Sci.* **1972**, *27*, 417-423.

(42) Herm, Z. R.; Wiers, B. M.; Van Baten, J. M.; Hudson, M. R.; Zajdel, P.; Brown, C. M.; Maschiocchi, N.; Krishna, R.; Long, J. R. Separation of Hexane Isomers in a Metal-Organic Framework with Triangular Channels *Science* **2013**, *340*, 960-964. https://www.science.org/doi/10.1126/science.1234071.

(43) Krishna, R.; van Baten, J. M. Screening of zeolite adsorbents for separation of hexane isomers: A molecular simulation study. *Sep. Purif. Technol.* **2007**, *55*, 246-255. https://doi.org/10.1016/j.seppur.2006.12.011.

(44) Dubbeldam, D.; Krishna, R.; Calero, S.; Yazaydın, A. Ö. Computer-Assisted Screening of Ordered Crystalline Nanoporous Adsorbents for Separation of Alkane Isomers. *Angew. Chem. Int. Ed.* **2012**, *51*, 11867-11871. https://doi.org/10.1002/anie.201205040.

(45) Dandekar, H. W.; Funk, G. A.; Gillespie, R. D.; Zinnen, H. A.; McGonegal, C. P.; Kojima, M.; Hobbs, S. H., Process for alkane isomerization using reactive chromatography. UOP, Des Plaines, Illinois, USA., *U.S. Pat.*, US 5763730, 1999.

(46) Dandekar, H. W.; Funk, G. A.; Zinnen, H. A., Process for separating and recovering multimethyl-branched alkanes. UOP LLC, Des Plaines, Illinois, USA., *U.S. Pat.*, US 6069289, 2000.

(47) Carr, R. W.; Dandekar, H. W. *Adsorption with reaction*. Reactive Separation Processes; 2nd, Edited by S. Kulprathipanja, 115-154, Taylor & Francis: New York, USA, 2001.(

(48) Krishna, R.; Smit, B.; Calero, S. Entropy effects during sorption of alkanes in zeolites. *Chem. Soc. Rev.* **2002**, *31*, 185-194.

(49) Vlugt, T. J. H.; Zhu, W.; Kapteijn, F.; Moulijn, J. A.; Smit, B.; Krishna, R. Adsorption of linear and branched alkanes in the silicalite-1. *J. Am. Chem. Soc.* **1998**, *120*, 5599-5600.

(50) Vlugt, T. J. H.; Krishna, R.; Smit, B. Molecular Simulations of Adsorption Isotherms for Linear and Branched Alkanes and Their Mixtures in Silicalite. *J. Phys. Chem. B* **1999**, *103*, 1102-1118.

(51) Schenk, M.; Vidal, S. L.; Vlugt, T. J. H.; Smit, B.; Krishna, R. Separation of alkane isomers by exploiting entropy effects during adsorption on silicalite-1: A configurational-bias Monte Carlo simulation study. *Langmuir* **2001**, *17*, 1558-1570.

(52) Titze, T.; Chmelik, C.; Kärger, J.; van Baten, J. M.; Krishna, R. Uncommon Synergy Between Adsorption and Diffusion of Hexane Isomer Mixtures in MFI Zeolite Induced by Configurational Entropy Effects *J. Phys. Chem. C* **2014**, *118*, 2660-2665. https://doi.org/10.1021/jp412526t.

(53) Krishna, R. Highlighting the Influence of Thermodynamic Coupling on Kinetic Separations with Microporous Crystalline Materials. *ACS Omega* **2019**, *4*, 3409-3419. https://doi.org/10.1021/acsomega.8b03480.

(54) Schuring, D.; Jansen, A. P. J.; van Santen, R. A. Concentration and chainlength dependence of the diffusivity of alkanes in zeolites studied with MD simulations. *J. Phys. Chem. B* **2000**, *104*, 941-948.

(55) Krishna, R.; van Baten, J. M. Diffusion of Hydrocarbon Mixtures in MFI Zeolite: Influence of Intersection Blocking. *Chem. Eng. J.* **2008**, *140*, 614-620.

(56) Krishna, R.; Van Baten, J. M. Elucidating Traffic Junction Effects in MFI Zeolite using Kinetic Monte Carlo Simulations. *ACS Omega* **2019**, *4*, 10761-10766. https://doi.org/10.1021/acsomega.9b01369.

(57) Krishna, R.; van Baten, J. M. Using Molecular Dynamics Simulations for Elucidation of Molecular Traffic in Ordered Crystalline Microporous Materials. *Microporous Mesoporous Mater.* **2018**, *258*, 151-169. https://doi.org/10.1016/j.micromeso.2017.09.014.

(58) Cavalcante, C. L.; Ruthven, D. M. Adsorption of Branched and Cyclic Paraffins in Silicalite .2. Kinetics. *Ind. Eng. Chem. Res.* **1995**, *34*, 185-191.

(59) Jolimaître, E.; Tayakout-Fayolle, M.; Jallut, C.; Ragil, K. Determination of mass transfer and thermodynamic properties of branched paraffins in silicalite by inverse chromatography technique. *Ind. Eng. Chem. Res.* **2001**, *40*, 914-926.

(60) Jolimaître, E.; Ragil, K.; Tayakout-Fayolle, M.; Jallut, C. Separation of Mono- and Dibranched Hydrocarbons on Silicalite. *A.I.Ch.E.J.* **2002**, *48*, 1927-1937.

(61) Peralta, D.; Chaplais, G.; Simon-Masseron, A.; Barthelet, K.; Pirngruber, G. D. Separation of C6 paraffins using Zeolitic Imidazolate Frameworks: comparison with zeolite 5A. *Ind. Eng. Chem. Res.* **2012**, *51*, 4692-4702.

(62) Krishna, R.; van Baten, J. M. In silico screening of metal-organic frameworks in separation applications. *Phys. Chem. Chem. Phys.* **2011**, *13*, 10593-10616. https://doi.org/10.1039/C1CP20282K.

(63) Krishna, R. Maxwell-Stefan Modelling of Mixture Desorption Kinetics in Microporous Crystalline Materials. *Sep. Purif. Technol.* **2019**, *229*, 115790. https://doi.org/10.1016/j.seppur.2019.115790.

(64) Binder, T.; Lauerer, A.; Chmelik, C.; Haase, J.; Kärger, J.; Ruthven, D. M. Micro-imaging of transient intracrystalline concentration profiles during two-component uptake of light hydrocarbon - carbon dioxide mixtures by DDR-type zeolites. *Ind. Eng. Chem. Res.* **2015**, *54*, 8997-9004. https://doi.org/10.1021/acs.iecr.5b02163.

(65) Lauerer, A.; Binder, T.; Chmelik, C.; Miersemann, E.; Haase, J.; Ruthven, D. M.; Kärger, J. Uphill Diffusion and Overshooting in the Adsorption of Binary Mixtures in Nanoporous Solids. *Nat. Commun.* **2015**, *6*, 7697. http://dx.doi.org/doi:10.1038/ncomms8697.

(66) Binder, T. *Mass Transport in Nanoporous Materials: New Insights from Micro-Imaging by Interference Microscopy*. Ph.D. Dissertation, Universität Leipzig, Leipzig, 2013.

(67) Krishna, R. Diffusing Uphill with James Clerk Maxwell and Josef Stefan. *Chem. Eng. Sci.* **2019**, *195*, 851-880. https://doi.org/10.1016/j.ces.2018.10.032.

(68) Lastari, F.; Pareek, V.; Trebble, M.; Tade, M. O.; Chinn, D.; Tsai, N. C.; Chan, K. I. Extractive Distillation for CO_2–Ethane Azeotrope Separation. *Chem. Eng. Process.* **2012**, *52*, 155-161. https://doi.org/10.1016/j.cep.2011.10.001.

(69) Ribeiro, C. P.; Freeman, B. D.; Paul, D. R. Pure- and Mixed-Gas Carbon Dioxide/Ethane Permeability and Diffusivity in a Cross-linked Poly(ethylene oxide) Copolymer. *J. Membr. Sci.* **2011**, *377*, 110-123.

(70) Krishna, R. Describing Mixture Permeation across Polymeric Membranes by a Combination of Maxwell-Stefan and Flory-Huggins Models. *Polymer* **2016**, *103*, 124-131.

(71) Krishna, R.; van Baten, J. M. Using the Spreading Pressure to Inter-Relate the Characteristics of Unary, Binary and Ternary Mixture Permeation across Microporous Membranes. *J. Membr. Sci.* **2022**, *643*, 120049. https://doi.org/10.1016/j.memsci.2021.120049.

(72) Lin, R.-B.; Li, L.; Zhou, H.-L.; Wu, H.; He, C.; Li, S.; Krishna, R.; Li, J.; Zhou, W.; Chen, B. Molecular Sieving of Ethylene from Ethane using a Rigid Metal-Organic Framework. *Nature Materials* **2018**, *17*, 1128-1133. http://dx.doi.org/10.1038/s41563-018-0206-2.

(73) Matsuda, R.; Kitaura, R.; Kitagawa, S.; Kubota, Y.; Belosludov, R. V.; Kobayashi, T. C.; Sakamoto, H.; Chiba, T.; Takata, M.; Kawazoe, Y.; Mita, Y. Highly controlled acetylene accommodation in a metal–organic microporous material. *Nature* **2005**, *436*, 238-241.

(74) Fischer, M.; Hoffmann, F.; Fröba, M. New Microporous Materials for Acetylene Storage and C_2H_2/CO_2 Separation: Insights from Molecular Simulations. *ChemPhysChem* **2010**, *11*, 2220-2229.

(75) Li, P.; He, Y.; Zhao, Y.; Weng, L.; Wang, H.; Krishna, R.; Wu, H.; Zhou, W.; O'Keeffe, M.; Han, Y.; Chen, B. A Rod-Packing Microporous Hydrogen-Bonded Organic Framework for Highly Selective Separation of C_2H_2/CO_2 at Room Temperature. *Angew. Chem. Int. Ed.* **2015**, *54*, 574-577.

(76) Chen, K.-J.; Scott, H. S.; Madden, D. G.; Pham, T.; Kumar, A.; Bajpai, A.; Lusi, M.; Forrest, K. A.; Space, B.; Perry IV, J. J.; Zaworotko, M. J. Benchmark C_2H_2/CO_2 and CO_2/C_2H_2 Separation by Two Closely Related Hybrid Ultramicroporous Materials. *Chem* **2016**, *1*, 753-765. https://dx.doi.org/10.1016/j.chempr.2016.10.009.

(77) Jiang, M.; Cui, X.; Yang, L.; Yang, Q.; Zhang, Z.; Yang, Y.; Xing, H. A thermostable anion-pillared metal-organic framework for C_2H_2/C_2H_4 and C_2H_2/CO_2 separations. *Chem. Eng. J.* **2018**, *352*, 803-810. https://doi.org/10.1016/j.cej.2018.07.104.

(78) Luo, F.; Yan, C.; Dang, L.; Krishna, R.; Zhou, W.; Wu, H.; Dong, X.; Han, Y.; Hu, T.-L.; O'Keeffe, M.; Wang, L.; Luo, M.; Lin, R.-B.; Chen, B. UTSA-74: A MOF-74 Isomer with Two Accessible Binding Sites per Metal Center for Highly Selective Gas Separation. *J. Am. Chem. Soc.* **2016**, *138*, 5678-5684.

(79) Ye, Y.; Ma, Z.; Lin, R.-B.; Krishna, R.; Zhou, W.; Lin, Q.; Zhang, Z.; Xiang, S.; Chen, B. Pore Space Partition within a Metal-Organic Framework for Highly Efficient C_2H_2/CO_2 Separation. *J. Am. Chem. Soc.* **2019**, *141*, 4130-4136. https://doi.org/10.1021/jacs.9b00232.

(80) Gao, J.; Qian, X.; Lin, R.-B.; Krishna, R.; Wu, H.; Zhou, W.; Chen, B. Mixed Metal-Organic Framework with Multiple Binding Sites for Efficient C_2H_2/CO_2 Separation. *Angew. Chem. Int. Ed.* **2020**, *59*, 4396-4400. https://doi.org/10.1002/anie.202000323.

(81) Zhang, Y.; Hu, J.; Krishna, R.; Wang, L.; Yang, L.; Cui, X.; Duttwyler, S.; Xing, H. Rational design of microporous MOFs with anionic boron cluster functionality and cooperative dihydrogen binding sites for highly selective capture of acetylene. *Angew. Chem. Int. Ed.* **2020**, *59*, 17664-17669. https://doi.org/10.1002/anie.202007681.

(82) Yang, L.; Yan, L.; Wang, Y.; Liu, Z.; He, J.; Fu, Q.; Liu, D.; Gu, X.; Dai, P.; Li, L.; Zhao, X. Adsorption Site Selective Occupation Strategy within a Metal–Organic Framework for Highly Efficient Sieving Acetylene from Carbon Dioxide. *Angew. Chem. Int. Ed.* **2021**, *60*, 4580-4574. https://doi.org/10.1002/anie.202013965.

(83) Wang, L.; Sun, W.; Zhang, Y.; Xu, N.; Krishna, R.; Hu, J.; Jiang, Y.; He, Y.; Xing, H. Interpenetration symmetry control within ultramicroporous robust boron cluster hybrid MOFs for benchmark purification of acetylene from carbon dioxide. *Angew. Chem. Int. Ed.* **2021**, *xx*, xx. https://doi.org/10.1002/anie.202107963.

(84) Zhang, L.; Jiang, K.; Yang, L.; Li, L.; Hu, E.; Yang, L.; Shao, K.; Xing, H.; Cui, Y.; Yang, Y.; Li, B.; Chen, B.; Qian, G. Benchmark C_2H_2/CO_2 Separation in an Ultramicroporous Metal–Organic Framework via Copper(I)-Alkynyl Chemistry. *Angew. Chem. Int. Ed.* **2021**, *60*, 15995-16002. https://doi.org/10.1002/anie.202102810.

(85) Cui, J.; Qiu, Z.; Yang, L.; Zhang, Z.; Cui, X.; Xing, H. Kinetic-Sieving of Carbon Dioxide from Acetylene through a Novel Sulfonic Ultramicroporous Material. *Angew. Chem. Int. Ed.* **2022**, *61*, e202208756. https://doi.org/10.1002/anie.202208756.

(86) Zhang, Z.; Peh, S. B.; Krishna, R.; Kang, C.; Chai, K.; Wang, Y.; Shi, D.; Zhao, D. Optimal Pore Chemistry in An Ultramicroporous Metal-Organic Framework for Benchmark Inverse CO_2/C_2H_2 Separation. *Angew. Chem. Int. Ed.* **2021**, *60*, 17198–17204. https://doi.org/10.1002/anie.202106769.

(87) He, C.; Zhang, P.; Wang, Y.; Zhang, Y.; Hu, T.; Li, L.; Li, J. Thermodynamic and kinetic synergetic separation of CO_2/C_2H_2 in an ultramicroporous metal-organic framework. *Sep. Purif. Technol.* **2023**, *304*, 122318. https://doi.org/10.1016/j.seppur.2022.122318.

(88) Bhadra, S. J.; Farooq, S. Separation of Methane Nitrogen Mixture by Pressure Swing Adsorption for Natural Gas Upgrading. *Ind. Eng. Chem. Res.* **2011**, *50*, 14030-14045.

(89) Tagliabue, M.; Farrusseng, D.; Valencia, S.; Aguado, S.; Ravon, U.; Rizzo, C.; Corma, A.; Mirodatos, C. Natural gas treating by selective adsorption: Material science and chemical engineering interplay. *Chem. Eng. J.* **2009**, *155*, 553-566.

(90) Majumdar, B.; Bhadra, S. J.; Marathe, R. P.; Farooq, S. Adsorption and Diffusion of Methane and Nitrogen in Barium Exchanged ETS-4. *Ind. Eng. Chem. Res.* **2011**, *50*, 3021-3034. https://doi.org/10.1021/ie1014124.

(91) Wilkins, N. S.; Sawada, J. A.; Rajendran, A. Diffusion of CH_4 and N_2 in Barium-Exchanged Reduced Pore Zorite (Ba-RPZ) and Zeolite 4A. *Ind. Eng. Chem. Res.* **2021**, *60*, 10777-10790. https://doi.org/10.1021/acs.iecr.1c01714.

(92) Jayaraman, A.; Hernandez-Maldonado, A. J.; Yang, R. T.; Chinn, D.; Munson, C. L.; Mohr, D. H. Clinoptilolites for Nitrogen/Methane Separation. *Chem. Eng. Sci.* **2004**, *59*, 2407-2417.

(93) Yang, R. T. *Adsorbents: Fundamentals and Applications*. John Wiley & Sons, Inc.: Hoboken, New Jersey, 2003.

(94) Bhadra, S. J. *Methane-Nitrogen Separation by Pressure Swing Adsorption*. Ph.D. Dissertation, National University of Singapore, Singapore, 2007.

(95) Bloch, E. D.; Queen, W. L.; Krishna, R.; Zadrozny, J. M.; Brown, C. M.; Long, J. R. Hydrocarbon Separations in a Metal-Organic Framework with Open Iron(II) Coordination Sites. *Science* **2012**, *335*, 1606-1610. https://doi.org/10.1126/science.1217544.

(96) Cadiau, A.; Adil, K.; Bhatt, P. M.; Belmabkhout, Y.; Eddaoudi, M. A Metal-Organic Framework–Based Splitter for Separating Propylene from Propane. *Science* **2016**, *353*, 137-140. https://doi.org/10.1126/science.aaf6323.

(97) Yang, H.; Wang, Y.; Krishna, R.; Jia, X.; Wang, Y.; Hong, A. N.; Dang, C.; Castillo, H. E.; Bu, X.; Feng, P. Pore-Space-Partition-Enabled Exceptional Ethane Uptake and Ethane-Selective Ethane−Ethylene Separation. *J. Am. Chem. Soc.* **2020**, *142*, 2222-2227. https://doi.org/10.1021/jacs.9b12924.

(98) Bao, Z.; Wang, J.; Zhang, Z.; Xing, H.; Yang, Q.; Yang, Y.; Wu, H.; Krishna, R.; Zhou, W.; Chen, B.; Ren, Q. Molecular Sieving of Ethane from Ethylene through the molecular Cross-section Size Differentiation in Gallate-based Metal-Organic Frameworks. *Angew. Chem. Int. Ed.* **2018**, *57*, 16020-16025. https://doi.org/10.1002/anie.201808716.

(99) Li, L.; Lin, R.-B.; Krishna, R.; Li, H.; Xiang, S.; Wu, H.; Li, J.; Zhou, W.; Chen, B. Ethane/ethylene Separation in a Metal-Organic Framework with Iron-Peroxo Sites. *Science* **2018**, *362*, 443-446. https://doi.org/10.1126/science.aat0586.

(100) Zhang, X.; Li, L.; Wang, J.-X.; Wen, H.-M.; Krishna, R.; Wu, H.; Zhou, W.; Chen, Z.-N.; Li, B.; Qian, G.; Chen, B. Selective Ethane/Ethylene Separation in a Robust Microporous Hydrogen-Bonded Organic Framework. *J. Am. Chem. Soc.* **2020**, *142*, 633-640. https://doi.org/10.1021/jacs.9b07807.

(101) Da Silva, F. A.; Rodrigues, A. E. Vacuum swing adsorption for propylene/propane separation with 4A zeolite. *Ind. Eng. Chem. Res.* **2001**, *40*, 5758-5774.

(102) Grande, C. A.; Poplow, F.; Rodrigues, A. E. Vacuum pressure swing adsorption to produce polymer-grade polypropylene. *Separ. Sci. Technol.* **2010**, *45*, 1252-1259.

(103) Divekar, S.; Nanoti, A.; Dasgupta, S.; Aarti; Chauhan, R.; Gupta, P.; Garg, M. O.; Singh, S. P.; Mishra, I. M. Adsorption Equilibria of Propylene and Propane on Zeolites and Prediction of Their Binary Adsorption with the Ideal Adsorbed Solution Theory. *J. Chem. Eng. Data* **2016**, *61*, 2629-2637.

(104) Da Silva, F. A.; Rodrigues, A. E. PropylenePropane Separation by Vacuum Swing Adsorption Using 13X Zeolite. *A.I.Ch.E.J.* **2001**, *47*, 341-357.

(105) Geier, S. J.; Mason, J. A.; Bloch, E. D.; Queen, W. L.; Hudson, M. R.; Brown, C. M.; Long, J. R. Selective adsorption of ethylene over ethane and propylene over propane in the metal–organic frameworks M_2(dobdc) (M = Mg, Mn, Fe, Co, Ni, Zn). *Chem. Sci.* **2013**, *4*, 2054-2061.

(106) Bachman, J. E.; Reed, D. A.; Kapelewski, M. T.; Chachra, G.; Jonnavittula, D.; Radaelli, G.; Long, J. R. Enabling alternative ethylene production through its selective adsorption in the metal–organic framework Mn_2(*m*-dobdc). *Energy Environ. Sci.* **2018**, *11*, 2423-2431. http://dx.doi.org/doi:10.1039/c8ee01332b.

(107) Yoon, J. W.; Jang, I. T.; Lee, K.-Y.; Hwang, Y. K.; Chang, J.-S. Adsorptive Separation of Propylene and Propane on a Porous Metal-Organic Framework, Copper Trimesate. *Bull. Korean Chem. Soc.* **2010**, *31*, 220-223.

(108) Böhme, U.; Barth, B.; Paula, C.; Kuhnt, A.; Schwieger, W.; Mundstock, A.; Caro, J.; Hartmann, M. Ethene/Ethane and Propene/Propane Separation via the Olefin and Paraffin Selective Metal−Organic Framework Adsorbents CPO-27 and ZIF-8. *Langmuir* **2013**, *29*, 8592-8600.

(109) Khalighi, M.; Karimi, I. A.; Farooq, S. Comparing SiCHA and 4A Zeolite for Propylene/Propane Separation using a Surrogate-Based Simulation/Optimization Approach. *Ind. Eng. Chem. Res.* **2014**, *53*, 16973-16983.

(110) Liang, B.; Zhang, X.; Xie, Y.; R.-B., L.; Krishna, R.; Cui, H.; Li, Z.; Shi, Y.; Wu, H.; Zhou, W.; Chen, B. An Ultramicroporous Metal–Organic Framework for High Sieving Separation of Propylene from Propane. *J. Am. Chem. Soc.* **2020**, *142*, 17995-17801. https://doi.org/10.1021/jacs.0c09466.

(111) Wu, K.; Guo, L.; Zhang, Z.; Yang, Q.; Yang, Y.; Ren, Q.; Bao, Z. Shaping of Gallate-based Metal-Organic Frameworks for Adsorption Separation of Ethylene from Acetylene and Ethane. *J. Colloid Interface Sci.* **2021**, *581*, 177-184. https://doi.org/10.1016/j.jcis.2020.07.111.

(112) Yan, J.; Sheng, L.; Liu, Y.; Zheng, F.; Chen, L.; Zhang, Z.; Yang, Q.; Yang, Y.; Ren, Q.; Bao, Z. Separation of ethylene and ethane using Co-Gallate pellets in a vacuum swing adsorption process. *Sep. Purif. Technol.* **2023**, *319*, 124075. https://doi.org/10.1016/j.seppur.2023.124075.

(113) Chen, D.-L.; Shang, H.; Zhu, W.; Krishna, R. Transient Breakthroughs of CO_2/CH_4 and C_3H_6/C_3H_8 Mixtures in Fixed Beds packed with Ni-MOF-74. *Chem. Eng. Sci.* **2014**, *117*, 407-415. https://doi.org/10.1016/j.ces.2014.07.008.

(114) Olson, D. H.; Camblor, M. A.; Vallaescusa, L. A.; Kuehl, G. H. Light hydrocarbon sorption properties of pure silica Si-CHA and ITQ-3 and high silica ZSM-58. *Microporous Mesoporous Mater.* **2004**, *67*, 27-33.

(115) Hedin, N.; DeMartin, G. J.; Roth, W. J.; Strohmaier, K. G.; Reyes, S. C. PFG NMR self-diffusion of small hydrocarbons in high silica DDR, CHA and LTA structures. *Microporous Mesoporous Mater.* **2008**, *109*, 327-334.

(116) Ruthven, D. M.; Reyes, S. C. Adsorptive separation of light olefins from paraffins. *Microporous Mesoporous Mater.* **2007**, *104*, 59-66.

(117) Li, K.; Olson, D. H.; Seidel, J.; Emge, T. J.; Gong, H.; Zeng, H.; Li, J. Zeolitic Imidazolate Frameworks for Kinetic Separation of Propane and Propene. *J. Am. Chem. Soc.* **2009**, *131*, 10368-10369.

(118) Krishna, R. Evaluation of Procedures for Estimation of the Isosteric Heat of Adsorption in Microporous Materials. *Chem. Eng. Sci.* **2015**, *123*, 191-196.

(119) Sircar, S.; Myers, A. L. *Gas Separation by Zeolites, Chapter 22*. Handbook of Zeolite Science and Technology; Edited by S.M. Auerbach, K.A. Carrado and P.K. Dutta, 1063-1104, Marcel Dekker: New York, 2003.(

(120) Chng, M. L.; Xiao, Y.; Chung, T.-S.; Toriida, M.; Tamai, S. Enhanced propylene/propane separation by carbonaceous membrane derived from poly (aryl ether ketone)/2,6-bis(4-azidobenzylidene)-4-methyl-cyclohexanone interpenetrating network. *Carbon* **2009**, *47*, 1857-1866.